TWO-SCALE COMMAND SHAPING FOR FEEDFORWARD CONTROL OF NONLINEAR SYSTEMS

A Dissertation
Presented to
The Academic Faculty

by

Justin Wilbanks

In Partial Fulfillment
of the Requirements for the Degree
Doctor of Philosophy in the
George W. Woodruff School of Mechanical Engineering

Georgia Institute of Technology
May 2019

TWO-SCALE COMMAND SHAPING FOR FEEDFORWARD CONTROL OF NONLINEAR SYSTEMS

Approved by:

Dr. Michael J. Leamy, Advisor
School of Mechanical Engineering
Georgia Institute of Technology

Dr. Nader Sadegh
School of Mechanical Engineering
Georgia Institute of Technology

Dr. Kenneth A. Cunefare
School of Mechanical Engineering
Georgia Institute of Technology

Dr. David G. Taylor
School of Electrical and Computer Engineering
Georgia Institute of Technology

Dr. Aldo A. Ferri
School of Mechanical Engineering
Georgia Institute of Technology

Date Approved: January 7, 2019

In memory of Artlitz Collins (A. C.) Whitten and Barry Stanley Whitten

ACKNOWLEDGEMENTS

Above all else I would like to thank the endless support from my family; especially, my mother, Lori Wilbanks, and father, Jamie Wilbanks. The advice and support received from my parents was invaluable in completing my doctoral studies. The time spent around my grandfather, A. C. Whitten, served as the impetus for my pursuit of a degree in mechanical engineering, and without his advice throughout the years I would not have the practical knowledge and ideals that have served me so well through my studies and life. In addition, I would also like to thank my grandmother, Jan Whitten, for providing mental support as well as amazing meals throughout the years. Additionally, I would like to thank my uncle, Barry Whitten, who provided me with a good taste in music, taught me to drive a manual transmission, and showed me the need for a good proofreader.

I would also like to thank my advisor Dr. Leamy for his support throughout the pursuit of my PhD. The indispensable feedback and motivation provided throughout my time in graduate school kept me pushing forward. He also provided me time to prepare for qualifying examinations, presentation opportunities, deadlines to drive me forward, funding opportunities, and the all-important discussions about college football or cars. Without his guidance, I do not believe I would have been able to successfully navigate the completion of my PhD.

In addition, I would also like to thank the members of my reading committee: Dr. Kenneth Cunefare, Dr. Aldo Ferri, Dr. Nader Sadegh, and Dr. Taylor. They have provided insights and assistance during the completion of the work contained in this dissertation. Dr. Ferri also provided me with a great foundation in dynamics in his course during my first

year in graduate school. Additionally, Dr. Taylor provided invaluable assistance in the design of electric systems for the experimental apparatus used in this work. I would also like to thank Dr. Cunefare for providing me with a space to test my experimental apparatus safely. I am also indebted to the members of the Montgomery Machining Mall, specifically Steven Sheffield, Louis Boulanger, Nathan Mauldin, Scott Elliot, and Matthew Carroll, for the help provided in fabricating the experimental setup presented in this dissertation.

I am also thankful to my professors at Clemson University, with a special thanks to Dr. Mocko, Dr. Rebholz, and Dr. Xuan. My supervisors at Michelin Americas Research and Development Corporation, Jack Peterson, Lee Brandon, and Chris Baker, encouraged me to pursue graduate school and helped me towards the completion of a PhD, so I would not be here without their influence.

I would also like to thank the National Science Foundation for supporting the work contained in this dissertation through a National Science Foundation Graduate Research Fellowship under Grant No. DGE-1148903. Additionally, I would like to extend thanks to Ferrari S.p.A. for their technical and financial support during the first two years of my graduate studies. Without these funding sources I would not have been able to finish my PhD.

One of the most important factors in driving me forward in graduate school are the people that I have met during my time here as well as old friends that have helped keep me sane during this long journey. Firstly, the members of my lab group have always provided me with fascinating discussions about research and life in general. I am thankful for the discussions and time that I have spent with: Dr. Jason Kulpe, Oscar Peña, Douglas Cox,

Dr. Amir Darabi, Matt Fronk, Noah Schaich, and Saeid Loghavi. Outside of my lab group I have met some incredible, intelligent people. Without the discussions about soccer and the world with Oscar Peña and Dr. Amir Darabi, my time in graduate school would have been a lot harder. I am thankful for the long distance runs with Jonathan Warner, especially during qualifying exams. I am also thankful for the adventures around Atlanta that I have had with Andrew Carek, Brian Eberle, Andrew Leonard, Sam Seifert, and Zach Brooks. I am also thankful for the time spent with Jake Hawkins while finishing my BS at Clemson University. Additionally, I cannot begin to explain the importance of the trips to a concert or half marathon through a backwoods trail with Taylor Marchbanks and David Welter, respectively.

Lastly, I would like to thank Maggie McDonald and her endless support during my journey through graduate school. The amazing meals, exciting trips, and weekends spent exploring Atlanta helped me destress after the hardest periods of research. Without her support I couldn't have completed my research goals while staying healthy and happy. Also, I could not have made it through qualifying exams without her help and the company of Bernoulli. I am excited to see what the future holds with the knowledge that I have gained here at Georgia Institute of Technology and Clemson University.

TABLE OF CONTENTS

LIST OF TABLES

LIST OF FIGURES

NOMENCLATURE

Latin Symbols

A	Amplitude of residual vibrations
$\boldsymbol{A_A}$	Linearized state matrix for augmented system for EKF application
a_D	Diffusive combustion Wiebe correlation parameter
A_i	Amplitude of i^{th} impulse
a_M	Main combustion Wiebe correlation parameter
A_P	Piston crown area
a_P	Premixed combustion Wiebe correlation parameter
B	ICE cylinder bore
C	Polytropic process constant
$\boldsymbol{C_A}$	Linearized output matrix for EKF application
c_{CE}	Torsional damping of ICE mounts
c_{CL}	Torsional damping of shaft between EM and clutch driven plate assembly
c_{CM}	Torsional damping of EM mounts
c_E	Torsional damping of ICE output shaft
c_F	Torsional damping representing the experimental apparatus frame ground connection
c_{IE}	Torsional damping of inertial element input shaft
$c_{Internal}$	EM internal damping
c_M	Torsional damping of EM output shaft
c_{ME}	Rectilinear damping of ICE mounts
c_{MM}	Rectilinear damping of EM mounts
cn	Jacobi cosine function

cos	Cosine function
C_R	Compression ratio
c_T	Torsional damping representing vehicle suspension and tires
D	Derivative control coefficient
d_{CL}	Diameter of clutch driven plate assembly
d_M	Diameter of the EM body
D_n	Time derivative with respect to T_n
dn	Jacobi delta function
d_R	EM rotor diameter
$\boldsymbol{e}$	Error in estimated state compared to measured output for RLS application
e	Base of the natural logarithm
$\boldsymbol{F}$	Additive process noise matrix of original system for EKF application
F	Input force for Duffing oscillator
$\boldsymbol{f}$	Dynamics of unaugmented system for EKF application
f	Frequency
F_0	Input force magnitude
$F_{0_{Shaped}}$	Linear scale input defined through shaping zero-order problem for Duffing oscillator
F_1	Time-varying component used to mitigate oscillations arising from nonlinear behavior of Duffing oscillator
$\boldsymbol{F_A}$	Augmented additive process noise matrix for EKF application
$\boldsymbol{f_A}$	Dynamics of augmented system for EKF application
F_F	Coulomb friction magnitude for Duffing oscillator
F_{FBL}	Feedback linearization input force for Duffing oscillator
$F_{Inertial}$	Apparent force due to the ICE components in reciprocating motion

f_N New input after feedback linearization of Duffing oscillator

f_{NL} Generalized nonlinear component of the Duffing equation

F_{TSCS} Two-scale command shaping input force for Duffing oscillator

$\boldsymbol{G}$ Additive measurement noise matrix

$\boldsymbol{g_A}$ Dynamics of observed system output for EKF application

H Heaviside function

h_E ICE block height

$\boldsymbol{I}$ Identity matrix

I Integral control coefficient

i_a Armature circuit current

I_i Input shaper designed for mode *i* of a system

J_C Mass moment of inertia of the vehicle chassis

J_{CL} Approximate mass moment of inertia of the clutch driven plate assembly

J_E Equivalent mass moment of inertia of the ICE crankshaft

J_{EB} Approximate mass moment of inertia of the ICE block

J_F Mass moment of inertia of the experimental apparatus frame

J_{G1} Mass moment of inertia of gear on ICE output shaft of experimental apparatus

J_{G2} Mass moment of inertia of gear on EM output shaft of experimental apparatus

J_{IE} Mass moment of inertia of inertial element of experimental apparatus

J_M Equivalent mass moment of inertia of the EM rotor

J_{MB} Approximate mass moment of inertia of the EM housing

K Input shaper amplitude constant

k Discrete time step for EKF application

$\mathbf{K}_{\boldsymbol{A}}$	Kalman gain for EKF application
K_b	EM electromotive force constant
k_{CE}	Torsional stiffness of ICE mounts
k_{CL}	Torsional stiffness of shaft between EM and clutch driven plate assembly
k_{CM}	Torsional stiffness of EM mounts
k_E	Torsional stiffness of ICE output shaft
K_{EI}	Complete elliptic integral of the first kind
k_F	Torsional stiffness representing the experimental apparatus frame ground connection
k_{IE}	Torsional stiffness of inertial element input shaft
${k_{JE}}^2$	Modulus of Jacobi elliptic function
k_M	Torsional stiffness of EM output shaft
k_{ME}	Rectilinear stiffness of ICE mounts
k_{MM}	Rectilinear stiffness of EM mounts
k_p	Pressure friction torque coefficient
K_t	EM torque constant
k_T	Torsional stiffness representing vehicle suspension and tires
k_{ω_1}	First-order angular velocity friction torque coefficient
k_{ω_2}	Second-order angular velocity friction torque coefficient
L	Total prediction error
l	ICE connecting rod length
L_a	Armature circuit impedance
l_E	ICE block width
LHV	Lower heating value of the diesel fuel
l_M	EM housing width

m	Mass of Duffing oscillator
m_{CL}	Clutch mass
m_D	Diffusive combustion shape factor
m_{EB}	ICE block mass
Mi	Vibration mode i
m_{iD}	Mass of fuel injected during diffusive combustion
m_{iM}	Mass of fuel injected during main combustion
$M_{Inertial}$	ICE reciprocating component mass
m_{iP}	Mass of fuel injected during premixed combustion
m_M	Main combustion shape factor
m_{MB}	EM housing mass
m_P	Premixed combustion shape factor
m_R	EM rotor mass
N	Filter coefficient
N_{G1}	Number of teeth on ICE spur gear
N_{G2}	Number of teeth on EM spur gear
$\boldsymbol{P}$	Estimator gain matrix
P	Proportional control coefficient
p	ICE in-cylinder pressure
$\boldsymbol{P_A}$	Error covariance matrix for EKF application
$p_{Ambient}$	Ambient Pressure
$\mathrm{PDF}(v)$	Probability density function of noise v
$\dot{\boldsymbol{P}}$	Time derivative of estimator gain matrix
$\widehat{\boldsymbol{P}}_{\boldsymbol{A}}$	Corrected error covariance matrix for EKF application

$\widetilde{\boldsymbol{P}}_{\boldsymbol{A}}$	Predicted error covariance matrix for EKF application
Q	Heat release due to combustion
q_A	Armature circuit charge
R	ICE rod ratio (l/r)
r	ICE crank radius
R_a	Armature circuit resistance
s	Complex variable resulting from Laplace transform
sgn	Signum function
sin	Sine function
sn	Jacobi sine function
T	General torque component
t	Time
T_0	EM torque applied to ICE without application of TSCS
$T_{0_{Shaped}}$	Shaped zero-order EM torque component
T_1	First-order EM torque component
t_d	Time delay
T_E	Total torque at the ICE crankshaft
$T_{Friction}$	ICE friction torque
$T_{Friction_0}$	Constant friction torque coefficient
t_i	Temporal location of i^{th} impulse
$T_{Indicated}$	ICE indicated torque
$T_{Inertial}$	ICE inertial torque
t_j	Temporal location of last impulse of an impulse sequence
T_M	EM output torque

t_R EM rotor thickness

T_S Sampling time for measured data for EKF application

t_S Settling time

$\boldsymbol{u}$ Input vector for unaugmented system for EKF application

$\bar{\boldsymbol{u}}$ Input value interpolated between $t(k\text{-}1)$ and $t(k)$

V ICE cylinder volume

$\boldsymbol{v}$ Independent, zero-mean additive white Gaussian measurement noise

v General noise term in definition of probability density function

$V_{0_{Shaped}}$ Shaped zero-order component of EM input voltage

V_1 First-order component of EM input voltage

V_A Armature circuit voltage input

V_C ICE clearance volume

v_{Plate} EM mounting plate velocity measured with LDV

V_S Swept cylinder volume

V_{Tol} Tolerable percentage of residual vibration amplitude for EI input shaper design

$\boldsymbol{W}$ Linear transformation of the parameter estimates to the system output space

$\boldsymbol{w}$ Independent, zero-mean additive white Gaussian process noise

$\boldsymbol{W_A}$ Augmented process noise vector for EKF application

X Amplitude of general solution of the Duffing equation

$\boldsymbol{x}$ Unaugmented state vector for EKF application

x Position of Duffing oscillator

$\boldsymbol{x_A}$ Augmented state vector for EKF application

x_{fD} Fraction of fuel burned during diffusive combustion

x_{fM} Fraction of fuel burned during main combustion

x_{fP} Fraction of fuel burned during premixed combustion

x_{IC} Initial position condition of Duffing oscillator

x_n n^{th} – order scale of position expansion

x_P ICE piston position

$\dot{x}$ Velocity of Duffing oscillator

$\dot{\boldsymbol{x}}_{\boldsymbol{A}}$ Time derivative of the augmented state vector for EKF application

$\dot{x}_{IC}$ Initial velocity condition of Duffing oscillator

$\dot{x}_n$ n^{th} – order scale of velocity expansion

$\dot{x}_P$ ICE piston velocity

$\ddot{x}$ Acceleration of Duffing oscillator

$\ddot{x}_n$ n^{th} – order scale of acceleration expansion

$\ddot{x}_P$ ICE piston acceleration

$\widehat{\boldsymbol{x}}_{\boldsymbol{A}}$ Corrected augmented state vector for EKF application

$\widetilde{\boldsymbol{x}}_{\boldsymbol{A}}$ Predicted augmented state vector for EKF application

$\boldsymbol{y}$ System output for EKF application

$\boldsymbol{y}_{\boldsymbol{RLS}}$ Measured output for RLS application

$\widetilde{\boldsymbol{y}}$ Predicted system output for EKF application

$\boldsymbol{z}$ Measured system output sampled at discrete points for EKF application

Greek Symbols

γ Air-fuel mixture specific heat ratio

γ_{NL} Nonlinear coefficient ratio ($\varepsilon/{\omega_n}^2$)

$\Delta\theta_D$ Diffusive combustion duration

$\Delta\theta_M$ Main combustion duration

$\Delta\theta_P$ Premixed combustion duration

ε Nonlinear coefficient / book-keeping parameter

ε_{UC} Unit consistency constant

ζ Damping ratio

ζ_c Chassis system damping ratio for input shaper design

ζ_p Powertrain system damping ratio for input shaper design

$\boldsymbol{\Theta}$ Vector of parameters to be estimated with EKF

θ Phase of Jacobi elliptic function

θ_C Chassis angular position

θ_{CL} Clutch driven plate assembly angular position

θ_E ICE crankshaft angular position

θ_{EB} ICE block angular position

θ_{En} n^{th} – order scale of ICE crankshaft angular position expansion

θ_F Experimental apparatus frame angular position

θ_{FE} Angle between firing events

θ_{G1} ICE spur gear angular position

θ_{G2} EM spur gear angular position

θ_{IE} Inertial element angular position

θ_M EM rotor angular position

θ_{MB} EM housing angular position

θ_n n^{th} component of the estimated parameter vector

$\boldsymbol{\theta_{RLS}}$ Set of parameters being estimated with RLS

θ_{SOCD} Start of diffusive combustion

θ_{SOCM} Start of main combustion

θ_{SOCP} Start of premixed combustion

$\dot{\theta}_C$ Chassis angular velocity

$\dot{\theta}_{CL}$ Clutch driven plate assembly angular velocity

$\dot{\theta}_E$ ICE crankshaft angular velocity

$\dot{\theta}_{EB}$ ICE block angular velocity

$\dot{\theta}_{En}$ n^{th} – order scale of ICE crankshaft angular velocity expansion

$\dot{\theta}_F$ Experimental apparatus frame angular velocity

$\dot{\theta}_{G1}$ ICE spur gear angular velocity

$\dot{\theta}_{G2}$ EM spur gear angular velocity

$\dot{\theta}_{IE}$ Inertial element angular velocity

$\dot{\theta}_M$ EM rotor angular velocity

$\dot{\theta}_{MB}$ EM housing angular velocity

$\dot{\boldsymbol{\theta}}_{\boldsymbol{RLS}}$ Time derivative of parameter vector for RLS application

$\dot{\theta}_{Unshaped}$ ICE crankshaft angular velocity observed with unshaped torque input

$\ddot{\theta}_C$ Chassis angular acceleration

$\ddot{\theta}_{CL}$ Clutch driven plate assembly angular acceleration

$\ddot{\theta}_E$ ICE crankshaft angular acceleration

$\ddot{\theta}_{EB}$ ICE block angular acceleration

$\ddot{\theta}_{En}$ n^{th} – order scale of ICE crankshaft angular acceleration expansion

$\ddot{\theta}_F$ Experimental apparatus frame angular acceleration

$\ddot{\theta}_{G1}$ ICE spur gear angular acceleration

$\ddot{\theta}_{G2}$ EM spur gear angular acceleration

$\ddot{\theta}_{IE}$ Inertial element angular acceleration

$\ddot{\theta}_M$	EM rotor angular acceleration
$\ddot{\theta}_{MB}$	EM housing angular acceleration
μ	Mean of a data distribution
σ	Variance of a set of data
T_n	n^{th} – order scale of time
τ	Dummy variable for an integral over time in RLS application
τ_{ND}	Non-dimensional time ($\omega_n t$)
$\boldsymbol{\Phi_A}$	Discrete time state-transition matrix for the system
ω	Frequency of Jacobi elliptic function
ω_d	Damped natural frequency
$\omega_{Modeled}$	Frequency used in the design of an input shaper in robustness studies
ω_n	Linear natural frequency
ω_{nc}	Chassis system natural frequency for input shaper design
$\omega_{NL,exact}$	Exact nonlinear response frequency for Duffing oscillator
$\omega_{NL,forced}$	Forced method of multiple scales approximation to Duffing oscillator nonlinear response frequency
$\omega_{NL,unforced}$	Unforced method of multiple scales approximation to Duffing oscillator nonlinear response frequency
ω_{np}	Powertrain system natural frequency for input shaper design

Other Symbols

$(\,)^{-1}$	Inverse of a matrix
$\dot{(\,)}$	First derivative with respect to time
$\ddot{(\,)}$	Second derivative with respect to time
$\widehat{(\,)}$	Corrected variable in EKF application
$\widetilde{(\,)}$	Predicted variable in EKF application

$( )^T$	Transpose of a matrix

Acronyms

AWGN	Additive white Gaussian noise
BAS	Belted alternator-starter
CAN	Controller Area Network
DC	Direct current
DDP	Deterministic dynamic programming
DOE	Design of experiments
ECU	Engine controller unit
EI	Extra-insensitive input shaper
EKF	Extended Kalman filtering
EM	Electric machine
ETC	Electronic throttle control
EVO	Exhaust valve opening
FBL	Feedback linearization
FRF	Frequency response function
GHG	Greenhouse gas
HEV	Hybrid electric vehicle
ICE	Internal combustion engine
IG	Interactive generator
ISG	Integrated starter-generator
IVC	Intake valve closing
JTD	Fiat Chrysler Automobiles uniJet Turbo Diesel engine
KF	Kalman filtering
LDV	Laser doppler vibrometer

LQR	Linear-quadratic regulator
MEMS	Microelectromechanical system
NVH	Noise, vibration, and harshness
PDF	Probability density function
PID	Proportional-integral-derivative controller
PMAC	Permanent magnet alternating current
PSD	Power spectral density
RLS	Recursive least-squares
RMS	Root mean square
RPDO	Receive process data object
SI	Specified insensitivity input shaper
SP-SDP	Shortest-path stochastic dynamic programming
SS	Steady-state
TDC	Top dead center
TPDO	Transmit process data object
TSCS	Two-scale command shaping
UM	Unity-magnitude input shaper
UM ZV	Unity-magnitude zero vibration input shaper
VCU	Vehicle controller unit
ZV	Zero vibration input shaper
ZVD	Zero vibration and derivative input shaper

SUMMARY

This research proposes a *two-scale command shaping* (TSCS) approach for tailoring control inputs to nonlinear, flexible systems aimed at reducing undesirable residual vibrations. These systems exhibit control complexities not present in traditional linear systems. The TSCS approach employs problem scale decomposition using an asymptotic method, command shaping of a linear subproblem, and cancellation of a remaining nonlinear subproblem. For traditional and nontraditional Duffing-like nonlinear systems, TSCS is shown herein to outperform other command shaping strategies recently presented in literature. Following initial development, the TSCS approach is further extended to nonlinear systems with uncertain parameters through the implementation of robust command shaping strategies and parameter estimation techniques. Undesirable vibrations arising from internal combustion engine (ICE) restart/shutdown, which occurs in both hybrid electric and conventional vehicles, provides a contemporary motivating problem ideal for TSCS application due to nonlinearities arising in ICE geometry and friction. Using analytical, computational, and experimental means, TSCS applied to this problem is shown to significantly reduce undesirable vibrations while leveraging existing vehicle components. It is anticipated that the developed TSCS approach can be applied to a wide array of nonlinear, flexible systems with little to no additional cost and complexity, making it attractive for further study and adoption.

CHAPTER 1. INTRODUCTION

1.1 Overview

This work is concerned with developing a technique for feedforward control of highly nonlinear systems. The technique developed is termed herein *two-scale command shaping* (TSCS), which applies a scale decomposition using an asymptotic method, cancellation of a nonlinear subproblem, and command shaping of a remaining linear subproblem. Traditional and nontraditional Duffing-like nonlinear systems are utilized to develop and validate the TSCS strategy and compare it to other command shaping strategies. Robust command shaping and parameter estimation techniques are used to extend applicability of TSCS to nonlinear systems with uncertain parameters. TSCS is then applied to mitigate undesirable vibrations arising during internal combustion engine (ICE) restart/shutdown, which is a problem occurring in both modern hybrid electric and conventional vehicles. Using TSCS to reduce oscillations during ICE restart/shutdown in vehicles provides an ideal application and experimental verification. The proposed TSCS strategy is applicable to a variety of nonlinear, flexible systems with minimal added complexity and cost, making it appealing for additional applications.

1.2 Feedforward control of nonlinear systems

Sharp input commands inevitably lead to undesirable oscillations in the response of flexible systems. These oscillations arise in numerous applications, such as in positioning of industrial cranes, movement of microelectromechanical systems (MEMS),

and operation of hybrid electric vehicles (HEVs) [1-7]. Various methods have been proposed for mitigating such oscillations, including feedback control, digital filtering, and command shaping. Feedback control is a common starting point when developing any controller due to its established design procedures and broad applicability. However, feedback control requires accurate, delay-sensitive sensor feedback and tuning of controller gains for adequate performance. In addition, feedback controllers act on an error signal instead of the input; therefore, feedback results in a slower control response than what is possible with a feedforward controller [2].

Feedforward controllers represent an attractive alternative to feedback controllers due to their minimal sensor requirements, decreased cost, lower control effort, and reduced packaging requirements, especially in micro- and nano-scaled systems [3, 4]. Both input shaping and digital filtering are widely-applied feedforward control methods that tailor input commands to reduce residual oscillations. Singhose and Vaughan showed that input shapers were easier to design and implement than digital filters due to closed-form expressions that exist for input shapers, which cannot be derived for the analogous digital filters [8-11]. In addition, the solution space for the input shaping impulse sequences includes the solution spaces for notch and low-pass filters; therefore, these filtering techniques can never be shorter in duration than input shapers [11].

The shaping of reference commands to reduce system residual vibration dates back to the work of Otto J. Smith in the mid-20th century [12, 13]. Smith demonstrated the application of step inputs divided into two or three excitations, and spaced by one-half or one-eighth, respectively, of the natural period of the system [12]. He termed his method

'Posicast control.' When incorporating Posicast control, the system moves with minimal residual vibration in either one-half or one-fourth of the natural period of the system, depending on whether the input is broken into two positive excitations or three excitations (two positive and one negative), respectively [12]. The application of subsequent excitations cancels residual oscillations caused by the first excitation.

With the advent of digital computing, Singer *et al*. [8, 10, 14] further developed and extended Smith's approach, terming it 'input shaping.' Specifically, they generalized the two-excitation formulation of Posicast control into a closed-form expression now commonly termed a zero vibration (ZV) input shaper [8, 10, 14]. A ZV input shaper consists of two impulses convolved with an input command to produce a response that results in zero residual vibration in a linear system because the principle of superposition is used explicitly in its development. Singer, Singhose, and Seering [8, 10] explored various explicit formulations of input shaping with varying levels of robustness to parameter variations by introducing the zero vibration and derivative (ZVD) and extra-insensitive (EI) input shapers. Both the ZVD and EI shapers provide robustness at the cost of an increased impulse sequence duration (a full damped period) in comparison to the one-half period required for the ZV input shaper [9]. By altering the constraint equations used to derive an input shaper, the detrimental effect of variations in the damping and natural frequency of a system are mitigated. The robustness gained from altering the constraint equations of an input shaper alleviates several shortcomings presented by Smith in his development of Posicast control [12, 13].

Singhose *et al.* also developed formal definitions for input shapers with positive and negative impulses, which were first introduced with Smith's Posicast control [12, 15]. Admitting negative impulses creates input shapers that result in significantly faster response times than possible with only positive impulses. In fact, some negative input shapers result in time-optimal control of flexible systems [15, 16]. However, the shorter duration of these shapers comes at the cost of larger energy usage and increased likelihood of exciting higher-order modes, which exacerbates the effect of nonlinearities [15].

Since its inception, use of command shaping for crane positioning has been a motivating application due to large sway oscillations commonly induced during maneuvers. As such, Smith used an undamped pendulum to introduce the idea of Posicast control in the 1950s [12]. Several years later Alsop *et al.* explored a form of input shaping by controlling the acceleration of a crane's trolley in several steps of constant acceleration until zero oscillation angle is reached in a multiple of a full period, at which point the trolley continues forward at constant velocity [17]. Once the trolley has approached its final position, a deceleration profile symmetric to the acceleration of the trolley is used to bring the crane to rest. In his development, Alsop used a linear approximation to the frequency of a simple crane model [17]. The input shaping solutions developed by Singhose, Singer, and Seering were applied to various industrial crane configurations, such as bridge, gantry, and tower cranes [18-20]. These studies include applying a multi-mode ZV input shaper to a double-pendulum bridge crane. The impulse sequence developed based on ZV input shaping was able to mitigate both modes of the double-pendulum payload with up to 10% and 20% variations in the low and high modes, respectively [18]. Singhose *et al.* also

explored the impact of payload hoisting on the efficacy of robust input shaping applied to a gantry crane with the payload hoisted during motion [19]. Vaughan *et al.* applied specified insensitivity (SI) input shapers to mitigate the two vibration modes of a tower crane with a double-pendulum payload traversing an obstacle course [20]. The SI input shapers allowed Vaughan *et al.* to specify frequency ranges over which residual vibrations are suppressed.

The application of command shaping is clearly not limited to cranes. Popa *et al.* applied a ZVD input shaper to the voltage input of a MEMS actuator [21]. A discrete model was used to define the impulse sequence of the ZVD input shaper, which was applied to a third-order nonlinear model based on finite element analysis displacement data. Residual oscillations persisted, however, due to the significant influence of the MEMS actuator nonlinearities. In vehicle applications, Togai and Platten applied command shaping to a driver torque request in the form of a notch filter designed with resonant frequencies obtained from a linearized powertrain model [22]. Residual oscillations persisted in the driveline, again due to the significant nonlinearities and changes in operating conditions of the powertrain. Singhose *et al.* applied ZVD and EI input shapers to reduce the residual vibrations of a flexible spacecraft resulting from a commanded position or velocity [23]. The shapers were designed to eliminate multiple known vibration modes of the spacecraft, but as in other studies, residual oscillations remained due to the nonlinearities present in the spacecraft model.

Since design of an input shaper only requires estimates of the natural frequency and damping ratio of the undesired vibration mode, most studies elect to linearize otherwise

nonlinear system models to obtain the requisite frequencies. When a system exhibits a large nonlinearity, the efficacy of an input shaper designed through linearization degrades, which was observed in the works of several researchers including Singhose *et al.*, Vaughan *et al.*, and Popa *et al.* [20, 21, 23]. The cause of the degradation depends on the type of nonlinearity, but primarily occurs due to the tailoring of the impulse sequence assuming the system is governed by a linear, time-invariant second order differential equation [2]. Several researchers have proposed methods to mitigate the impact of nonlinearities on the efficacy of input shaping. Sorensen presented multiple methods for treating nonlinearities arising in the operation of bridge and gantry cranes, such as saturation, dead-zone, rate limiting, finite-state actuation, and backlash [24]. Bradley *et al.* explored using input shaping on a system with a nonlinearity arising from asymmetrical acceleration of the actuator of a bridge crane [25]. Minimizing the effect of a nonlinear actuator on the implementation of a unity-magnitude (UM) ZV input shaper was accomplished by updating the temporal locations of the impulses of the shaper to minimize crane residual vibrations. Blackburn *et al.* addressed the nonlinearities arising from gyroscopic effects in rotational motion of a tower crane [26]. They updated their impulse sequence to account for the nonlinear dynamics of the tower crane undergoing a rotational, or slewing motion. J. Smith *et al.* [27] minimized the nonlinear effect of position-dependency in a natural frequency. The natural frequency for the impulse sequence was based on either the final frequency of the undesired vibration mode, the average frequency for the undesired vibration mode, or through an optimization process that minimizes the residual vibration

based on the potential and kinetic energy within the system. Updating the impulse sequence with these methods significantly improved the input shaping efficacy.

More recently, Daqaq *et al.* explored using nonlinear analysis techniques and input shaping on cranes and MEMS devices [1, 3]. The method of multiple scales was used in place of linearization to arrive at a frequency estimate. In the case of a crane, following obtainment of an estimated nonlinear frequency, the acceleration profile for the crane trolley was defined to minimize residual oscillations through a less explicit form of input shaping called bang-coast-bang control [1]. In a MEMS system, Daqaq *et al.* [3] again used the method of multiple of scales to define a first-order nonlinear approximate solution, which was then employed to redefine the impulse sequence of a ZV input shaper to minimize residual oscillation in a torsional micromirror [3]. The first-order nonlinear approximate solution was used alongside an expression of the total energy to recursively solve for the amplitude of the first impulse and temporal location of the second impulse. This is similar to the approach taken by Smith *et al.* [27] in their exploration of input shaping applied to a tower crane.

This dissertation introduces TSCS to extend feedforward command shaping to nonlinear systems. Unlike the approaches proposed by Daqaq *et al.* [1, 3] and Smith *et al.* [27], which effectively implement the linear input shaping technique using nonlinear frequency estimates, TSCS decomposes the fully nonlinear system and commanded forcing into two scales, with the zeroth-order scale governing the linear portion of the system, and the remaining scale governing the nonlinearity of the system. The nonlinear response, in an asymptotic sense, is canceled by the accompanying force component at the

same scale, while input shaping is applied to the zeroth-order linear problem to mitigate residual vibrations. The ease and effectiveness of the approach mainly arises from (i) applying input shaping to a *linear* problem, *vis-à-vis* a nonlinear problem as in other approaches, and (ii) cancellation of a generally nonlinear problem at a separate scale. The latter enables the technique, in principle, to be applied to generally nonlinear systems of analytic form, either weak or strong.

1.3 Vibration-related issues associated with internal combustion engine restart/shutdown

Undesirable vibrations in powertrains during ICE restart/shutdown, which occurs in both HEVs and modern conventional powertrains, provides a motivating problem suitable for TSCS due to nonlinearities that arise due to the ICE dynamics. The transportation sector in the United States accounted for 71% of the petroleum usage and 33% of the greenhouse gas (GHG) emissions in 2012 [28, 29]. Additionally, this sector is one of the most rapidly growing sources of CO_2 emissions [30]. By 2050, the emissions from the transportation sector are expected to double [30, 31]. Increasingly stringent governmental standards and consumer demand have made HEVs an expanding segment in the automotive market. HEVs benefit by operating downsized ICEs at efficient operating points with hybrid drive modes, which results in engines with less cylinders and higher efficiencies. This trend towards fewer cylinders is also occurring in conventional vehicles, where the wider use of forced induction and direct injection is making it possible to use smaller engines without sacrificing performance. However, increases in noise, vibration, and harshness (NVH) typically accompany cylinder reduction, and are particularly acute

in HEVs and conventional vehicles equipped with the increasingly ubiquitous stop-start features. These features can impact the drivability of vehicles by inducing undesirable vibrations during a consumer's daily drive, especially in cases where the engine has been downsized to improve the operating efficiency.

Drivability issues associated with stop-start features have been explicitly noted in the development of several recent vehicles. These issues ultimately affect the design choices and business decisions of large automotive manufacturers. Larry Nitz, General Motor's Executive Director of Hybrid and Electric Powertrain Engineering, noted that a down-sized three-cylinder engine was not used in the 2016 Chevrolet Volt because it "presents some NVH challenges, particularly at start-up, in an electrified vehicle where noise and vibration are not welcome in the drive experience [32]." Issues arising from ICE restart/shutdown also affect strategic business decisions, such as Mazda North American Operations choosing not to bring engine stop-start features to the US even though the technology has been present in Mazda Motor Corporation's vehicles in Japan since 2010 [33].

Not only does ICE restart/shutdown affect business and engineering decisions in relation to stop-start features, it also affects consumer's perception of the vehicles equipped with such features. A quick search through recent popular automotive publications reveals several examples of critical reviews of ICE stop-start features. In a review of the 2016 Mercedes Benz E-Class equipped with a turbocharged four-cylinder ICE, Autoweek's Senior Editor stated that the "stop/start engagement is also rough, compared to other Mercedes-Benzes with V engines [34]." When experiencing the operation of the engine

stop-start system of the 2015 Porsche Macan S, an Executive Editor at Edmunds noted that "the engine comes to life with a noticeable chug that has me looking for the off switch almost instantly [35]." The West Coast Editor of Automotive News went as far as to compare the engine stop-start system reengagement with "a bothersome child behind you, one who keeps kicking your seatback [36]." Therefore, it is important that improvements to fuel economy or emissions is not at the cost of consumer satisfaction, since they are commonly opposing goals.

Mitigating drivability issues in nontraditional powertrains is a focal point in vehicle research and development [5, 32, 34, 37-39]. Kum *et al.* studied the drivability issues arising during engine starts for a pre-transmission parallel HEV with a single electric machine (EM) [5]. Their study focused on the control algorithm optimization for the clutch and motor to minimize drivability issues during engine starts while reducing the required motor and battery power. Canova *et al.* explored a closed-loop control strategy to eliminate undesirable vibrations in a power-split HEV equipped with a belted alternator-starter (BAS) during engine on/off events [5]. Their research demonstrated that a lead-lag controller designed with the root locus method and optimized with design of experiments (DOE), or a controller created using the linear-quadratic regulator (LQR) technique, could be used to improve the vehicle's NVH signature during engine start. Zuo *et al.* also studied ICE start in a power-split HEV [7]. In their research, a rule-based control strategy was used to control the powertrain components to reduce vibrations from speed oscillations in the ICE and improve fuel economy during the engine start process by optimizing the engine operating point. Wang *et al.* explored control strategy optimization for the engine controller

unit (ECU) and vehicle controller unit (VCU) for improving fuel consumption without affecting drivability during engine starts and vehicle acceleration in an integrated starter-generator (ISG) parallel HEV [8]. Through analyzing the engine start process and control development, they could produce a control strategy that helped prevent vehicle jerk and fuel usage during vehicle acceleration as well as minimize fuel use during engine starts.

Command shaping would appear to be a promising technology for reducing vibrations in HEV powertrains during mode transitions and engine restart. Command shaping is a feed-forward control technique that reduces system vibrations using strategically shaped input commands [9]. The shaped input mitigates vibration caused by the equivalent unshaped command, often with little impact on cost, weight, and system complexity. Togai and Platten studied input torque shaping to reduce longitudinal vibrations arising from ICE torque fluctuations in a conventional powertrain caused by the driver's throttle input [10]. Park *et al.* explored command shaping with an electronic throttle control (ETC) system in a conventional vehicle with a manual transmission to minimize the shock-jerk phenomenon [11]. Their research showed that command shaping is more effective in reducing vibrations in the driveline than input filtering, a conclusion shared by Singhose and Vaughan in their theoretical and experimental portable bridge crane analyses [11-13].

1.4 Two-scale command shaping applied to internal combustion engine restart/shutdown

As reviewed above, existing research has focused on altering the supervisory controller using optimal control algorithms, such as shortest-path stochastic dynamic programming (SP-SDP), deterministic dynamic programming (DDP), or implementing novel feedback control strategies for the supervisory controller and/or lower level control systems. These control strategies significantly add to the vehicle controller complexity and require substantial tuning for each vehicle platform. Instead, this work proposes a two-scale command shaping strategy with straightforward implementation that avoids the need for accurate, delay-sensitive sensor feedback and controller gains. In HEVs or powertrains equipped with a stop-start feature, existing components (e.g., the onboard EM and its inverter) can be used to implement the method, which minimizes the cost and weight penalties associated with the proposed strategy.

When implementing the TSCS strategy in a real-time application, uncertainty in system parameters may decrease the strategy's effectiveness. The effect of variations in the driveline and chassis parameters can be mitigated by using robust command shaping strategies, such as ZVD, EI, and perturbation-based EI input shapers, since these variations affect only the vibration frequencies observed in the driveline and chassis [7, 9, 40-42]. Adaptive techniques can also be leveraged in place of robust input shapers to minimize the uncertainty in the vibration modes of system [43-45]. However, robust command shaping is unable to address misidentification of uncertain ICE parameters, such as friction

coefficients and equivalent inertia of the crankshaft and counterbalances, which affect the *nonlinear* character of the system response (and not just the system natural frequencies).

Parameter estimation is anticipated to be a critical component of fully-implemented TSCS strategies. Uncertain parameters can be estimated in a multitude of ways, including using recursive least-squares (RLS) and Bayesian estimation methods, such as extended Kalman filtering (EKF) [46-52]. Parameter estimation is ubiquitous in several fields including the automotive and aerospace industries [46, 53-56]. Parameters that present as linear in the system model can be analyzed with the RLS algorithm; however, the EKF method is required to estimate inherently nonlinear parameters.

Anticipating the need for accurate parameter estimation and robust implementation, this dissertation explores the application of TSCS with EKF and RLS to mitigate the effect of variations in ICE parameters. Additionally, robust command shaping is applied to lessen the impact of errors in the definition of the primary vibration modes of the powertrain and chassis.

1.5 Main results

The work contained in this dissertation provides several major results that contribute to the development of feedforward control of nonlinear systems. These results culminate in the application of the developed strategy in the topical problem of ICE restart/shutdown in HEVs and modern conventional powertrains. An overview of these results is as follows:

- TSCS has been developed for feedforward control of nonlinear systems

    - TSCS is proven to be more effective than direct input shaping methods in the cases considered
- Robust command shaping is applied alongside TSCS to mitigate the effect of vibration mode variations
- Parameter estimation techniques, such as RLS and EKF, have also been applied with TSCS to reduce the impact of parameter uncertainty
- TSCS serves as a cost-effective method for mitigating undesirable vibrations during ICE restart
    - Robust command shaping and parameter estimation techniques are shown to broaden the applicability of TSCS to a range of consumer vehicles by reducing the impact of vibration mode variations and system parameter uncertainties
- TSCS also serves as a theoretical solution to reduce vibrations during ICE shutdown in HEVs and modern conventional powertrains equipped with engine stop-start features
- An experimental apparatus was developed to physically observe the reported undesirable vibrations occurring in the powertrain and chassis of a vehicle during ICE restart and shutdown
- TSCS was experimentally validated for ICE restart

An outline of the work in this dissertation leading to these main results is presented in the next section.

1.6 Dissertation outline

In this dissertation, TSCS is introduced on traditional and nontraditional Duffing-like nonlinear systems in Chapter 2. In Chapter 2, TSCS is also directly compared to other command shaping strategies as well as feedback linearization approaches. Robust command shaping and parameter estimation techniques for extending applicability of the method are also introduced in Chapter 2. Chapter 3 introduces a model for ICE restart and applies the TSCS approach. Robust command shaping and parameter estimation techniques are also presented in Chapter 3 to mitigate the effect of uncertainty in vibration modes and ICE parameters. Chapter 4 explores the efficacy of TSCS in mitigating undesirable oscillations during ICE shutdown. An experimental apparatus is then introduced in Chapter 5 for validation of TSCS applied to ICE restart. Finally, Chapter 6 outlines notable contributions associated with the work contained in this dissertation and future work that builds on the presented research.

CHAPTER 2. INTRODUCTION OF TWO-SCALE COMMAND SHAPING FOR FEEDFORWARD CONTROL OF NONLINEAR SYSTEMS

In this chapter, TSCS is introduced and critically analyzed as applied to Duffing oscillators. When applied to these nonlinear systems, TSCS proves to be an effective method for feedforward control. The strategy outperforms conventional and nonlinearly-informed command shaping strategies in traditional and non-traditional Duffing systems (e.g., Duffing systems with quadratic nonlinearity and Coulomb damping). Comparisons between TSCS and feedback-based control approaches are also presented. The TSCS approach is then extended to nonlinear systems with uncertain parameters through the implementation of robust command shaping strategies and an EKF parameter estimation technique.

2.1 Introduction of the Duffing oscillator

The Duffing oscillator serves as the main system for assessing the TSCS technique and comparing it to existing feedforward control methods. Georg Duffing introduced his namesake equation in a book published in 1918 [57, 58]. Since its inception, the Duffing equation has been the focus of numerous studies due to its rich behavior and wide applicability [58]. For these reasons, and owing to its sufficient simplicity, it is chosen herein for applying and critically assessing TSCS.

The equation of motion for an undamped Duffing oscillator is given by

$$\ddot{x} + {\omega_n}^2 x + \varepsilon x^3 = \frac{F(t)}{m}$$
$$x(0) = x_{IC}, \dot{x}(0) = \dot{x}_{IC} \tag{2.1}$$

where $x(t)$ denotes the dependent variable (e.g., position), t the independent time variable, x_{IC} the initial position, $\dot{x}_{IC}$ the initial velocity, ω_n the linear natural frequency, ε the coefficient of the cubic nonlinear term, $F(t)$ the forcing function, m the mass, $\dot{()} = \frac{d}{dt}$, and $\ddot{()} = \frac{d^2}{dt^2}$ [58, 59]. Equation (2.1) is commonly referred to as the undamped Duffing equation. In all results presented, m is defined to be of unit value. The oscillator exhibits hardening when $\varepsilon > 0$ and softening when $\varepsilon < 0$. This work puts primary focus on systems exhibiting hardening.

When $F(t) = 0$, an exact solution exists for Eq. (2.1). The solution has the following forms [58]

$$\begin{aligned} \varepsilon > 0: &\quad x = X\mathrm{cn}\left(\omega t - \theta, {k_{JE}}^2\right) \\ \varepsilon < 0: &\quad x = X\mathrm{sn}\left(\omega t - \theta, {k_{JE}}^2\right) \end{aligned} \tag{2.2}$$

where cn is the Jacobi cosine function, sn is the Jacobi sine function, X is the amplitude of the response, θ is the phase, and

$$\varepsilon > 0: \quad \omega^2 = {\omega_n}^2 + \varepsilon X^2,\ {k_{JE}}^2 = \frac{\varepsilon X^2}{2({\omega_n}^2 + \varepsilon X^2)}$$
$$\varepsilon < 0: \quad \omega^2 = {\omega_n}^2 - \frac{\varepsilon X^2}{2},\ {k_{JE}}^2 = \frac{\varepsilon X^2}{2\left({\omega_n}^2 - \frac{\varepsilon X^2}{2}\right)} \tag{2.3}$$

The response amplitude X is expressed as

$$X = \left(-\frac{{\omega_n}^2}{\varepsilon} + \frac{{\omega_n}^2 + \varepsilon {x_{IC}}^2}{\varepsilon} \sqrt{1 + \frac{2\varepsilon \dot{x}_{IC}}{{\omega_n}^2}} \right)^{\frac{1}{2}} \tag{2.4}$$

while the phase satisfies

$$\frac{\mathrm{sn}\left(\theta, {k_{JE}}^2\right)}{\mathrm{cn}\left(\theta, {k_{JE}}^2\right)} \mathrm{dn}\left(\theta, {k_{JE}}^2\right) = -\frac{\dot{x}_{IC}}{\omega x_{IC}} \tag{2.5}$$

where dn is the Jacobi delta function.

Without loss of generality (the system is autonomous), initial conditions can identify zero time with zero position

$$x(0) = 0, \dot{x}(0) = \dot{x}_{IC} \tag{2.6}$$

and then the phase is given by

$$\theta = K_{EI}({k_{JE}}^2) \tag{2.7}$$

where K_{EI} is the complete elliptic integral of the first kind [58].

The response frequency follows from the solution, Eq. (2.2) [58]. For the hardening case, the exact nonlinear frequency, ω_{NL}, is given by

$$\omega_{NL,exact} = \frac{\pi\sqrt{{\omega_n}^2 + \varepsilon X^2}}{2K\left(\frac{\varepsilon X^2}{2({\omega_n}^2 + \varepsilon X^2)}\right)} \tag{2.8}$$

while for softening, it is given by

$$\omega_{NL,exact} = \frac{\pi\sqrt{{\omega_n}^2 - \frac{1}{2}\varepsilon X^2}}{2K\left(\frac{\varepsilon X^2}{2\left({\omega_n}^2 - \frac{1}{2}\varepsilon X^2\right)}\right)} \tag{2.9}$$

The exact frequencies in Eqs. (2.8) and (2.9) will later be used with direct application of ZV and UM input shapers, and then compared to TSCS.

The method of multiple scales provides an approximation to the nonlinear frequency [59-61], and is commonly employed in place of, or in the absence of, an exact solution. Daqaq *et al.* integrated multiple scales with input shaping in their analysis of a container crane. They applied the method to a base-excited simple pendulum governed by

$$\ddot{x} + {\omega_n}^2 \sin(x) = \frac{1}{m} F_0 \cos(x) H(t) \tag{2.10}$$

where $H(t)$ denotes the Heaviside function. F_0 is proportional to the commanded base acceleration in the work of Daqaq *et al.*, and notably, is included in the multiple scales-derived expression for the nonlinear response frequency. Here, their method is adopted, but instead applied to an undamped Duffing equation subjected to a constant force

$$\ddot{x} + {\omega_n}^2 (1 + \gamma_{NL} x^2) x = \frac{1}{m} F_0 H(t) \tag{2.11}$$

where γ_{NL} is equal to ${\varepsilon/\omega_n}^2$ and the system is subjected to zero initial conditions. Implementing the approach described in [1], time *t*, and the state *x*, are expanded as

$$t = \mathrm{T}_0 + \gamma_{NL} \mathrm{T}_1 + O({\gamma_{NL}}^2) \tag{2.12}$$

$$x(\mathrm{T}_0, \mathrm{T}_1, \dots) = x_0(\mathrm{T}_0, \mathrm{T}_1, \dots) + \gamma_{NL} x_1(\mathrm{T}_0, \mathrm{T}_1, \dots) + O({\gamma_{NL}}^2) \tag{2.13}$$

such that

$$\frac{d}{dt} = D_0 + \gamma_{NL} D_1 + O({\gamma_{NL}}^2) \tag{2.14}$$

$$\frac{d^2}{dt^2} = {D_0}^2 + 2\gamma_{NL} D_0 D_1 + O({\gamma_{NL}}^2) \tag{2.15}$$

where D_n denotes a time derivative with respect to T_n.

Introducing Eqs. (2.12)-(2.15) in Eq. (2.11), and separating orders of γ_{NL}, results in the following expressions

$$\mathrm{O}({\gamma_{NL}}^0): \quad {D_0}^2 x_0 + {\omega_n}^2 x_0 = \frac{1}{m} F_0 H(t) \tag{2.16}$$

$$\mathrm{O}({\gamma_{NL}}^1): \quad {D_0}^2 x_1 + {\omega_n}^2 x_1 = -{\omega_n}^2 {x_0}^3 - 2 D_0 D_1 x_0 \tag{2.17}$$

Solving sequentially Eqs. (2.16) and (2.17) while eliminating secular terms yields the desired approximation to the nonlinear frequency

$$\omega_{NL,forced} = \left(1 + \frac{3\gamma_{NL} {X_0}^2}{8} + \frac{3\gamma_{NL} {F_0}^2}{2m^2 {\omega_n}^4}\right) \omega_n \tag{2.18}$$

where X_0 is the amplitude of the general solution to Eq. (2.16) with zero initial conditions. The forcing-informed multiple scales frequency, Eq. (2.18), will also be used with direct application of ZV input shapers and then compared to TSCS.

Since input shaping requires the system response *between* inputs, it is reasonable to apply the multiple scales procedure to the *unforced* system to obtain a frequency estimate. This small change to Daqaq *et al.*'s method is also assessed herein. Applying the method

of multiple scales to the unforced system results in the approximation to the nonlinear frequency given by

$$\omega_{NL,unforced} = \left(1 + \frac{3\gamma_{NL}{X_0}^2}{8}\right)\omega_n \tag{2.19}$$

2.2 Two-scale command shaping development

2.2.1 Scale separation

The TSCS strategy decomposes the input forcing into linear and nonlinear terms

$$F_{TSCS}(t) = F_{0_{Shaped}}(t) + \varepsilon F_1(t) \tag{2.20}$$

where $F_{0_{Shaped}}$ denotes the linear component of the input later specified using command shaping with the zeroth-order problem, F_1 the time-varying component used to mitigate oscillations arising from nonlinear behavior, and ε is either a parameter appearing with the nonlinearity or a book-keeping parameter used to order linear and nonlinear effects [59-61].

An undamped Duffing oscillator (and other nonlinear systems) employing the TSCS strategy can be written as

$$\ddot{x} + \omega_n^2 x + \varepsilon f_{NL}(x, \dot{x}) = \frac{1}{m} F_{TSCS}(t) \tag{2.21}$$

where f_{NL} denotes the nonlinear component of the differential equation, ω_n the linear natural frequency, and ε the (small) strength of the nonlinearity [59]. An asymptotic approximation is introduced for x using ε

$$x(t) = x_0(t) + \varepsilon x_1(t) + \varepsilon^2 x_2(t) + O(\varepsilon^3) \tag{2.22}$$

where Eq. (2.22) is used within Eq. (2.21) to isolate the zeroth- and first-order expressions required for TSCS. Separating orders of ε in Eq. (2.21) via Eq. (2.22), the zeroth-order expression follows as

$$\ddot{x}_0 + \omega_n^2 x_0 = \frac{1}{m} F_{0_{Shaped}}(t) \tag{2.23}$$

and the first-order expression as

$$\ddot{x}_1 + \omega_n^2 x_1 + f_{NL}(x_o, \dot{x}_0) = \frac{1}{m} F_1(t) \tag{2.24}$$

It is desired for residual oscillations appearing with x_1 to be eliminated – thus x_1 is set to zero, effectively specifying the requisite form for $F_1(t)$

$$F_1(t) = m f_{NL}(x_o, \dot{x}_0) \tag{2.25}$$

The second, linear component of the input, $F_{0_{Shaped}}(t)$, is specified next using command shaping, ultimately providing the response quantities $x_o, \dot{x}_0$ required to complete the specification of $F_1(t)$ and the first-order expression.

2.2.2 Command shaping

Command shaping addresses the linear forcing component appearing in Eq. (2.23) under the assumption that a discontinuous step-like command input would otherwise be applied to the system. The residual vibration amplitude at the time of the last impulse of a sequence of impulses applied to a linear mass-spring-damper is given by

$$A = \frac{\omega_n}{\sqrt{1-\zeta^2}} e^{-\zeta\omega_n t_j} * \sqrt{\left[\sum_{i=1}^{j} A_i e^{\zeta\omega_n t_i}(\cos\omega_d t_i)\right]^2 + \left[\sum_{i=1}^{j} A_i e^{\zeta\omega_n t_i}(\sin\omega_d t_i)\right]^2} \tag{2.26}$$

where ω_n denotes the linear natural frequency, t_j the time of application of the last impulse, and A_i the amplitude of the i^{th} impulse that occurs at time t_i [2]. When the command shaping strategy is correctly implemented, the amplitude A in Eq. (2.26) will be zero or below a user-defined tolerance value.

A ZV input shaper has a simple formulation that eliminates residual vibrations at a single frequency, which represents one vibration mode for a system. A ZV input shaper impulse sequence is defined as

$$\begin{bmatrix} A_1 & A_2 \\ t_1 & t_2 \end{bmatrix} = \begin{bmatrix} \frac{1}{1+K} & \frac{K}{1+K} \\ 0 & \frac{\pi}{\omega_d} \end{bmatrix} \tag{2.27}$$

$$K = e^{\frac{-\zeta\pi}{\sqrt{1-\zeta^2}}} \tag{2.28}$$

where ω_d and ζ are the damped natural frequency and damping ratio, respectively. Two constraints yield Eq. (2.27): the amplitudes must sum to one and the second impulse must occur at the half-period—i.e., the smallest possible time guaranteeing zero residual vibration.

Figure 2-1 presents the results of using a ZV approach to shape a unity impulse, which is then applied to an ideal linear mass-spring-damper system. The solid line denotes system response from the two-impulse sequence of a ZV shaper; the dashed line denotes system response of the stationary system excited by the second impulse at time t_2; and the dashed-dotted line denotes the system response excited by the first impulse applied at time zero (and absent of the second impulse). For this ideal case, it is possible to eliminate all residual vibrations using the ZV approach. Note that a ZV input shaper is equivalent to defining a zero at the flexible poles associated with the design frequency, as shown in the inset of Figure 2-1. Shaper robustness to error in the design frequency may be increased by including additional zeros, and (optionally) changing their location relative to the flexible

poles. This has been explored by several researchers through the development of follow-on command shaping strategies, such as ZVD and EI input shapers [9-11, 41, 62].

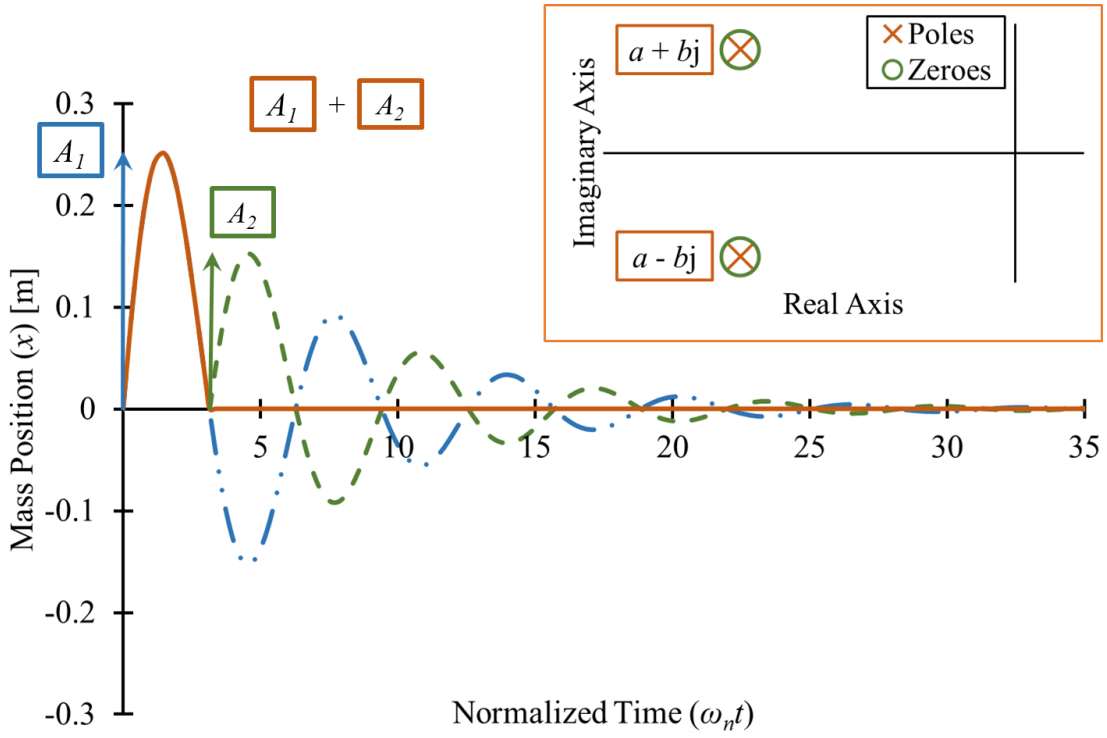

Figure 2-1 – Impulse sequence and system response for zero vibration of an ideal mass-spring-damper, and (inset) ZV input shaper represented as pole-zero cancellation.

ZVD input shapers are an extension of the ZV shapers introduced above. The impulse sequence requires three impulses and a full damped period of the pole. It is derived using the constraints presented for the ZV shaper in addition to the requirement that the partial derivative of the residual vibration amplitude, Eq. (2.26), with respect to frequency is zero at the design frequency [2, 9, 10]. Using the additional constraint, the impulse sequence for the ZVD shaper is

$$\begin{bmatrix} A_1 & A_2 & A_3 \\ t_1 & t_2 & t_3 \end{bmatrix} = \begin{bmatrix} \frac{1}{(1+K)^2} & \frac{2K}{(1+K)^2} & \frac{K^2}{(1+K)^2} \\ 0 & \frac{\pi}{\omega_d} & \frac{2\pi}{\omega_d} \end{bmatrix} \tag{2.29}$$

where K is defined with Eq. (2.28) [10]. Imposing that the partial derivative must be zero increases the robustness of the input shaper while increasing the duration to a full damped period. A ZVD input shaper is represented as placing repeated zeros on a flexible pole, as shown in Figure 2-2.

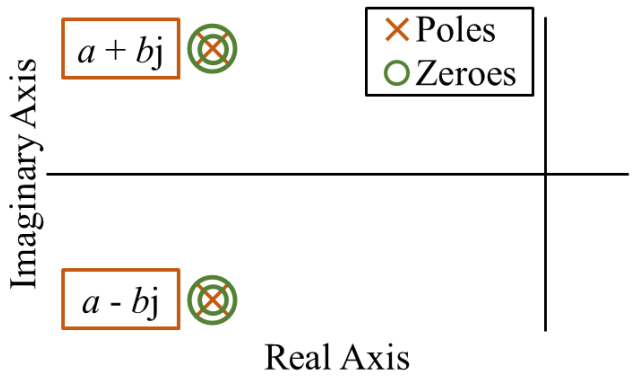

Figure 2-2 – ZVD input shaper represented as pole-zero cancellation.

In addition to robust input shaping, negative input shapers increase the speed at which a system moves [15]. A simple form is a UM ZV input shaper. In place of the constraint requiring the sum of the amplitudes must equal one, the amplitudes of the negative input shaper must satisfy

$$A_i = (-1)^{i+1}, \quad i = 1, \ldots, j \tag{2.30}$$

where j denotes the number of impulses in the sequence. Using the constraint defined in Eq. (2.30) prevents actuator saturation from occurring, which is a concern with negative input shapers [15]. Combining the constraint in Eq. (2.30) with the constraints of a traditional ZV input shaper provides the following impulse sequence for an undamped system

$$\begin{bmatrix} A_1 & A_2 & A_3 \\ t_1 & t_2 & t_3 \end{bmatrix} = \begin{bmatrix} 1 & -1 & 1 \\ 0 & \frac{\cos^{-1}(0.5)}{\omega_n} & \frac{\cos^{-1}(-0.5)}{\omega_n} \end{bmatrix} \tag{2.31}$$

where ω_n is the linear natural frequency [15]. For a damped system, the temporal locations for the impulses are complex functions. Note that the time required to execute the impulse sequence for a UM ZV input shaper is one-third the period of the system's oscillations, which is 33% faster than a traditional ZV shaper [15]. Increasing the system response speed requires more actuator effort, excites higher order modes, and may accentuate the effect of nonlinearities.

After the correct sequence of impulses has been determined, inputs of any general form (stepped up and down inputs in this chapter) can be convolved with the impulse sequence to generate a shaped command function that minimizes residual oscillations

$$F_{0_{Shaped}}(t) = F_0(t) * I_1(t) * I_2(t) * \dots \tag{2.32}$$

where $I_i(t)$ is the ZV, ZVD, or UM ZV input shaper defined to mitigate one of the n vibration modes of the system. Note that if a combination of ZV input shapers must cancel n vibration modes, the number of shaper impulses increases to $2n$ impulses [2].

2.3 Two-scale command shaping efficacy

2.3.1 Comparison of two-scale command shaping to direct implementations of zero vibration input shaping

A Duffing oscillator with a small cubic nonlinearity is used to compare TSCS to methods of direct input shaping. Figure 2-3a and Figure 2-3b compare the methods for Duffing oscillators exhibiting hardening and softening, respectively. The nonlinearity in the cases presented in Fig. 3 is weak since the ratio ε/ω_n^2 was chosen to have a magnitude of 0.4. With a change of variables for non-dimensional time, $\tau_{ND} = \omega_n t$, it can be shown that only one system parameter needs definition, which is the ratio ε/ω_n^2. A ratio of less than 1 results in a weak nonlinearity, where a ratio greater than 1 is typically considered a strong nonlinearity [58]. A multi-step, unit magnitude input is applied to observe the transient and steady-state performance of the methods. The direct methods use the standard ZV input shaping approach with estimates of the natural frequency based on either ω_n, $\omega_{NL,exact}$, $\omega_{NL,forced}$, or $\omega_{NL,unforced}$. In Figure 2-3, the dashed blue line denotes the response with a shaper based on ω_n, dotted purple line $\omega_{NL,exact}$, dashed red line $\omega_{NL,forced}$, and dash-dotted yellow line $\omega_{NL,unforced}$.

Figure 2-3 indicates that TSCS results in less residual vibrations than all direct ZV input shaping implementations. TSCS reduces the steady-state residual oscillation of the best direct input shaping implementation by 12.0 dB and 2.3 dB in the hardening and softening cases, respectively. Including the forcing term in the multiple scales-informed nonlinear frequency estimate decreases the efficacy of the ZV input shaping; however, without the forcing term, the direct approach with a multiple scales-informed nonlinear frequency performs as well as the direct method using an exact nonlinear frequency. This can be expected as the design of the ZV impulse sequence minimizes oscillations associated with free response, and the multiple scales' estimate of the nonlinear frequency is known to be accurate for small to moderate motions. Note also that, for the small cubic nonlinearity and amplitudes considered, the direct ZV method based on the linear natural frequency still performs satisfactorily in comparison to the other direct methods.

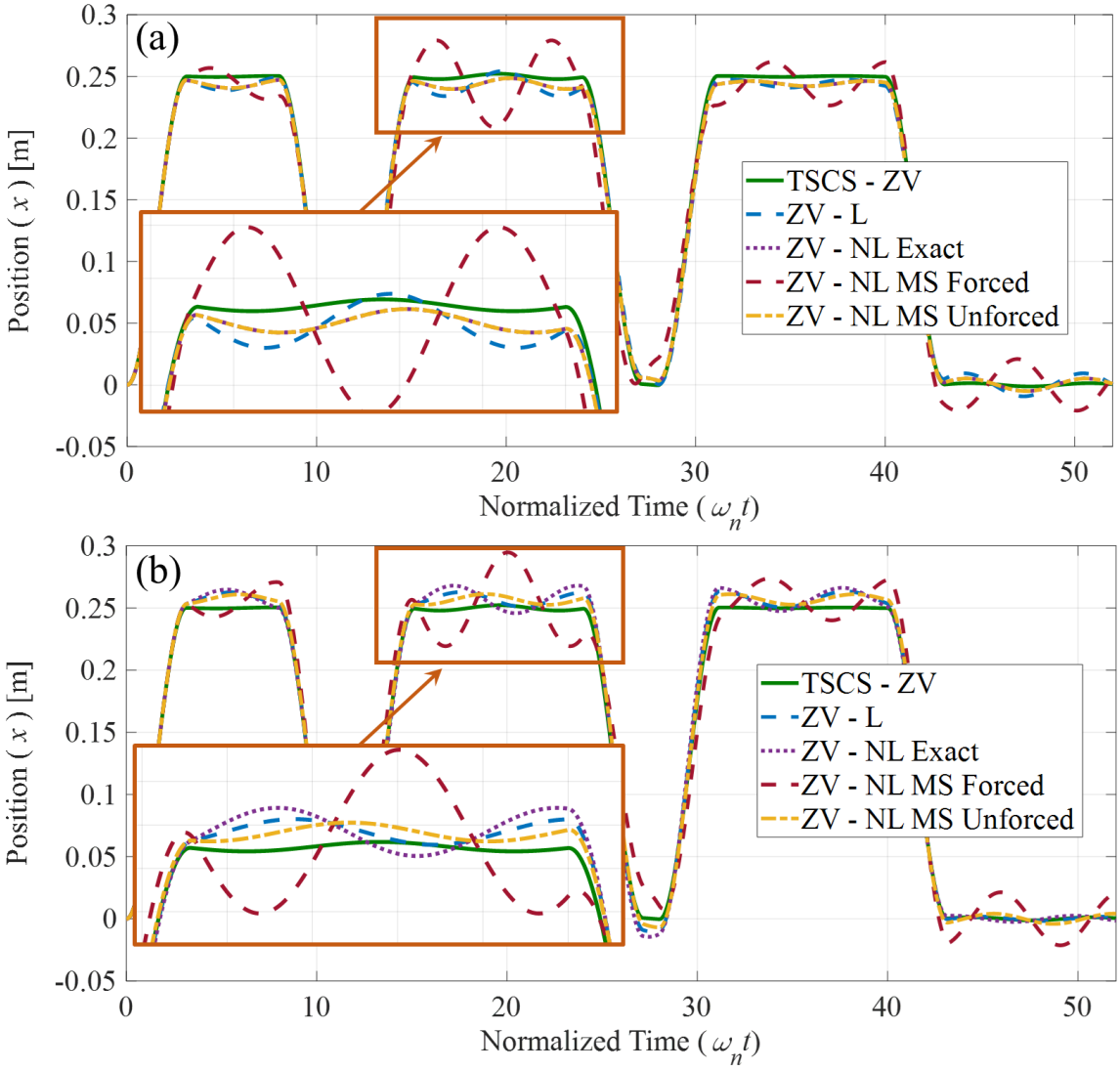

Figure 2-3 – Comparison of the efficacy of TSCS and direct implementations of a ZV input shaper, designed for various frequency values, in reducing residual vibrations in the position of an undamped Duffing oscillator with (a) a small positive cubic nonlinearity (ω_n = 2 rad/s, ε = 1.6 1/(m^{2}s^2), F_0 = 1 N) and (b) a small negative cubic nonlinearity (ω_n = 2 rad/s, ε = -1.6 1/(m^{2}s^2), F_0 = 1 N).

As the nonlinearity and motion amplitude increases, differences between the methods become more evident. Figure 2-4 illustrates the effect of increasing the nonlinear coefficient on the performance of TSCS and the direct ZV input shaping methods. The ratio ε/ω_n^2 was chosen to have a magnitude of 2 to result in a strong nonlinearity. It can be

expected that the direct methods' performance will decrease as the nonlinear coefficient increases due to the superposition assumption underlying the impulse sequence design. TSCS is expected to avoid this issue as it applies command shaping to a strictly linear subproblem. The direct methods using nonlinear frequency estimates now significantly outperform the direct method employing a linear frequency estimate, except for the case where forcing is used in the nonlinear frequency estimate. Figure 2-4 documents that TSCS continues to be highly effective, resulting in residual oscillation reductions on the order of 20 dB when compared to the best direct input shaping method.

The results of Figure 2-3 and Figure 2-4 demonstrate that the best direct method employs the exact nonlinear frequency. Therefore, for the remainder of the chapter, only this nonlinear direct method will be retained. The direct method with the linear natural frequency is also retained for ultimately assessing the improvements possible with TSCS and nonlinearly informed direct input shaping methods.

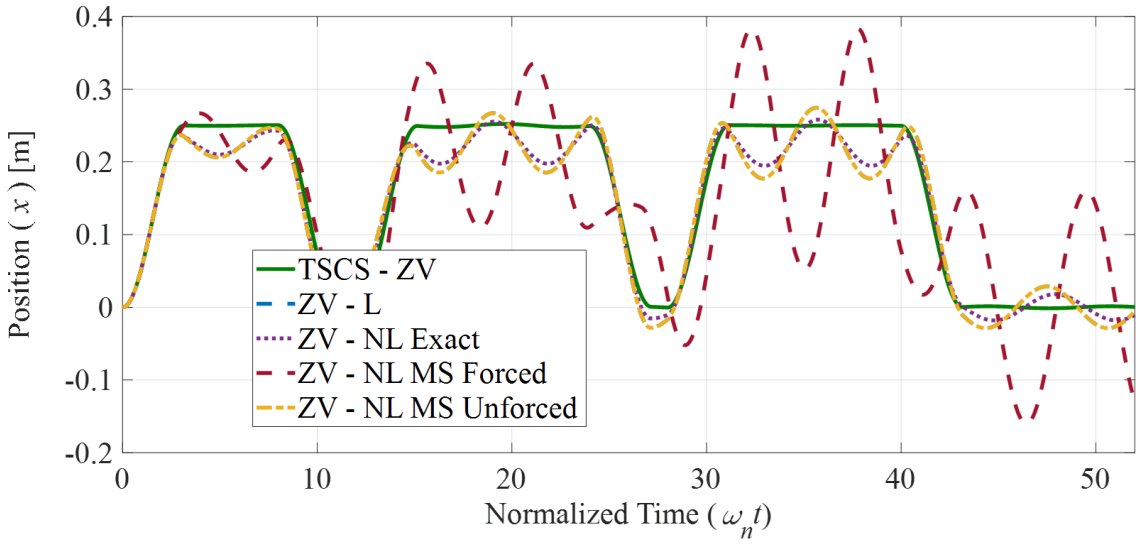

Figure 2-4 – Comparison of the efficacy of TSCS and direct implementations of a ZV input shaper, designed for various frequency values, in reducing residual vibrations in the position of an undamped Duffing oscillator with a large positive cubic nonlinearity and multi-step input profile (ω_n = 2 rad/s, ε = 8 1/(m^{2}s^2), F_0 = 1 N).

Figure 2-5a and Figure 2-5b compare the effectiveness of the remaining command shaping strategies as a function of unshaped input amplitude and nonlinear coefficient, respectively. In these analyses, ω_n is fixed at a value of 2 rad/s for direct comparison with the systems in Figure 2-3 and Figure 2-4. Both standard ZV input shapers perform near-equivalently for input amplitudes, F_0, less than approximately 0.5 N when the nonlinear coefficient, ε, equals 0.5 1/(m^{2}s^2)), which results in a weak nonlinearity since the ratio ε/ω_n^2 has a magnitude of 0.125 (Figure 2-5a). At an unshaped input amplitude of 1.0 N (Figure 2-5b), the two direct methods deviate in their performance at even small values of ε. Both subfigures clearly demonstrate that TSCS performs better than the direct implementations regardless of input amplitude or nonlinear coefficient.

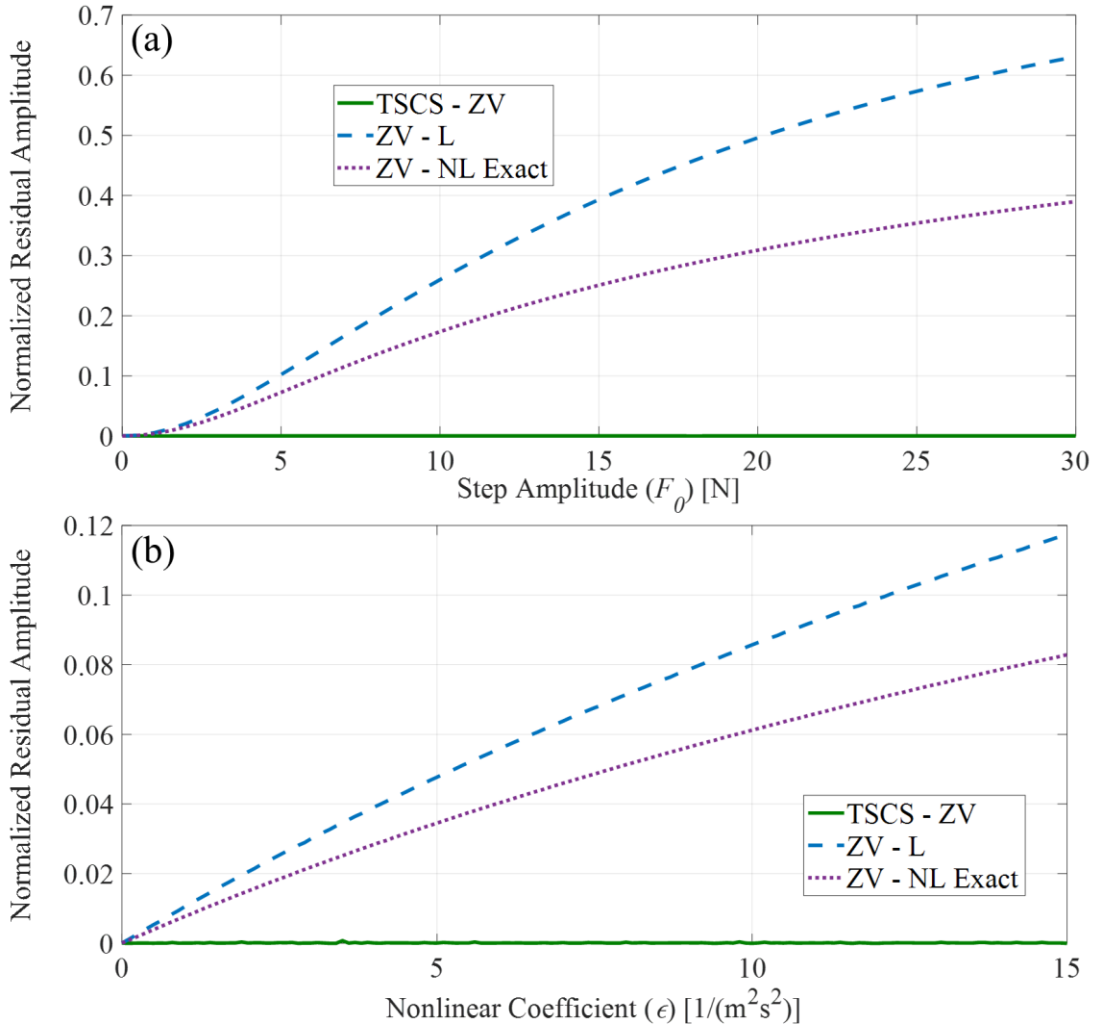

Figure 2-5 – Normalized undamped Duffing oscillator residual vibration amplitude comparison for TSCS and direct implementations of a ZV input shaper as a function of (a) unshaped input amplitude (with ω_n = 2 rad/s, ε = 0.5 1/(m^{2}s^2)) and (b) nonlinear coefficient (with ω_n = 2 rad/s, F_0 = 1 N).

Although Figure 2-3 through Figure 2-5 clearly demonstrate very good TSCS performance with respect to residual oscillations, the approach has one disadvantage in comparison to the direct methods. Due to the scale separation and feeding back of the zeroth-order response into the first-order shaped input, the response amplitude following two-scale shaping can differ from that desired. Direct implementations do not change the

amplitude of the response. This disadvantage can be rectified by a feedback element, which can effectively eliminate the offset. Figure 2-6 depicts the application of the TSCS with an integral controller designed iteratively with the Zeigler-Nichols method for a system with significant nonlinearity, the magnitude of ε/ω_n^2 is 2.5. Iteratively designing the integral control provides a choice between overshoot and response time. The feedback controller can be either applied in conjunction with TSCS (dash-dotted orange line) or used offline to determine the unshaped input amplitude required (dashed blue line). Applying the controller offline, informed by previous applications of TSCS, enables the strategy to remain feedforward.

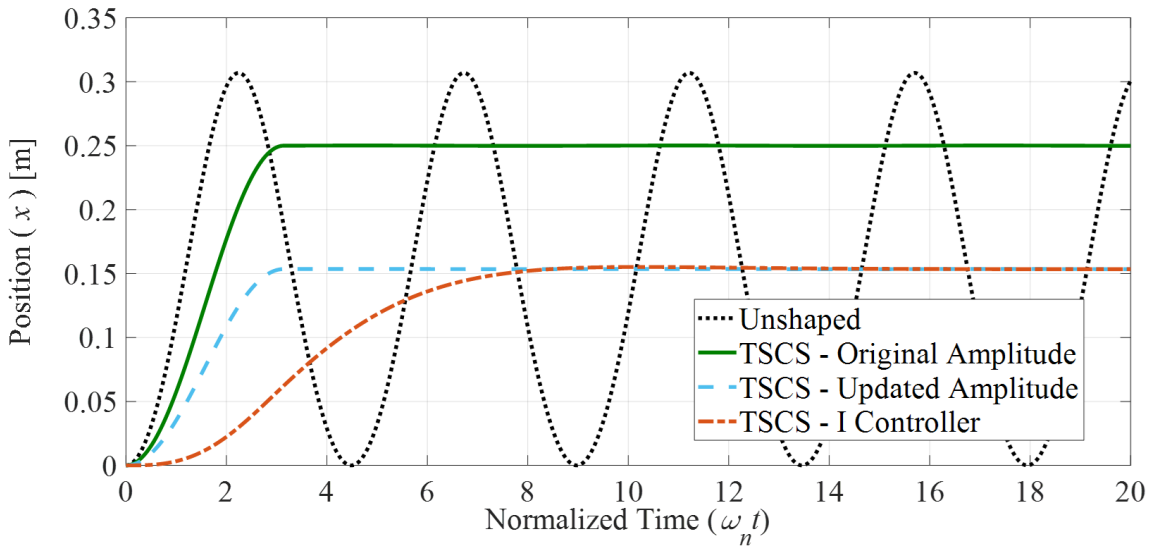

Figure 2-6 – Application of TSCS on an undamped Duffing oscillator with a large cubic nonlinearity (ω_n = 2 rad/s, ε = 10 1/(m^{2}s^2), F_0 = 1 N) and an integral feedback controller used to update the original input amplitude.

2.3.2 Application of two-scale command shaping to an undamped Duffing oscillator considering negative input shapers

This section explores UM input shaping with the TSCS strategy and the two remaining direct methods. Figure 2-7a compares the unshaped response to TSCS response results generated using ZV and UM ZV input shaping, and Figure 2-7b provides the corresponding input forces applied to the system. The ratio ε/ω_n^2 is defined to have a magnitude of 0.125 to result in a system with a weak nonlinearity for an effective comparison of the methods. Both TSCS strategies mitigate the residual vibration amplitude, but the TSCS strategy with a UM ZV input shaper reduces the response time by 0.5 s. The faster response time comes at the cost of a larger and more complex input profile, as documented in Figure 2-7b.

Figure 2-7c and Figure 2-7d compare the effectiveness of the TSCS strategy with a UM ZV input shaper to the two direct implementations of UM ZV input shaping with variations in the force amplitude and nonlinear coefficient, respectively. Figure 2-7c demonstrates that direct implementations of UM ZV input shaping results in equivalent vibration reduction to TSCS at inputs smaller than approximately 0.5 N for a system with weak nonlinearity, the magnitude of ε/ω_n^2 is 0.125. Beyond 0.5 N, the UM ZV shaper designed with the nonlinear frequency performs better than the shaper designed with the linear frequency. For amplitudes greater than 0.5 N, Figure 2-7c clearly demonstrates that TSCS performs better than both direct methods. Figure 2-7d demonstrates that under a nonlinear coefficient of 0.3, the UM ZV input shaper designed with the nonlinear frequency

performs near-equivalently to TSCS. Beyond a coefficient of 0.3, TSCS performs better than the direct shapers designed with linear and nonlinear frequencies.

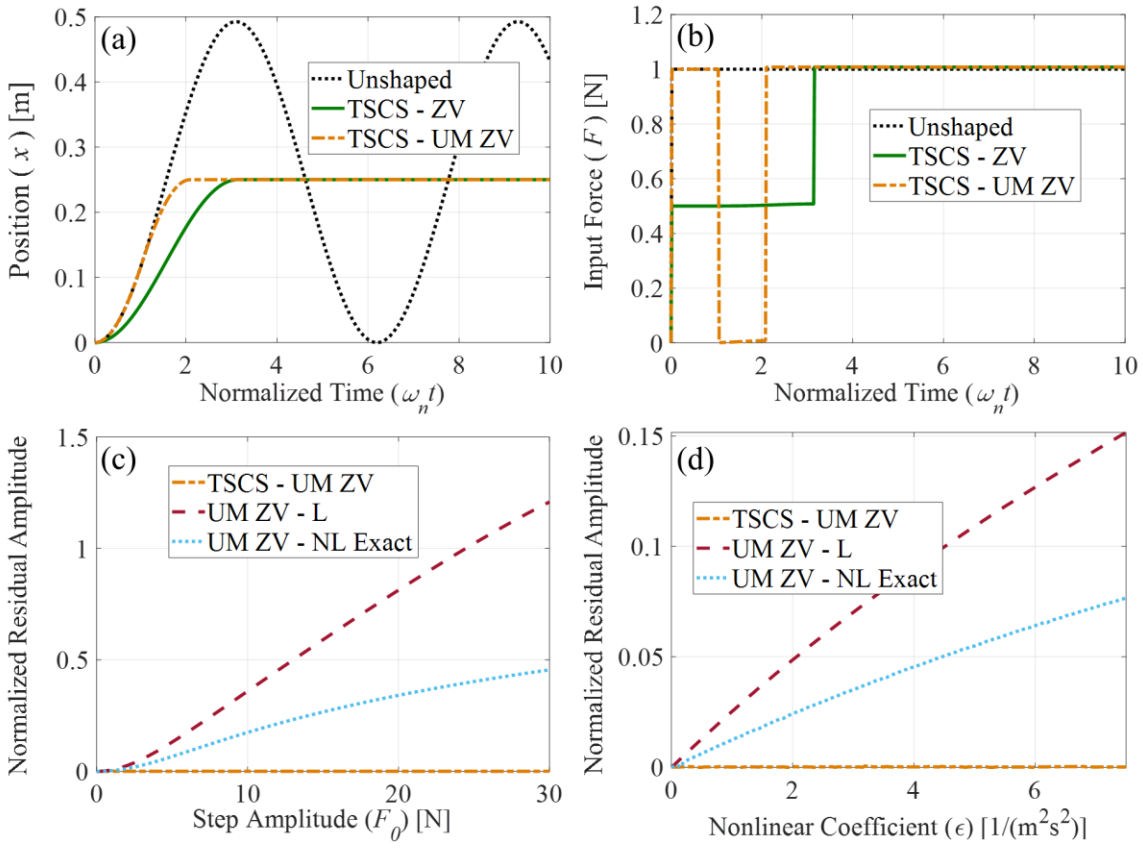

Figure 2-7 – (a) Comparison of undamped Duffing oscillator position resulting from inputs defined with TSCS with ZV and UM ZV input shapers with a small cubic nonlinearity (ω_n = 2 rad/s, ε = 0.5 1/(m^{2}s^2), F_0 = 1 N) and (b) the corresponding input force required. Normalized residual vibration amplitude comparison for TSCS and direct implementation of a UM ZV input shaper as a function of (c) unshaped input amplitude (with ω_n = 2 rad/s, ε = 0.5 1/(m^{2}s^2)) and (d) nonlinear coefficient (with ω_n = 2 rad/s, F_0 = 1 N).

2.3.3 *Application of two-scale command shaping to non-traditional Duffing systems*

Figure 2-8 displays the efficacy of TSCS when applied to an undamped Duffing oscillator with cubic and quadratic nonlinearities. Both the cubic and quadratic nonlinearities are ordered at the same scale such that f_{NL} is given as $x^3+\varepsilon_{UC}x^2$ in Eq. (2.21), where ε_{UC} is for unit consistency and has unity magnitude with units of meters for these cases.

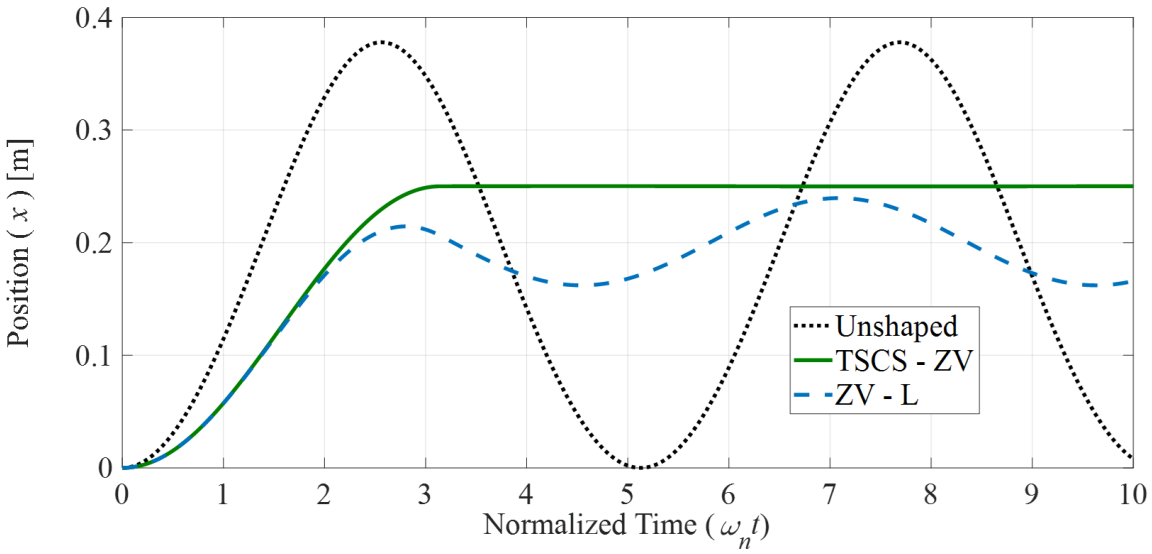

Figure 2-8 – Comparison of the efficacy of TSCS and direct implementation of a ZV input shaper in reducing residual vibrations in the position of an undamped Duffing oscillator with moderate cubic and quadratic nonlinearities (ω_n = 2 rad/s, ε = 4 1/(m^{2}s^2), F_0 = 1 N).

Figure 2-8 demonstrates that a linear ZV input shaper's effectiveness decreases further by adding the quadratic nonlinearity. Adding the quadratic term effectively increases the nonlinear coefficient. In the case presented in Figure 2-8, the ratio ε/ω_n^2 was defined to have a magnitude of 1 to result in a moderate nonlinearity. Direct application of

a ZV input shaper designed with the linear natural frequency reduces the unshaped residual vibration amplitude by 17.1 dB compared to the reduction of 63.1 dB with TSCS. Note that the exact and approximate nonlinear frequencies given by Eqs. (2.8) and (2.19) no longer apply due to the addition of the quadratic nonlinearity. An approximate frequency for both quadratic and cubic nonlinearities can be obtained using multiple scales, but this is not pursued herein.

The presence of Coulomb (nonlinear) damping also does not degrade TSCS's effectiveness. Coulomb friction is added to the undamped Duffing oscillator

$$\ddot{x}_0 + \omega_n^2 x_0 + \varepsilon(x^3 + \varepsilon_{UC} x^2) + \frac{1}{m} F_F \mathrm{sgn}(\dot{x}) = \frac{1}{m} F_{TSCS}(t) \tag{2.33}$$

where F_F is the friction magnitude. Note that the Coulomb friction is not ordered with the other nonlinearities; this reduces the nonlinear forcing, F_1, and serves to increase system stability. Thus, the nonlinear forcing f_{NL} remains as $x^3 + \varepsilon_{UC} x^2$ in Eq. (2.25) , where ε_{UC} is for consistency of units since x is associated with a unit of length.

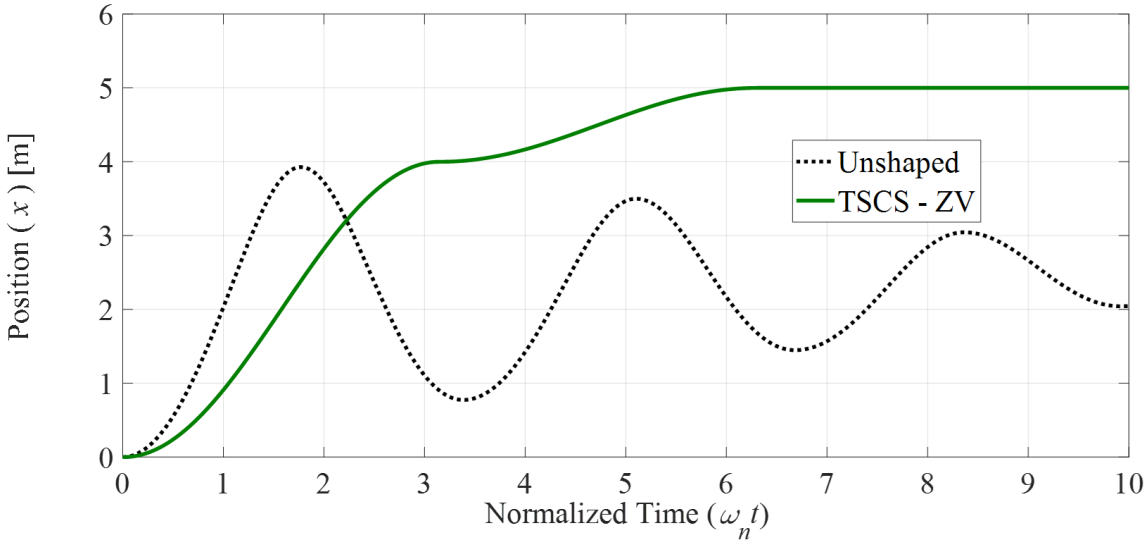

Figure 2-9 – Efficacy of TSCS in reducing the residual vibrations in the position of a damped Duffing oscillator with small cubic and quadratic nonlinearities, Coulomb friction, and large input amplitude (ω_n = 2 rad/s, ε = 0.5 1/(m^{2}s^2), F_0 = 20 N).

Figure 2-9 presents the results of applying TSCS to the modified Duffing oscillator with Coulomb friction, input amplitude large enough to overcome frictional effects, and a small nonlinearity, magnitude of ε/ω_n^2 is 0.125. TSCS eliminates the residual vibrations in the system, but requires an additional 3.18 normalized time units compared to the undamped system with cubic and quadratic nonlinearities. Additionally, the offset in amplitude remains unchanged relative to the undamped system.

2.3.4 Comparing two-scale command shaping to feedback control and linearization

This section directly compares the TSCS strategy to feedback control and linearization in terms of performance and controller effort. Observing the generalized form of the Duffing oscillator

$$\ddot{x} + {\omega_n}^2 x + \varepsilon(x^3 + \varepsilon_{UC} x^2) = \frac{F_{FBL}(t)}{m} \tag{2.34}$$

where the F_{FBL} can be chosen as

$$F_{FBL}(t) = \varepsilon(x^3 + \varepsilon_{UC} x^2) + f_N(t) \tag{2.35}$$

and $f_N(t)$ acts as the new input with the resulting system dynamics being linear [52]. To implement a proportional-integral-derivative controller (PID) in the feedback linearization (FBL) case given in Eq. (2.34), $f_N(t)$ can be expressed in the frequency domain as

$$f_N(s) = F_0(s) + P + I\frac{1}{s} + D\frac{N}{1 + N\frac{1}{s}} \tag{2.36}$$

where $F_0(s)$is the Laplace transform of the original input of the Duffing oscillator. In Eq. (2.36), *P* denotes the proportional control coefficient, *I* the integral control coefficient, *D* the derivative control coefficient, and *N* the filter coefficient.

The coefficients found in Eq. (2.36) are defined through tuning methodologies, such as the Zeigler-Nichols method, to provide the required performance. In the comparison between feedback control and TSCS, these parameters were chosen to provide comparable settling times between the control strategies. Table 2-1 provides the controller parameters for the tuned feedback controllers used in the comparison with TSCS.

Table 2-1 – PID controller parameters.

Parameter	Value
Proportional Control Coefficient (P), Unitless	1.31E+02
Integral Control Coefficient (I), Unitless	1.64E+02
Derivative Control Coefficient (D), Unitless	2.58E+01
Filter Coefficient (N), Unitless	1.45E+02

One of the main costs of using feedback control compared to TSCS is the increase in controller effort required for these methodologies. Table 2-2 provides the percent increases in energy cost and maximum input force of the feedback control methodologies relative to the TSCS strategy. The energy cost of the PID and PID FBL cases is over 6000% of what is observed with the TSCS control methodology. In addition, the PID and PID FBL control methodologies have a peak input force that is over 16,000% greater than what is observed in the input specified by TSCS.

Figure 2-10 compares the impact of the PID and PID FBL control methodologies to TSCS in their ability to reduce residual vibrations in a Duffing oscillator with cubic and quadratic nonlinearities. TSCS settles to its final value 32.4% faster than the PID control strategy and 257% slower than the PID strategy with FBL. The increased performance of the PID FBL strategy comes at the cost of the increased energy cost observed in Table 2-2. In addition, the feedback control methodologies require additional sensors to provide the necessary data required to define the control input and make the control delay sensitive.

Table 2-2 – Input requirements comparison between feedback control methodologies and TSCS.

Parameter	Value
PID Energy Cost Increase, %	6.14E+03
PID FBL Energy Cost Increase, %	6.11E+03
PID Maximum Force Increase, %	1.61E+04
PID FBL Maximum Force Increase, %	1.61E+04

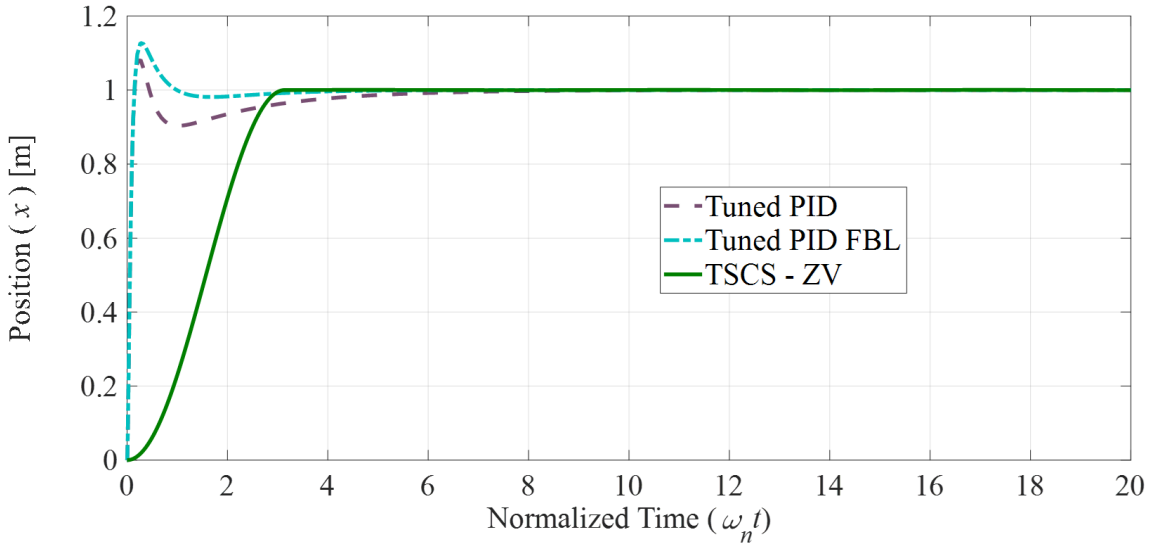

Figure 2-10 – Efficacy comparison between feedback control methodologies and TSCS in reducing residual vibrations in the position of a Duffing oscillator with large cubic and quadratic nonlinearities (ω_n = 2 rad/s, ε = 10 1/(m^{2}s^2)).

If there is a delay in the feedback of the system, the performance of both the PID and PID FBL strategies is compromised. Figure 2-11 shows the effect of a 0.08 normalized feedback delay on the feedback control strategies and TSCS. Since TSCS is a feedforward control methodology, feedback delay does not impact the application of the TSCS. Observing the two feedback control strategies, significant oscillations develop in the response of the oscillator. Figure 2-12 compares the performance of TSCS to the feedback control strategies as a function of feedback delay, in terms of time required to move the

system to its final position with residual vibrations that are less than 2% of the final position.

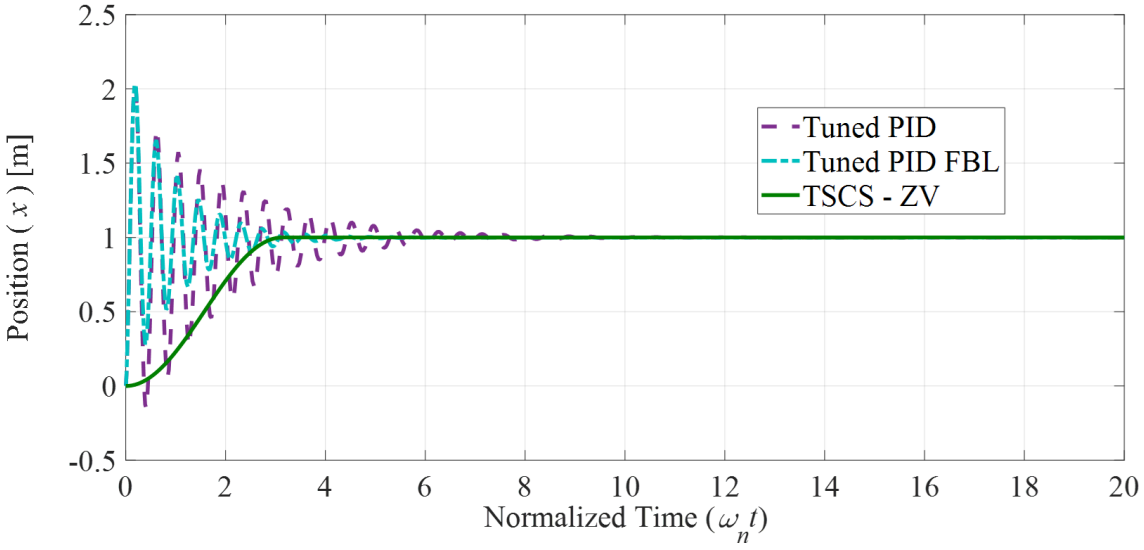

Figure 2-11 – Efficacy comparison between feedback control methodologies and TSCS in reducing residual vibrations in the position of a Duffing oscillator with large cubic and quadratic nonlinearities and a feedback delay of 0.08 (ω_n = 2 rad/s, ε = 10 1/(m^{2}s^2)).

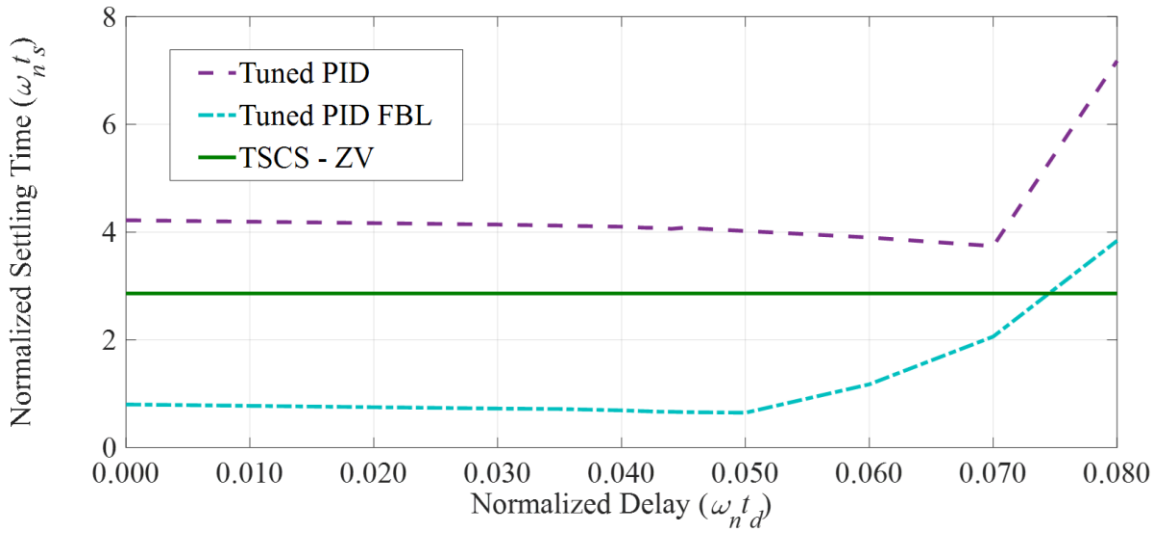

Figure 2-12 – Effect of normalized feedback delay on the normalized settling time of feedback control methodologies and TSCS (ω_n = 2 rad/s, ε = 10 1/(m^{2}s^2)).

With a constant set of feedback parameters, the PID FBL strategy settles to its final value with minimal residual vibration in less time than observed for the PID and TSCS strategies. Until the normalized feedback delay is 0.0744, PID FBL moves the system quicker than TSCS with mitigation of the residual vibrations. However, TSCS outperforms the PID strategy with and without feedback delay.

The feedback strategies also benefit from the ability to handle parameter variations without implementing parameter estimation techniques. Figure 2-13 shows the effect of a +25% parameter uncertainty in the nonlinear coefficient and linear natural frequency of the Duffing oscillator. Without using a parameter estimation technique, TSCS cannot mitigate all the undesirable residual vibrations in the motion of the oscillator. However, the PID and PID FBL strategies can handle these uncertainties because the control is based off the observed behavior of the system. Both feedback strategies can handle parameter uncertainties, with a +50% uncertainty only increasing the 2% settling time of the PID

strategy by 32.7% and PID FBL by 35.9%. Figure 2-14 shows the 2% settling time of the feedback control strategies as a function of the parameter variation. The 2% settling time of the PID strategy varies linearly as the parameters are increased from their design value; whereas, the settling time of the PID FBL strategy increases with positive and negative parameter variations because of the linearization process.

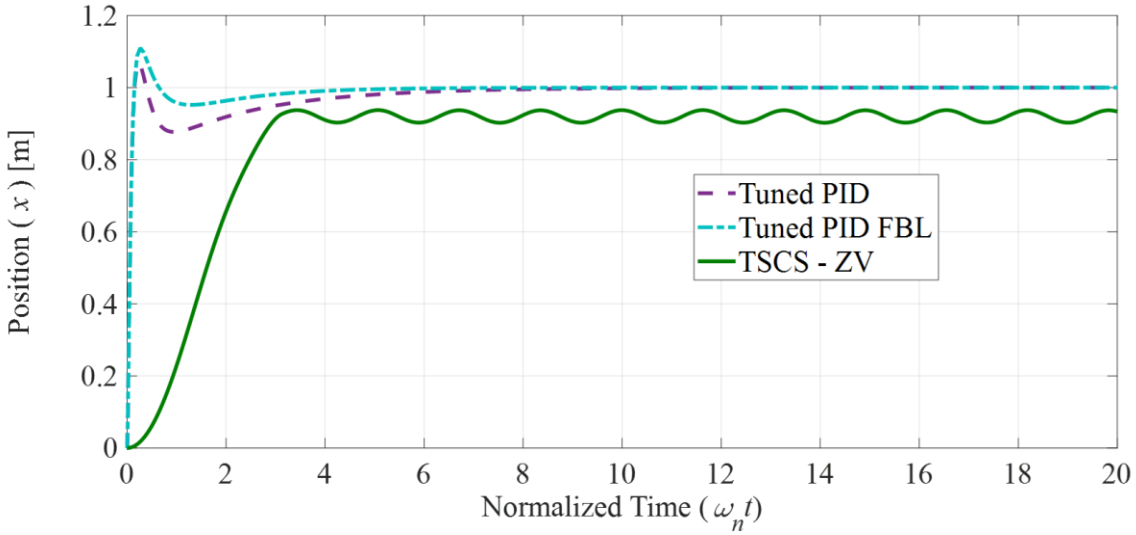

Figure 2-13 – Efficacy comparison between feedback control methodologies and TSCS in reducing residual vibrations in the position of a Duffing oscillator with large cubic and quadratic nonlinearities and a parameter variation of +25% (ω_n = 2 rad/s, ε = 10 1/(m^{2}s^2)).

Unlike the feedback strategies, the control input for TSCS is not based on the observed behavior of the Duffing oscillator, so parameter variations have serious impact on the mitigation of residual vibrations with TSCS. Without a parameter estimation technique, uncertainty in the linear natural frequency and nonlinear coefficient of the Duffing oscillator affects the reduction of residual vibration. Figure 2-15 shows residual vibration reduction as a percentage of the vibration of the unshaped case as a function of parameter variation. With no variation in system parameters, TSCS reduces the unshaped

residual vibration of the duffing oscillator by 60 dB. As the variation of the nonlinear coefficient and linear natural frequency is increased from -50% to 50%, the residual vibration reduction of TSCS varies from 11.3 dB to 22.1 dB, respectively.

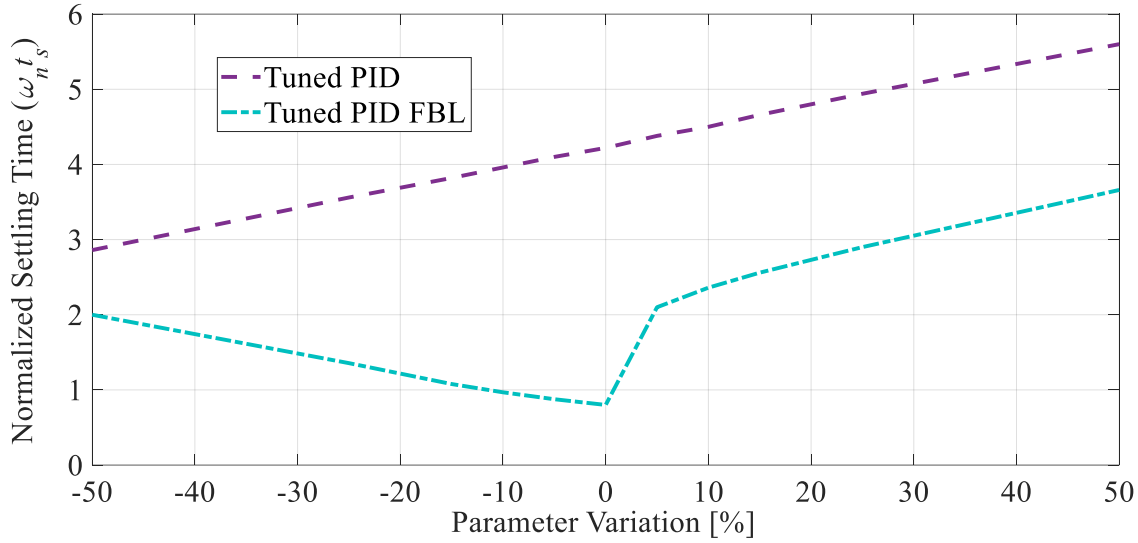

Figure 2-14 – Effect of parameter variation on the normalized settling time of the feedback control methodologies (ω_n = 2 rad/s, ε = 10 1/(m^{2}s^2)).

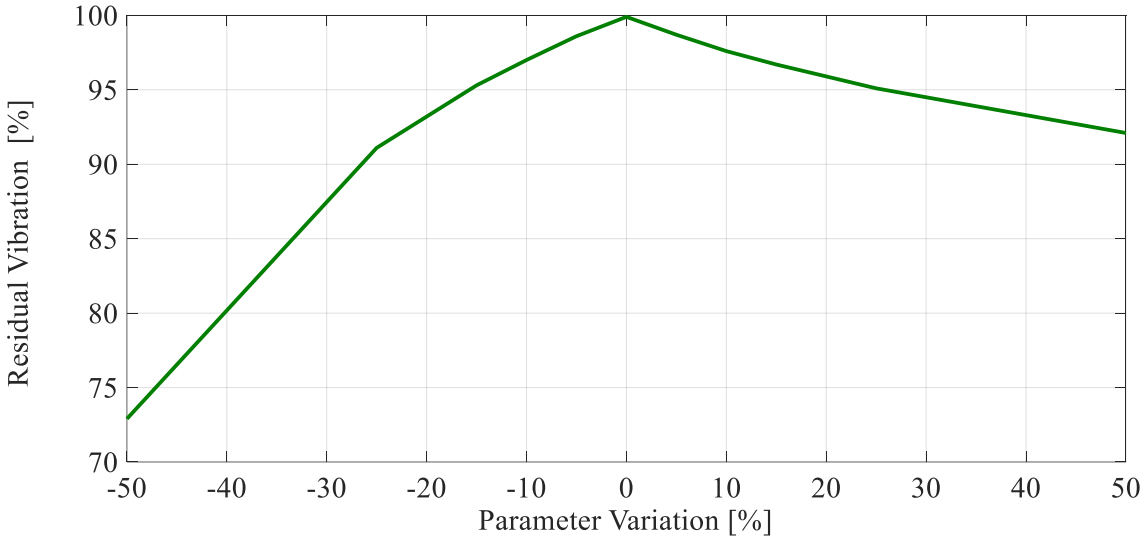

Figure 2-15 – Effect of parameter variation on residual vibration reduction with TSCS (ω_n = 2 rad/s, ε = 10 1/(m^{2}s^2)).

2.4 Robust two-scale command shaping strategy

2.4.1 Robust command shaping

As with any of the methods discussed, variations in the natural frequency and nonlinear coefficient impact TSCS's effectiveness. Robust command shaping strategies, such as ZVD input shaping, reduce the detrimental impact of variations in natural frequency. Figure 2-16a and Figure 2-16b present the performance of TSCS, with and without robust command shaping, in an undamped Duffing system with cubic and quadratic nonlinearities, with a 10% (Figure 2-16a) and 20% (Figure 2-16b) mismatch between the actual and expected linear natural frequency. As documented in Figure 2-16a, TSCS with only ZV input shaping reduces the unshaped residual amplitude by 14.1 dB, whereas TSCS with ZVD input shaping reduces the residual vibration's amplitude by 30.2 dB. When the variation is increased to 20% (Figure 2-16b), TSCS with only ZV input shaping reduces the unshaped residual vibration amplitude by 17.4 dB, whereas TSCS with ZVD input shaping reduces the residual vibration's amplitude by 24.9 dB. Thus, for 10% and 20% mismatch in the expected and actual linear natural frequency, TSCS with ZVD input shaping reduces the amplitude of residual vibrations observed with TSCS with only ZV shaping by 16.1 dB and 7.5 dB, respectively.

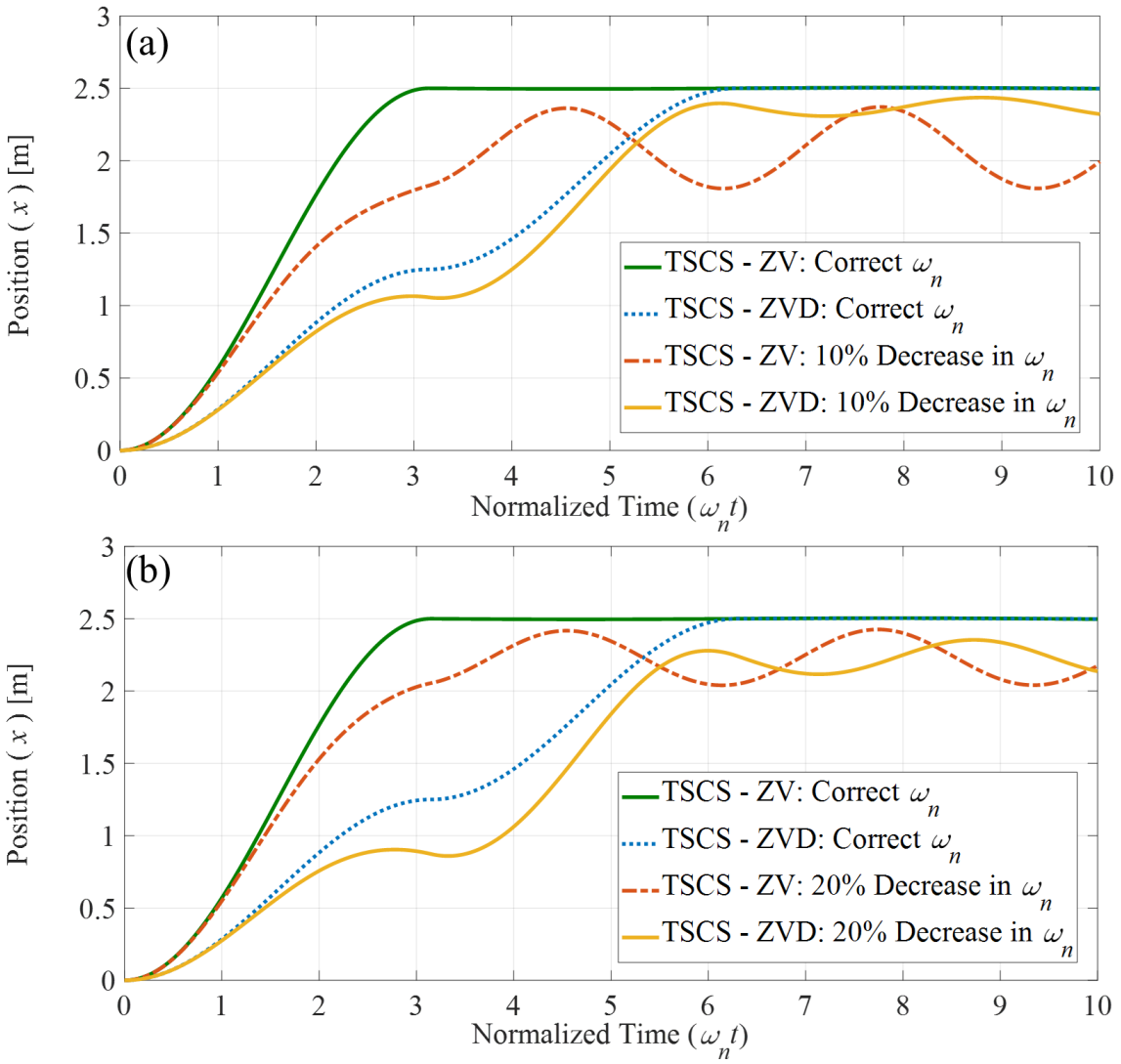

Figure 2-16 – Application of TSCS with ZV and ZVD input shaping on an undamped Duffing oscillator with small cubic and quadratic nonlinearities (ω_n = 2 rad/s, ε = 0.5 1/(m^{2}s^2), F_0 = 10 N) and (a) a 10% or (b) 20% mismatch between the expected and actual linear natural frequency.

2.4.2 Extended Kalman filtering with two-scale command shaping

Unlike mismatch in the expected linear natural frequency, variations in the nonlinear coefficients cannot be addressed with robust command shaping. Therefore, an alternate approach is required to mitigate these variations. Figure 2-17 shows the extent to which variations in the nonlinear coefficient lead to residual vibrations using TSCS. To

overcome these residual artifacts, EKF is next combined with TSCS to mitigate variations in the nonlinear coefficient and other system parameters.

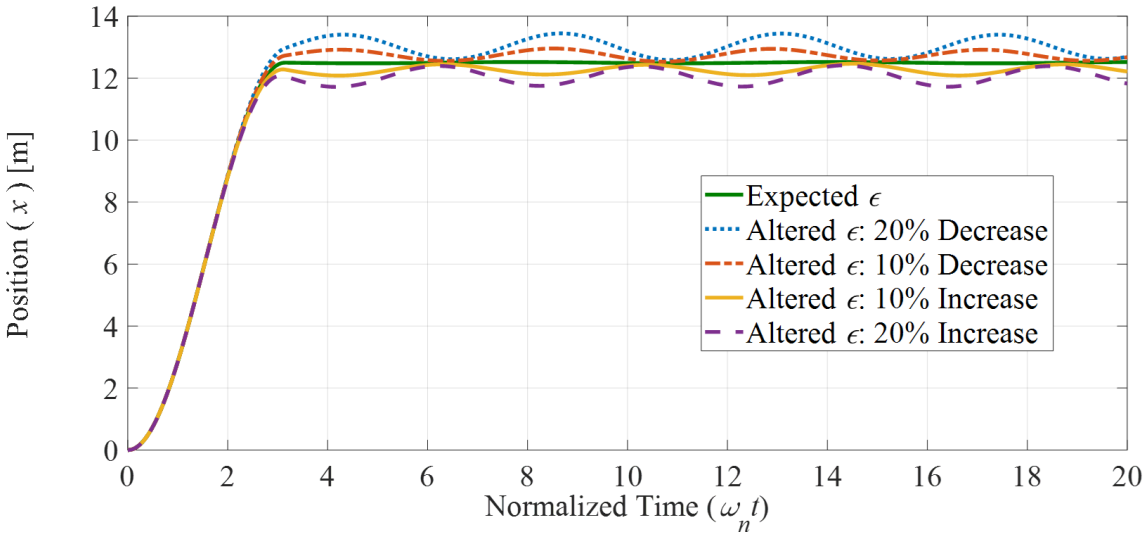

Figure 2-17 – Effect of nonlinear coefficient variations on TSCS effectiveness in reducing residual vibration in the position of an undamped Duffing oscillator with small cubic and quadratic nonlinearities (ω_n = 2 rad/s, ε = 0.01 1/(m^{2}s^2), F_0 = 50 N).

EKF provides a means for estimating the nonlinear coefficients of the undamped Duffing oscillator, as well as its linear natural frequency. EKF is essentially Kalman filtering (KF) implemented for nonlinear systems [63]. Further documentation of the EKF algorithm is given in [46, 63, 64]. In the present application, EKF requires multiple cycles of the TSCS procedure to iteratively infer the correct coefficients. To do so, an augmented system parameter estimation with EKF is defined herein as

$$\dot{\boldsymbol{x}}_{\boldsymbol{A}}(t) = \boldsymbol{f}_{\boldsymbol{A}}\big(\boldsymbol{x}_{\boldsymbol{A}}(t), \boldsymbol{u}(t)\big) + \boldsymbol{F}_{\boldsymbol{A}}\boldsymbol{W}_{\boldsymbol{A}}(t) = \begin{bmatrix} \boldsymbol{f}(\boldsymbol{x}(t), \boldsymbol{u}(t), \boldsymbol{\Theta}) \\ 0 \end{bmatrix} + \begin{bmatrix} \boldsymbol{F} & 0 \\ 0 & 0 \end{bmatrix} \begin{bmatrix} \boldsymbol{w}(t) \\ 0 \end{bmatrix} \tag{2.37}$$

$$\boldsymbol{y}(t) = \boldsymbol{g_A}\left(\boldsymbol{x_A}(t), \boldsymbol{u}(t)\right) \tag{2.38}$$

$$\boldsymbol{z}(k) = \boldsymbol{y}(k) + \boldsymbol{G}\boldsymbol{v}(k) \tag{2.39}$$

where $\boldsymbol{x}$ denotes the unaugmented state vector, $\boldsymbol{x_A}$ the augmented state vector (more details below), $\boldsymbol{u}$ the input vector, $\boldsymbol{f_A}$ the augmented function containing the dynamics of the system and parameters being inferred, $\boldsymbol{f}$ the original expression for the dynamics of the analyzed system, $\boldsymbol{F_A}$ the augmented additive process noise matrix, $\boldsymbol{F}$ the additive process noise matrix for the original system, $\boldsymbol{w}(t)$ the independent, zero-mean additive white Gaussian noise (AWGN) in the process, $\boldsymbol{W_A}(t)$ the augmented process noise vector, $\boldsymbol{y}$ the defined output of the system, $\boldsymbol{g_A}$ the expression representing observed output quantities, and $\boldsymbol{\Theta}$ a parameter vector to be estimated with EKF. The zeros in Eq. (2.37) arise since the parameters being estimated are assumed to be time invariant, i.e.

$$\dot{\boldsymbol{\Theta}} = 0 \tag{2.40}$$

Equation (2.39) represents the measurement vector, $\boldsymbol{z}$, populated by sampling $\boldsymbol{y}$ with a sampling time of T_S at N discrete time steps where $\boldsymbol{v}(k)$ is the independent, zero-mean AWGN of the measurements and $\boldsymbol{G}$ is the additive measurement noise matrix [46]. AWGN is added to the system response and output with the properties of a constant power spectral density (PSD) with a normal distribution characterized by the probability density function (PDF)

$$\mathrm{PDF}(v) = \frac{1}{\sqrt{2\pi\sigma^2}} e^{-\frac{(v-\mu)^2}{2\sigma^2}} \tag{2.41}$$

where μ denotes the mean of the distribution (which is zero for Gaussian noise), v the noise, and σ the variance of the data [65].

The augmented system is a representation of the original dynamic system with the parameters being estimated included in the system's state vector. The vector of estimated parameters used is

$$\boldsymbol{\Theta} = \begin{bmatrix} \theta_1 \\ \theta_2 \end{bmatrix} = \begin{bmatrix} \varepsilon \\ \omega_n \end{bmatrix} \tag{2.42}$$

where Eq. (2.40) implies that the estimated parameters are not time-varying in a single data set. Therefore, the complete state vector for the analysis with EKF is

$$\boldsymbol{x_A}(t) = \begin{bmatrix} x_1 \\ x_2 \\ \theta_1 \\ \theta_2 \end{bmatrix} = \begin{bmatrix} x \\ \dot{x} \\ \varepsilon \\ \omega_n \end{bmatrix} \tag{2.43}$$

The EKF algorithm is implemented for parameter estimation using the augmented system defined in Eqs. (2.37) through (2.39) and the corresponding state vector provided in Eq. (2.43). The control input vector, $\boldsymbol{u}(t)$, in Eqs. (2.37) and (2.38) is the input force being applied to the undamped Duffing oscillator.

EKF consists of two steps, prediction and update. The development followed for the undamped Duffing oscillator is taken from [46, 66, 67]. A hat accent denotes a corrected

value in the update step, and a tilde accent denotes a predicted value in the extrapolation stage. The extrapolation stage is defined with the following calculations

$$\widetilde{\boldsymbol{x}}_{\boldsymbol{A}}(k) = \widehat{\boldsymbol{x}}_{\boldsymbol{A}}(k-1) + \int_{t(k-1)}^{t(k)} \boldsymbol{f}_{\boldsymbol{A}}(\widehat{\boldsymbol{x}}_{\boldsymbol{A}}(t), \overline{\boldsymbol{u}}(k))dt \tag{2.44}$$

$$\widetilde{\boldsymbol{P}}_{\boldsymbol{A}}(k) \approx \boldsymbol{\Phi}_{\boldsymbol{A}}(k)\widehat{\boldsymbol{P}}_{\boldsymbol{A}}(k-1)\boldsymbol{\Phi}_{\boldsymbol{A}}^{T}(k) + T_S\boldsymbol{F}_{\boldsymbol{A}}\boldsymbol{F}_{\boldsymbol{A}}^{T} \tag{2.45}$$

where $\boldsymbol{P}_{\boldsymbol{A}}$ denotes the error covariance matrix, $\boldsymbol{\Phi}_{\boldsymbol{A}}(k)$ a discrete time state-transition matrix for the system (defined below) at the discrete time $t(k)$, and $\overline{\boldsymbol{u}}$ the input value interpolated between $t(k\text{-}1)$ and $t(k)$ [46, 66, 67]. The predicted state of the system arises from integration of Equation (2.37), without consideration of noise, between times $t(k\text{-}1)$ and $t(k)$. Equation (2.45) is a linear approximation of the error covariance matrix for small sampling times, T_S, which neglects higher-order terms and causes EKF to be a non-optimal approximation of KF for nonlinear systems [46, 68]. The discrete time state-transition matrix of the augmented system is expressed as

$$\boldsymbol{\Phi}_{\boldsymbol{A}}(k) = e^{\mathbf{A}_{\boldsymbol{A}}(k)T_S} \tag{2.46}$$

where $\boldsymbol{A}_{\boldsymbol{A}}(k)$ is the linearized state matrix for the augmented system

$$\mathbf{A}_{\boldsymbol{A}}(k) = \left.\frac{\partial \boldsymbol{f}_{\boldsymbol{A}}}{\partial \boldsymbol{x}_{\boldsymbol{a}}}\right|_{\boldsymbol{x}_{\boldsymbol{A}}=\widehat{\boldsymbol{x}}_{\boldsymbol{A}}(k-1)} = \left.\begin{bmatrix} \dfrac{\partial \boldsymbol{f}}{\partial \boldsymbol{x}} & \dfrac{\partial \boldsymbol{f}}{\partial \boldsymbol{\Theta}} \\ 0 & 0 \end{bmatrix}\right|_{\boldsymbol{x}_{\boldsymbol{A}}=\widehat{\boldsymbol{x}}_{\boldsymbol{A}}(k-1)} \tag{2.47}$$

The complete expression for the linearized state matrix of the augmented system consisting of the undamped Duffing oscillator and associated parameters is found in Eq. (A.1) in Appendix A.

The update stage is defined with the following calculations

$$\tilde{\boldsymbol{y}}(k) = \boldsymbol{g}_{\boldsymbol{A}}(\tilde{\boldsymbol{x}}_{\boldsymbol{A}}(k), \boldsymbol{u}(k)) \tag{2.48}$$

$$\mathbf{K}_{\boldsymbol{A}}(k) = \tilde{\boldsymbol{P}}_{\boldsymbol{A}}(k)\boldsymbol{C}_{\boldsymbol{A}}^{T}(k)[\boldsymbol{C}_{\boldsymbol{A}}(k)\tilde{\boldsymbol{P}}_{\boldsymbol{A}}(k)\boldsymbol{C}_{\boldsymbol{A}}^{T}(k) + \boldsymbol{G}\boldsymbol{G}^{T}]^{-1} \tag{2.49}$$

$$\hat{\boldsymbol{x}}_{\boldsymbol{A}}(k) = \tilde{\boldsymbol{x}}_{\boldsymbol{A}}(k) + \mathbf{K}_{\boldsymbol{A}}(k)[\boldsymbol{z}(k) - \tilde{\boldsymbol{y}}(k)] \tag{2.50}$$

$$\hat{\boldsymbol{P}}_{\boldsymbol{A}}(k) = [\boldsymbol{I} - \boldsymbol{K}_{\boldsymbol{A}}(k)\boldsymbol{C}_{\boldsymbol{A}}(k)]\tilde{\boldsymbol{P}}_{\boldsymbol{A}}(k)[\boldsymbol{I} - \boldsymbol{K}_{\boldsymbol{A}}(k)\boldsymbol{C}_{\boldsymbol{A}}(k)]^{T} + \boldsymbol{K}_{\boldsymbol{A}}(k)\boldsymbol{G}\boldsymbol{G}^{T}\boldsymbol{K}_{\boldsymbol{A}}^{T}(k) \tag{2.51}$$

where the output of the undamped Duffing oscillator model is defined as the position and velocity [46]. Equation (2.48) is used to calculate the predicted output variables that are compared to measurements. The Kalman gain in Eq. (2.49) is the linear filter gain that minimizes the mean square error between the predicted output and measured data using Eq. (2.50) to arrive at the corrected state values [47]. Equation (2.51) updates the value of the error covariance matrix for the extrapolation stage in the next time step based on the current Kalman gain. The $\boldsymbol{C}_{\boldsymbol{A}}$ in Eqs. (2.49) and (2.51) is the linearized output matrix

$$\boldsymbol{C_A}(k) = \frac{\partial \boldsymbol{g_A}}{\partial \boldsymbol{x_a}}\bigg|_{\boldsymbol{x_A}=\tilde{\boldsymbol{x}}_{\boldsymbol{A}}(k)} = \begin{bmatrix} 1 & 0 & 0 & 0 \\ 0 & 1 & 0 & 0 \end{bmatrix} \tag{2.52}$$

where $\boldsymbol{C_A}$ has the simple representation given because the output vector is defined as the position and velocity of the oscillator. To implement this approach, several values must be defined, such as the initial value for $\boldsymbol{P_A}$ as well as the values for $\boldsymbol{F}$ and $\boldsymbol{G}$. The initial definition of $\boldsymbol{P_A}$ is a representation of the confidence in initial state estimates. $\boldsymbol{FF}^T$ and $\boldsymbol{GG}^T$ are the process and measurement covariance matrices, respectively. The measurement covariance matrix is calibrated based on the sensors and measurements taken, but trial and error or an adaptive filtering technique may be required to define the process covariance matrix [46].

Figure 2-18a and Figure 2-18b show the result of applying EKF for parameter estimation with the output and input case representing an unshaped input before the application of TSCS. Defining an original error of 200% on both the nonlinear coefficient and linear natural frequency, EKF converges to values that are adequate to implement with TSCS. Figure 2-18a shows the convergence of the nonlinear coefficient of the Duffing oscillator, where the converged value is 0.0095. The converged value for the nonlinear coefficient has an error of less than 4.5%. The initial value of $\boldsymbol{P_A}$ offers the user a choice between the competing goals of convergence speed and overshoot of the parameters from initial values. If the estimates converge, the final values obtained from applying EKF to data set are satisfactory for TSCS implementation.

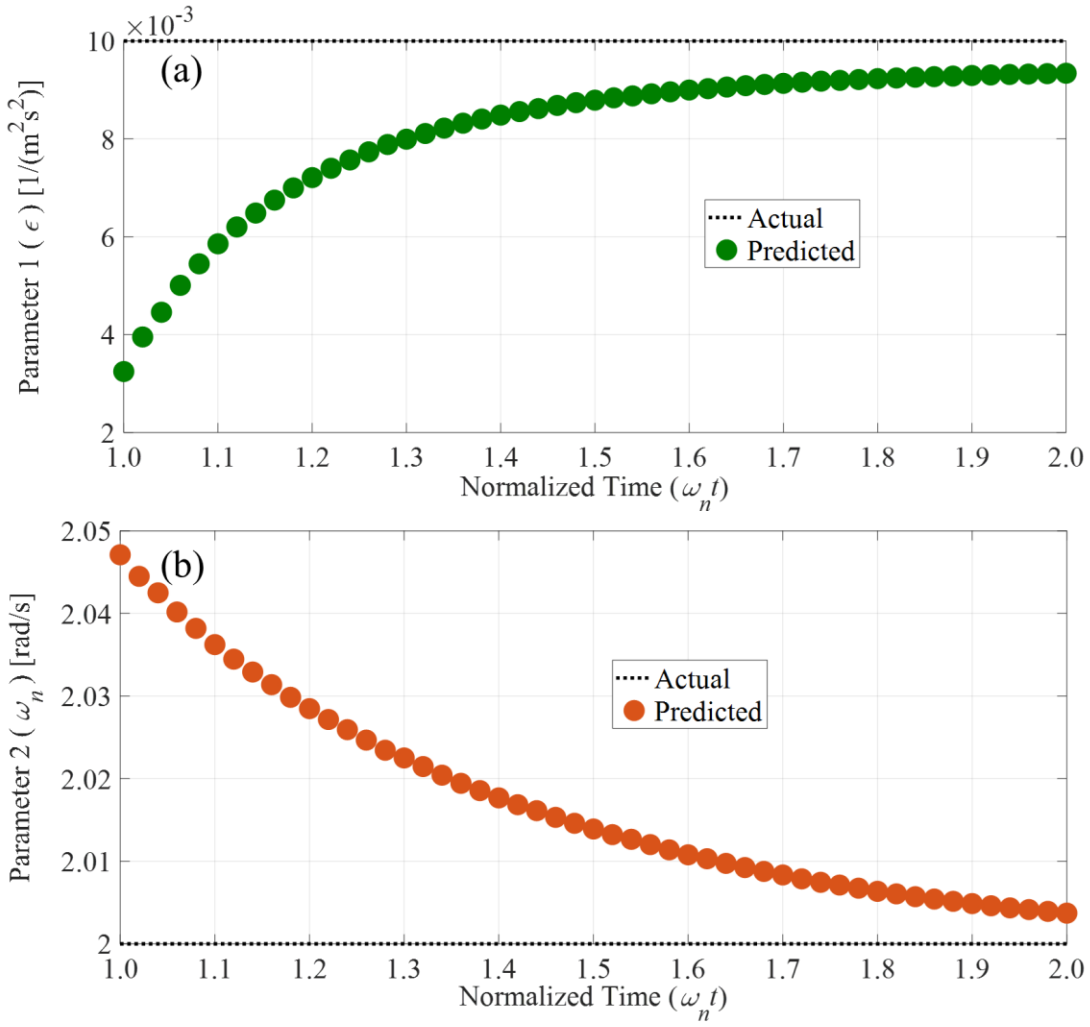

Figure 2-18 – Convergence of (a) the nonlinear coefficient and (b) linear natural frequency of an undamped Duffing oscillator with EKF (ω_n = 2 rad/s, ε = 0.01 1/(m^{2}s^2), F_0 = 50 N).

Figure 2-18b shows the convergence of the linear natural frequency. In addition to the convergence of the nonlinear coefficient, the linear natural frequency converged to 1.991, which gives the estimate an error of 0.4%. Using EKF to estimate the linear natural frequency of the oscillator serves as an alternative to robust command shaping. Applying TSCS with the converged parameter values significantly improves the strategy's effectiveness. Figure 2-19 presents the effect of mitigating a variation in the natural

frequency and nonlinear coefficient with EKF. TSCS applied with EKF reduces the residual vibration observed with a 100% increase in the nonlinear coefficient and linear natural frequency by 28.1 dB.

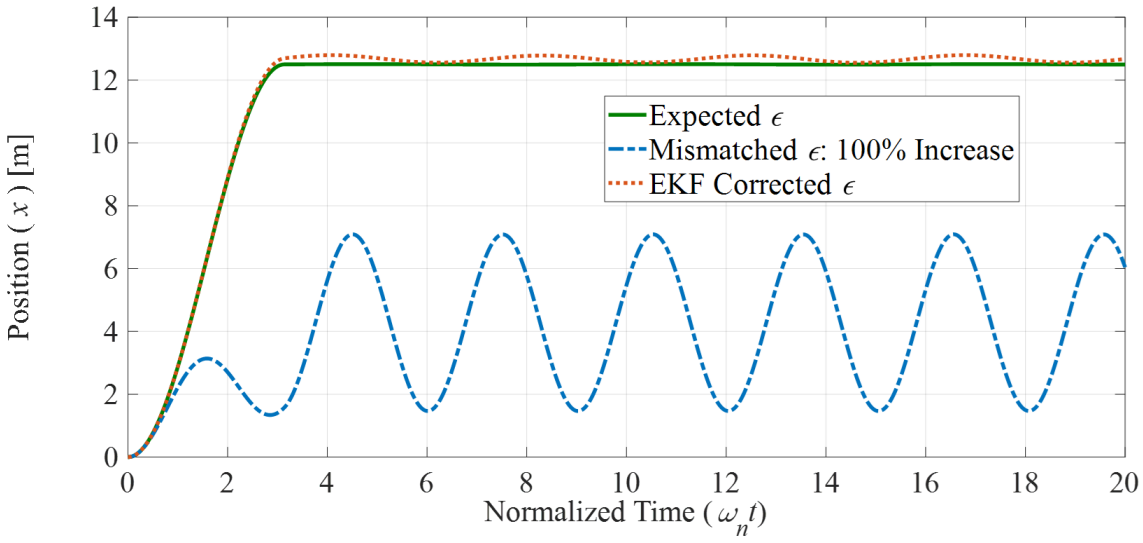

Figure 2-19 – EKF mitigation of severe parameter variations on TSCS effectiveness in reducing residual vibration in the position of an undamped Duffing oscillator with small cubic and quadratic nonlinearities (ω_n = 2 rad/s, ε = 0.01 1/(m^{2}s^2), F_0 = 50 N).

2.5 Conclusions

This chapter has introduced TSCS and demonstrated its effectiveness in reducing residual vibrations in a commanded nonlinear system. Specifically, the TSCS strategy was applied to several variants of the Duffing equation and compared to direct command shaping approaches employing linear and nonlinear response frequencies. In all cases considered, TSCS outperforms the direct input shaping methods. Due to the use of scale separation and command shaping of a linear subsystem, TSCS avoids large residual vibrations observed in the direct approaches, these vibrations being exacerbated by large

input commands, strong nonlinearities, and negative command impulses. A small drawback to the TSCS strategy is a noticeable discrepancy between the desired and achieved response amplitude, especially for highly nonlinear systems. This can be effectively mitigated, however, through either online or offline feedback control. Additionally, TSCS has been compared to feedback control strategies to show the possible benefits and costs of using the strategy. Finally, in nonlinear systems with uncertainties, robust input shaping and parameter estimation with EKF have been shown to effectively mitigate residual vibrations resulting from mismatches in expected and actual system parameters (e.g., linear natural frequency and nonlinear coefficients).

CHAPTER 3. TWO-SCALE COMMAND SHAPING FOR REDUCING POWERTRAIN VIBRATION DURING INTERNAL COMBUSTION ENGINE RESTART

This chapter leverages the techniques developed in Chapter 2 and applies a two-scale command shaping strategy for reducing vibrations in conventional and HEV powertrains during engine restart. The approach introduces no additional system components and thus few additional costs. The torque profile from an EM is tailored to start the ICE while minimizing residual vibrations. It is shown that the tailored EM torque profile, composed of a linear combination of constant and time-varying components, results in significant mitigation of powertrain vibrations and smoother ICE startup. The time-varying EM torque component is calculated using an analytical ICE model and a perturbation technique for separating scales, which isolates the ICE nonlinear response. Command shaping is then applied to the linear problem at the remaining scale. Simulation results suggest a promising and straightforward technique for reducing vibrations and improving drivability during ICE restart.

Additionally, this chapter applies RLS and EKF approaches for estimating uncertain engine friction and inertial parameters necessary for reduced-vibration engine restart using a TSCS strategy. Robust command shaping methods are also explored to decrease the impact of system parameter variations on the efficacy of TSCS. For full implementation, the TSCS strategy requires input parameters characterizing the ICE which may be a) difficult to quantify, and/or b) uncertain due to their dependence on engine

operating temperature and other environmental considerations. RLS and EKF algorithms tailored to TSCS are presented herein for estimating such parameters. It is shown that both the RLS and EKF algorithms can be used to estimate the necessary ICE parameters and increase effectiveness of the TSCS strategy. The EKF algorithm estimates uncertain ICE parameters with minimal measurement requirements, giving it an advantage over the presented RLS algorithm. Robust command shaping methods are also explored to decrease the impact of variations in system vibration modes on the efficacy of command shaping.

3.1 Analytical models for concept validation

3.1.1 Internal combustion engine model

The model used to define the output torque from the ICE is adopted from the work of Canova *et al.* and the general techniques developed by Ramos and Taylor [5, 69, 70]. The ICE model represents a 1.3 L inline 4-cylinder (I4) uniJet Turbo Diesel (JTD) engine produced cooperatively by Fiat and General Motors and experimentally characterized using parameters and data provided by Ponti *et al.* [71]. The piston position of a single cylinder is defined through a geometric analysis of the crank slider mechanism demonstrated in Figure 3-1. The distance from the crank radius center to the piston pin, as a function of crank angle, is defined as

$$x_P(\theta_E) = r\cos(\theta_E) + \sqrt{l^2 - r^2\sin^2\theta_E} \tag{3.1}$$

where r denotes the crank radius, l the connecting rod length, and θ_E the crank angle. Utilizing an equivalent geometric analysis, the instantaneous volume of a single cylinder is

$$V(\theta_E) = V_C + \frac{\pi B^2 r}{4}\left[\frac{l}{r} + (1 - \cos\theta_E) - \sqrt{\frac{l^2}{r^2} - \sin^2\theta_E}\right] \tag{3.2}$$

where V_C and B are the clearance volume and cylinder bore, respectively.

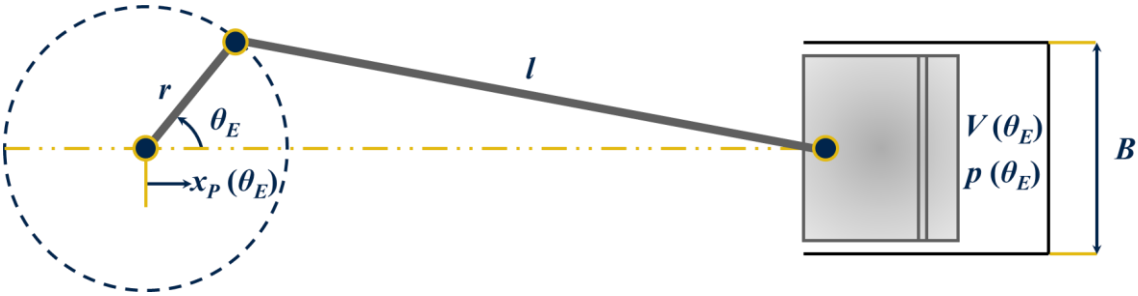

Figure 3-1 – Diagram of the crank-slider system representing ICE crankshaft kinematics.

Once the instantaneous volume is defined for a cylinder, the pressure is governed from intake valve closing (IVC) to exhaust valve opening (EVO) via the differential equation governing in-cylinder pressure p

$$\frac{dp}{d\theta_E} = -\gamma\frac{p}{V}\frac{dV}{d\theta_E} + \frac{(\gamma - 1)}{V}\frac{dQ}{d\theta_E} \tag{3.3}$$

where V denotes the cylinder volume and γ the specific heat ratio for the air-fuel mixture. Numerous research groups have used this approach to model ICE dynamics [5, 69, 71]. The second term of Eq. (3.3) is approximated through three Wiebe functions used to

represent the heat release rate for the premixed, main, and diffusive combustion periods in the 1.3 L JTD engine

$$\frac{dQ}{d\theta_E} = \left(m_{iP} x_{fP} LHV \frac{a_P(m_P+1)}{\Delta\theta_P} \frac{\theta_E - \theta_{SOCP}}{\Delta\theta_P} e^{\left[-a_P\left(\frac{\theta_E-\theta_{SOCP}}{\Delta\theta_P}\right)^{m_P+1}\right]} \right) H(\theta_E - \theta_{SOCP})$$
$$+ \left(m_{iM} x_{fM} LHV \frac{a_M(m_M+1)}{\Delta\theta_M} \frac{\theta_E - \theta_{SOCM}}{\Delta\theta_M} e^{\left[-a_M\left(\frac{\theta_E-\theta_{SOCM}}{\Delta\theta_M}\right)^{m_M+1}\right]} \right) H(\theta_E - \theta_{SOCM}) \quad (3.4)$$
$$+ \left(m_{iD} x_{fD} LHV \frac{a_D(m_D+1)}{\Delta\theta_D} \frac{\theta_E - \theta_{SOCD}}{\Delta\theta_D} e^{\left[-a_D\left(\frac{\theta_E-\theta_{SOCD}}{\Delta\theta_D}\right)^{m_D+1}\right]} \right) H(\theta_E - \theta_{SOCD})$$

where subscripts *P*, *M*, and *D* distinguish whether the expression is for the premixed, main, or diffusive combustion period, respectively [69, 72, 73]. In Eq. (3.4), m_{iZ} denote the mass of fuel injected, x_{fZ} the fraction of fuel burned, a_Z the Wiebe correlation parameter, m_Z the shape factor, $\Delta\theta_Z$ the energy release duration expressed as a crank angle, and θ_{SOCZ} the crank angle at the start of the combustion period denoted with subscript *Z*. The subscript *Z* would be *P*, *M*, or *D* for the premixed, main, and diffusive combustion periods, respectively. *LHV* is the lower heating value for diesel fuel.

Equation (3.3) simplifies during the initial cranking phase

$$\frac{dp}{d\theta_E} = -\gamma \frac{p}{V} \frac{dV}{d\theta_E} \quad (3.5)$$

since the heat release from combustion is absent. Solving Eq. (3.5) yields

$$p(\theta_E) = CV^{-\gamma} \quad (3.6)$$

which represents a polytropic thermodynamic process. The coefficient C is a constant determined by known ICE operating points. Figure 3-2 documents the calculated in-cylinder pressure, with combustion, as implemented herein and compared to that measured experimentally by Ponti *et al*. [71]. When combustion is present, the differential equation given in Eq. (3.3) must be solved numerically alongside the differential equations governing the powertrain and chassis motion, which are presented in Section 3.1.2. The initial conditions for the differential equation governing pressure are given through solution of Eq. (3.6) with the initial position of the ICE.

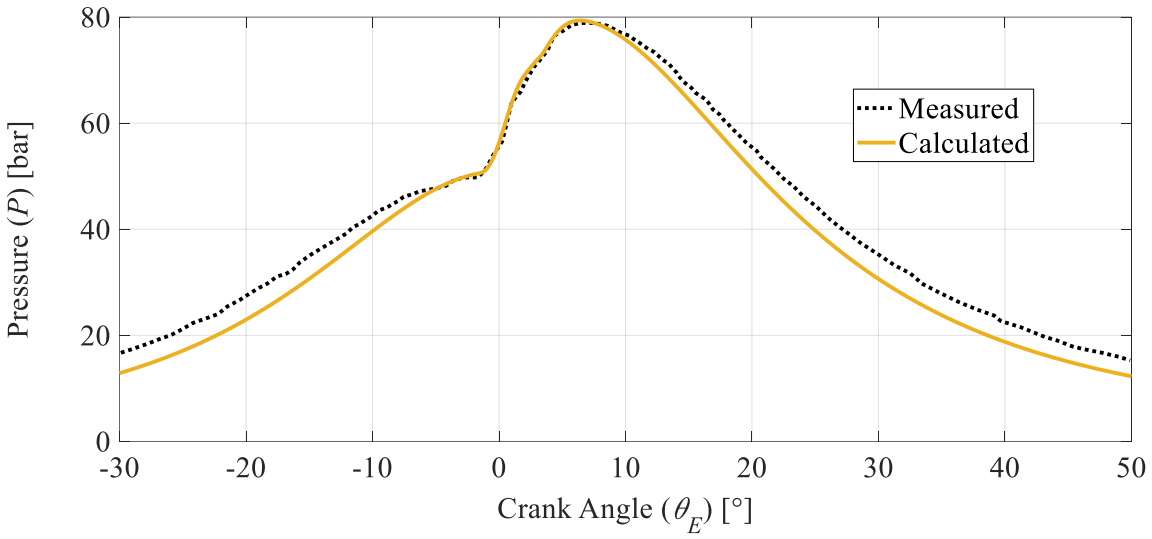

Figure 3-2 – Comparison of the in-cylinder pressure of a single cylinder of the 1.3 L JTD ICE calculated with three Wiebe functions to experimental data.

The torque acting at the crankshaft decomposes into three components

$$T_E(\theta_E) = T_{Indicated}(\theta_E) + T_{Inertial}(\theta_E) - T_{Friction}(\theta_E) \tag{3.7}$$

where $T_{Indicated}$ denotes the indicated torque from the ICE that arises from the in-cylinder pressure, $T_{Inertial}$ the inertial torque due to the apparent forces arising from the ICE components in reciprocating motion, and $T_{Friction}$ the approximate torque due to frictional losses. The indicated torque derives from the force exerted on the piston due to the in-cylinder pressure, which is given as

$$T_{Indicated}(\theta_E) = rA_P(p(\theta_E) - p_{Ambient})\left(\sin\theta_E + \frac{\sin\theta_E \cos\theta_E}{\sqrt{R^2 - \sin^2\theta_E}}\right) \tag{3.8}$$

where A_P denotes the piston crown area. The inertial torque is defined as

$$T_{Inertial}(\theta_E) = rF_{Inertial}(\theta_E)\left(\sin\theta_E + \frac{\sin\theta_E \cos\theta_E}{\sqrt{R^2 - \sin^2\theta_E}}\right) \tag{3.9}$$

where $F_{Inertial}$ denotes the apparent force due to the ICE components in reciprocating motion. Observing the crank-slider mechanism outlined in Figure 3-1 and using the chain rule to calculate the second derivative of Eq. (3.1), the inertial force is given as

$$F_{Inertial}(\theta_E) = M_{Inertial}\ddot{x}_P = M_{Inertial}\left(\frac{dx_P}{d\theta_E}\ddot{\theta}_E + \frac{d^2x_P}{d\theta_E^2}\dot{\theta}_E^2\right) \tag{3.10}$$

where $M_{Inertial}$ denotes the mass of ICE components in reciprocating motion. The friction torque is approximated using a polynomial expression defined using the instantaneous ICE speed and the in-cylinder pressure, as provided by Canova *et al.* and Chen *et al.* [5, 74]. Using a polynomial approximation, the friction torque is expressed as

$$T_{Friction}(\theta_E) = T_{Friction_0} + k_p p(\theta_E) + k_{\omega_1}\dot{\theta}_E + k_{\omega_2}\dot{\theta}_E{}^2 \tag{3.11}$$

where $T_{Friction_0}$, k_p, k_{ω_1}, and k_{ω_2} are experimentally defined parameters that fit the model to measured data. Equation (3.11) is valid for a single temperature; however, Canova *et al.* have shown that a lumped thermal system undergoing cooling due to convection, and heating due to friction, accurately accounts for variations in engine temperature [5].

The above development is for a single cylinder of the ICE, which can be extended to the complete engine by adding the correct phase lag for each cylinder that represents the crank rotation between firing events. For a four-stroke engine with four cylinders, the degrees between firing events is 180°. In the analysis of the 1.3 L JTD engine, the maximum inertial torque is less than 3% of the peak indicated torque, which can be observed graphically in Figure 3-3. Therefore, the inertial torque is neglected from this point forward. In addition, a quasi-static friction model is used in which the fitted coefficients are assumed constant since the ICE temperature undergoes minimal variation during an ICE start/restart. The parameters used in the model of the 1.3 L JTD engine, presented in Table B-1 in the Appendix, are taken from the work of Canova *et al.*, Ramos, and Ponti *et al.* [5, 69, 71].

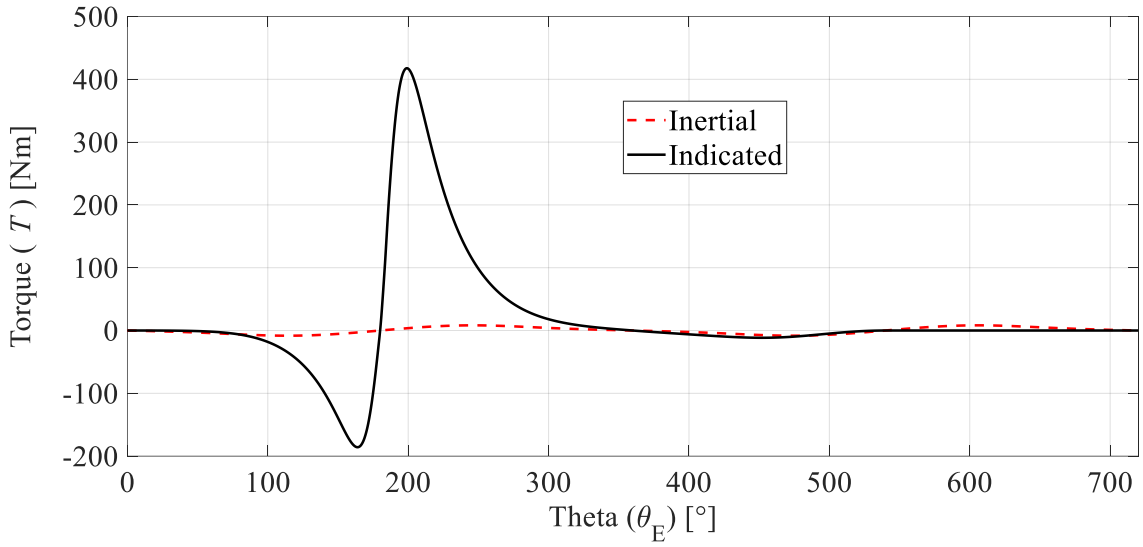

Figure 3-3 – Comparison of the indicated and inertial torque of a single cylinder of the 1.3 L JTD ICE.

3.1.2 Powertrain model

Figure 3-4 provides the lumped-parameter torsional powertrain model used to study ICE crankshaft, EM rotor, and clutch dynamics during stationary ICE restart. The clutch and flexible coupling capture the important essence of a powertrain flexible pole – this and other powertrain poles can arise in many forms, and the approach presented easily generalizes to accommodate such poles. The importance of the flexible powertrain pole is that the engine restart remediation cannot be done in isolation – i.e., less-informed remediation treatments will likely lead to undesirable excitation of flexible poles downstream of the engine. Note that the powertrain is modeled as being decoupled (e.g., clutch disengaged) from the wheels, and hence the vehicle is *stationary* during restart – this can be contrasted with the more difficult problem of *launch* operation where the clutch engages during restart.

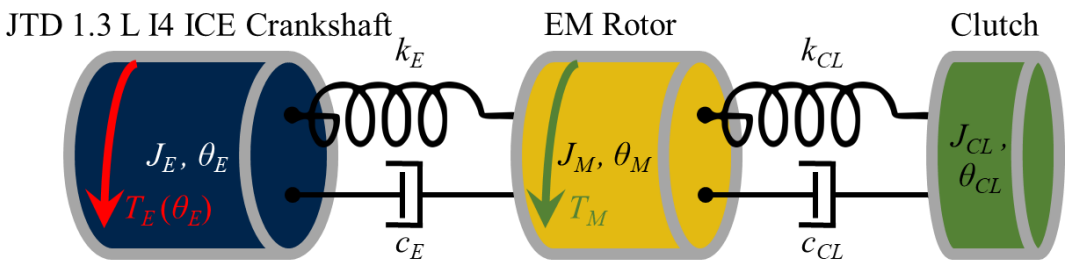

Figure 3-4 – Lumped-parameter torsional powertrain model.

As shown in Figure 3-4, the model consists of equivalent inertias representing the ICE crankshaft and counterbalances, EM rotor, and clutch assembly. Light, flexible shafts couple these inertias. The resulting dynamic model in state-space form is given as

$$\begin{bmatrix} J_E & 0 & 0 \\ 0 & J_M & 0 \\ 0 & 0 & J_{CL} \end{bmatrix} \begin{bmatrix} \ddot{\theta}_E \\ \ddot{\theta}_M \\ \ddot{\theta}_{CL} \end{bmatrix} + \begin{bmatrix} c_E & -c_E & 0 \\ -c_E & c_E + c_{CL} & -c_{CL} \\ 0 & -c_{CL} & c_{CL} \end{bmatrix} \begin{bmatrix} \dot{\theta}_E \\ \dot{\theta}_M \\ \dot{\theta}_{CL} \end{bmatrix} + \begin{bmatrix} k_E & -k_E & 0 \\ -k_E & k_E + k_{CL} & -k_{CL} \\ 0 & -k_{CL} & k_{CL} \end{bmatrix} \begin{bmatrix} \theta_E \\ \theta_M \\ \theta_{CL} \end{bmatrix} = \begin{bmatrix} T_E(\theta_E) \\ T_M \\ 0 \end{bmatrix} \quad (3.12)$$

where the mass moment of inertia of the clutch, J_{CL}, is that of the driven plate assembly considering the clutch to be disengaged. J_E and J_M represent the equivalent moments of inertia of the crankshaft and the EM rotor, respectively. Torsional stiffness and damping coefficients for the shaft coupling between the ICE and EM are denoted as k_E and c_E, respectively. The corresponding values for the flexible coupling between the EM and the clutch are k_{CL} and c_{CL}. The indicated torque of the ICE and EM act as external excitations, where EM indicated torque arises from electromagnetic forces the stator exerts on the rotor. The state vector of Eq. (3.12) contains the engine crankshaft, EM rotor, and clutch absolute rotational degrees-of-freedom.

Figure 3-5 depicts the coupling between the ICE and EM housings (e.g., engine block and stator, respectively) and the chassis with suspension. Like the inclusion of powertrain flexible poles, this second submodel captures downstream coupling of the ICE block to additional flexible poles, which represent the rotational motion of chassis in the model shown in Figure 3-5. In an equal and opposite sense, indicated torque from the ICE and EM act as external excitation on the submodel. Figure 3-6 depicts the EM rotor and stator coupling as well as the mount geometry used to define stiffness and damping. The equations of motion capturing the chassis coupling are

$$\begin{bmatrix} J_{EB} & 0 & 0 \\ 0 & J_{MB} & 0 \\ 0 & 0 & J_C \end{bmatrix} \begin{bmatrix} \ddot{\theta}_{EB} \\ \ddot{\theta}_{MB} \\ \ddot{\theta}_C \end{bmatrix} + \begin{bmatrix} c_{CE} & 0 & -c_{CE} \\ 0 & c_{CM} & -c_{CM} \\ -c_{CE} & -c_{CM} & c_{CE} + c_{CM} + c_T \end{bmatrix} \begin{bmatrix} \dot{\theta}_{EB} \\ \dot{\theta}_{MB} \\ \dot{\theta}_C \end{bmatrix} + \begin{bmatrix} k_{CE} & 0 & -k_{CE} \\ 0 & k_{CM} & -k_{CM} \\ -k_{CE} & -k_{CM} & k_{CE} + k_{CM} + k_T \end{bmatrix} \begin{bmatrix} \theta_{EB} \\ \theta_{MB} \\ \theta_C \end{bmatrix} = \begin{bmatrix} -T_E(\theta_E) \\ -T_M \\ 0 \end{bmatrix} \tag{3.13}$$

where J_{EB} and J_{MB} denote the moments of inertia of the engine block and EM housing, respectively, and J_C denotes the chassis' roll equivalent moment of inertia. The state vector of Eq. (3.13) contains the rotational degrees-of-freedom of the engine block, EM housing, and chassis. Alternatively, a modal model can be employed with appropriate chassis modes - this is not pursued herein but would result in similar matrix equations with (potentially) higher dimension.

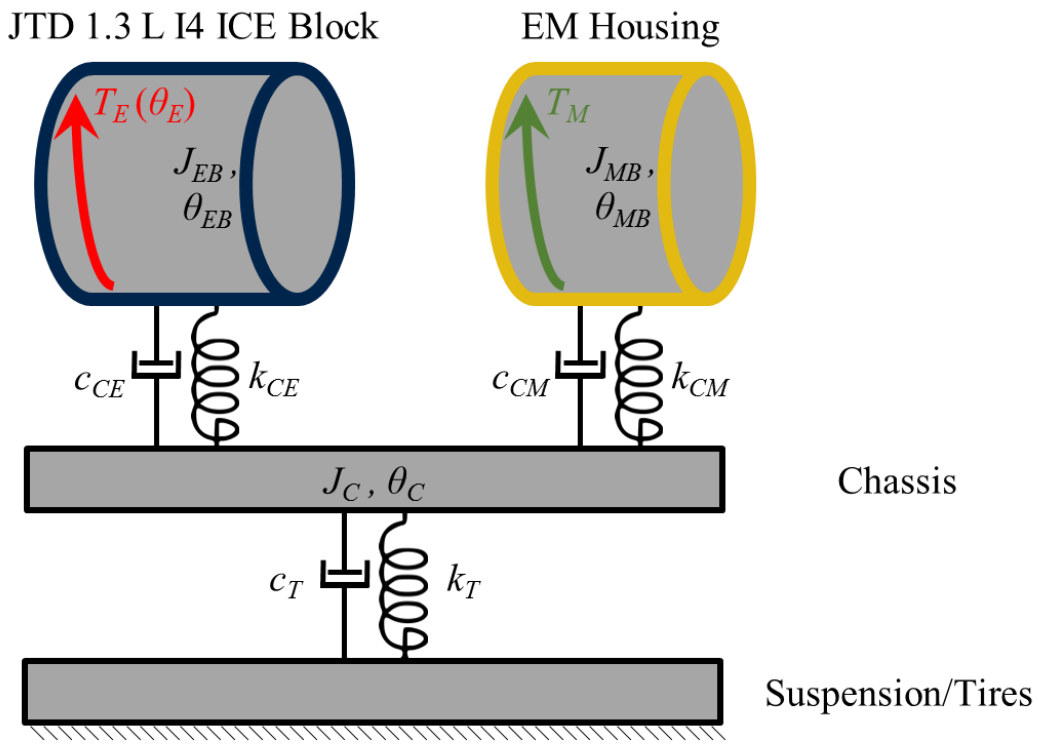

Figure 3-5 – Lumped-parameter chassis and suspension motion model.

Damping and stiffness values representing the coupling between the chassis and the EM are calculated from the approximate EM geometry and its mounts as shown in Figure 3-6. Given mount rectilinear damping and stiffness (c_{MM} and k_{MM}, respectively), the torsional damping and stiffness values (c_{CM} and k_{CM}) are expressed as $\frac{l_M^2 c_{MM}}{2}$ and $\frac{l_M^2 k_{MM}}{2}$, respectively. Analogous expressions follow for the ICE block such that c_{CE} and k_{CE} are given as $\frac{l_E^2 c_{ME}}{2}$ and $\frac{l_E^2 k_{ME}}{2}$, respectively. The damping and stiffness values (c_T and k_T) representing the suspension and tires are based on vehicle roll stiffness.

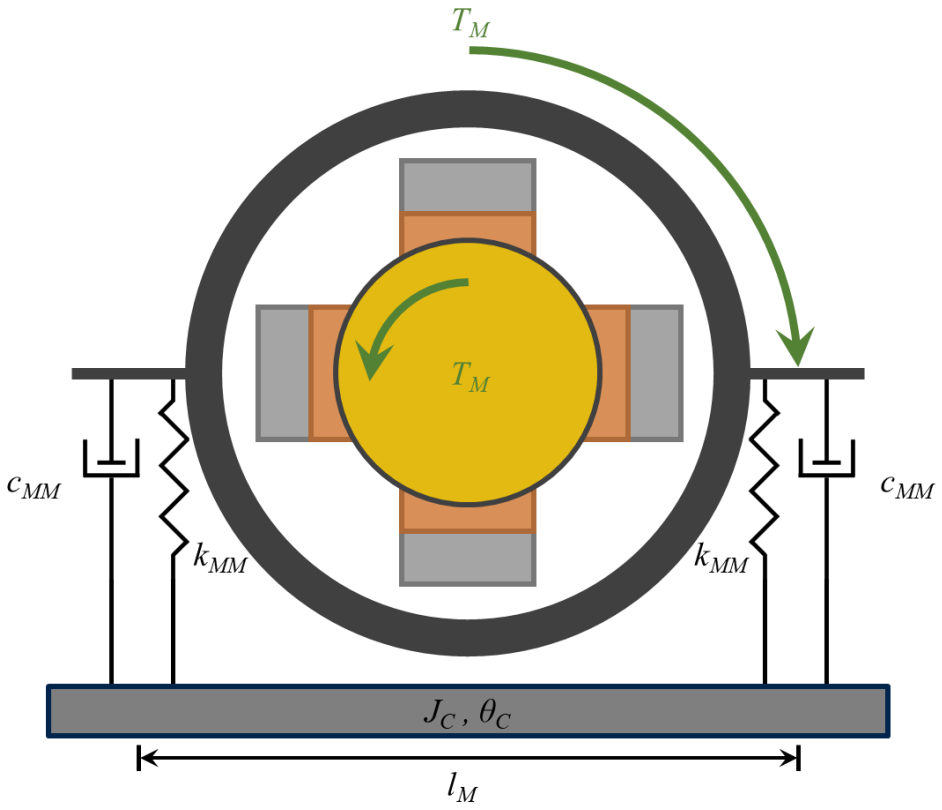

Figure 3-6 – Model used to estimate the equivalent torsional stiffness and damping of the EM mounts.

Table 3-1 provides representative numerical values for the model parameters detailed above [75-80]. The stiffness parameters for the powertrain are obtained using a powertrain CAD model of the General Motors Alpha platform [78] and general material data [79, 80]. A flexible coupling is used between the EM and the clutch of the vehicle for the powertrain analyzed, which defines the k_{CL} and c_{CL} values [79, 80]. Table 3-2 provides the numerical values used in the analyses for the system governing chassis rotational motion [53, 81-84]. The moments of inertia of the engine block and EM housing are approximated using the mass specified by the manufacturer assuming simple geometric shapes represent them [81, 82].

Table 3-1 – Torsional powertrain model parameters.

Parameter	Value
Moment of inertia of the ICE crankshaft (J_E), kgm^2 [75]	1.08E-01
Moment of inertia of the EM rotor (J_M), kgm^2 [76]	9.00E-02
Approximate moment of inertia of the driven plate assembly of the clutch (J_{CL}), kgm^2 [77]	5.20E-02
Diameter of the clutch (d_{CL}), m [77]	1.85E-01
Mass of the clutch (m_{CL}), kg [77]	1.21E+01
Stiffness element between EM and driven plate assembly of clutch (k_{CL}), Nm/rad [78-80]	2.20E+04
Diameter of the rotor of the EM (d_R), m [76]	3.00E-01
Thickness of the rotor of the EM (t_R), m [76]	5.00E-02
Rotor mass (m_R), kg [76]	8.00E+00

In the analysis case presented, the EM and ICE coupling is defined to be a pre-transmission configuration, such as the Honda ISG. With the pre-transmission configuration, the coupling between the EM and ICE is approximated as being rigid with negligible damping and the EM is mounted with the same mounts as the ICE block, which defines the values k_E, c_E, k_{CM}, and c_{CM}. Proportional damping matrices based on available parameter values are used in the test case.

Table 3-2 – Chassis rotational motion model parameters.

Parameter	Value
Approximate Moment of Inertia of the ICE block (J_{EB}), kgm^2 [81]	7.29E+00
Approximate Moment of Inertia of the EM housing (J_{MB}), kgm^2 [82]	8.87E-01
Moment of inertia representing the chassis (J_C), kgm^2 [83]	3.65E+02
Mass of the ICE block (m_{EB}), kg [81]	1.30E+02
Mass of the EM housing (m_{MB}), kg [82]	3.80E+01
Width of the ICE block (l_E), m [81]	5.00E-01
Height of the ICE block (h_E), m [81]	6.50E-01
Width of the EM housing (l_M), m [82]	4.32E-01
Stiffness element representing ICE/EM mounts (k_{CE}/k_{CM}), Nm/rad [84]	1.45E+04
Stiffness element representing suspension and tires (k_T), Nm/rad [53]	7.56E+04
Damping element representing suspension and tires (c_T), Nms/rad [53]	3.77E+03

3.2 Two-scale command shaping strategy applied to internal combustion engine restart

3.2.1 Application of scale separation

In the proposed two-scale command shaping strategy, the applied torque delivered by the EM is first decomposed into two terms

$$T_M(t) = T_{0_{Shaped}}(t) + \varepsilon T_1(t) \tag{3.14}$$

where T_1 is tailored to eliminate oscillations associated with the nonlinear engine crankshaft response. In Eq. (3.14), ε is introduced as a small book-keeping parameter [59, 60] used to order linear and nonlinear effects and later set to unity. As detailed in Sec. 3.2.2, $T_{0_{Shaped}}$ is tailored through command shaping to remove selected flexible poles (and associated vibrations) of the powertrain and/or chassis system. T_0 is the input applied to the system without application of TSCS, which is a step input in this chapter.

The rotational motion of the crankshaft and EM rotor is governed by the first two rows of Eq. (3.12)

$$\begin{aligned} J_E\ddot{\theta}_E + c_E\left(\dot{\theta}_E - \dot{\theta}_M\right) + k_E(\theta_E - \theta_M) &= T_E(\theta_E) \\ &= \varepsilon\left(rA_P(p(\theta_E) - p_{Ambient})\left(\sin\theta_E + \frac{\sin\theta_E\cos\theta_E}{\sqrt{R^2 - \sin^2\theta_E}}\right)\right) + T_{Friction}(\theta_E) \end{aligned} \tag{3.15}$$

$$J_M\ddot{\theta}_M + c_E\left(\dot{\theta}_M - \dot{\theta}_E\right) + c_{CL}\left(\dot{\theta}_M - \dot{\theta}_{CL}\right) + k_E(\theta_M - \theta_E) + k_{CL}(\theta_M - \theta_{CL}) = T_M = T_0 + \varepsilon T_1(t) \tag{3.16}$$

where the parameters of these expressions were defined in the introduction of Eq. (3.12). Recall that in Eq. (3.15) the inertial torque is neglected. The nonlinear indicated torque

from the ICE, as well as the time-varying portion, are ordered at the ε^1-scale such that $T_1(t)$ can be used to eliminate the oscillations associated with the nonlinear engine crankshaft response. In the analysis presented, the EM and ICE coupling is defined to be a pre-transmission configuration. Therefore, the coupling between the components is approximately rigid, which allows Eq. (3.15) and Eq. (3.16) to be combined as

$$\ddot{\theta}_E = \frac{T_0 + \varepsilon T_1(t)}{J_E + J_M} + \frac{\varepsilon}{J_E + J_M}\left(rA_P(p(\theta_E) - p_{Ambient})\left(\sin\theta_E + \frac{\sin\theta_E \cos\theta_E}{\sqrt{R^2 - \sin^2\theta_E}}\right)\right) + \frac{T_{Friction}(\theta_E)}{J_E + J_M} + \frac{c_{CL}}{J_E + J_M}(\dot{\theta}_{CL} - \dot{\theta}_E) + \frac{k_{CL}}{J_E + J_M}(\theta_{CL} - \theta_E) \tag{3.17}$$

Next, an asymptotic approximation is introduced for θ_E using the book-keeping parameter

$$\theta_E = \theta_{E0}(t) + \varepsilon\theta_{E1}(t) + \varepsilon^2\theta_{E2}(t) + O(\varepsilon^3) \tag{3.18}$$

Separating the problem scales in Eq. (3.17) via Eq. (3.18), the zeroth-order equation is given as

$$\ddot{\theta}_{E0} = \frac{T_0}{J_E + J_M} + \frac{T_{Friction}(\theta_{E0})}{J_E + J_M} + \frac{c_{CL}}{J_E + J_M}(\dot{\theta}_{CL} - \dot{\theta}_{E0}) + \frac{k_{CL}}{J_E + J_M}(\theta_{CL} - \theta_{E0}) \tag{3.19}$$

Equation (3.19) is treated in Sec. 3.2.2 when command shaping is discussed. The friction torque component is defined at the zero-order, ε^0, scale. Defining the friction torque at the zero-order scale reduces the dynamic torque component, $T_1(t)$, required from the EM

without decreasing the impact of the strategy. The ICE nonlinear dynamics are governed by the first-order equation

$$\ddot{\theta}_{E1} = \frac{T_1(t)}{J_E + J_M} + \frac{1}{J_E + J_M}\left(rA_P(p(\theta_{E0}) - p_{Ambient})\left(\sin\theta_{E0} + \frac{\sin\theta_{E0}\cos\theta_{E0}}{\sqrt{R^2 - \sin^2\theta_{E0}}}\right)\right) - \frac{c_{CL}}{J_E + J_M}\dot{\theta}_{E1} - \frac{k_{CL}}{J_E + J_M}\theta_{E1} \tag{3.20}$$

Re-arranging Eq. (3.20) and setting θ_{E1} and its subsequent time derivatives to zero yields the time-varying EM torque component required to mitigate nonlinear ICE dynamics

$$T_1(t) = -\left(rA_P(p(\theta_{E0}) - p_{Ambient})\left(\sin\theta_{E0} + \frac{\sin\theta_{E0}\cos\theta_{E0}}{\sqrt{R^2 - \sin^2\theta_{E0}}}\right)\right) \tag{3.21}$$

Equation (3.21) represents the first half of the tailored EM torque expression needed in the proposed approach.

3.2.2 Application of command shaping to engine restart

A command shaping technique that can be used to mitigate the excitation of flexible modes of the powertrain and chassis coupling is multi-mode input shaping developed on the basis of Posicast Control [9, 12, 41]. The multi-mode input shaping process can be implemented with the zeroth-order expression in Eq. (3.19) and the zeroth-order torque component, T_0, which results in

$$T_{0_{Shaped}}(t) = T_0 * I_1(t) * I_2(t) * \ldots \tag{3.22}$$

where $T_{0_{Shaped}}(t)$ denotes the zeroth-order torque component following shaping and I_i(t) represents the input shaper designed for one of the *n* vibration frequencies of the powertrain

and chassis models convolved with the original torque command. Several input shapers have been developed, including robust strategies such as ZVD and EI input shapers [9, 40, 41]. ZV and ZVD input shaping is detailed in Section 2.2.2 in Eqs. (2.27) and (2.28) and Eqs. (2.28) and (2.29), respectively.

3.3 Results of two-scale command shaping applied to internal combustion engine restart

3.3.1 Efficacy of two-scale command shaping

The two-scale command shaping strategy effectiveness is studied through direct numerical integration of Eqs. (3.12) and (3.13) using the torque profile defined with Eqs. (3.14), (3.21), and (3.22). Table 3-3 provides the natural frequencies and damping ratios for command shaping the systems' flexible modes. Note that four total impulses are used to address two flexible poles: one for the powertrain and one for the chassis. Higher fidelity models composed of a larger number of flexible poles may require more impulses depending on the number of frequencies deemed to adversely affect drivability.

Table 3-3 – Natural frequencies and damping ratios for the powertrain and chassis subsystems used in application of TSCS strategy.

Parameter	Value
Powertrain system natural frequency (ω_{np}), rad/s	7.32E+02
Powertrain system damping ratio (ζ_p), Unitless	7.32E-02
Chassis system natural frequency (ω_{nc}), rad/s	1.42E+01
Chassis system damping ratio (ζ_c), Unitless	3.55E-01

Figure 3-7 provides the crankshaft response of the ICE from an unshaped step input, post-T_1 input, and a shaped input with the tailored multi-mode ZV shaper designed for

either (a) the vibration frequencies for the powertrain system alone, or (b) the frequencies for both powertrain and chassis subsystems. The first 0.75 s of Figure 3-7 is highlighted since this transient response region is most relevant for ICE restart. The TSCS strategy is only applied for 1 s, at which point the ICE is restarted and left idling. Applying the time-varying EM torque component to the crankshaft together with the unshaped constant torque component, which is denoted as the post-T_1, or post-perturbation, input, results in significant reduction of the undesirable crankshaft oscillations. In fact, further command shaping is not necessary. With application of the post-T_1 input, the peak frequency content and total energy in the crankshaft response is reduced by 52.1% and 66.6%, respectively. However, oscillations remain in the chassis due to the excitation of the systems' flexible poles, as demonstrated in Figure 3-8 (chassis angular velocity) and Figure 3-9 (chassis angular position). These undesirable oscillations are sensed by the vehicle's driver and passengers, reducing their comfort and affecting consumer perception of the vehicle. Therefore, the shaping component of TSCS is required to mitigate the impact of the ICE restart event on consumer comfort. As expected, shaping the input based on the flexible poles of the powertrain system alone is not effective in mitigating the chassis oscillations. A convolved input shaper accounting for the chassis flexible poles is needed to reduce the residual chassis oscillation, as documented by Figure 3-8 and Figure 3-9

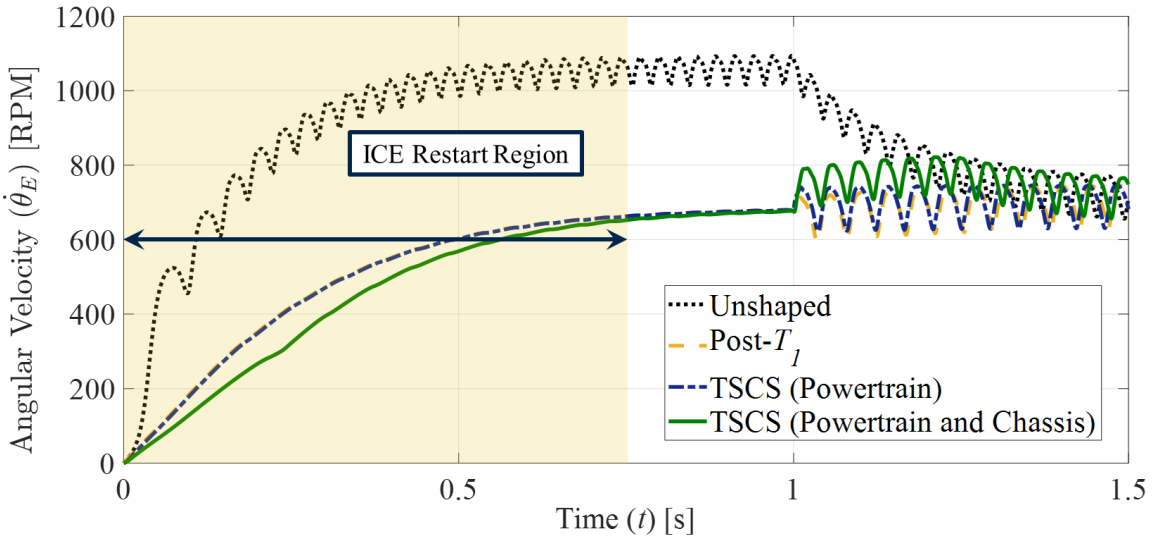

Figure 3-7 – Angular velocity of the 1.3 L JTD ICE crankshaft during a stationary restart as a function of time with unshaped, post-T_1, and TSCS inputs.

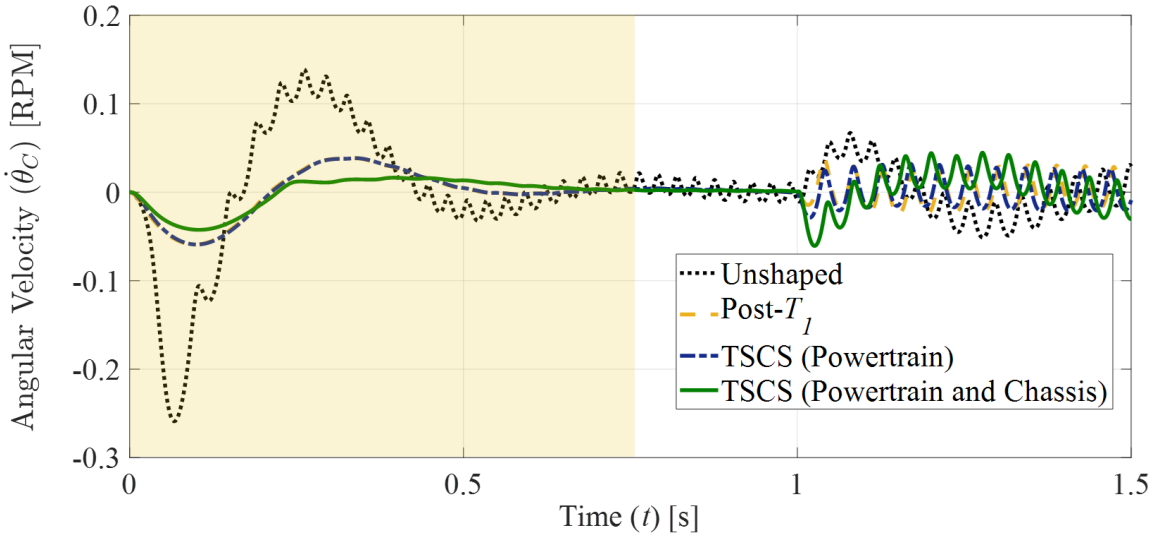

Figure 3-8 – Angular velocity of the vehicle chassis during a stationary restart as a function of time with unshaped, post-T_1, and TSCS inputs.

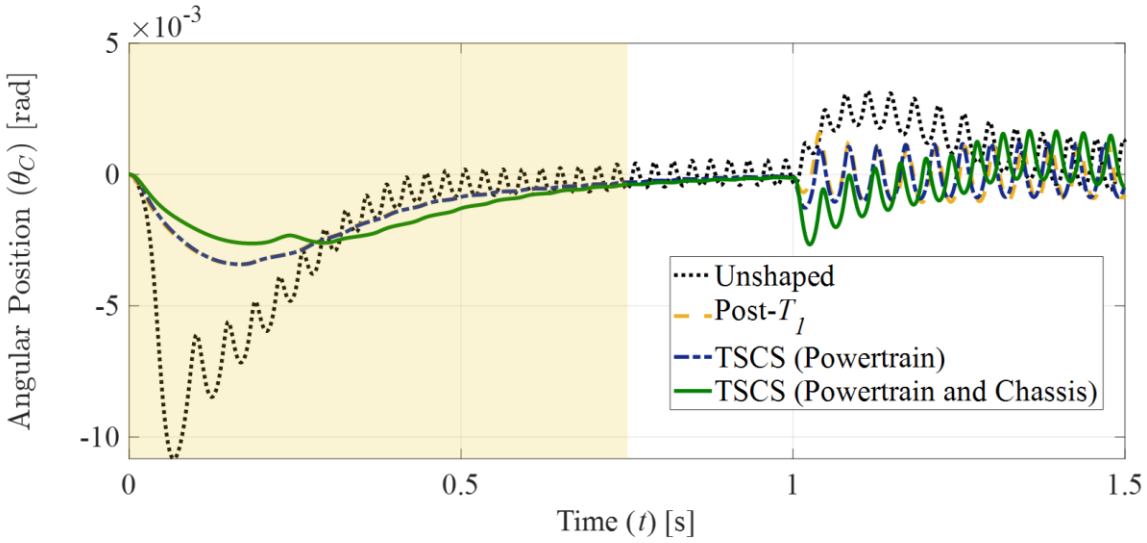

Figure 3-9 – Angular position of the vehicle chassis during a stationary restart as a function of time with unshaped, post-T_1, and TSCS inputs.

The strategy developed is also effective in mitigating drivetrain component oscillations. Figure 3-10 depicts the clutch response during ICE restart using unshaped, post- T_1, and shaped inputs. With the two-scale command shaping strategy, the clutch oscillations are effectively mitigated when the flexible poles of the powertrain are included in command shaping.

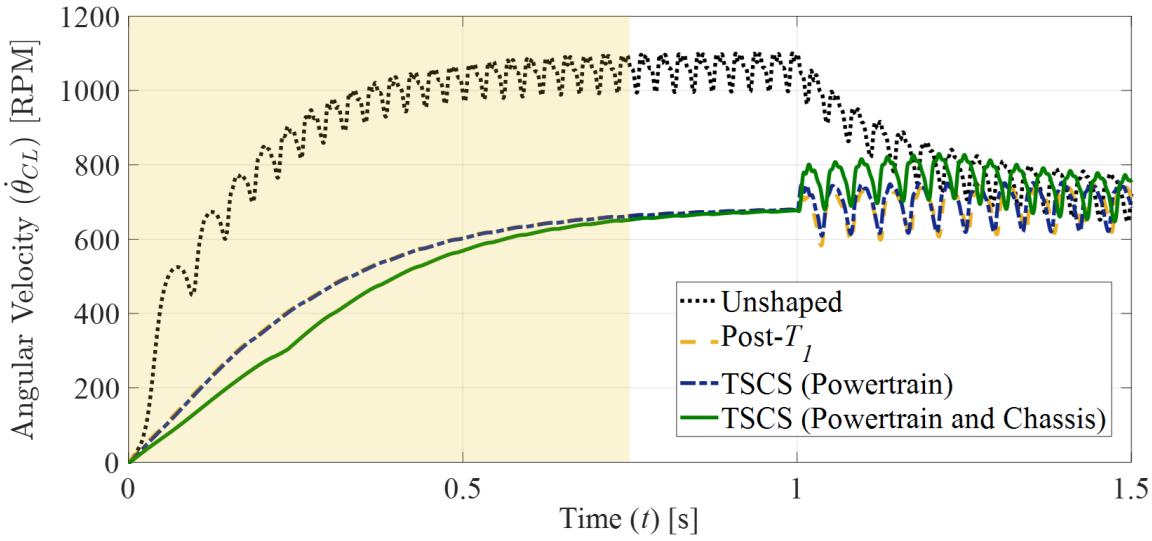

Figure 3-10 – Angular velocity of the driven plate assembly of the clutch of the powertrain during a stationary restart as a function of time with unshaped, post-T_1, and TSCS inputs.

Once the ICE is brought to idle and the application of the TSCS ceases, oscillations will redevelop in the angular velocity of the ICE crankshaft, which can be observed in Figure 3-7. This can be mitigated through steady-state (SS) application of a torque to offset these oscillations, which is demonstrated by other research groups and in Figure 3-11 [5]. Applying the SS mitigation, the oscillations at idle can be reduced as observed in the purple curve in Figure 3-11 when compared to the yellow curve due to the post-T_1 input.

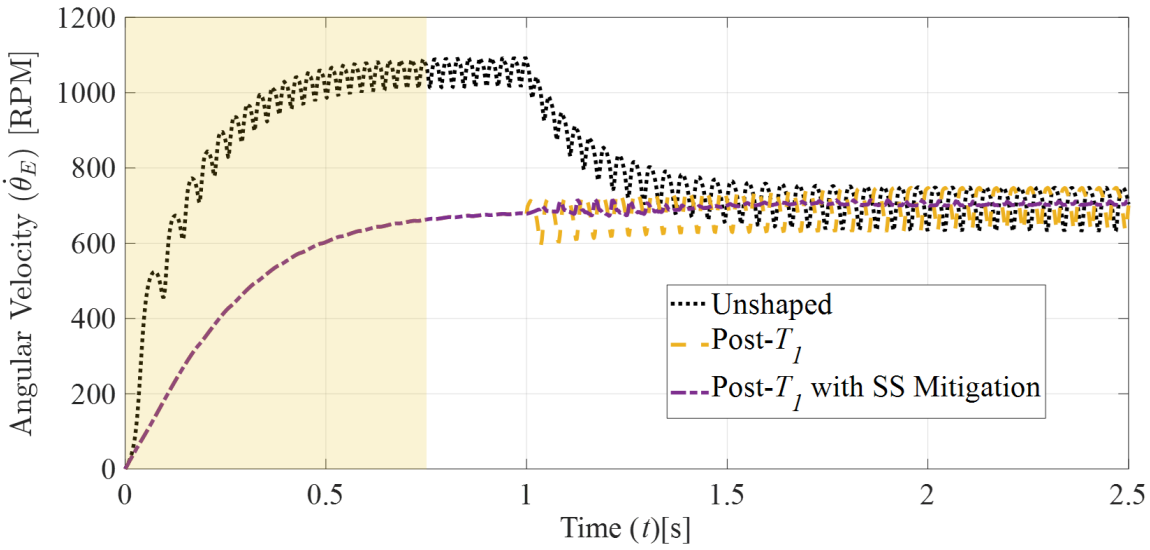

Figure 3-11 – Angular velocity of the 1.3 L JTD ICE crankshaft during a stationary restart as a function of time with unshaped, post-T_1, and post-T_1 with SS mitigation inputs.

3.3.2 Impact of electric machine implementation

The strategy proposed thus far assumes an ideal torque source, which must ultimately be implemented using an EM, hydraulic motor, or other actuator. This section assesses the effectiveness of the strategy when implementing a conventional direct current (DC) electric motor. Figure 3-12 provides the shaped torque profile required from the EM to restart the 1.3 L JTD ICE based on the results of the two-scale command shaping strategy. The speed profile required to mitigate the drivetrain and chassis oscillations is presented in Figure 3-13. Observing the torque profile in Figure 3-12, the dominant frequency content is found below 100 Hz, specifically at 4.88 Hz, 21.36 Hz, 43.95 Hz, and 65.92 Hz. The mechanical time constant of the EM due to its inertia is lumped together with the ICE in the previously presented plots. Mechanical time constants for a typical DC motor are on the order of 10 ms, which implies that any frequency content approaching

100 Hz will be reaching the EM operating limit [85]. The electrical time constant for an electric motor is characteristically an order of magnitude faster than the mechanical time constant [86]. Therefore, a standard EM for traction in HEVs should be compatible with the two-scale command shaping strategy proposed herein. Care should be taken when implementing the TSCS on vehicles that are not equipped with motors sized for traction purposes to ensure the electric motor used for restart can handle the torque and power demanded.

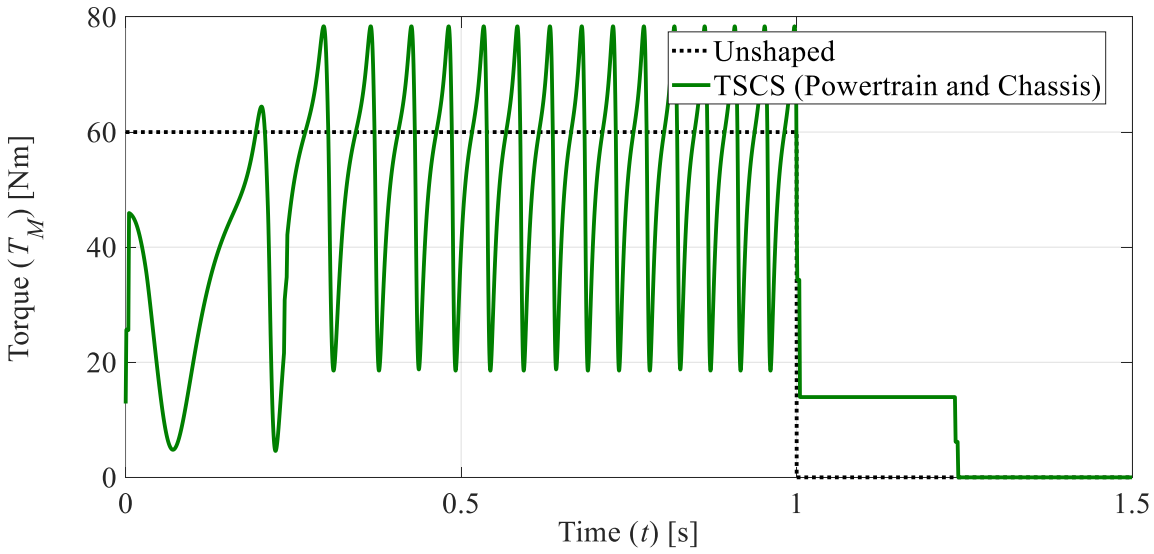

Figure 3-12 – EM torque profile (solid line) needed by the TSCS strategy to restart the 1.3 L JTD ICE compared to the unshaped profile (dotted line).

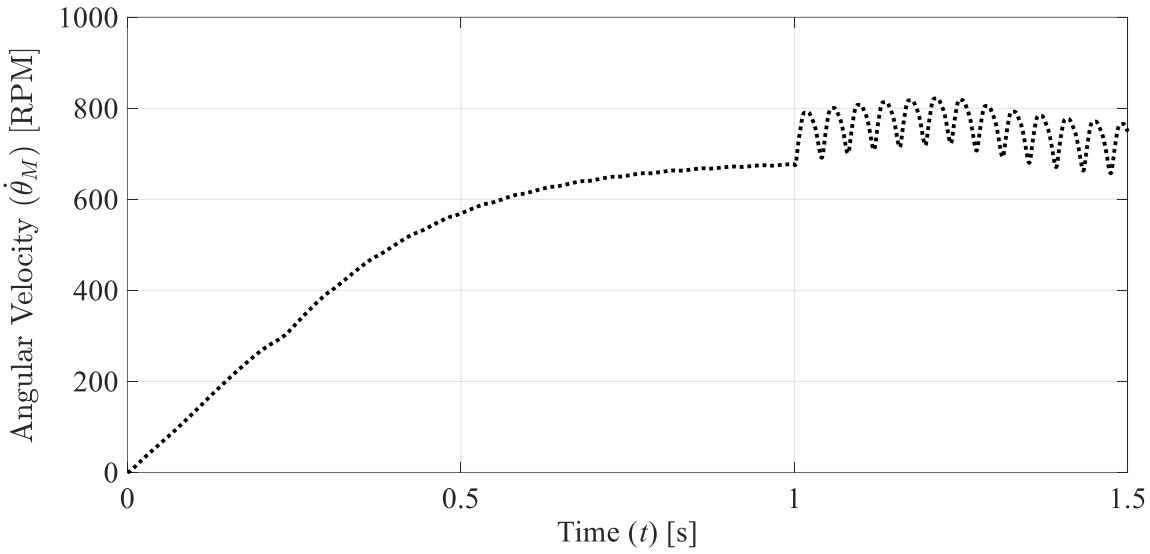

Figure 3-13 – EM speed profile resulting from the TSCS strategy.

To explore further the impact of implementing an EM, a permanent magnet DC motor model was coupled to the existing equations of motion presented in Eqs. (3.12) and (3.13). Equation (3.23) provides the differential equation that governs the EM armature circuit behavior and Eq. (3.24) defines the EM dynamics and torque

$$L_a \frac{di_a}{dt} + R_a i_a + K_b \dot{\theta}_M = V_A \tag{3.23}$$

$$J_M \ddot{\theta}_M + c_{Internal} \dot{\theta}_M = K_t i_a - c_E(\dot{\theta}_M - \dot{\theta}_E) - k_E(\theta_M - \theta_E) - c_{CL}(\dot{\theta}_M - \dot{\theta}_{CL}) - k_{CL}(\theta_M - \theta_{CL}) \tag{3.24}$$

where L_A denotes the impedance in the armature circuit, R_A the resistance in the armature circuit, K_b the electromotive force constant, K_t the torque constant, and $c_{Internal}$ the internal damping. Table 3-4 provides the parameter values that define the permanent magnet DC

motor model and its coupling with the ICE crankshaft. The remaining parameters for the model are reported in Table 3-1 and Table 3-2.

Table 3-4 – Permanent magnet DC motor model parameters.

Parameter	Value
Impedance of armature circuit (L_a), H [87]	1.00E-01
Resistance of armature circuit (R_a), Ω [87]	5.00E-02
Internal damping of EM ($c_{Internal}$), Nms/rad [87]	1.75E+00
Electromotive force constant of EM (K_b), Vs/rad [87]	5.00E-01
Torque constant of EM (K_t), Nm/A [87]	2.80E+00
Stiffness element between ICE and EM (k_E), Nm/rad [78]	5.30E+08

Including the electromechanically coupled equations in the original equations of motion results in the torque input in the original system being replaced by a voltage command in the armature circuit along with the corresponding armature current

$$\begin{bmatrix} J_E & 0 & 0 & 0 \\ 0 & J_M & 0 & 0 \\ 0 & 0 & J_{CL} & 0 \\ 0 & 0 & 0 & L_A \end{bmatrix} \begin{bmatrix} \ddot{\theta}_E \\ \ddot{\theta}_M \\ \ddot{\theta}_{CL} \\ \ddot{q}_A \end{bmatrix} + \begin{bmatrix} c_E & -c_E & 0 & 0 \\ -c_E & c_{CL} + c_{CL} + c_{Internal} & -c_{CL} & -K_t \\ 0 & -c_{CL} & c_{CL} & 0 \\ 0 & K_b & 0 & R_a \end{bmatrix} \begin{bmatrix} \dot{\theta}_E \\ \dot{\theta}_M \\ \dot{\theta}_{CL} \\ \dot{q}_A \end{bmatrix} + \begin{bmatrix} k_E & -k_E & 0 & 0 \\ -k_E & k_E + k_{CL} & -k_{CL} & 0 \\ 0 & -k_{CL} & k_{CL} & 0 \\ 0 & 0 & 0 & 0 \end{bmatrix} \begin{bmatrix} \theta_E \\ \theta_M \\ \theta_{CL} \\ q_A \end{bmatrix} = \begin{bmatrix} T_E(\theta_E) \\ 0 \\ 0 \\ V_A \end{bmatrix} \tag{3.25}$$

where the armature voltage V_A is decomposed into a linear combination of two terms

$$V_A = V_{0_{Shaped}}(t) + V_1(t) \tag{3.26}$$

using the same techniques developed previously for the shaped EM torque profile. The state vector of Eq. (3.25) contains the charge in the armature circuit, or integral of the

current i_A, as well as the ICE crankshaft, EM rotor, and clutch rotational degrees-of-freedom.

Figure 3-14 through Figure 3-16 provide the crankshaft, clutch driven plate, and chassis responses during application of TSCS, respectively, when considering the EM dynamics. Table 3-5 provides the damping ratios and natural frequencies of the vibration modes cancelled with command shaping. Including the EM dynamics alters the response due to the additional degrees-of-freedom, but otherwise has a small effect on the system response. This is largely due to additional dissipation due to the internal EM damping and the resistance element in the armature circuit. Observing Figure 3-14 through Figure 3-16, the proposed method continues to mitigate the undesirable oscillations in the powertrain. The peak unshaped residual vibration amplitude in the chassis response decreases by 14.0 dB.

Table 3-5 – Natural frequencies and damping ratios for the powertrain and chassis subsystems with the coupled DC EM model.

Parameter	**Value**
Powertrain system natural frequency (ω_{np}), rad/s	7.32E+02
Powertrain system damping ratio (ζ_p), Unitless	7.45E-02
Chassis system natural frequency (ω_{nc}), rad/s	1.42E+01
Chassis system damping ratio (ζ_c), Unitless	3.55E-01

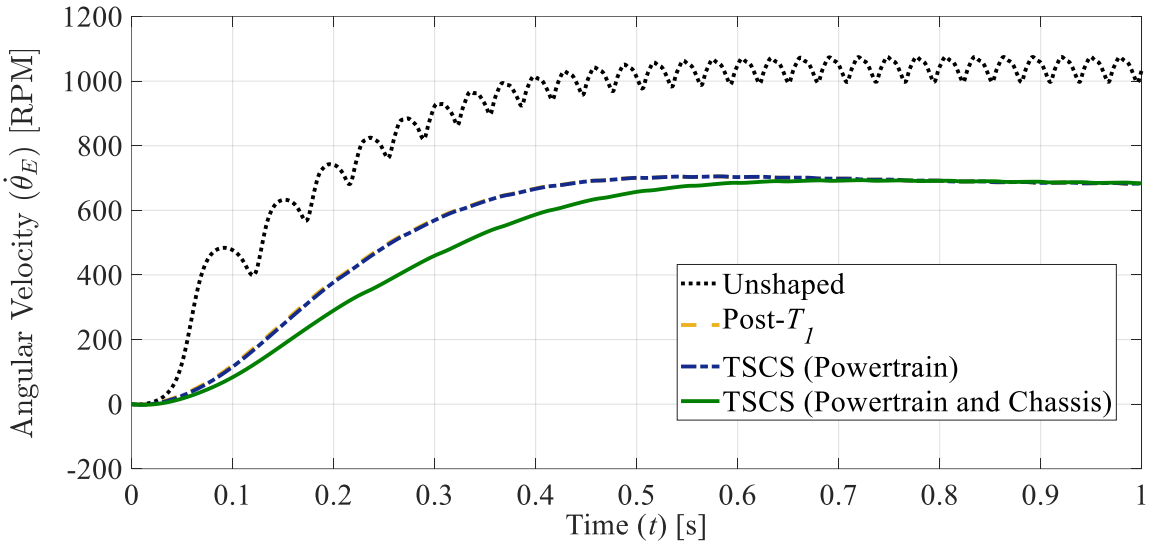

Figure 3-14 – Effect of EM dynamics on the angular velocity of the 1.3 L JTD ICE crankshaft with TSCS applied.

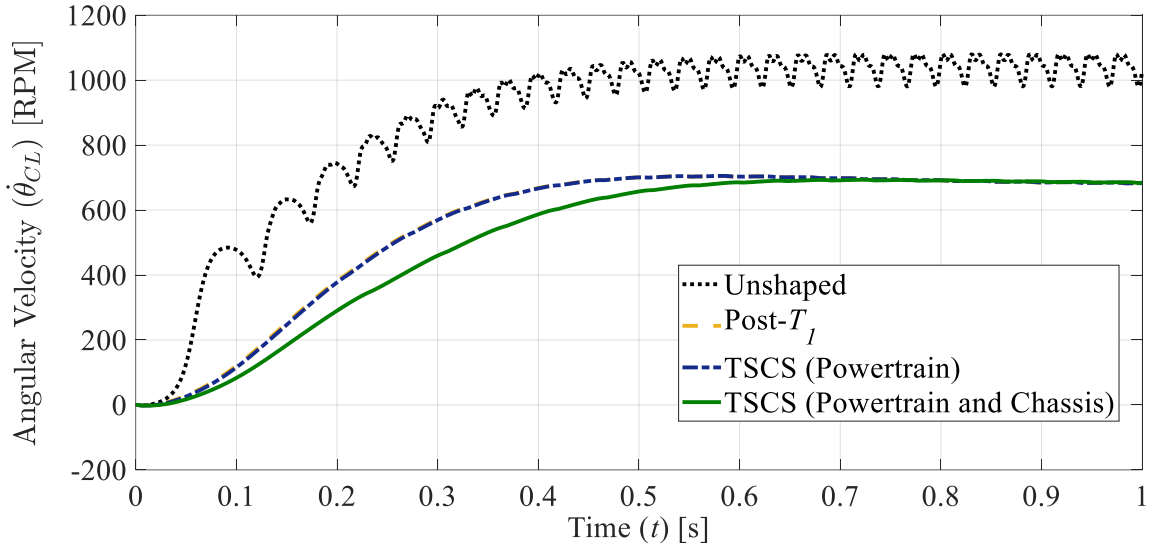

Figure 3-15 – Effect of EM dynamics on the angular velocity of the driven plate of the clutch assembly with TSCS applied.

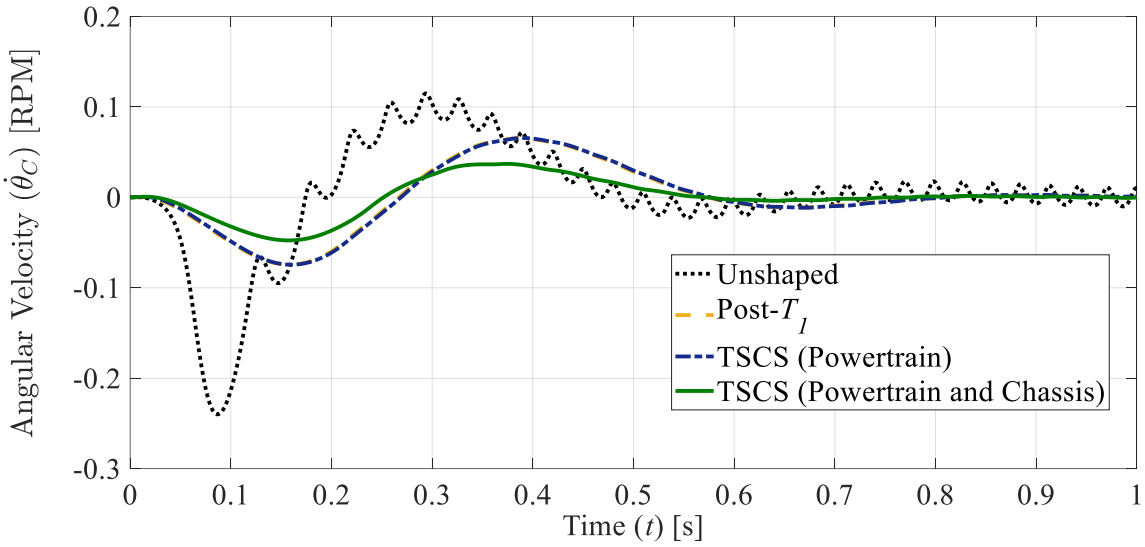

Figure 3-16 – Effect of EM dynamics on the angular velocity of the chassis with TSCS applied.

3.4 Parameter estimation for internal combustion engine model with recursive least-squares and extended Kalman filtering

In real-time implementation, TSCS will likely suffer from inaccuracies and variations in the ICE parameters, or modes of the powertrain and chassis systems. Robust command shaping can compensate for vibration mode variations [40]. However, robust command shaping cannot mitigate the effect of variations in the ICE parameters since these variations impact the indicated torque of the ICE, which acts as an excitation. Figure 3-17a and Figure 3-17b provide the effect of variations in cylinder geometry and friction parameters, respectively, on the performance of the TSCS strategy in the transient region of the ICE crankshaft response. Inaccuracies in cylinder geometry, such as the clearance volume and bore, have limited impact on TSCS up to approximately ±25% variations. Since only a small variation in cylinder volume is expected over the lifetime of a vehicle,

the accommodation of a large range in variation indicates uncertainty in cylinder volume is acceptable as is.

However, inaccuracies in ICE friction parameters can cause substantial changes in the steady-state crankshaft response. As shown in Figure 3-17b, ICE restart exhibits detrimental effects due to friction uncertainty starting after approximately 0.20 s. The TSCS strategy is robust only to ±10% changes in the friction parameters. Engine restart typically engages after the engine is fully warmed, decreasing some uncertainty in friction parameters. However, these parameters may still vary day-to-day depending on environmental conditions, and thus it is important to have a means for estimating their value. A friction model dependent on temperature could be used to improve effectiveness of TSCS [5]. An alternative is to estimate the friction parameters with RLS and EKF algorithms based on data from previous restarts. Once the engine is fully warmed, most restarts will occur under similar conditions, which implies that data from previous restarts can be used to inform future restarts. Both the RLS and EKF algorithms can be written as filters implemented alongside the TSCS strategy to provide an adaptive control strategy. A single engine restart period may not provide enough data for the parameter estimation algorithms, but a single data set could be extended by mirroring it about a vertical axis at the final time and combining the mirrored and original components of the signal. Alternatively, before attempting a restart, the EM could spin the crankshaft of the ICE with a known input with or without combustion when the vehicle is temporarily stationary (e.g., at a stop light).

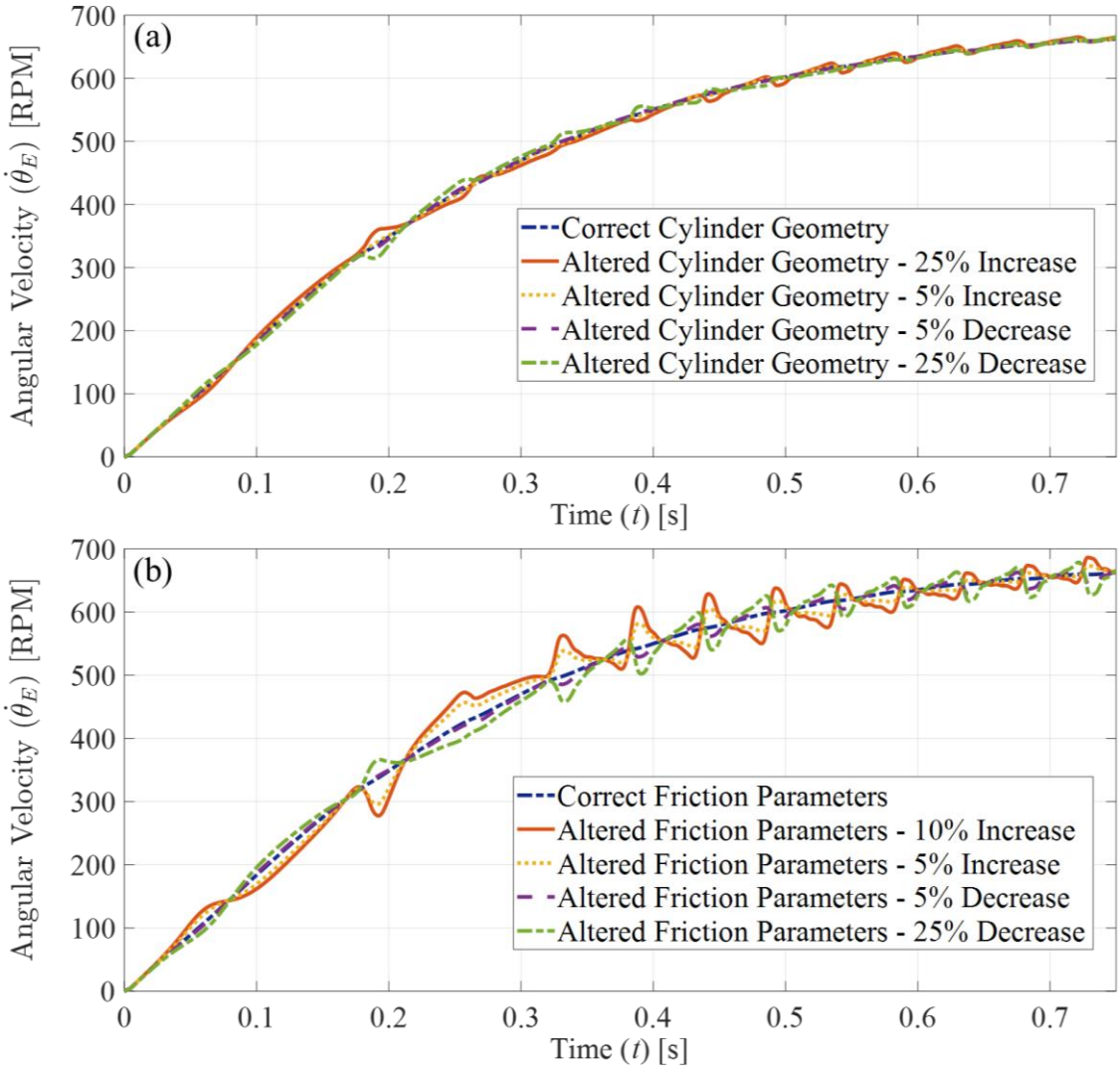

Figure 3-17 – Impact of variations in (a) ICE geometry and (b) friction parameters on TSCS effectiveness in reducing undesirable oscillations in the ICE crankshaft angular velocity.

3.4.1 Parameter estimation with recursive least-squares

The objective of least squares is to estimate a set of parameters, $\boldsymbol{\theta_{RLS}} \in \mathbb{R}^m$, which minimizes the squared error

$$L = \int_0^t \boldsymbol{e}^2(\tau)d\tau,\ \boldsymbol{e}(t) = \boldsymbol{W}^T(t)\boldsymbol{\theta_{RLS}}(t) - \boldsymbol{y_{RLS}}(t) \tag{3.27}$$

where $\boldsymbol{e}$ denotes the error in the estimated state compared to the measured output $\boldsymbol{y_{RLS}}$ calculated with the system parameter estimates and $\boldsymbol{W}$, which is a linear transformation of the parameter estimates to the system output space [52]. The $\boldsymbol{\theta_{RLS}}$ that solves Eq. (3.27) and minimizes the error due to the parameter estimates is then

$$\boldsymbol{\theta_{RLS}}(t) = \left[\int_0^t \boldsymbol{W}(\tau)\boldsymbol{W}^T(\tau)d\tau\right]^{-1}\left[\int_0^t \boldsymbol{W}(\tau)\boldsymbol{y_{RLS}}(\tau)d\tau\right] \tag{3.28}$$

The RLS algorithm applies the above approach recursively. Introducing an estimator gain matrix

$$\boldsymbol{P}(t) = \left[\int_0^t \boldsymbol{W}(\tau)\boldsymbol{W}^T(\tau)d\tau\right]^{-1} \tag{3.29}$$

enables expressing the parameter estimates for time *t* as

$$\boldsymbol{\theta_{RLS}}(t) = \boldsymbol{P}(t)\int_0^t \boldsymbol{W}(\tau)\boldsymbol{y_{RLS}}(\tau)d\tau \tag{3.30}$$

The time derivative of the estimator gain matrix is given by [52]

$$\frac{d}{dt}[\boldsymbol{P}(t)] = \boldsymbol{W^T}(t)\boldsymbol{W}(t) \tag{3.31}$$

In addition, the derivative of the product of $\boldsymbol{P}$ and its inverse provides the following identity

$$\tfrac{d}{dt}[\boldsymbol{P}(t)\boldsymbol{P}^{-1}(t)] = \dot{\boldsymbol{P}}(t)\boldsymbol{P}^{-1}(t) + \boldsymbol{P}(t)\tfrac{d}{dt}[\boldsymbol{P}^{-1}(t)] = 0 \tag{3.32}$$

The differential equations used to update the parameter estimates is

$$\dot{\boldsymbol{\theta}}_{\boldsymbol{RLS}}(t) = -\boldsymbol{P}(t)\boldsymbol{W}(t)\boldsymbol{e}(t) \tag{3.33}$$

which arises from the differentiation of Eq. (3.28) using Eqs. (3.29) and (3.31). Variation of the estimator gain matrix, $\boldsymbol{P}$, is governed by

$$\dot{\boldsymbol{P}}(t) = -\boldsymbol{P}(t)\boldsymbol{W}(t)\boldsymbol{W}^T(t)\boldsymbol{P}(t), \boldsymbol{P}(0) > 0 \tag{3.34}$$

which arises from the identity given in Eq. (3.32). The differential equations given in Eqs. (3.33) and (3.34) can be used to implement the RLS algorithm [52] for the powertrain system used in the validation of TSCS.

To use the RLS algorithm to estimate friction parameters, the complete ICE torque, angular position, and angular velocity must be measurable, and the ICE geometry must be well-defined. The set of parameters to be estimated with RLS is

$$\boldsymbol{\theta_{RLS}}(t) = \begin{bmatrix} T_{Friction_0} \\ k_p \\ k_{\omega_1} \\ k_{\omega_2} \end{bmatrix} \tag{3.35}$$

where the transformation used to map the parameter estimates to the output space is

$$\boldsymbol{W}(\tau) = \begin{bmatrix} 1 & p(\theta_E) & \dot{\theta}_E & \dot{\theta}_E{}^2 \end{bmatrix} \tag{3.36}$$

$T_{Friction}$ serves as the observable output space, $\boldsymbol{y_{RLS}}$, for the estimation of the friction parameters. One can then pose the full RLS problem as follows

$$T_{Friction}(\theta_E) = T_{Indicated}(\theta_E) + T_{Inertial}(\theta_E) - T_E(\theta_E) = \begin{bmatrix} 1 & p(\theta_E) & \dot{\theta}_E & \dot{\theta}_E{}^2 \end{bmatrix} \begin{bmatrix} T_{Friction_0} \\ k_p \\ k_{\omega_1} \\ k_{\omega_2} \end{bmatrix} \tag{3.37}$$

Note that this approach estimates the friction parameters without using a temperature-

dependent model, but requires real-time measurement of ICE torque and accurate ICE geometry.

3.4.2 Parameter estimation with extended Kalman filtering

In place of the RLS algorithm, EKF estimates friction parameters without an explicit torque measurement. General parameter estimation with EKF is coved in Section 2.4.2. The states of the original dynamic system and the parameters to be estimated compose the augmented system's state vector. Like RLS, the vector of estimated parameters is

$$\boldsymbol{\Theta} = \begin{bmatrix} \theta_1 \\ \theta_2 \\ \theta_3 \\ \theta_4 \end{bmatrix} = \begin{bmatrix} T_{Friction_0} \\ k_p \\ k_{\omega_1} \\ k_{\omega_2} \end{bmatrix} \tag{3.38}$$

where Eq. (2.40) implies time-invariant estimated parameters during a single restart period of data. Therefore, the complete state vector for the analysis of the pre-transmission powertrain configuration with EKF is

$$\boldsymbol{x_A}(t) = \begin{bmatrix} x_1 \\ x_2 \\ x_3 \\ x_4 \\ \theta_1 \\ \theta_2 \\ \theta_3 \\ \theta_4 \end{bmatrix} = \begin{bmatrix} \theta_E \\ \theta_{CL} \\ \dot{\theta}_E \\ \dot{\theta}_{CL} \\ T_{Friction_0} \\ k_p \\ k_{\omega_1} \\ k_{\omega_2} \end{bmatrix} \tag{3.39}$$

Note that Eq. (3.39) combines the rotational motion of the ICE crankshaft and EM rotor since their coupling is considered rigid. The torque applied to the ICE from the EM

represents the control input vector, $\boldsymbol{u}(t)$, appearing in Eqs. (2.37) and (2.38). With the augmented system defined in Eqs. (2.37) through (2.39) and the corresponding state vector provided in Eq. (3.39), the EKF formalism can be used for parameter estimation.

The complete linearized state matrix of the augmented system consisting of the powertrain model can be found in Appendix A in Eq. (A.2). Angular position and velocity of the crankshaft and driven plate assembly of the clutch are defined as the output of the powertrain model. $\boldsymbol{C_A}$ in Eqs. (2.49) and (2.51) is the linearized output matrix,

$$\boldsymbol{C_A}(k) = \frac{\partial \boldsymbol{g_A}}{\partial \boldsymbol{x_a}}\bigg|_{\boldsymbol{x_A}=\tilde{\boldsymbol{x}}_{\boldsymbol{A}}(k)} = \begin{bmatrix} 1 & 0 & 0 & 0 & 0 & 0 & 0 & 0 \\ 0 & 1 & 0 & 0 & 0 & 0 & 0 & 0 \\ 0 & 0 & 1 & 0 & 0 & 0 & 0 & 0 \\ 0 & 0 & 0 & 1 & 0 & 0 & 0 & 0 \end{bmatrix} \tag{3.40}$$

where $\boldsymbol{C_A}$ has the simple representation given because the output vector is defined as the angular position and velocity of the ICE crankshaft and driven plate assembly of the clutch.

In addition to estimating the parameters for the friction torque of the ICE, EKF can also provide an estimate of the inertia of the crankshaft and counterbalances of the ICE. For these parameters taken alone,

$$\boldsymbol{\Theta} = [\theta_1] = [J_E] \tag{3.41}$$

$$\boldsymbol{x_A}(t) = \begin{bmatrix} x_1 \\ x_2 \\ x_3 \\ x_4 \\ \theta_1 \end{bmatrix} = \begin{bmatrix} \theta_E \\ \theta_{CL} \\ \dot{\theta}_E \\ \dot{\theta}_{CL} \\ J_E \end{bmatrix} \tag{3.42}$$

where the estimated parameter vector, Eq. (3.41), and the augmented state vector, Eq.

(3.42), takes the place of Eqs. (3.38) and (3.39), respectively. The output matrix used in the previous analysis of the friction torque parameters, Eq. (3.40), still applies. Expressions for the augmented system's linearized state matrix is again given in Appendix A in Eqs. (A.3) and (A.4).

3.5 Robust command shaping strategies for the internal combustion engine restart problem

TSCS may also suffer from inaccuracies in the definition of the vibration modes for the powertrain or chassis, such as variations in the natural frequencies that define the modes. These inaccuracies could affect the impact of the shaping process on mitigation of undesirable oscillations in the chassis. As remarked earlier, robust command shaping can mitigate the adverse effect of vibration mode variations. Including additional zeros, or changing the zero locations relative to the flexible poles, increases a shaper's robustness. Several research groups have developed robust approaches, such as ZVD and EI input shapers [9-11, 41, 88]. ZV and ZVD input shapers are introduced in Section 2.2.2 in Eqs. (2.27) and (2.28) and Eqs. (2.28) and (2.29), respectively.

The impulse sequences for the ZVD and EI input shapers require three impulses and a full damped period of the cancelled pole, but the EI shaper has superior robustness. The EI shaper's additional robustness arises from relaxing the amplitude constraint such that the amplitude need only remain below a tolerable percentage, V_{Tol}. This results, following optimization, in an EI input shaper impulse sequence

$$\begin{bmatrix} A_i \\ \cdots \\ t_i \end{bmatrix} = \begin{bmatrix} A_1 & 1-(A_1+A_3) & A_3 \\ 0 & t_2 & \frac{2\pi}{\omega_d} \end{bmatrix} \tag{3.43}$$

where A_1, A_3, and t_2 for a damped second-order system have been obtained numerically and are given by

$$A_1 = 0.2497 + 0.2496V_{Tol} + 0.8001\zeta + 1.2330V_{Tol}\zeta + 0.4960\zeta^2 + 3.1730V_{Tol}\zeta^2 \tag{3.44}$$

$$A_3 = 0.2515 + 0.2147V_{Tol} - 0.8325\zeta + 1.4150V_{Tol}\zeta + 0.8518\zeta^2 - 4.9010V_{Tol}\zeta^2 \tag{3.45}$$

$$t_2 = \frac{2\pi}{\omega_d}(0.5000 + 0.4616V_{Tol}\zeta + 4.2620V_{Tol}\zeta^2 + 1.7560V_{Tol}\zeta^3 + 8.5780{V_{Tol}}^2\zeta\text{-}108.6000{V_{Tol}}^2\zeta^2 + 337.0000{V_{Tol}}^2\zeta^3) \tag{3.46}$$

for $0 \leq V_{Tol} \leq 0.15$ and $0 \leq \xi \leq 0.3$ [10]. Figure 3-18 illustrates the location of the poles and zeroes in the complex plane for the robust shapers. The ZVD input shaper arises from placing an additional zero on the cancelled flexible pole [10, 88], while the EI input shaper's relaxed constraint results in zeros near (not on) the pole [10, 88].

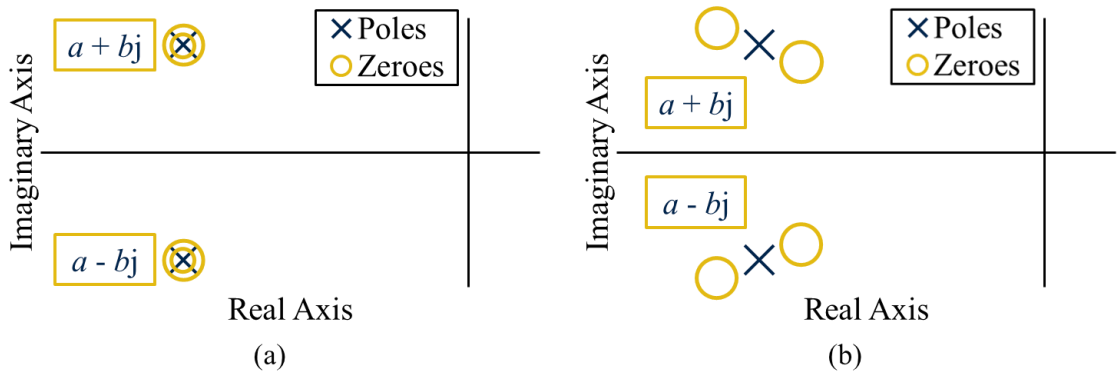

Figure 3-18 – Comparison of (a) ZVD and (b) EI input shapers represented as pole-zero cancellation.

3.6 Result of adding robustness to the two-scale command shaping strategy for internal combustion engine restart

A sample data set was generated for a case where the ICE is motored by the EM through direct numerical integration of Eqs. (3.12) and (3.13) without combustion in Eq. (3.3) to compare the efficacy of friction torque estimation with the RLS and EKF algorithms. Table 3-1, Table 3-2, and Table B-1, in Appendix B, list all parameters used for the ICE, powertrain, and chassis models. Estimation occurs over a 5 second sample of the crankshaft response to an unshaped motoring command. The degree of mismatch between actual and initial parameter estimates was explored to determine the effectiveness of each algorithm in deducing the correct friction torque profile. The effect of robust command shaping on mitigation of vibration mode variations is then explored with an accurate ICE model.

3.6.1 Efficacy of recursive least-squares in estimating friction parameters

When the torque, angular position, and angular velocity of the ICE can be

measured, and the ICE geometry is well-known, RLS offers a straight-forward method to estimate the friction parameters since the parameters can be written in the linear form shown in Eq. (3.37). Assuming an initial estimate with all friction parameters set to zero, the RLS algorithm converges to estimates of k_p, k_{ω_1}, and k_{ω_2} within 2% of their actual values, in less than 0.4 s. The estimation of the $T_{Friction_0}$ has a higher percent error of 11.5% since it is a constant parameter in the friction torque expression in Eq. (3.37), reducing the effectiveness of RLS in its estimation since it does not undergo persistent excitation [89]. Without persistent excitation, the data collected may not be informative enough for RLS to uniquely identify $T_{Friction_0}$. Figure 3-19 documents the convergence of the estimated friction parameters. It can be observed that $T_{Friction_0}$ takes significantly longer to converge to an estimation, approximately 2.5 s, compared to the 0.4 s required for k_p, k_{ω_1}, and k_{ω_2}. Figure 3-20 provides a comparison between the estimated and actual friction torque. The complete estimated friction torque expression consisting of the converged parameters accurately represents the actual friction torque with an average percent error of 0.02%.

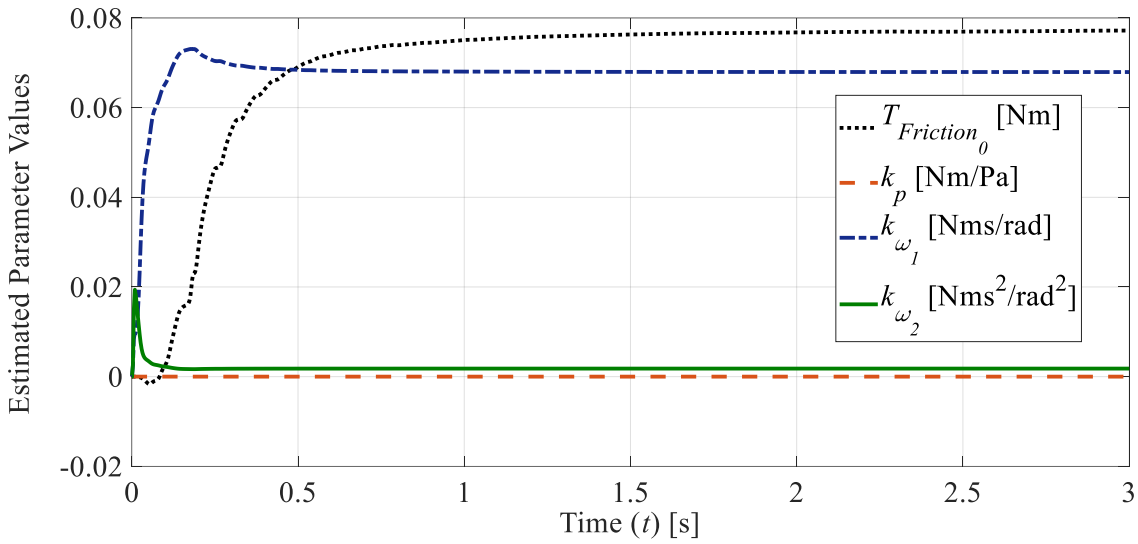

Figure 3-19 – RLS estimation of the friction parameters of the four-cylinder ICE.

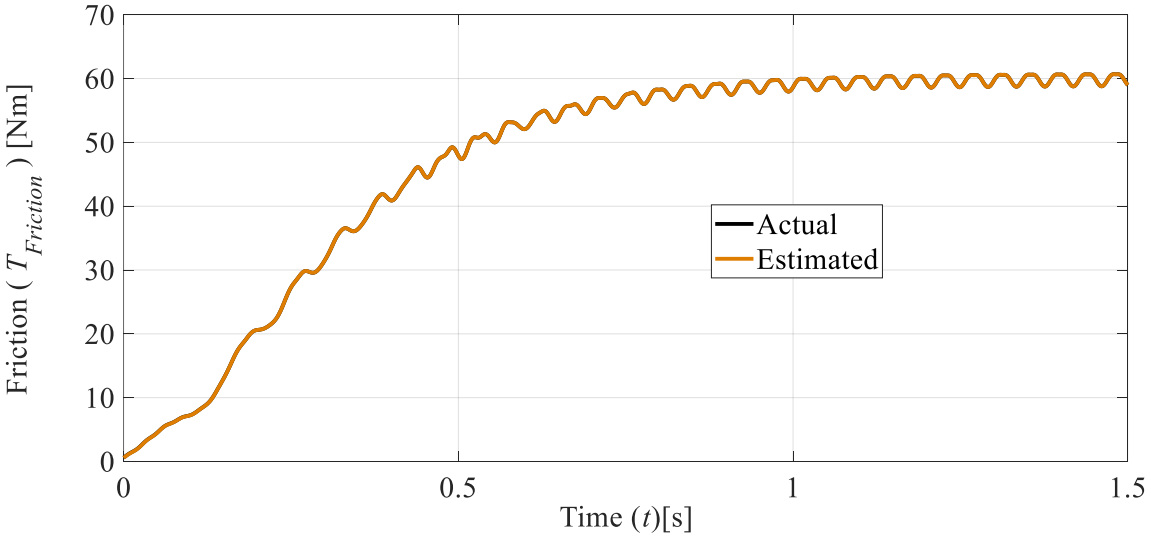

Figure 3-20 – RLS estimation of the friction torque of the four-cylinder ICE.

3.6.2 Efficacy of extended Kalman filtering in estimating friction and inertial parameters

If the ICE torque measurement is unavailable, and/or the engine geometry is uncertain, the EKF approach can be employed to estimate the friction parameters since it

only requires measurements of the angular position and velocity of the ICE crankshaft. Figure 3-21a compares the EKF-estimated and actual friction torque curves for a +10% misidentification of all friction parameters, while Figure 3-21b presents the same comparison for a +37.5% misidentification. In both cases, the converged EKF algorithm results in estimated friction parameters that closely resemble the actual friction torque of the four-cylinder ICE. Even with a large inaccuracy in friction parameters, up to +37.5%, the EKF algorithm provides an implementable approximation to the friction torque of the ICE that maintains an average percent error of 1.69%. The average percent error for the friction torque reduces to 0.03% for an inaccuracy of +10%. The EKF process applied can also handle zero and negative initial estimates of the friction parameters.

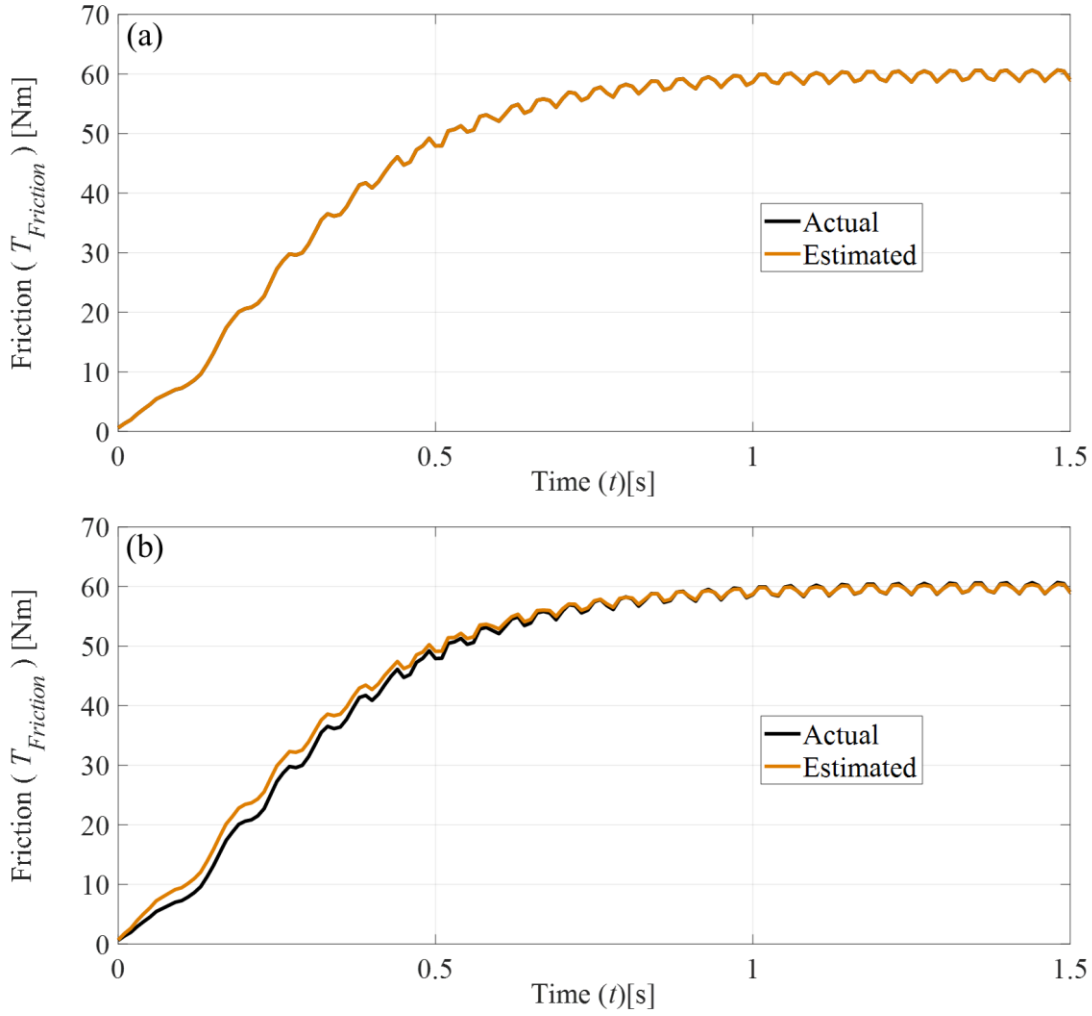

Figure 3-21 – EKF estimation of the friction torque of the four-cylinder ICE – (a) +10% initial inaccuracy and (b) +37.5% initial inaccuracy.

When observing the convergence of each friction parameter separately in Figure 3-22a through Figure 3-22d, it is noted that the parameters do not converge to the values defined for the four-cylinder ICE, but instead converge to an alternative solution that minimizes the error in the estimation of the friction torque for the ICE.

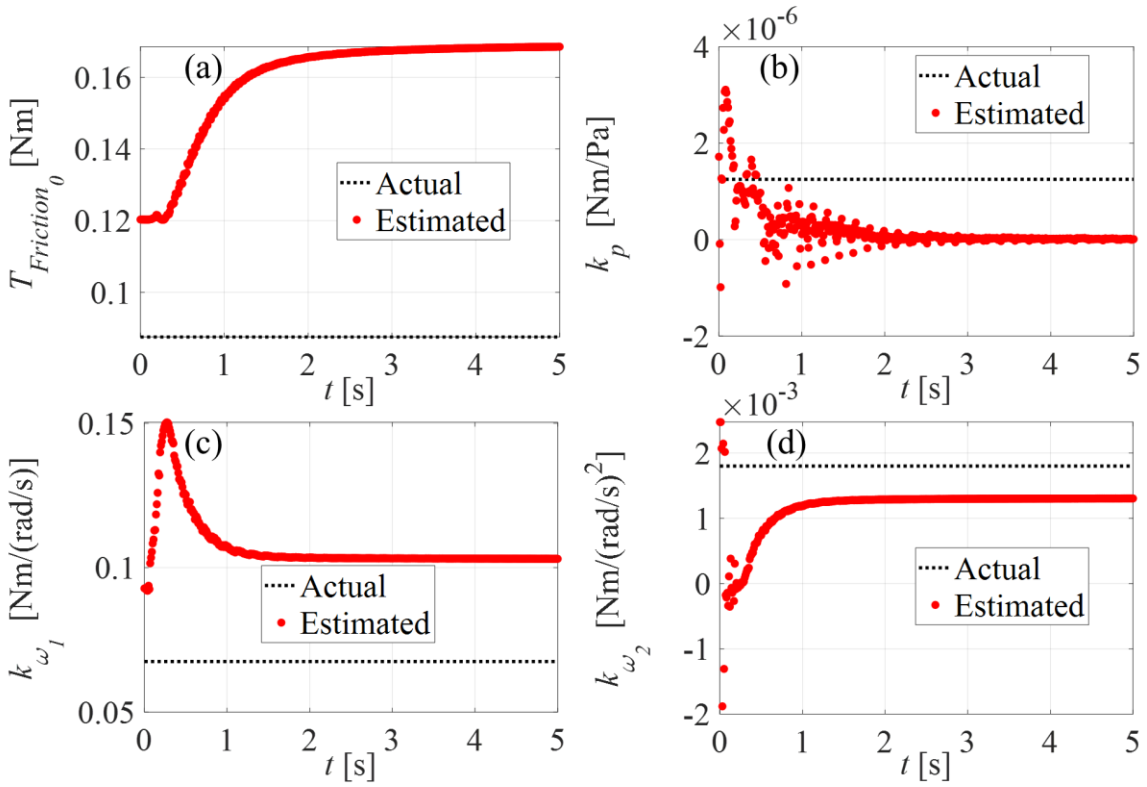

Figure 3-22 – EKF estimation of (a) $T_{Friction_0}$, (b) k_p, (c) k_{ω_1}, and (d) k_{ω_2} – +37.5% initial inaccuracy.

The convergence of the friction parameters of the ICE to an alternative solution implies non-uniqueness in the specification of the friction torque parameters. Non-uniqueness arises due to the rank of the observability matrix of the augmented system becoming deficient at one or more time steps of the data set as well as the lack of persistent excitation of $T_{Friction_0}$ [89]. Convergence of the friction parameters of the ICE to alternate values does not adversely affect the efficacy of using the EKF algorithm to correct inaccuracies in the definition of the ICE as shown in Figure 3-21a and Figure 3-21b. The formulation of EKF presented in Section 3.4.2 can also be used to identify other unknown parameters for the ICE, such as the equivalent inertia of the crankshaft and counterbalances, or cylinder geometry.

Figure 3-23 shows the convergence of the inertia of the crankshaft, counterbalances, and EM rotor using the formulation of the EKF presented in Section 3.4.2, with the state vector given in Eq. (3.42). The inertia of the crankshaft and counterbalances is combined with the rotor of the EM since it was assumed that the coupling was modeled as rigid. The initial value for the equivalent inertia of the crankshaft and counterbalances of the ICE and the rotor of the EM had a variation of +30%. The converged value for the inertial parameter had a percent error of 0.0005%.

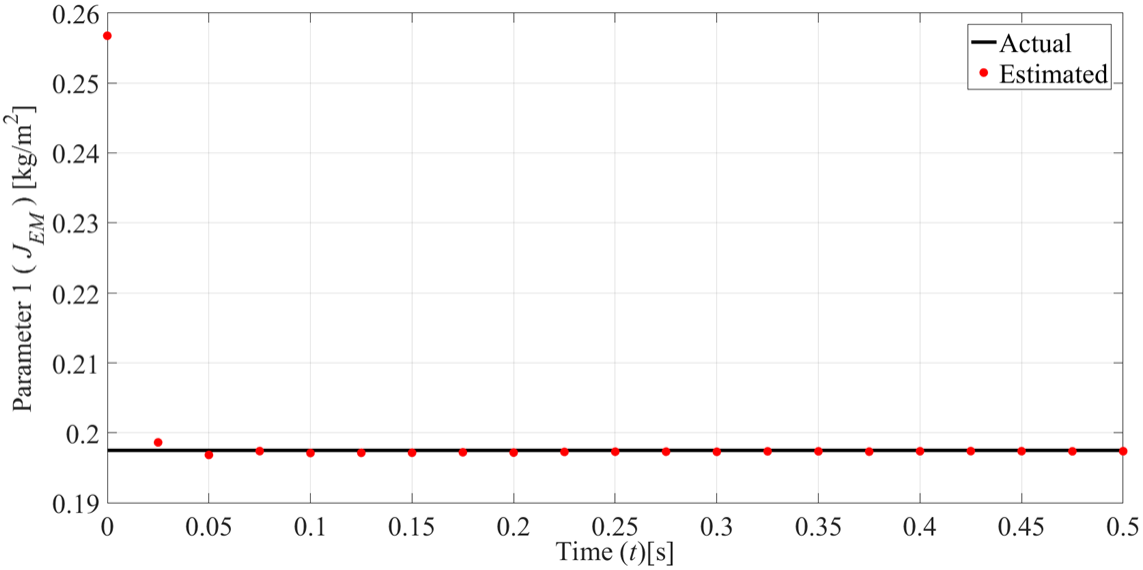

Figure 3-23 – EKF estimation of J_{EM} – +30% initial inaccuracy.

EKF is effective in approximating both friction torque parameters as well as other parameters, such as inertial quantities in the system in the motoring case presented. Once parameter estimation is used to update inaccuracies in the system definition, the TSCS strategy can be initiated with scale separation followed by the command shaping technique chosen to prevent excitation of vibration modes of the coupled powertrain and chassis systems during ICE restart.

3.6.3 Efficacy of robust command shaping

Two-scale command shaping mitigates the undesirable vibrations in the drivetrain and chassis systems that could negatively impact drivability. Once inaccuracies in the system are mitigated with the parameter estimation techniques of Section 3.4, the scale separation portion of TSCS can be completed successfully, but the command shaping process may be affected by vibration mode misidentification. When implemented on a physical system, variations in the systems' vibration modes occur due to misinformation or wear of the vehicle. Vibration mode variations, in the form of changes in natural frequency, impact the efficacy of the shaping process of TSCS even when the linear scale of the system is isolated successfully with the aid of parameter estimation. Robust command shaping, specifically ZVD and EI shapers, mitigates the effect of variations in vibration modes [9-11, 41, 88]. ZVD shapers are outlined in Eqs. (2.28) and (2.29), whereas EI shapers are introduced in Eqs. (3.43) through (3.46). Figure 3-24a and Figure 3-24b show the effect of ZVD and EI shapers on the robustness of the shaping process in the response of the crankshaft and chassis, respectively.

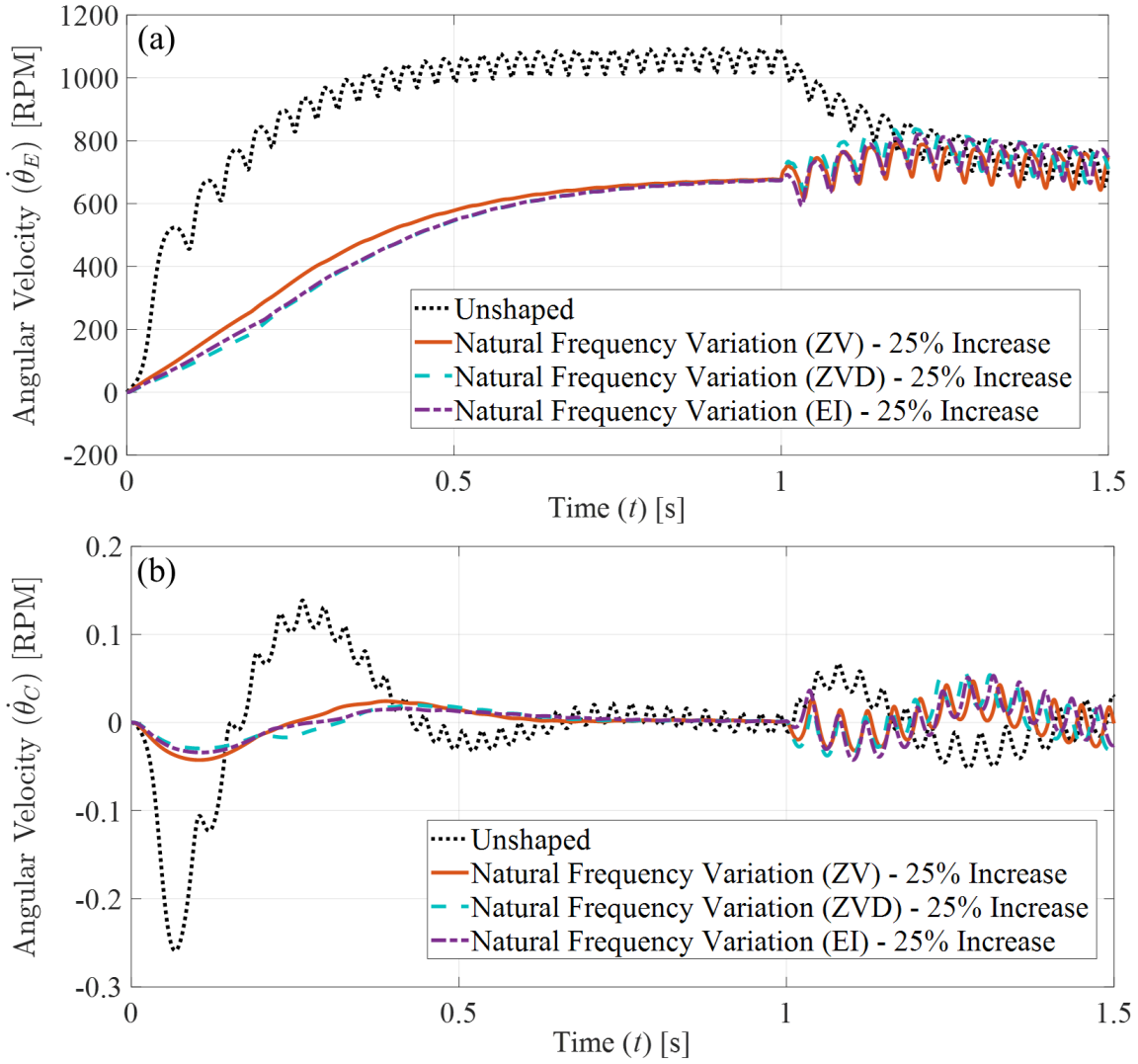

Figure 3-24 – Impact of a 25% increase in the natural frequencies on TSCS effectiveness in reducing the undesirable oscillations in the (a) 1.3 L JTD ICE crankshaft and (b) chassis angular velocity with ZV, ZVD, and EI input shapers.

Robust shapers decrease the effect that variations in the natural frequencies of the system have on TSCS. Since the powertrain system's vibration modes are comprised of high frequency vibrations that are primarily mitigated through the time-varying EM torque component, a 25% increase does not have a prominent impact on elimination of the undesirable oscillations in the powertrain. However, this is not the case for the chassis

system.

Table 3-6 provides the time required for the residual vibration to settle within 0.002 RPM of their steady-state value with the TSCS input applied. Figure 3-24b provides the corresponding plot for the case where the shaped natural frequencies designed for are 25% higher than the actual values. The ZVD and EI shapers require a larger settling time when the designed frequency is correct due to their longer duration, but under variations in the natural frequencies the ZVD and EI input shaper provide a noticeable reduction in the time required for the undesirable oscillations to be within 0.002 RPM of the steady-state value with TSCS applied. The ZVD and EI shapers reduce the settling time of the chassis by 16.6% and 29.7%, respectively, compared to TSCS with a ZV shaper under a 25% increase in the natural frequency of the designed vibration modes. If variations in the vibration modes become substantial, the correct robust command shaper can mitigate the possible issues.

Table 3-6 – Effect of robust command shaping on the settling time of the chassis response.

Shaper	$\omega_{Modeled} / \omega_n = 1$	$\omega_{Modeled} / \omega_n = 1.25$
ZV [s]	4.20E-01	7.40E-01
ZVD [s]	5.07E-01	6.17E-01
EI [s]	4.88E-01	5.20E-01

Figure 3-25 compares the robust command shaping strategies based on the Fourier transform of the chassis angular velocity under a 25% increase in the natural frequencies of the powertrain and chassis systems. TSCS substantially reduces the frequency content of the chassis with each shaping strategy. Both the ZVD and EI shapers improve the performance of the TSCS strategy under variations in the system's vibration modes. Using

a ZVD or EI shaper with TSCS reduces the peak frequency content of the chassis by 18.4% and 21.4% of the value observed with TSCS implemented with a ZV input shaper, respectively. Therefore, robust shaping strategies improve the settling time of the chassis and amplitude of the chassis residual vibrations during restart.

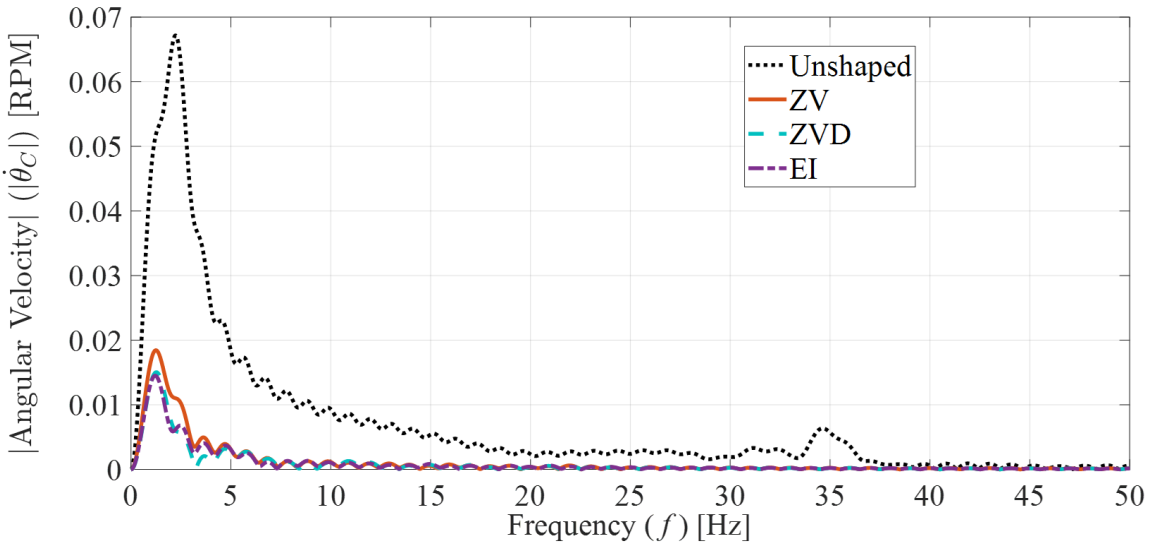

Figure 3-25 – Efficacy of robust command shaping in mitigating the effect of a 25% increase in the natural frequencies on TSCS effectiveness in reducing the frequency content of the chassis response.

3.7 Conclusions

Addressing vibration issues associated with engine restart and shutdown is a topical issue facing automotive engineers. This issue has limited the implementation of fuel-saving features and downsized engines in modern powertrains. In this chapter, a two-scale command shaping strategy has been applied to reduce engine crankshaft and chassis vibration during ICE restart. Simulation results suggest that the technique can effectively mitigate vibrations associated with reduced drivability, even in situations where small to moderate uncertainty exists in system parameters. The strategy has the advantage that

existing hardware can be leveraged without introducing significant cost, particularly in hybrid electric vehicles where powerful electric machines reside onboard.

For full implementation, TSCS will have to remain robust to variations in engine parameters and inaccuracies in the definition of vibration modes of the coupled powertrain and chassis systems. This chapter has shown that parameter estimation techniques, such as RLS and EKF, can be used to estimate uncertain engine parameters, while robust command shaping can accommodate variations in vibration modes. RLS presents a simple approach that can be used if the geometry of the ICE is accurately defined and the ICE torque output can be measured. If these conditions cannot be met, the EKF algorithm can be used when only the angular position and velocity are measured. Once uncertain system parameters are estimated using either technique, robust command shaping can then be used to ensure TSCS effectiveness under vibration mode variations.

CHAPTER 4. TWO-SCALE COMMAND SHAPING APPLIED TO INTERNAL COMBUSTION ENGINE SHUTDOWN

Chapter 3 showed that the TSCS feedforward control methodology mitigates vibration-related issues with ICE restart; however, ICE shutdown can also impact a consumer's satisfaction with a vehicle. As highlighted by automotive manufacturers' design choices and reviews in popular automotive magazines, engine stop-start features impact consumers' perceptions of vehicle quality [32-36]. There are two instances during which a consumer could be disturbed by a stop-start feature, ICE shutdown and restart. Figure 4-1 displays the typical oscillations observed along the driveline during the shutdown process of an ICE.

Unlike restart, during shutdown the ICE crankshaft experiences positive and negative angular velocities when it can no longer complete the compression stroke of a cylinder. During shutdown, the crankshaft does not require an input to cease motion after combustion concludes. Therefore, applying TSCS to ICE shutdown will require an initial command profile that can be defined during the application of the strategy. The choice of the command profile allows the TSCS strategy to be used to reduce undesirable oscillations in the powertrain and chassis of the vehicle as well as decrease the shutdown time of an ICE after combustion ceases.

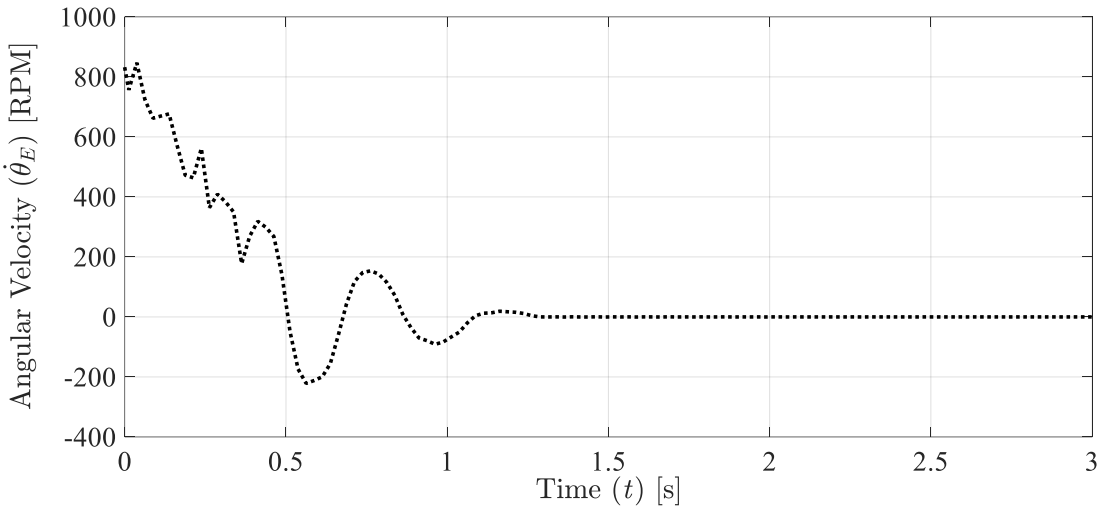

Figure 4-1 – Typical crankshaft angular velocity profile during shutdown.

4.1 Two-scale command shaping strategy applied to internal combustion engine shutdown

4.1.1 Analytical model for internal combustion engine shutdown

The lumped parameter models for the powertrain and chassis motion outlined in Chapter 3 can also be utilized in the theoretical application of TSCS to ICE shutdown. Figure 3-4 and Figure 3-5 are graphical representations of the powertrain and chassis torsional motion models, respectively. The powertrain system is governed by the matrix differential equation given in Eq. (3.12) and the chassis motion system is governed by Eq. (3.13). Table 3-1 and Table 3-2 provide the parameters that characterize the powertrain and chassis motion models.

The efficacy of TSCS as applied to ICE shutdown is analyzed with the one-dimensional model outlined in Section 3.1.1 for the 1.3 L I4 JTD engine that was developed

based on the work of Canova *et al.*, Ramos, and Taylor [5, 69, 70]. Table B-1 in the Appendix supplies the parameters for the 1.3 L I4 JTD engine. The piston motion and instantaneous cylinder volume for the ICE during shutdown is governed by Eqs. (3.1) and (3.2), which are derived using the crank-slider mechanism shown in Figure 3-1.

Once combustion ceases, the pressure within the cylinder of the ICE is governed by the differential equation outlined Eq. (3.5) that has a solution given by Eq. (3.6). In the case of shutdown, the specific heat ratio can be approximated as that of air, 1.40, and the initial conditions for the crankshaft can be taken as the idle speed of the 1.3 L I4 JTD engine [69, 70]. The torque from the ICE in the shutdown case can be modeled with the same techniques presented in Section 3.1.1, with the complete expression given in Eq. (3.7) and components provided in Eqs. (3.8) through (3.11).

4.1.2 Development of two-scale command shaping for internal combustion engine shutdown

The development of the TSCS input provided in Section 3.2 can also be used for ICE shutdown. Equation (3.14) provides the complete input for ICE shutdown for the application of the TSCS strategy. The time-varying term, T_1, is used to compensate for the oscillations in the powertrain caused by the nonlinearities in the response of the ICE crankshaft and is given in Eq. (3.21), where $p(\theta_{E0})$ is given through the zeroth-order scale and differential equation given in Eq. (3.5) when combustion ceases in the shutdown process. Section 3.2.1 provides the development of T_1, which is still valid for the shutdown case if Eq. (3.5) is used to define $p(\theta_{E0})$.

The other component of the TSCS input, T_0, is tailored through multi-mode input shaping process presented in Section 3.2.2 to avoid the excitation of flexible poles in the powertrain and chassis subsystems [9, 12, 41]. Application of multi-mode input shaping to the zeroth-order expression, Eq. (3.19), and zeroth-order torque component of Eq. (3.14) is provided in Eq. (3.22). The I_i(t) terms in Eq. (3.22) are the input shapers designed to mitigate the excitation of the n vibration frequencies deemed detrimental to system performance. Various methods can be used to define each of the I_i(t) terms depending on the certainty one has in the definition of the vibration mode in question. These methods include ZV, ZVD, and EI input shapers presented in Sections 2.2.2 and 3.5 [9, 40, 41]. Equations (2.27) and (2.28) provide the definition of ZV input shaping. Its extension, ZVD input shaping, is given in Eqs. (2.28) and (2.29). EI input shaping is defined in Eqs. (3.43) through (3.46).

4.2 Results of two-scale command shaping applied to internal combustion engine shutdown

4.2.1 Application of two-scale command shaping to internal combustion engine shutdown

Utilizing the one-dimensional ICE formulation of the 1.3 L I4 JTD engine and the lumped parameter models provided in Figure 3-4 and Figure 3-5, an unforced shutdown from an idle speed of 700 RPM was conducted. Figure 4-2 provides the simulated unforced velocity profile during shutdown for the 1.3 L I4 JTD. Without the application of torque, the crankshaft settles to rest in 2 s. TSCS cannot be applied to the case of ICE shutdown

unless an input torque is being applied to the system; therefore, a simple rectangular input profile is used as T_0 to develop the complete TSCS input.

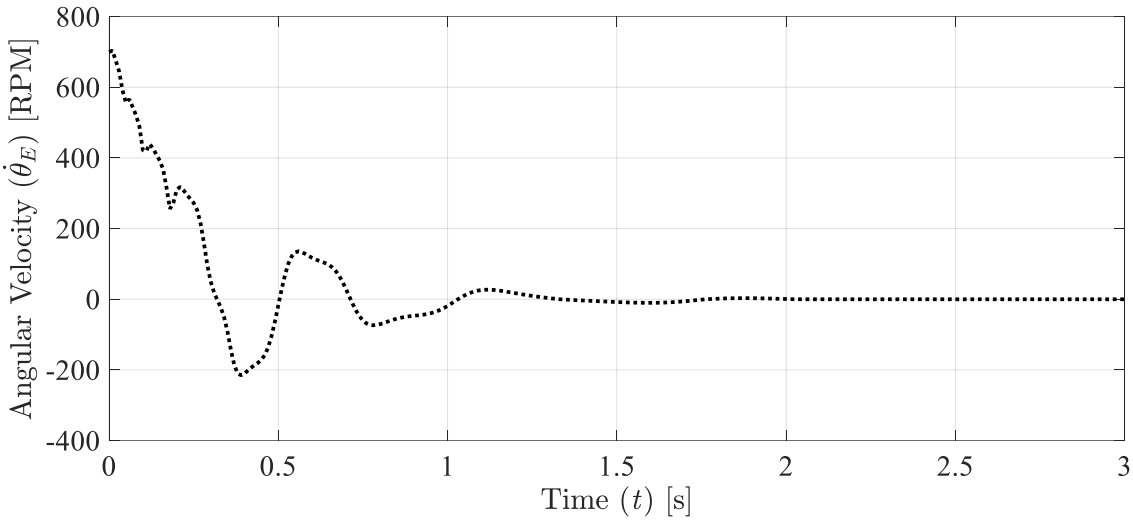

Figure 4-2 – Simulated unforced velocity profile for the 1.3 L I4 JTD ICE crankshaft.

Figure 4-3 provides the rectangular profile used to establish the foundation required to apply the TSCS strategy to ICE shutdown. Applying this torque alone increases the rate at which the crankshaft approaches rest without the TSCS strategy and reduces the peak negative angular velocity. Figure 4-4 provides the response for the ICE with the rectangular torque defined in Figure 4-3 applied. With T_0 applied, the peak negative velocity is reduced by 20.1% and the ICE comes to rest 7.5% faster.

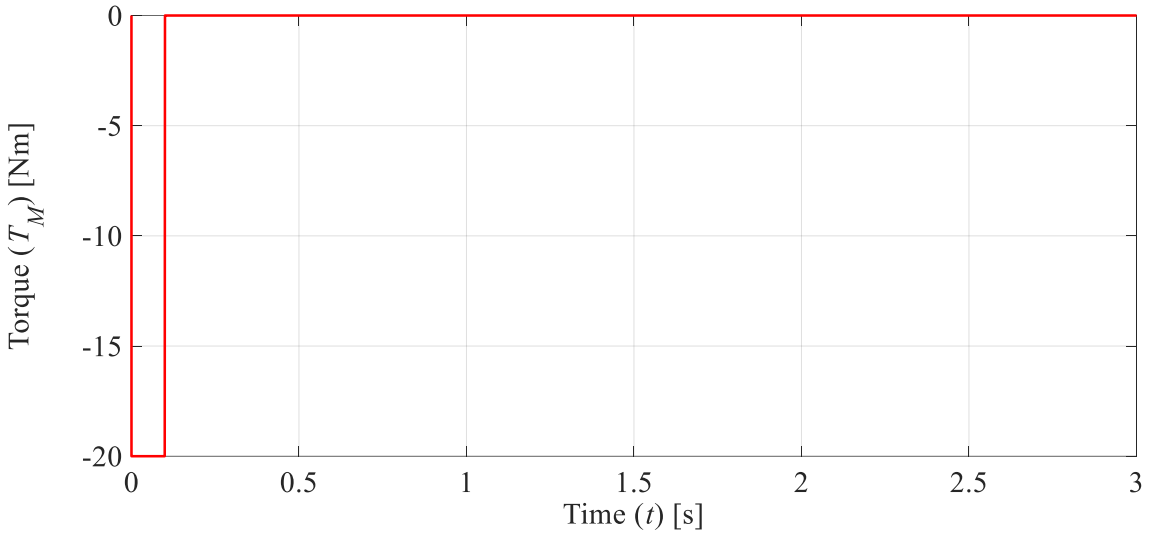

Figure 4-3 – Unshaped input force, T_0, for application of TSCS to ICE shutdown.

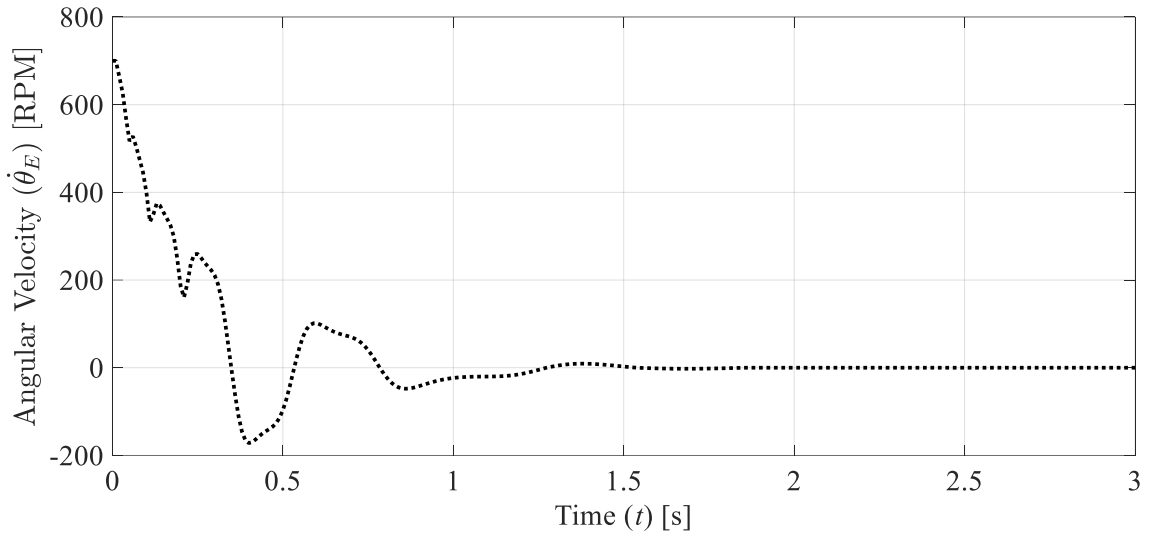

Figure 4-4 – Simulated unshaped velocity profile for the 1.3 L I4 JTD ICE crankshaft with T_0 applied.

The TSCS strategy can be applied with the rectangular profile presented in Figure 4-3. Developing the TSCS input torque profile based on the method outlined in Section 4.1.2 creates a shaped rectangular profile, $T_{0_{Shaped}}$, and a nonlinear torque component, T_1, to mitigate the oscillations in the ICE crankshaft response due to the nonlinearities of the

system. Figure 4-5 provides the unshaped input profile along with the complete TSCS input for the case of ICE shutdown. Applying TSCS to ICE shutdown requires energy to be supplied and absorbed during shutdown. When applied in a HEV powertrain, a full-size EM is available to apply the TSCS input to the ICE during shutdown along with a battery pack to absorb power generated during the shutdown process. During the shutdown with TSCS, the vehicle must be able to absorb up to 8.66 kW, which will be transferred to the battery pack of a HEV. In addition, TSCS will also require a maximum power input of 6.68 kW.

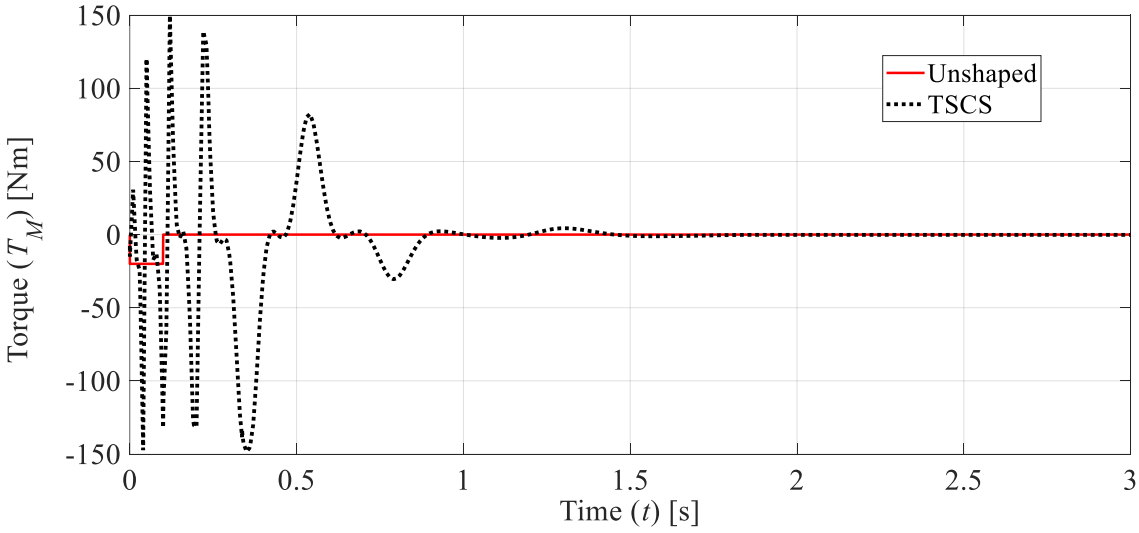

Figure 4-5 – Comparison of unshaped input force, T_0, to complete TSCS input for ICE shutdown.

The results of applying the TSCS input to ICE shutdown can be observed in Figure 4-6. As observed in the results obtained in the application of TSCS to stationary ICE restart provided in Section 3.3.1, the response of the crankshaft is satisfactory after application of the nonlinear component of the complete TSCS input, T_1. In Figure 4-6, the dotted line

denotes the unshaped response, the dashed line the response after the nonlinear component is added to the unshaped rectangular input profile, and the solid line denotes the crankshaft response from the complete TSCS input, accounting for the vibration modes of only the chassis motion model since the crankshaft response is satisfactory after T_1 application.

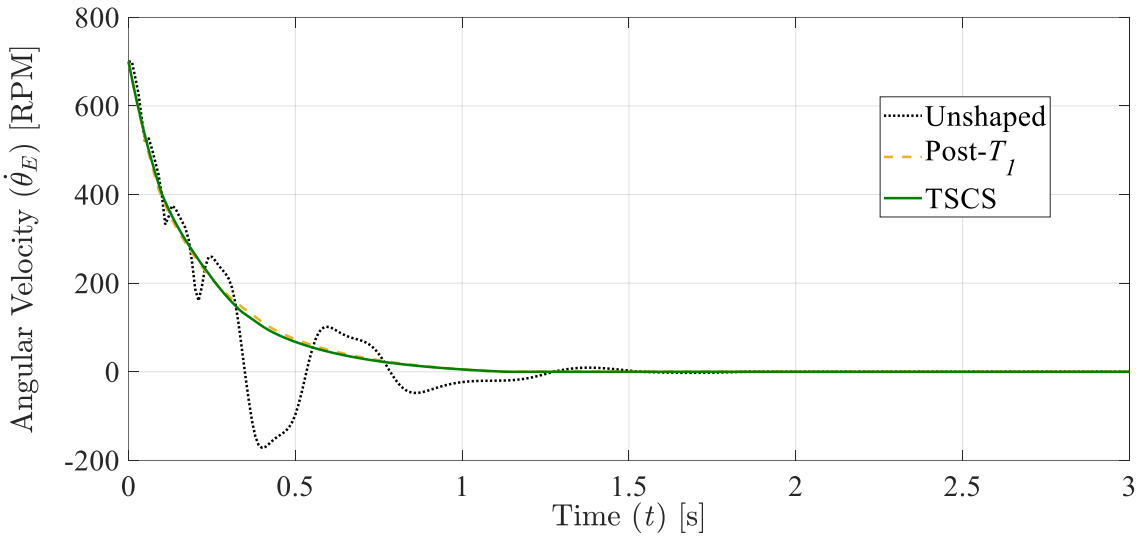

Figure 4-6 – Angular velocity of the crankshaft for shutdown as a function of time with unshaped, post-T_1, and TSCS inputs.

Utilizing the TSCS strategy also mitigates the undesirable oscillations in the motion of the chassis of the vehicle. Figure 4-7 provides the response of the chassis of the vehicle to unshaped, post-T_1, and TSCS inputs. Applying the rectangular torque profile alongside the nonlinear term, T_1, of the TSCS strategy reduces the oscillations in the chassis. Shaping for the vibration modes of the chassis further reduces the peaks of the oscillations in the chassis motion. Adding in the T_1 component reduces the maximum unshaped oscillation amplitude by 8.0 dB where the complete TSCS input reduces it by 8.6 dB. In terms of settling time, applying the T_1component and full TSCS input both reduce the time that the

system takes to settle to an angular velocity of less than 0.002 RPM by 55.62% relative to the unshaped case.

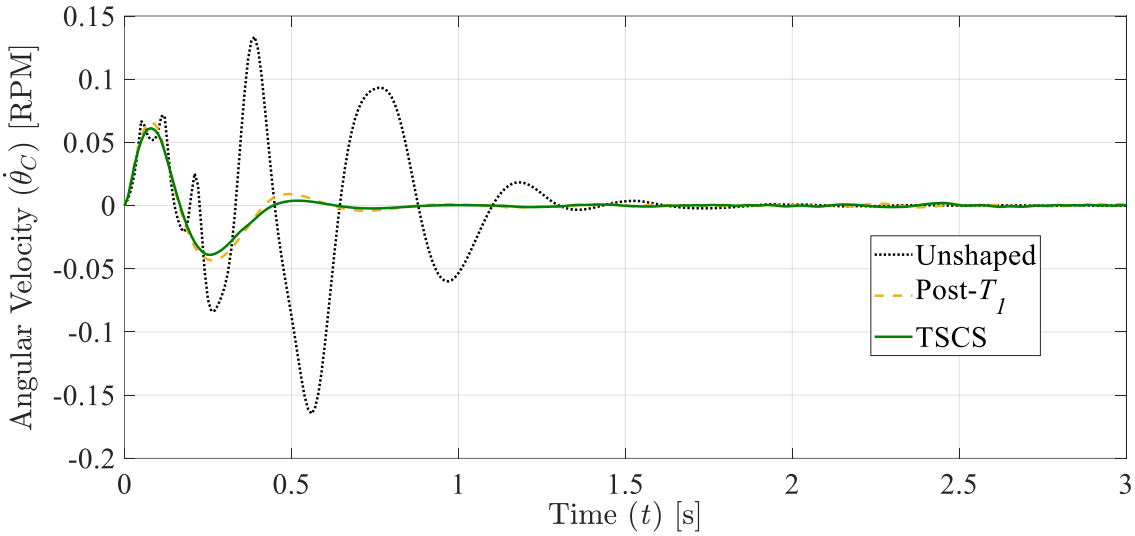

Figure 4-7 – Angular velocity of the chassis for shutdown as a function of time with unshaped, post-T_1, and TSCS inputs.

4.2.2 Effect of T_0 amplitude and duration on efficacy of two-scale command shaping

The duration and amplitude of the unshaped T_0 term used in the development of the TSCS input for ICE shutdown affects the performance of the strategy. Figure 4-8 and Figure 4-9 show the effect of increasing the duration of T_0 on the efficacy of TSCS in mitigation of the undesirable oscillations in the response of the crankshaft and chassis, respectively. Observing Figure 4-8, increasing the duration of T_0 to 0.2 s from 0.1 s reduces the time required for the crankshaft to settle to under 1 RPM by 33.3%. However, increasing the duration to 0.4 s only reduces the time to reach an angular velocity of less than 1 RPM by 15.3%, since this duration results in the crankshaft being forced to a larger negative angular velocity. The maximum peak of the chassis response does not change with

increasing T_0 duration in Figure 4-9, but the secondary peak as well as the settling characteristics are both affected by varying the duration.

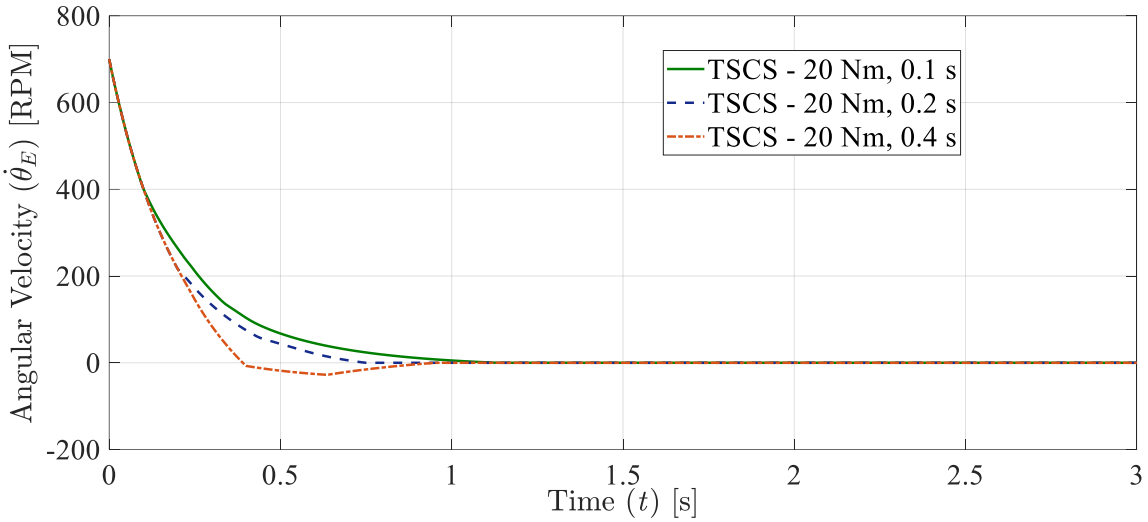

Figure 4-8 – Effect of T_0 duration on the efficacy of TSCS in mitigating undesirable oscillations of the crankshaft angular velocity during ICE shutdown.

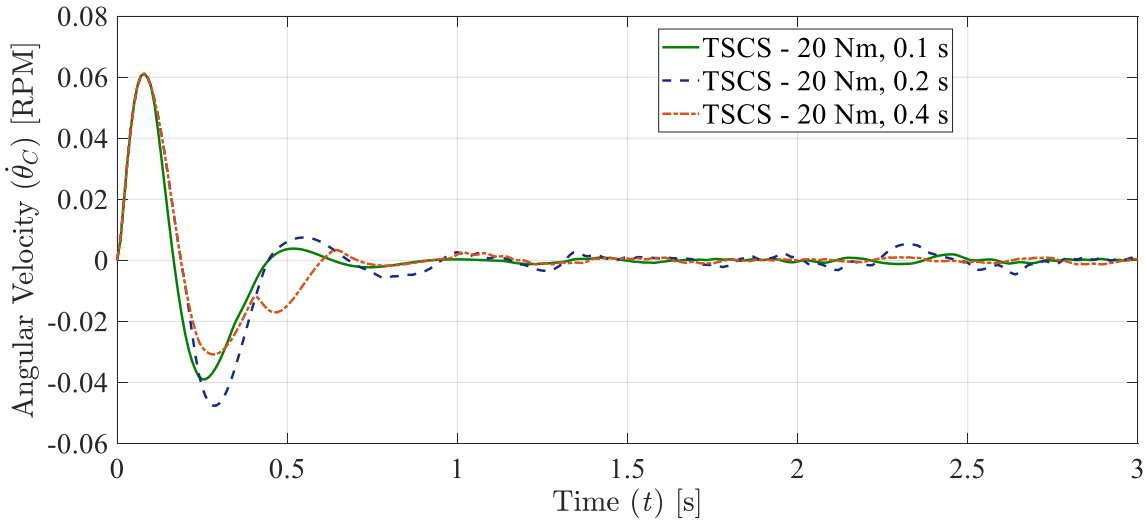

Figure 4-9 – Effect of T_0 duration on the efficacy of TSCS in mitigating undesirable oscillations of the chassis angular velocity during ICE shutdown.

Figure 4-10 and Figure 4-11 show the impact of the unshaped amplitude of T_0 on the efficacy of TSCS during the ICE shutdown process on the response of the crankshaft and chassis, respectively. Increasing the amplitude of T_0 reduces the settling time of the crankshaft response when TSCS is applied as observed in Figure 4-10. When T_0 is increased from 20 Nm to 100 Nm, the time required for the crankshaft to settle within 1 RPM is reduced by 98.59%.

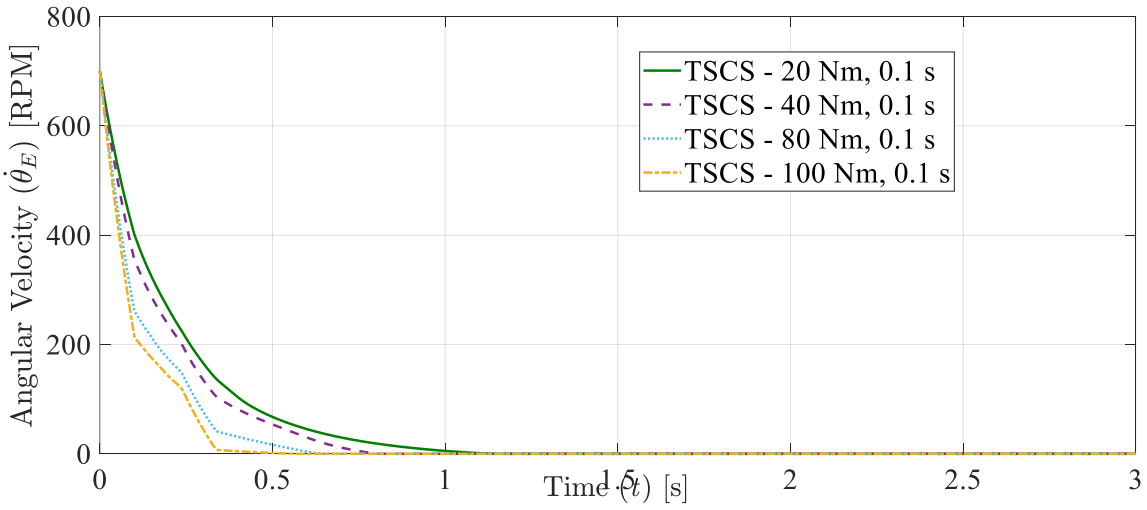

Figure 4-10 – Effect of T_0 amplitude on the efficacy of TSCS in mitigating undesirable oscillations of the crankshaft angular velocity during ICE shutdown.

However, increasing the amplitude of T_0 increases the maximum amplitude of the undesirable oscillations in the chassis, which can be seen in Figure 4-11. Increasing the amplitude of T_0 from 20 Nm to 100 Nm increases the maximum oscillation amplitude in the response of the chassis from the TSCS input by 3.6 dB. Therefore, the unshaped amplitude and duration of T_0 provides an additional design parameter that can impact the efficacy of TSCS as well as increase the speed at which the ICE shutdown process occurs.

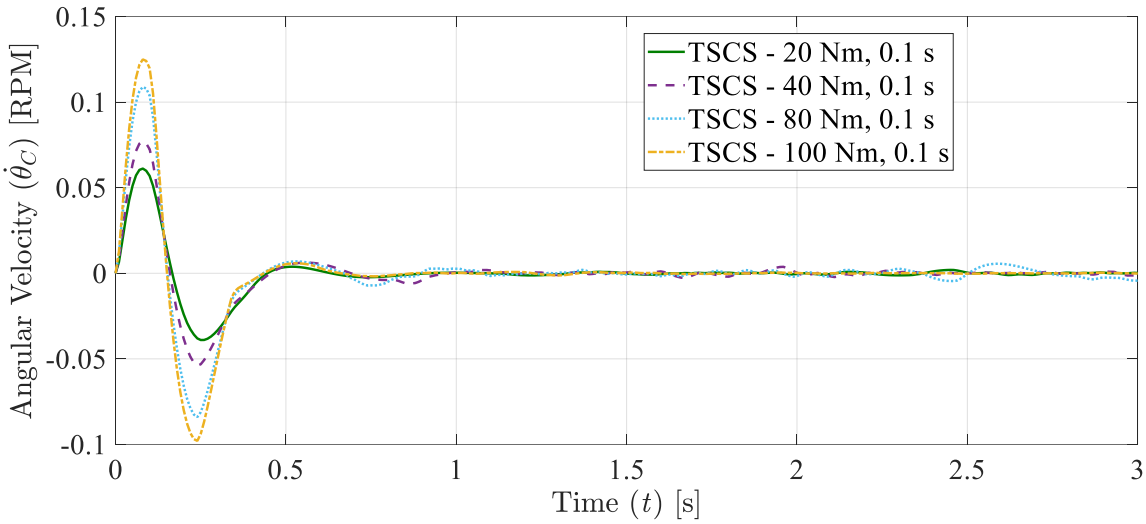

Figure 4-11 – Effect of T_0 amplitude on the efficacy of TSCS in mitigating undesirable oscillations of the chassis angular velocity during ICE shutdown.

4.3 Conclusions

Another problem associated with fuel-saving features in HEV and modern conventional powertrains is vibration-related issues associated with ICE shutdown. By enforcing a rectangular torque profile during the shutdown process, the TSCS strategy can be effectively applied. In addition, the choice of initial duration and amplitude of T_0 provides the ability to affect the rate of the ICE shutdown process as well as the efficacy of the TSCS strategy. By combining robust command shaping strategies and parameter estimation techniques with the TSCS development presented in this chapter, TSCS can serve as an effective strategy to reduce undesirable vibrations in the response of the crankshaft and chassis of a vehicle during the shutdown process.

CHAPTER 5. EXPERIMENTAL VERIFICATION OF TWO-SCALE COMMAND SHAPING APPLIED TO INTERNAL COMBUSTION ENGINE RESTART

This chapter introduces an experimental apparatus, representing a typical HEV powertrain, which allows for the assessment of the nonlinear dynamics of ICE restart and shutdown. The apparatus consists of a permanent magnet alternating current (PMAC) EM coupled to a three-cylinder diesel ICE. In addition to observing the nonlinear behavior of the ICE, validation of TSCS is completed by specifying the torque profile provided from the EM to the ICE for restart based on the strategy. The sensors used to document the nonlinear behavior of the ICE are then used to measure the resulting reduction in undesirable oscillation in the driveline and frame (representing the chassis of the vehicle).

5.1 Two-scale command shaping applied to a lumped parameter model of the experimental apparatus

5.1.1 Two-scale command shaping overview

Two-scale command shaping is confirmed here as applied to the experimental apparatus. The design consists of a Kohler 1.03 L, inline, three-cylinder diesel ICE coupled to a Parker PMAC EM through a spur gear coupling. The three-cylinder diesel ICE was used in place of the four-cylinder engine presented in previous simulation results due to its smaller size, simple mounting points, and its purported harsher vibration characteristics

[32]. Figure 5-1 depicts the lumped-parameter model used to capture the system dynamics of the apparatus powertrain.

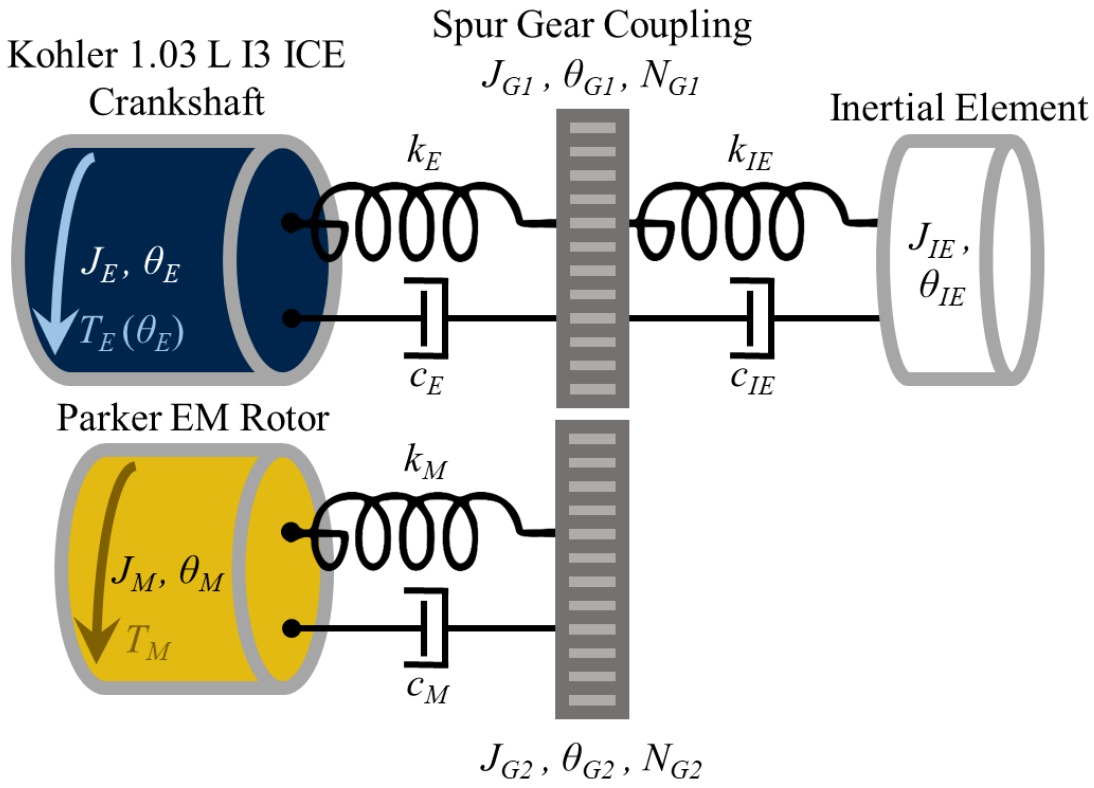

Figure 5-1 – Lumped-parameter torsional model of the powertrain of the experimental apparatus.

The lumped-parameter model is governed by the following set of equations

$$[J]\begin{bmatrix}\ddot{\theta}_E\\ \ddot{\theta}_{G1}\\ \ddot{\theta}_{IE}\\ \ddot{\theta}_{G2}\\ \ddot{\theta}_M\end{bmatrix}+[C]\begin{bmatrix}\dot{\theta}_E\\ \dot{\theta}_{G1}\\ \dot{\theta}_{IE}\\ \dot{\theta}_{G2}\\ \dot{\theta}_M\end{bmatrix}+[K]\begin{bmatrix}\theta_E\\ \theta_{G1}\\ \theta_{IE}\\ \theta_{G2}\\ \theta_M\end{bmatrix}=\begin{bmatrix}T_E(\theta_E)\\ 0\\ 0\\ 0\\ T_M\end{bmatrix} \tag{5.1}$$

where the inertia, stiffness, and damping matrices can be expressed as

$$[J] = \begin{bmatrix} J_E & 0 & 0 & 0 & 0 \\ 0 & J_{G1} & 0 & 0 & 0 \\ 0 & 0 & J_{IE} & 0 & 0 \\ 0 & 0 & 0 & J_{G2} & 0 \\ 0 & 0 & 0 & 0 & J_M \end{bmatrix} \tag{5.2}$$

$$[C] = \begin{bmatrix} c_E & -c_E & 0 & 0 & 0 \\ -c_E & c_E + c_{IE} + \left(\frac{N_{G1}}{N_{G2}}\right)^2 c_M & -c_M & 0 & -\frac{N_{G1}}{N_{G2}} c_M \\ 0 & -c_{IE} & c_{IE} & 0 & 0 \\ -\frac{N_{G2}}{N_{G1}} c_E & 0 & -\frac{N_{G2}}{N_{G1}} c_{IE} & \left(\frac{N_{G2}}{N_{G1}}\right)^2 c_E + \left(\frac{N_{G2}}{N_{G1}}\right)^2 c_{IE} + c_M & -c_M \\ 0 & 0 & 0 & -c_M & c_M \end{bmatrix} \tag{5.3}$$

$$[K] = \begin{bmatrix} k_E & -k_E & 0 & 0 & 0 \\ -k_E & k_E + k_{IE} + \left(\frac{N_{G1}}{N_{G2}}\right)^2 k_M & -k_{IE} & 0 & -\frac{N_{G1}}{N_{G2}} k_M \\ 0 & -k_{IE} & k_{IE} & 0 & 0 \\ -\frac{N_{G2}}{N_{G1}} k_E & 0 & -\frac{N_{G2}}{N_{G1}} k_{IE} & \left(\frac{N_{G2}}{N_{G1}}\right)^2 k_E + \left(\frac{N_{G2}}{N_{G1}}\right)^2 k_{IE} + k_M & -k_M \\ 0 & 0 & 0 & -k_M & k_M \end{bmatrix} \tag{5.4}$$

where J_E and J_M are the equivalent polar moment of inertias for the ICE crankshaft and counterbalances and EM rotor, respectively. The polar moment of inertia for the gears on the ICE and EM output shafts are J_{G1} and J_{G2}, respectively. J_{IE} is the polar moment of inertia of an inertial element simulating additional powertrain elements, such as the driven plate assembly of a clutch. The shafts between each element of the setup are characterized by a stiffness, k, and damping coefficient, c, with the subscript denoting the terminal connection

of the shaft. Table B-2 contains the apparatus parameters used in the theoretical overview of TSCS. The state vector of Eq. (5.1) contains the ICE crankshaft, ICE spur gear, EM spur gear, inertial element, and EM rotor absolute rotational degrees-of-freedom.

Figure 5-2 depicts the lumped-parameter model representing the coupling between the motion of the EM body and ICE block in relation to the frame. Casters with extendable rubber feet are used to aid in the isolation of the apparatus vibration from the surrounding test cell. Theorical parameters to characterize the frame motion model are found in Table B-3 for overview of the TSCS strategy. In practice, model identification or a modal model can be used to define the pertinent vibration modes based on experimental data as shown in Sections 5.3.2 and 5.4.

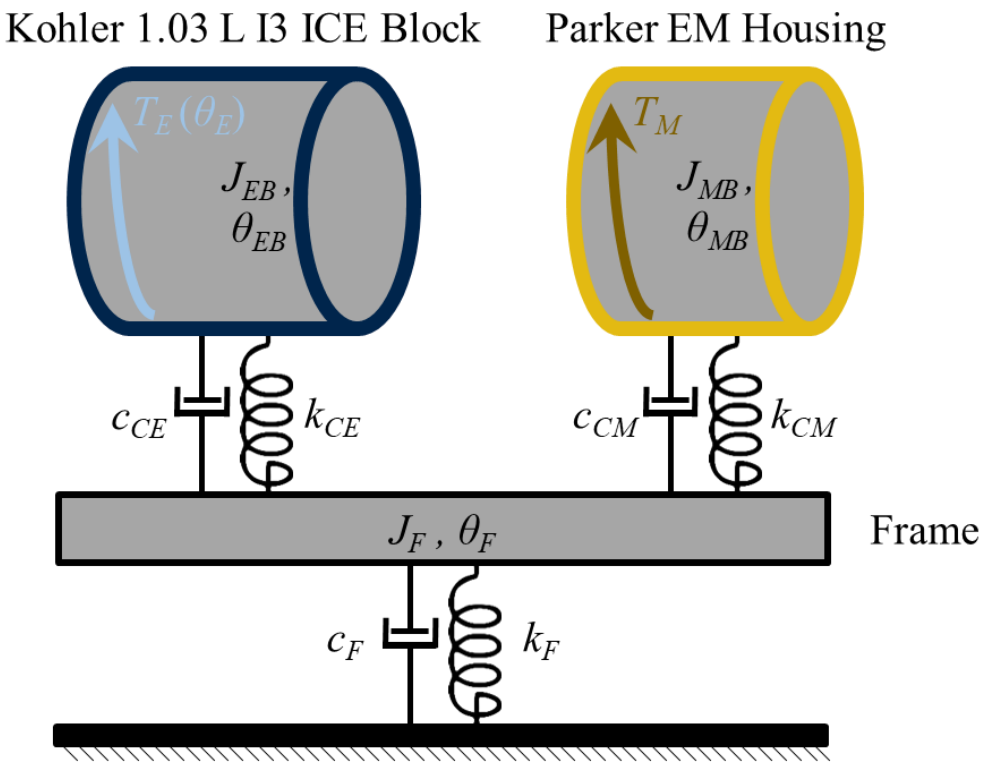

Figure 5-2 – Lumped-parameter torsional model of the experimental apparatus frame.

The model shown in Figure 5-2 is governed by

$$\begin{bmatrix} J_{EB} & 0 & 0 \\ 0 & J_{MB} & 0 \\ 0 & 0 & J_F \end{bmatrix} \begin{bmatrix} \ddot{\theta}_{EB} \\ \ddot{\theta}_{MB} \\ \ddot{\theta}_F \end{bmatrix} + \begin{bmatrix} c_{CE} & 0 & -c_{CE} \\ 0 & c_{CM} & -c_{CM} \\ -c_{CE} & -c_{CM} & c_{CE} + c_{CM} + c_F \end{bmatrix} \begin{bmatrix} \dot{\theta}_{EB} \\ \dot{\theta}_{MB} \\ \dot{\theta}_F \end{bmatrix} + \begin{bmatrix} k_{CE} & 0 & -k_{CE} \\ 0 & k_{CM} & -k_{CM} \\ -k_{CE} & -k_{CM} & k_{CE} + k_{CM} + k_F \end{bmatrix} \begin{bmatrix} \theta_{EB} \\ \theta_{MB} \\ \theta_F \end{bmatrix} = \begin{bmatrix} -T_E(\theta_E) \\ -T_M \\ 0 \end{bmatrix} \tag{5.5}$$

where J_{MB} and J_{EB} are the polar moments of inertia of the EM housing and ICE block, respectively. J_F is the polar moment of inertia of the apparatus frame. Modeling the motion of the frame with the system shown in Figure 5-2 provides a means to account for additional flexible poles for mitigation with TSCS. The external inputs for Eq. (5.5) arise from the

reactionary torques from the torques exerted on the crankshaft and EM rotor. The state vector of Eq. (5.5) consists of the absolute rotational degrees-of-freedom of the ICE block, EM housing, and frame.

The torque arising from the ICE in Eqs. (5.1) and (5.5) is defined using a one-dimensional model adapted from the methods documented by Canova *et al.*, Taylor, and Ramos, which was introduced in Chapter 3 [5, 69, 70]. The output torque of a single-cylinder of an ICE is a linear combination of three components and is governed by the expression given in Eq. (3.7). The torque components found in Eq. (3.7) are defined in Eqs. (3.8)-(3.11). Defining indicated torque using Eq. (3.8) requires an expression for the in-cylinder pressure, which is given by solving the differential equation provided in Eq. (3.3) using the methods outlined in Chapter 3. Canova *et al.* showed that a lumped-thermal system can be used to account for the temperature dependency of the parameters contained in friction expression of Eq. (3.11) [5]. It has also been shown theoretically that parameter estimation techniques, such as EKF, can be used to update these parameters [90]. As stated in Chapter 3, the above expressions are for a single cylinder of the ICE. To extend these expressions to model the complete three-cylinder Kohler engine, a phase lag for each cylinder is introduced to represent the crank rotation between firing events, which is 240° for a three-cylinder engine.

As shown in Chapter 3, the torque from the EM in the TSCS strategy for the experimental apparatus is expressed as

$$T_M = T_{0_{Shaped}}(t) + \varepsilon T_1(t) \tag{5.6}$$

where $T_{0_{Shaped}}$ denotes the component of the input defined utilizing command shaping applied to the zeroth-order problem and T_1 the time-varying component used to mitigate nonlinear behavior of the ICE [7, 40, 90-91]. ε in Eq. (5.6) is a bookkeeping term utilized to order linear and nonlinear behavior and is defined as unity after scale separation. The scale separation process of TSCS is covered extensively in Chapters 2 and 3 and documented in [7, 91]. By applying the scale separation process, it can be shown for mitigation of the nonlinear behavior of the ICE that the time-varying EM component is defined as

$$T_1(t) = -\frac{N_{G1}}{N_{G2}}\left(rA_P(p(\theta_{E0}) - p_{Ambient})\left(sin\,\theta_{E0} + \frac{sin\,\theta_{E0}\,cos\,\theta_{E0}}{\sqrt{R^2 - sin^2\,\theta_{E0}}}\right)\right) \tag{5.7}$$

where θ_{E0} is the solution of the zeroth-order equation governing the linear motion of the ICE crankshaft. Equation (5.7) is one of the two components required to completely define the EM torque in the TSCS strategy; the other component is given by command shaping the zeroth-order, or linear, dynamics of the apparatus [7, 40, 90-91].

Multi-mode input shaping can be used to mitigate the excitation of vibration modes of the powertrain and frame [9, 12, 41]. The multi-mode input shaping process is applied to the zeroth-order differential equation governing the linear dynamics of the apparatus and the initial EM torque, T_0, that is defined to be zeroth-order. As shown previously, applying the shaping process results in

$$T_{0_{Shaped}}(t) = T_0 * I_1(t) * I_2(t) * \ldots \tag{5.8}$$

where $I_i(t)$ represents the input shaper designed for one of the n vibration frequencies of the powertrain and frame convolved with the original torque command to create a shaped zeroth-order torque component, $T_{0_{Shaped}}(t)$. There are multiple formulations that can be used to define the input shapers of Eq. (5.8), such as ZV shapers or robust strategies, which include EI and ZVD shapers [9, 40, 41]. Due to their simplicity and minimal duration, ZV input shapers are used in the initial application of the TSCS strategy to the experimental apparatus. The definition of a ZV input shaper is given in Eqs. (2.27) and (2.28). If uncertainty in vibration modes affect the efficacy of TSCS, robust strategies can be implemented in place of ZV input shapers to improve the performance of TSCS.

Once the input shapers are defined, they are convolved with the original unshaped component of the EM torque, T_0, which is a step function in the ICE restart application presented. The input shapers are defined for the pertinent vibration frequencies during ICE restart. A more in-depth discussion about the development of the TSCS strategy can be found in Chapters 2 and 3 as well as [7, 91]. The vibration frequencies of the experimental apparatus can either be obtained through analysis of the differential equations governing it, Eqs. (5.1) through (5.5), or through an experimental modal analysis. In the shaping process, two pulses are required to eliminate each vibration frequency with ZV input shaping.

5.1.2 Two-scale command shaping application

Figure 5-3 and Figure 5-4 show the theoretical efficacy of TSCS in reducing undesirable oscillations in the response of the crankshaft and frame, respectively, with the theoretical parameters listed in Table B-2 and Table B-3. TSCS is assessed by applying the torque profile defined with Eqs. (5.6), (5.7), and (5.8) to Eqs. (5.1) through (5.5) governing the motion of the experimental apparatus, which are solved through direct numerical integration. In Figure 5-3 and Figure 5-4, the dotted curve is the response from the original step command without application of TSCS, the dashed curve from the original unshaped torque command and $T_1(t)$, and the dashed-dotted curve from the complete TSCS EM torque shaped for pertinent vibration frequencies of the powertrain and frame. The initial 0.75 s of these plots are highlighted since this transient region is critical for vibration mitigation to result in a smooth ICE restart and where the TSCS strategy is applied.

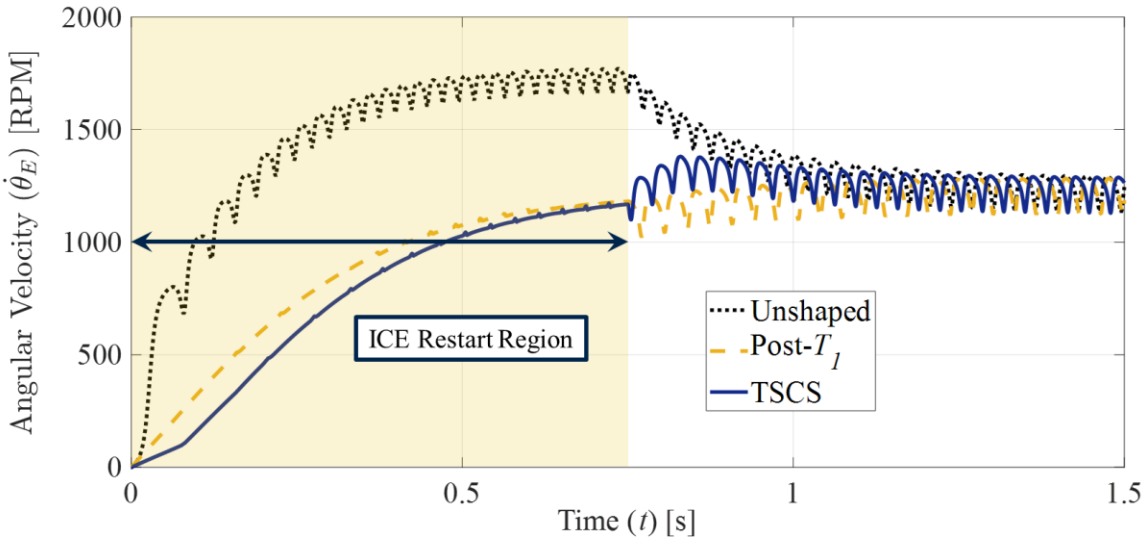

Figure 5-3 – Simulated angular velocity of the three-cylinder ICE crankshaft to unshaped, post-T_1, and TSCS commands.

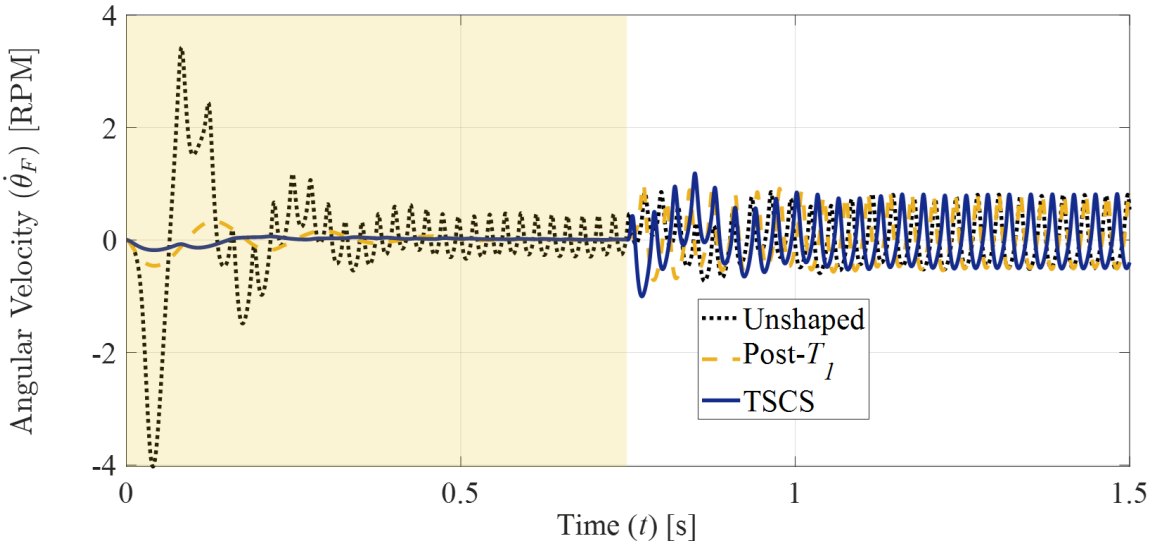

Figure 5-4 – Simulated angular velocity of the experimental apparatus frame to unshaped, post-T_1, and TSCS commands.

After application of $T_1(t)$, the undesirable oscillations from the nonlinear behavior of the crankshaft is reduced to an acceptable level without application of command shaping. However, oscillations still persist in the frame, which was also observed in

previous analyses found in Chapter 3 and [7, 40, 90]. Including the command shaping process to form the complete TSCS input, while focusing on the frame's flexible modes, mitigates the remaining vibrations shown in Figure 5-4. Once TSCS is applied to restart the ICE, the TSCS input is concluded and the ICE crankshaft oscillates about the idle speed as expected without the application of an additional steady-state mitigation strategy.

5.1.3 Using robust command shaping strategies with two-scale command shaping

TSCS may suffer from uncertainties in the definition of the vibration modes for the powertrain or frame. Figure 5-5 shows the impact of a variation in the frequency of the vibration modes of the frame of the apparatus on the mitigation of the undesirable oscillations. With a ZV-based TSCS strategy, a 65% increase in the natural frequency results in the reduction of the dominant residual vibration amplitude being 88.8% compared to the 92.1% that was observed with the correct design frequencies. Additionally, the time required for the residual vibration to settle to 1% of its peak unshaped value for the frame system increases from 0.23 s to 0.50 s, a 117.4% increase.

As remarked earlier, robust command shaping can mitigate the adverse effect of vibration mode variations. Alternatively, robust command shaping can be viewed as increasing the frequency range which is mitigated with a single shaper, which can increase the overall performance of TSCS. Including additional zeros or changing the zero locations relative to the flexible poles, increases a shaper's robustness. Several research groups have developed robust approaches, such as previously introduced ZVD and EI input shapers [9-

11, 41, 88].

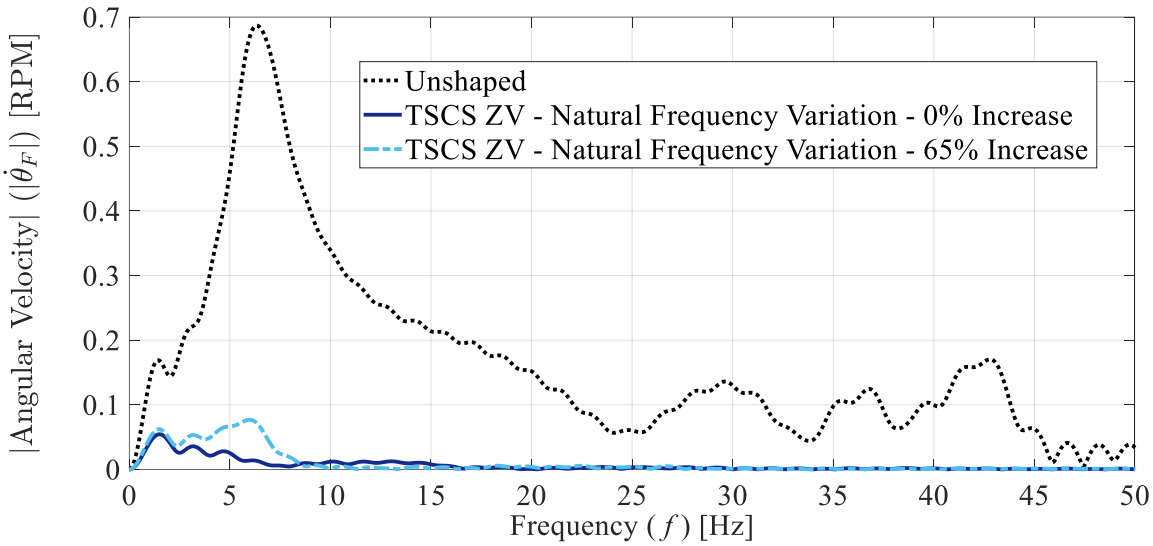

Figure 5-5 – Impact of variations in the natural frequency of the vibration modes of the apparatus on the efficacy of TSCS with ZV input shaping in reducing frequency content of the simulated frame angular velocity.

Robust command shaping was introduced in Sections 2.2.2 and 3.5 for ZVD and EI input shaping, respectively. Both these shaping strategies require three impulses and a full damped period of the cancelled pole. Figure 5-6 and Figure 5-7 show the impact of robust command shaping strategies in the reduction of the undesirable vibrations in the frame of the apparatus. The simulated responses of the frame to an unshaped input as well as TSCS inputs using ZV, ZVD, and EI input shaping under the effect of a +65% uncertainty in the dominant vibration modes of the frame are shown in Figure 5-6. Significant oscillations remain in the response when developing the TSCS input with ZV shaping, but these oscillations are reduced when applying TSCS with ZVD and EI input shaping. This can be observed in the Fourier transform of the frame response, which is provided in Figure 5-7. TSCS with ZVD and EI input shaping both reduce the vibration

amplitude at the dominant frequency by 92.1%, which is equivalent to the performance observed with the TSCS strategy applied with ZV input shaping with no uncertainty in the vibration modes. Using ZVD and EI input shaping in the development of the TSCS input reduces the 1% settling time of the frame response observed with an erroneously designed ZV input shaping process by 19.9% and 23.4%, respectively.

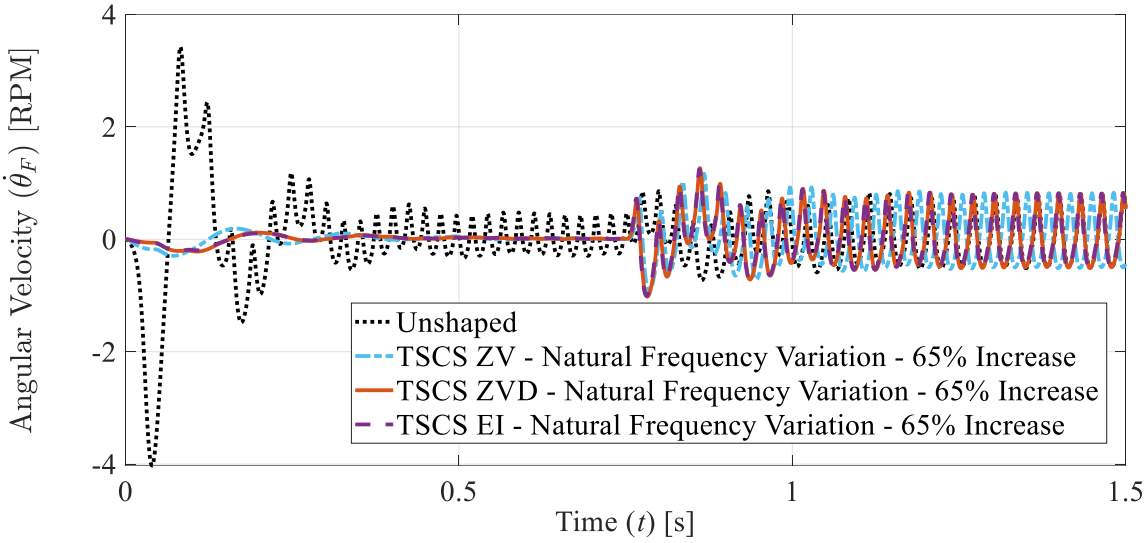

Figure 5-6 – Simulated angular velocity of the frame with a 65% increase in the natural frequencies of the vibration modes of the apparatus with TSCS applied using ZV, ZVD, and EI input shaping.

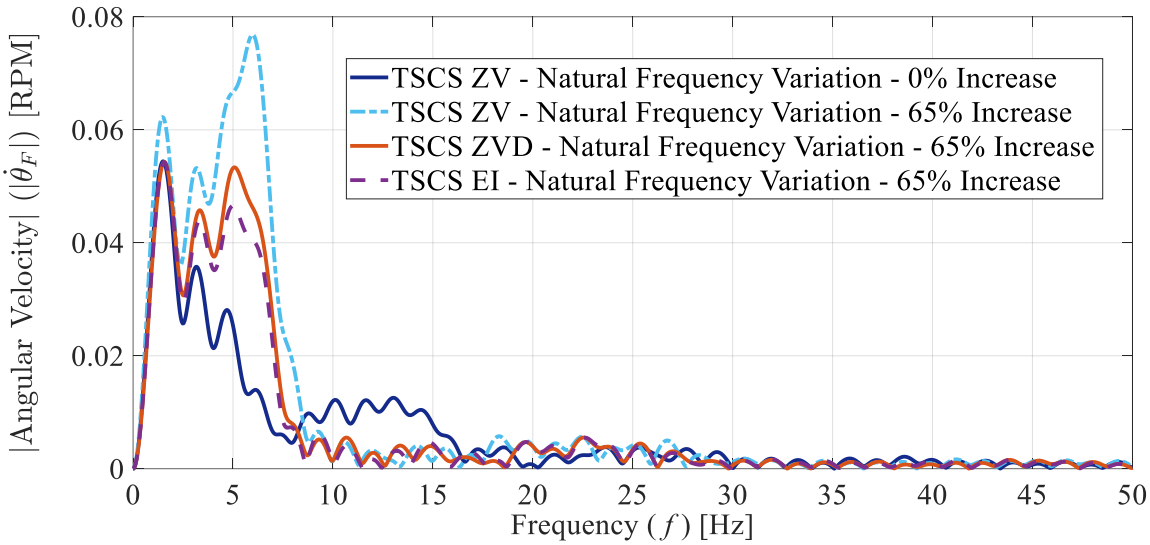

Figure 5-7 – Impact of robust command shaping in mitigating the effect of a 65% increase in the natural frequencies on TSCS efficacy in reducing the frequency content of the simulated frame angular velocity.

Robust command shaping can also improve the impact of TSCS when the vibration modes are correctly defined, which can be shown with the Fourier transform of the frame when subjected to a TSCS input defined with correctly designed ZVD and EI input shapers, which is provided in Figure 5-8. ZVD and EI input shaping improve the vibration amplitude reduction of the TSCS input by 25.2% and 27.2%, respectively. The only drawback to this improvement in performance and robustness is an increase in the time required for the input to fully develop, which equates to 15.74 ms. This effect can be observed in Figure 5-9.

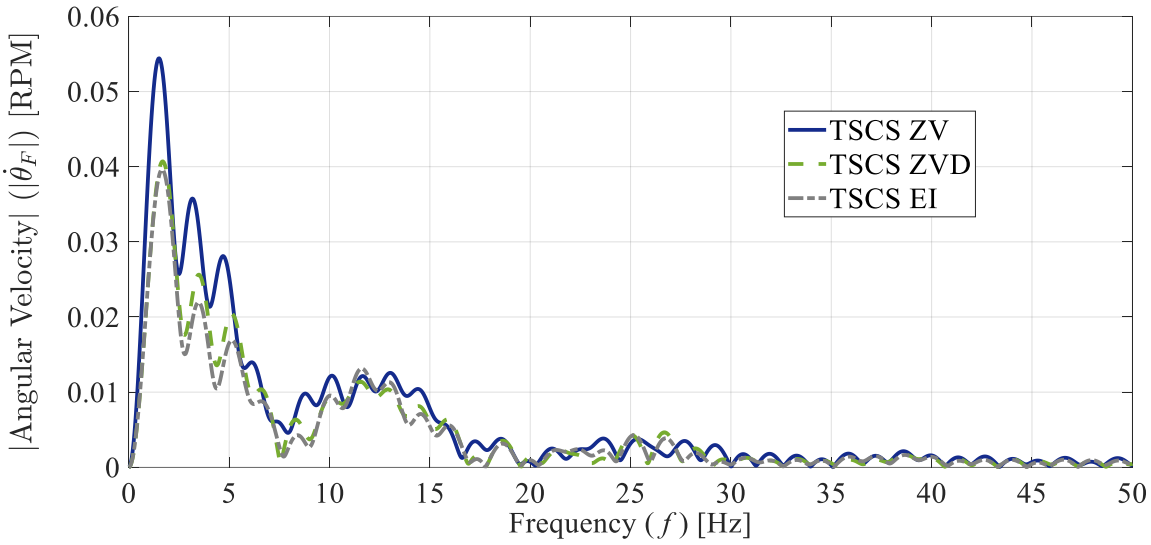

Figure 5-8 – Theoretical efficacy of robust command shaping on reducing the frequency content of the angular velocity of the frame with correctly defined vibration modes.

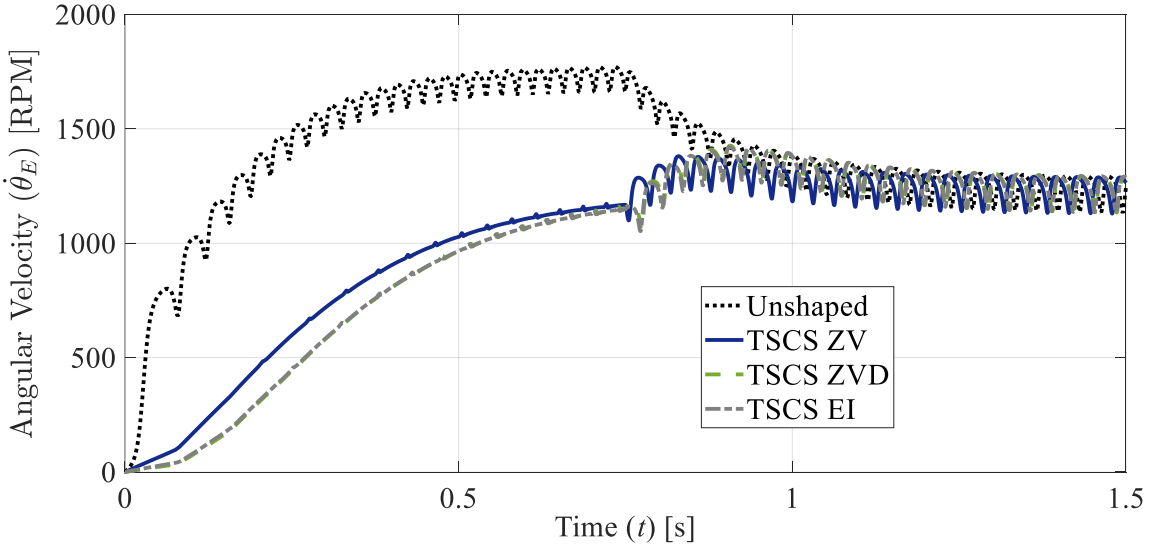

Figure 5-9 – Theoretical efficacy of robust command shaping on mitigating the undesirable crankshaft oscillations with correctly defined vibration modes.

5.2 Introduction of the experimental apparatus for observing internal combustion engine behavior during restart and shutdown

A CAD rendering of the apparatus design is provided in Figure 5-10 with pertinent components labeled. Two views of the completed setup are shown in Figure 5-11. Component 1 in Figure 5-10 is the leveling casters used to isolate the vibration of the experiment from the surrounding test cell. The frame and mounting points for the ICE are denoted as Component 2. As presented earlier, the ICE is an inline three-cylinder diesel engine produced by Kohler. The output power and volumetric displacement of the ICE are 17.45 kW and 1.03 L, respectively. Table B-4 provides parameters from several sources to approximate the behavior of the Kohler ICE. The engine was acquired off-the-shelf without technical support from Kohler; thus, the exact operating characteristics of the engine were unknown *a priori*.

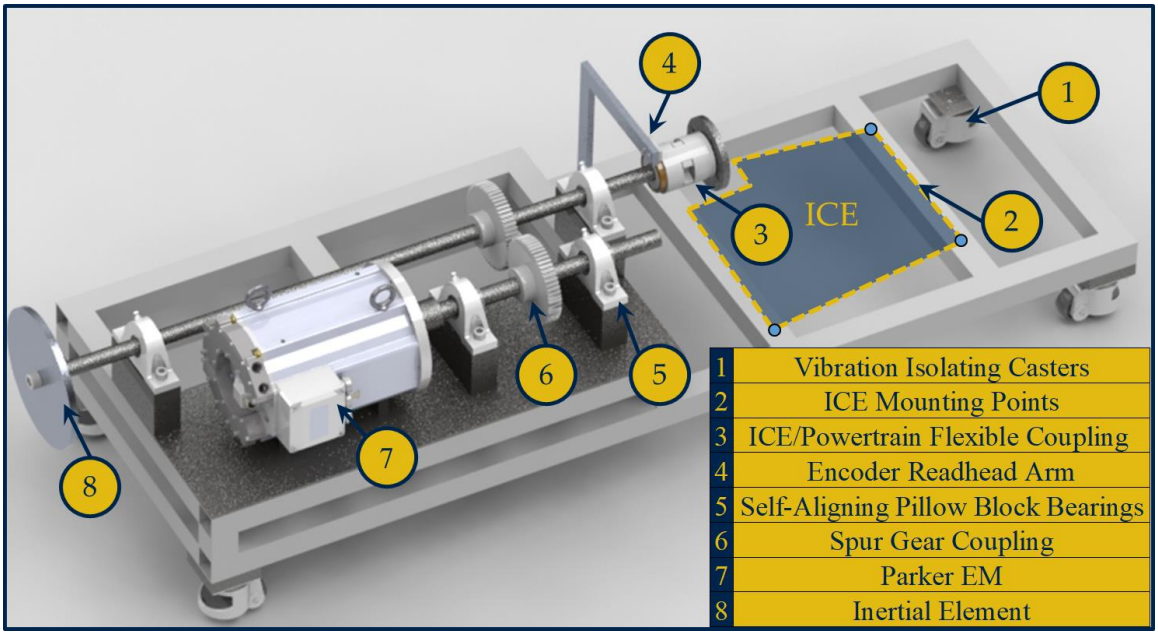

Figure 5-10 – Component design for the experimental apparatus.

The power from the ICE is transmitted to an AISI 4340 steel driveshaft that is connected to the ICE through a flexible coupling with an adapter machined specifically to connect to the bellhousing of the three-cylinder Kohler engine, denoted as Component 3 in Figure 5-10. The flexible coupling provides mitigation of any parallel and angular misalignments of 0.381 mm and 0.5°, respectively. Both the output shaft of the ICE and EM are supported by self-aligning pillow block bearings, which are denoted as Component 5 in Figure 5-10. These bearings mitigate alignment problems between the output shafts of the ICE and EM.

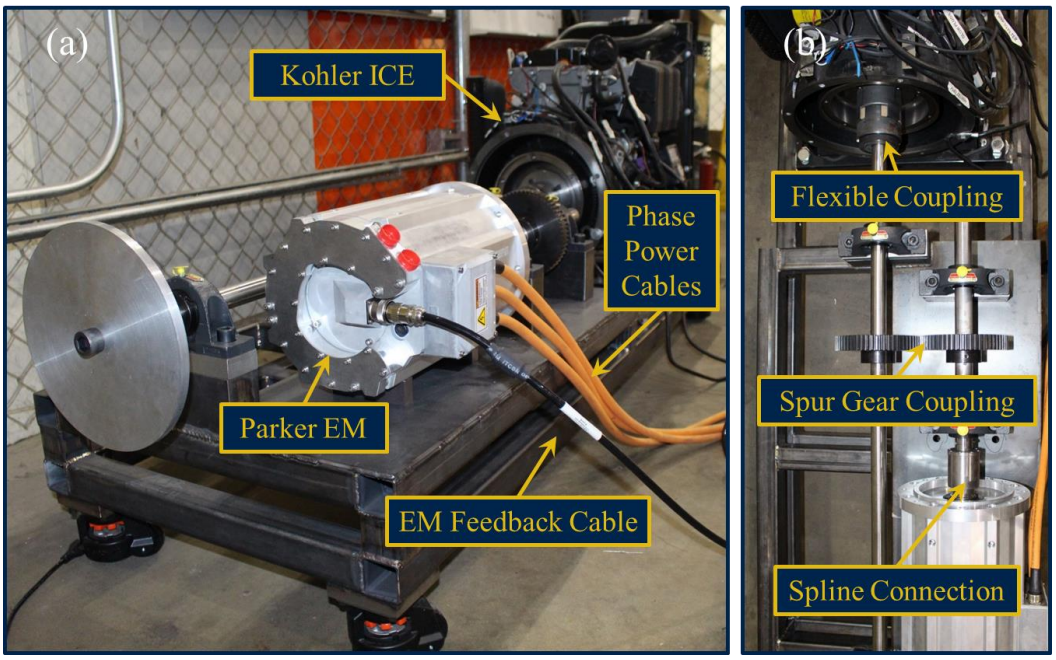

Figure 5-11 – (a) Completed experimental apparatus and (b) detail view of spur gear coupling between EM and ICE of setup.

The output shaft of the ICE is coupled to the EM through a spur gear coupling denoted as Component 6. Both gears have the same number of teeth, 60, resulting in a gear ratio of 1:1 between the EM and ICE. Component 7 is the EM of the setup, which is a Parker GVM210-150P6 PMAC EM that produces a peak torque of 256.8 Nm with a rated shaft output power of 66.4 kW. The Parker EM was chosen because it is representative of an EM that would be found in a HEV powertrain, and it also allows for a 1:1 gear ratio to be used for the experiments due to its large output torque. The EM output shaft is connected to an AISI 4340 steel shaft through the appropriate spline connection. Component 8 of Figure 5-10 is an inertial element, machined from 6061-T6 aluminum, used to simulate the connections between the ICE and downstream powertrain components. A detailed view of

the coupling between the output shafts of the EM and ICE is given in Figure 5-11b along with the coupling between the shafts and connected components.

The Parker EM is controlled through a Sevcon Gen4 Size 8 inverter powered by a bidirectional, direct-to-mains power supply produced by Elmo MC. A 480 VAC three-phase feed is fed through a transformer to stepdown the voltage to the level required for the power supply to provide an adequate current at a voltage in range for the inverter. The inverter supplies power to the Parker EM though phase power cables and receives feedback for control purposes from the motor, which can be observed in Figure 5-11a. The proprietary Sevcon DVT software and IXXAT USB-to-CAN cable are used to make changes to the device configuration file for the inverter. A Vector CANcaseXL Log is then used alongside their CANoe software to specify the required torque profile from the EM for execution of the TSCS strategy through Controller Area Network (CAN) messaging.

Figure 5-12 provides a schematic diagram of the connections of the experimental apparatus components and flow of signals to apply the TSCS input from the Parker EM to the Kohler ICE. MATLAB is used to generate the torque input specified by the TSCS strategy as a .vgf file that is read by the CANoe software and translated into a CAN message, a receive process data object (RPDO). The Vector CANcaseXL Log is used to transmit the CAN message to the Sevcon inverter from a laptop computer, which then supplies the required current and voltage to the Parker EM for application of the TSCS torque input to the Kohler ICE for restart. In addition, the Parker EM provides CAN messages back to the inverter that can be sent back to a laptop for processing as a .blf file.

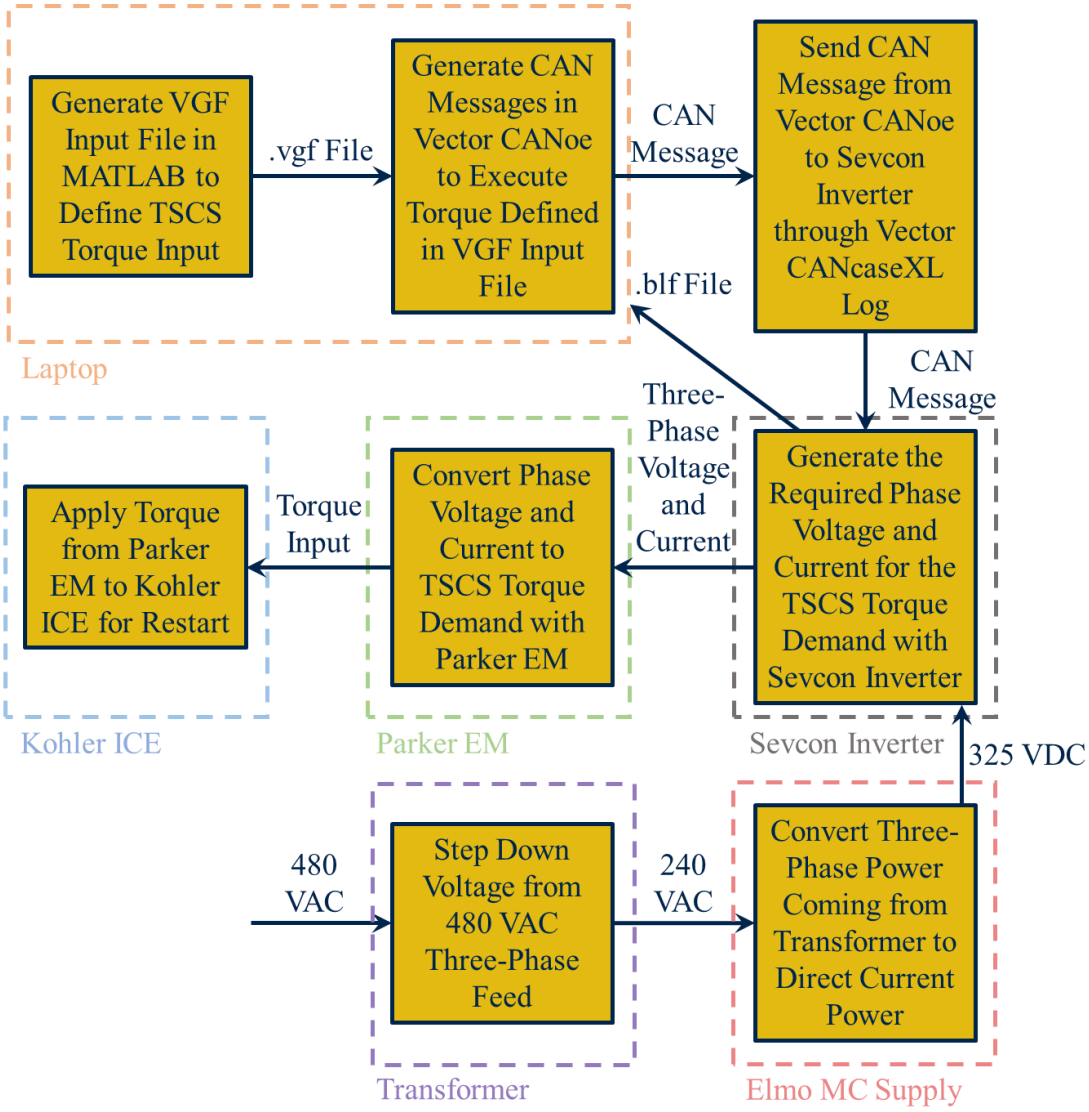

Figure 5-12 – Schematic diagram for the application of TSCS input torque from the Parker EM to the Kohler ICE.

Figure 5-13 shows the interactive generator (IG) in Vector CANoe. In this window, the user can define the RPDOs being sent to the Sevcon inverter. With these RPDOs, the inverter is placed in a traction state with the *controlword* signal, the maximum speed for the EM is set with the *Max_motor_speed* signal, and the EM torque is defined with the

Target_torque signal. These signals are defined in the area highlighted by the yellow rectangle in Figure 5-13.

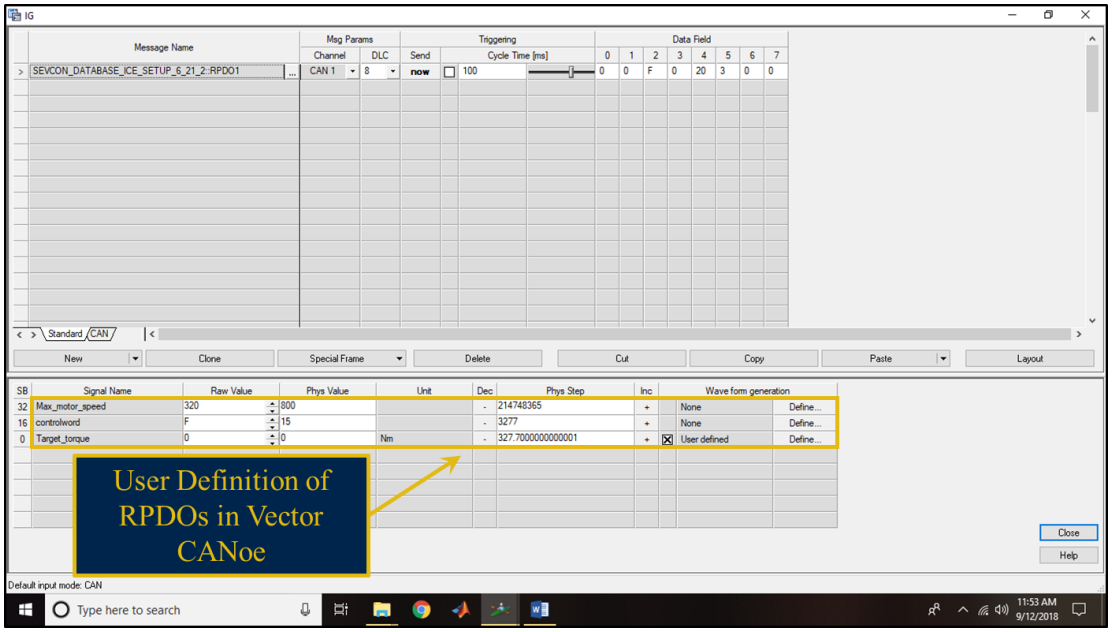

Figure 5-13 –IG in Vector CANoe for CAN signal definition for the Parker EM of the experimental apparatus.

To define a time-dependent torque signal for the EM, such as a complete TSCS input, a user-defined wave form can be used. Figure 5-14 provides the definition of a time-dependent torque signal, a step in the example, in the Vector CANoe environment. When the user-defined wave form option is selected within the blue rectangle of Figure 5-14, the window highlighted by the yellow rectangle will allow for the RPDO representing the EM torque to be defined as a time series within the window or alternatively through an external .vgf file. A MATLAB script is used to generate the required .vgf file to represent a complete TSCS input for the experimental apparatus system.

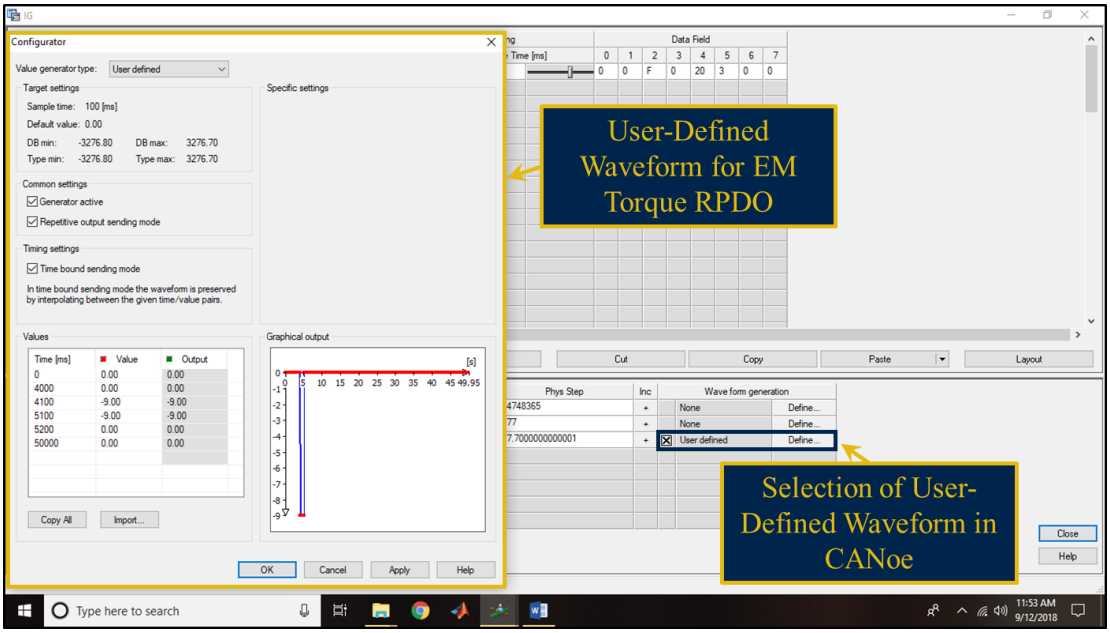

Figure 5-14 – Definition of a user-defined waveform for EM torque RPDO in Vector CANoe.

Additionally, the Vector CANoe software alongside the CANcase XL Log allows for transmit process data objects (TPDOs) to be observed and stored as a .blf file. During the operation of the Parker EM with the CANoe software, TPDOs can be observed in the trace window of CANoe, which is shown in the yellow rectangle of Figure 5-15. The TPDOs that are observed during operation are also saved to the laptop running CANoe for analysis in the stored .blf file.

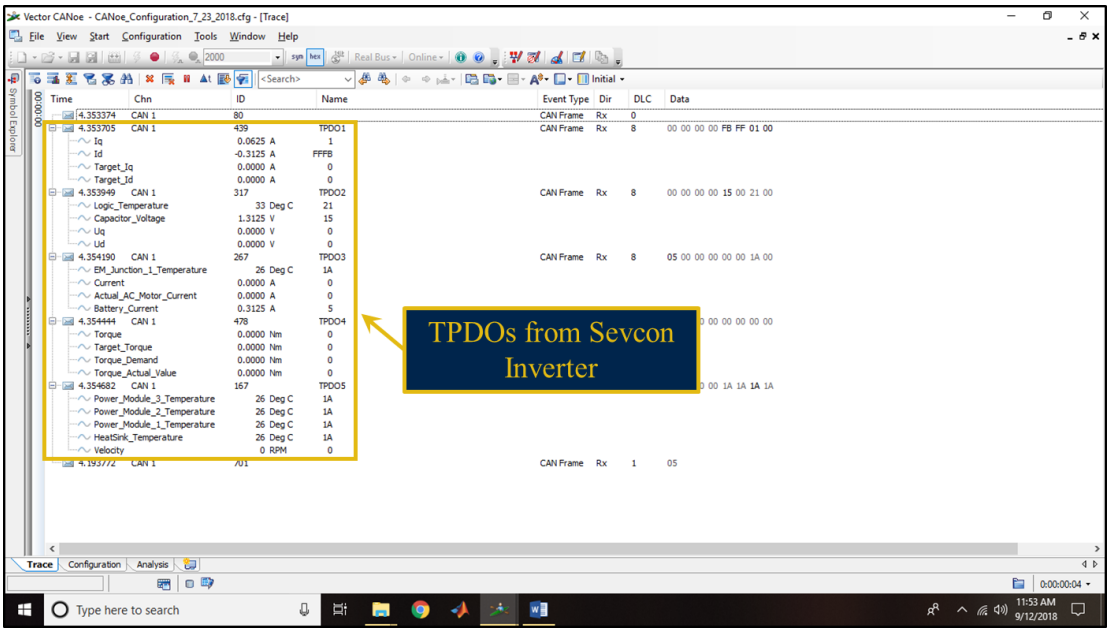

Figure 5-15 – Trace of TPDOs from Sevcon inverter in Vector CANoe.

Component 4 in Figure 5-10 denotes the arm to which an RLS LM10 incremental encoder readhead is attached to read an RLS radial magnetic ring. The LM10 encoder readhead has an angle resolution of 0.01179° and is attached to a National Instruments (NI) 9401 module in a cDAQ-9174 chassis through a NI 9924 terminal block, which allows for the undesirable oscillations of the powertrain to be captured in the data. NI LabVIEW and SignalExpress is then used to process the signals from the RLS readhead. Additionally, there is also a resolver in the Parker EM allowing for measurement of the angular velocity within the powertrain. The angle resolution for this resolver is 0.01667°.

In addition to processing the encoder signals, a NI 9215 module is used in the cDAQ-9174 to process the output of a laser doppler vibrometer (LDV), Polytec PDV 100, used to measure the motion of the frame. Figure 5-16 shows the Polytec LDV setup to measure the frame motion. The LDV is used to measure the vertical translational velocity

of the EM mounting plate, the steel plate welded to the apparatus frame used to mount the Parker EM, to observe the impact of TSCS on the motion of the frame of the apparatus. An example measurement point on the EM mounting plate can be seen in Figure 5-16. Additionally, the LDV alongside a PCB Piezotronics 086C03 impact hammer are used to experimentally identify the vibration modes of the frame for the command shaping component of the TSCS strategy in place of the lumped-parameter model governing the frame motion.

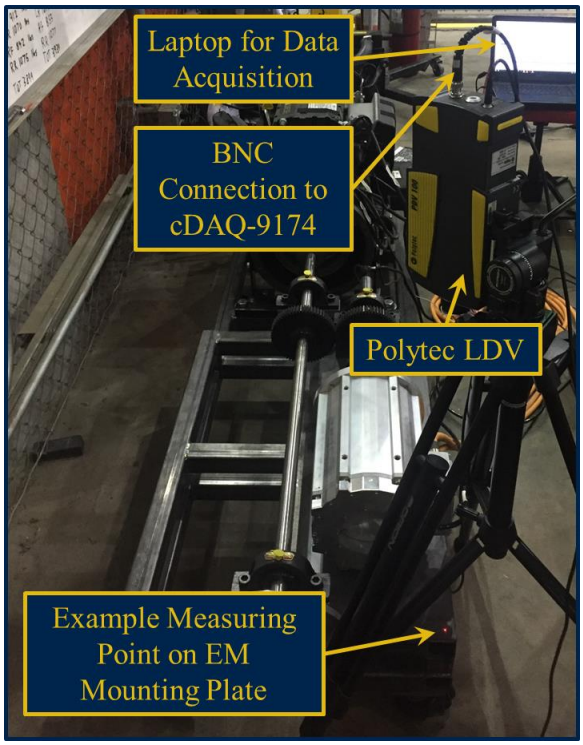

Figure 5-16 – Polytec PDV 100 setup to measure frame motion of the experimental apparatus.

5.3 Measurements from the experimental apparatus

5.3.1 Measurements from the apparatus of the powertrain motion to observe internal combustion engine nonlinear behavior

To verify the integrity of the setup and data acquisition components, the response of the crankshaft for a standard restart and shutdown were recorded at 40 samples/second. Figure 5-17 shows the response of the three-cylinder crankshaft during restart with the 12 V starter motor of the engine. The behavior of the crankshaft is qualitatively comparable to the predicted response of the lumped-parameter models governed by Eqs. (5.1) and (5.5). On average, the oscillations in the transient and steady-state regions for the simulations are within 13.65% and 20.80% of the experimental response, respectively. Observing Figure 5-17, the oscillations in the crankshaft of the response imply possible benefit from the application of the TSCS strategy.

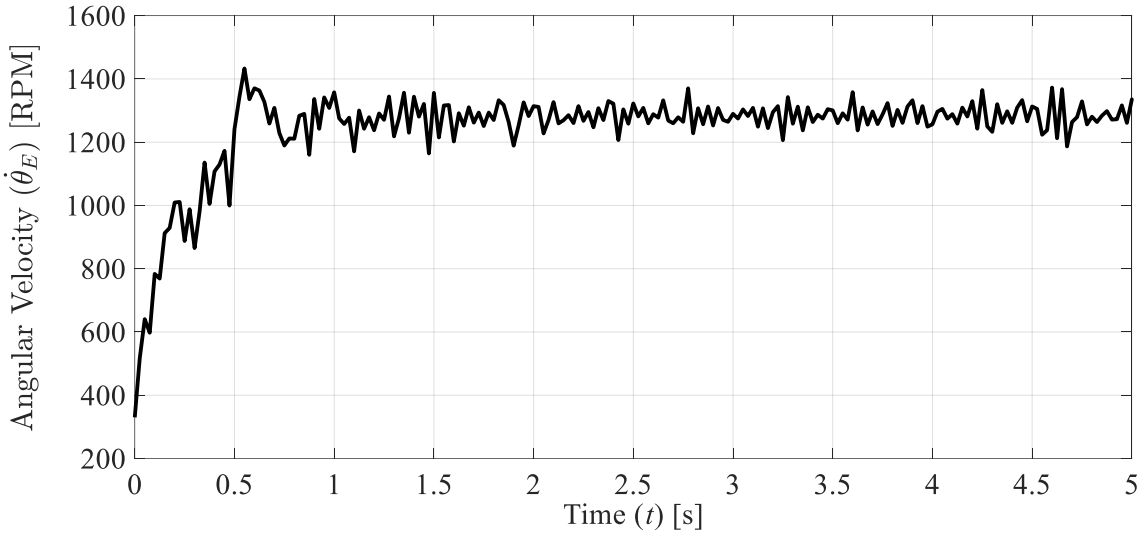

Figure 5-17 – Experimental response of the three-cylinder ICE crankshaft during restart with a 12 V starter motor.

Additionally, the response of the apparatus frame to an unshaped input for ICE restart results in an average root mean square (RMS) acceleration magnitude of 3.06 m/s^2. This value can be compared to studies that have been completed on vibration and human comfort to determine the possible impact of this event on a driver. Forthergill and Griffin developed a semantic scale based on seated subjects being exposed to 10 Hz sinusoidal vibrations, which can be observed in Table 5-1 [92, 93]. Comparing the response of the apparatus frame to an ICE restart event to the scale shows that the motion transmitted to the frame would be perceived as very uncomfortable by a driver highlighting the need for TSCS.

Table 5-1 – Semantic scale developed for a seated subject exposed to a 10 Hz sinusoidal vibration of varying magnitude [92, 93].

Scale	Mean Magnitude [m/s^2 RMS]
Very uncomfortable	2.7
Uncomfortable	1.8
Mildly uncomfortable	1.1
Noticeable, but no uncomfortable	0.4

Figure 5-18 depicts the oscillations of the crankshaft during shutdown from idle. Unlike restart, oscillations between negative and positive angular velocity occur, suggesting greater drivability issues than experienced during restart. Taken together, Figure 5-17 and Figure 5-18 also show that the designed experimental apparatus can capture the nonlinear dynamics of the ICE during both restart and shutdown.

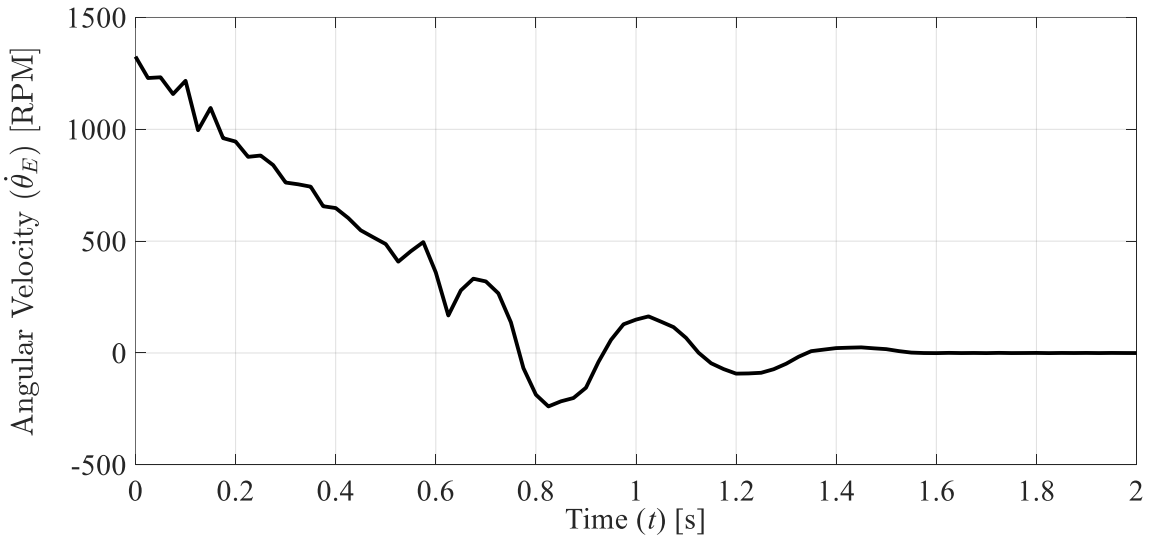

Figure 5-18 – Experimental response of the three-cylinder ICE crankshaft during shutdown.

To test the repeatability of the data collection, five tests were conducted in which the engine was run until fully warmed and then shutdown from idle. Figure 5-19 presents

the results of these tests. Oscillations between positive and negative angular velocities occurred in each test at a consistent period and amplitude. Consistent behavior at the crankshaft of the ICE suggests a strong likelihood that a feedforward control technique can mitigate undesirable oscillations. Comparing all subsequent tests with the initial measurement of the crankshaft velocity profile during shutdown, it can be calculated that the maximum normalized mean square error for these cases is 3.6%, which implies consistent crankshaft behavior since a value of 0% represents a perfect match between cases.

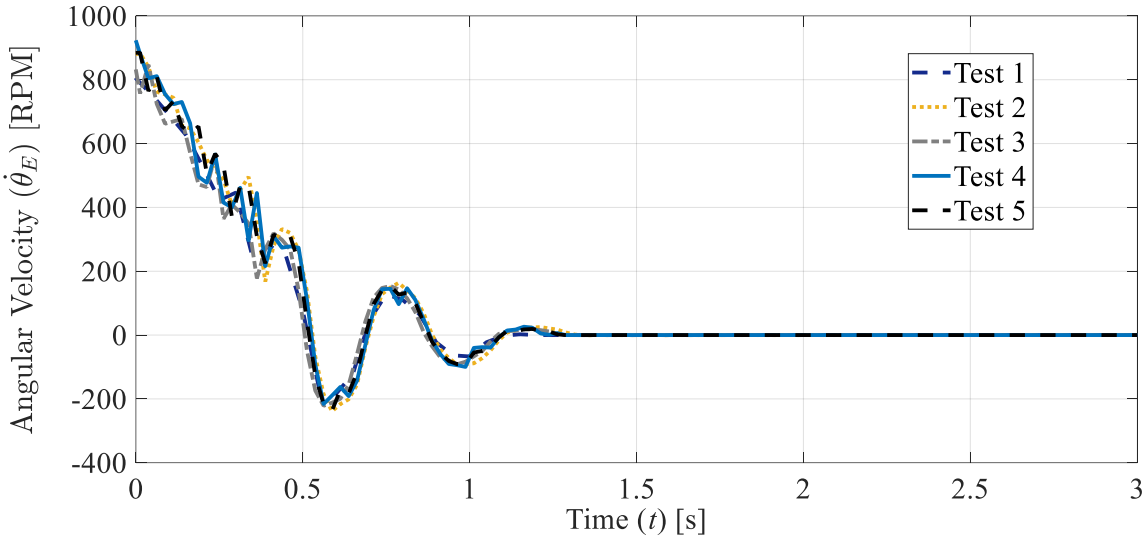

Figure 5-19 – Repeatability of the experimental crankshaft response of the three-cylinder ICE during shutdown.

To further observe the repeatability of measurements with the apparatus, the EM was used to apply a small step input torque to the ICE, which was placed at a consistent initial condition of 360° for the crank angle. The datum used to set the initial condition was top dead center (TDC) of the cylinder closest to the bellhousing of the ICE during its

compression stroke. Figure 5-20 shows the crankshaft velocity profile for five of the repeatability tests conducted to verify initial conditions and consistency of crankshaft behavior. Using the first test as a basis for comparison, the maximum normalized mean square error for subsequent cases is 4.9%, further implying consistency in crankshaft behavior as well as the repeatability of setting the initial position condition.

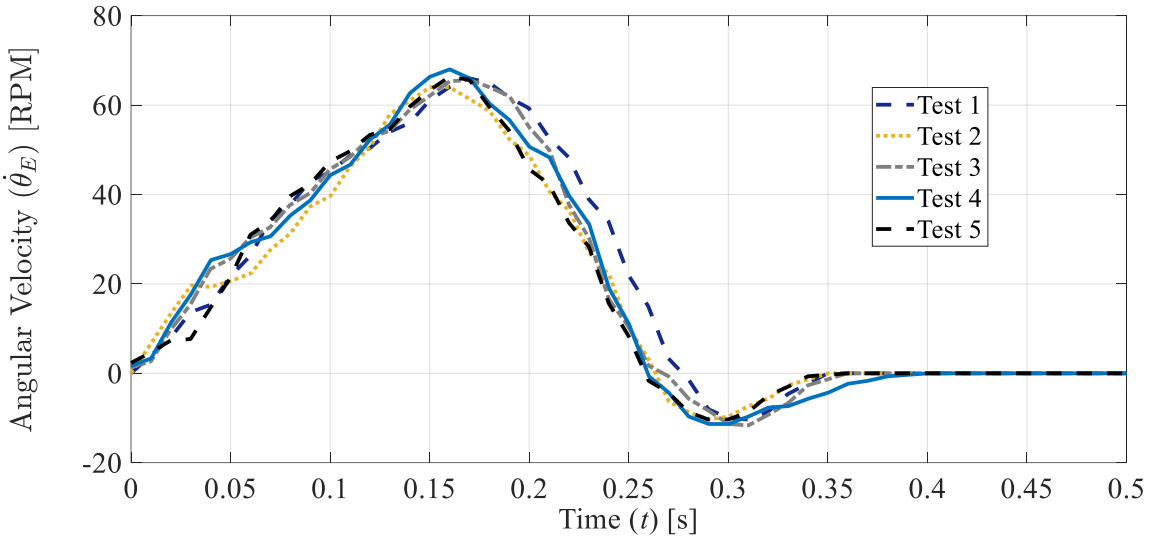

Figure 5-20 – Repeatability of the initial conditions and experimental crankshaft response of the three-cylinder ICE during a small step input torque from the EM.

Figure 5-21 provides the velocity profile during the startup of the three-cylinder ICE with an unshaped T_0 defined as a step torque from the EM applied with the crankshaft set at an initial position of 360°. The response of the crankshaft is relatively consistent for these tests. Again, using the first test as a basis for comparison, the largest deviation observed resulted in a normalized mean square error for subsequent cases of 4.7%, which signifies the consistency of the tests. There is some variation in the engine response as it

reaches idle, which can be observed in Figure 5-21. This variation arises due to changes in what point of the crankshaft rotation the application of the EM torque ceases.

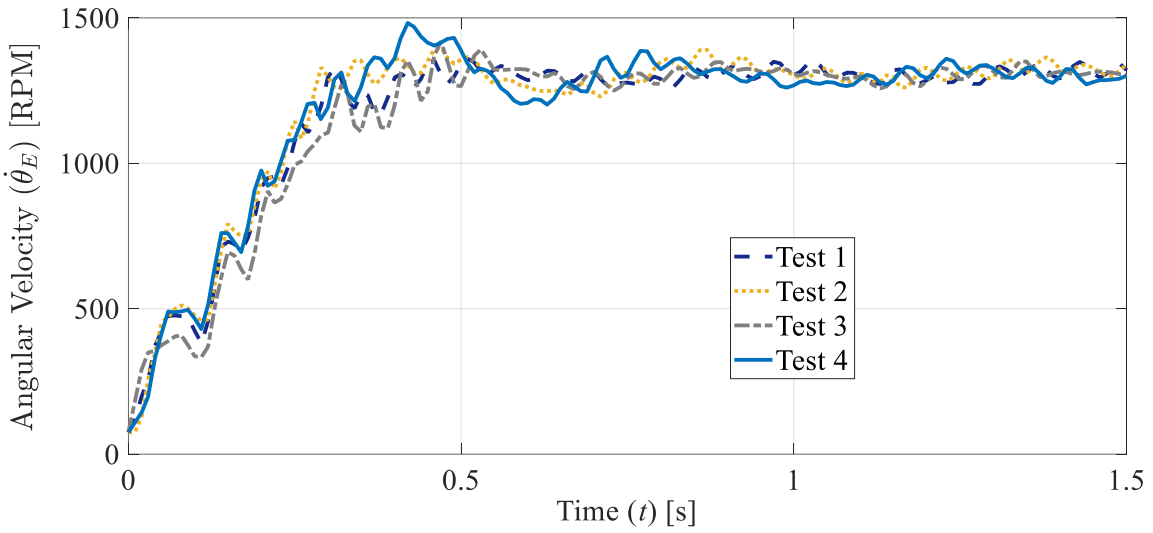

Figure 5-21 – Repeatability of undesirable vibrations during the restart response of the three-cylinder ICE crankshaft.

5.3.2 Measurements of the frame motion of the apparatus to identify vibration modes of the apparatus

Additionally, a vibration mode analysis was conducted on the experimental apparatus to determine the frame modes as well as test the data collection capability of the apparatus. Figure 5-22 provides a representative sample of the frequency response data obtained through excitation with an impact hammer and data collection in LabVIEW. The provided plot displays the magnitude of the frequency response function (FRF) of the EM mounting plate velocity with respect to the impact hammer force. The frame was excited in various locations with the impact hammer to obtain resonant frequencies below 100 Hz, which are tabulated in Appendix B in Table B-5. Measurements with the Polytec LDV

were taken at various points on the EM mounting plate, an example measurement point is shown in Figure 5-16. These frequencies can be used in the command shaping process to mitigate the excitation of several of the corresponding vibration modes of the apparatus. The focus of vibration reduction and mitigation is for frequencies under 100 Hz, since lower frequencies are more disturbing to consumers, especially frequencies around 10 Hz [92-94].

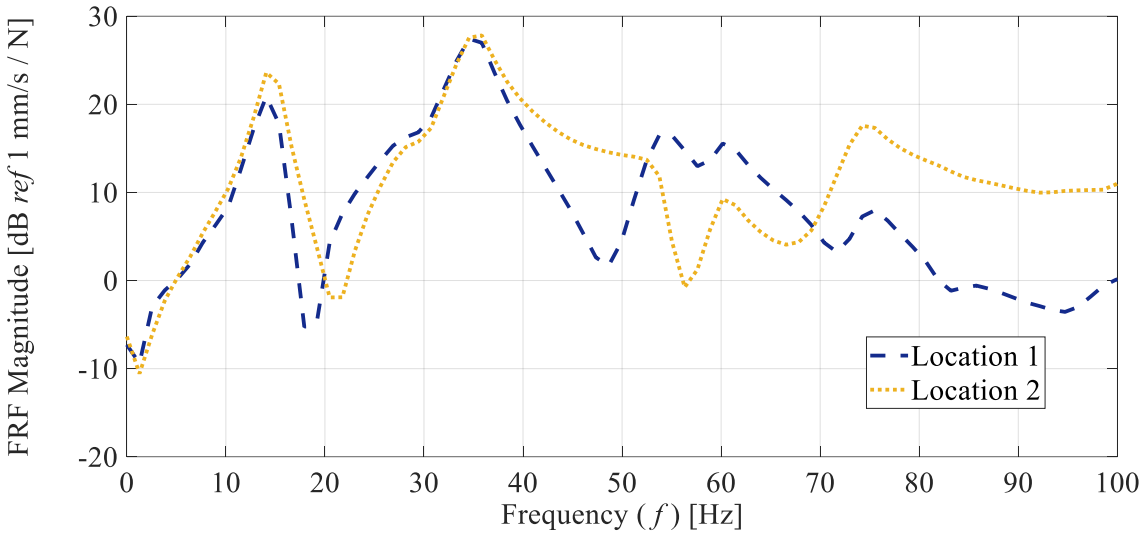

Figure 5-22 – Magnitude of the frequency response function of the frame during impact hammer tests of the experimental apparatus.

The LDV was also used to measure the EM mounting plate velocity during an application of an input torque from the EM to verify the vibration modes measured through impact hammer testing and determine which frequencies are dominant in the EM mounting plate response during ICE restart. Figure 5-23 shows the Fourier transform of the EM mounting plate velocity response to a step torque input from the EM to the ICE crankshaft. Observing this plot, the two dominant vibration modes requiring mitigation are at 14 Hz

and 35 Hz. Additionally, the dominant vibration mode frequencies in the frequency content of the EM mounting plate of the apparatus agree with the impact hammer testing results.

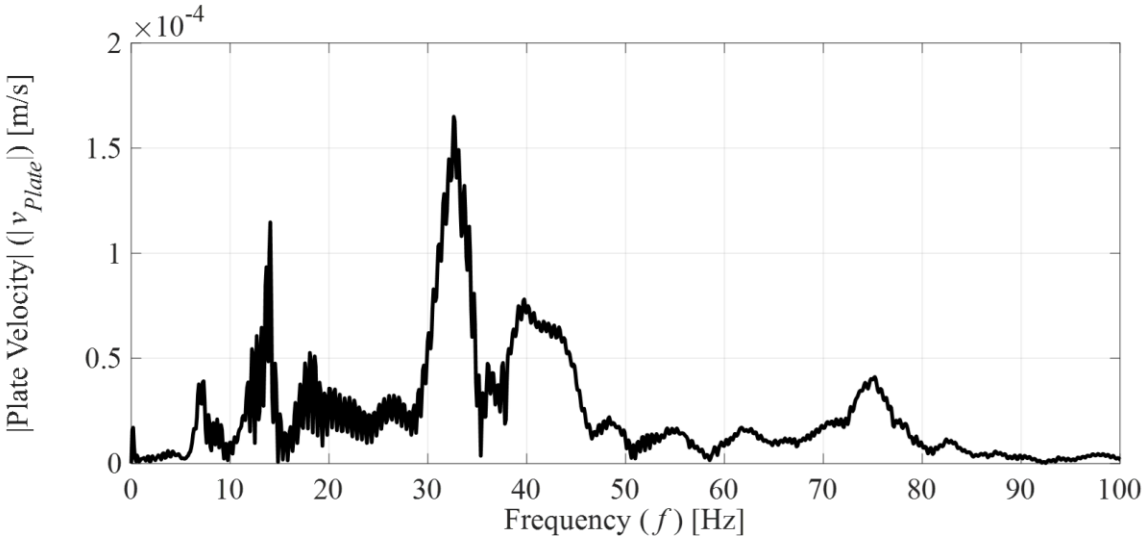

Figure 5-23 – Fourier transform of the velocity response of the EM mounting plate during excitation with the EM of the apparatus.

5.4 Validation of two-scale command shaping applied to internal combustion engine restart

The first step in developing an effective TSCS input is verifying the engine parameters used based on the crankshaft experimental response. A step EM torque was applied to the ICE, which provided the measured velocity profiles, greyscale lines, shown in Figure 5-24. Several techniques can be used to reduce the effect of uncertain parameters on the efficacy of TSCS, such as EKF or RLS [90].

When improving the definition of these parameters offline with limited knowledge *a priori*, existing techniques and programs can be leveraged, such as the System

Identification and Optimization Toolboxes in MATLAB. A nonlinear grey-box model can be created representing the lumped-parameter powertrain model introduced in Figure 5-1 and then solved through the Trust-Region Reflective Newton method of nonlinear least-squares. Through this process, uncertain parameters, such as the equivalent polar moment of inertia of the ICE crankshaft and counterbalances as well as the powertrain stiffness and damping values, were estimated. Using a grey-box model to update uncertain parameters results in the modeled response, solid yellow line, in Figure 5-24. The powertrain model results in a maximum normalized mean square error of 6.9% when compared to the experimental cases shown, which is acceptable for the relatively simple model being used for the complex physical system of the powertrain. The mismatch observed in Figure 5-24 will lead to a mismatch between the actual nonlinearities of the ICE and the T_1 term used to mitigate them, which likely reduces the efficacy of TSCS. The deviation in the response arises due to the lack of *a priori* knowledge of the ICE as well as the inability to remove compression in the cylinders of the engine, decreasing the ability to isolate the analysis of the friction and inertial terms representing the system.

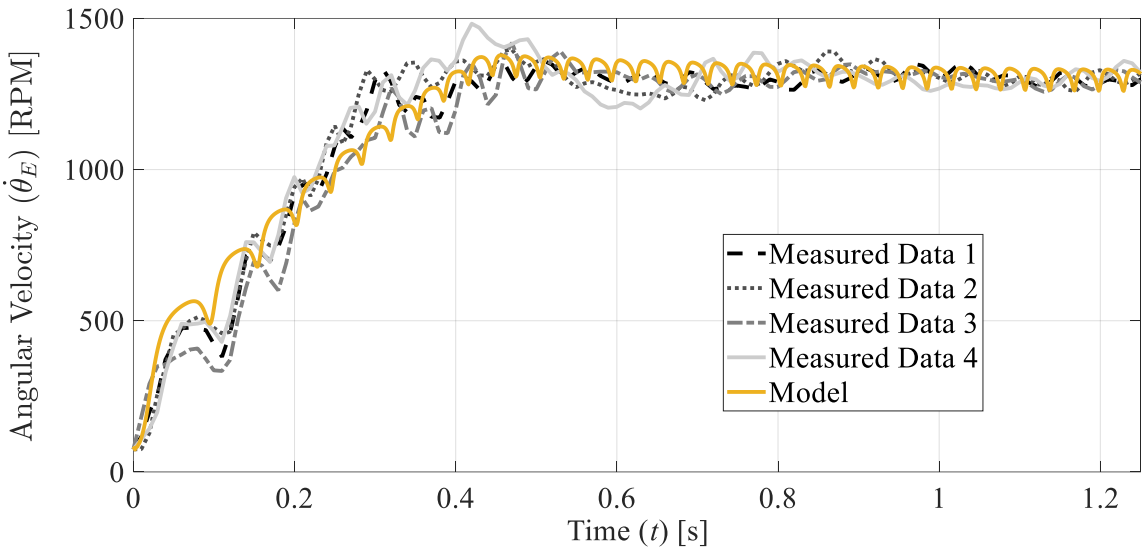

Figure 5-24 – Experimental response of the engine crankshaft to a step input torque from the EM compared to a refined experimental model.

With the updated model, the post-T_1 input can be verified for the Kohler ICE, which is a combination of the initial unshaped step input and the nonlinear torque component, T_1, provided in Eq. (5.7). Introducing T_1 creates a signal that has a maximum value which is 21.3% greater than the original signal with a maximum power requirement that is 19.1% greater. Figure 5-25 provides the original and post-T_1 inputs for comparison. The Parker EM and power supply can handle this demand for the powertrain of the apparatus.

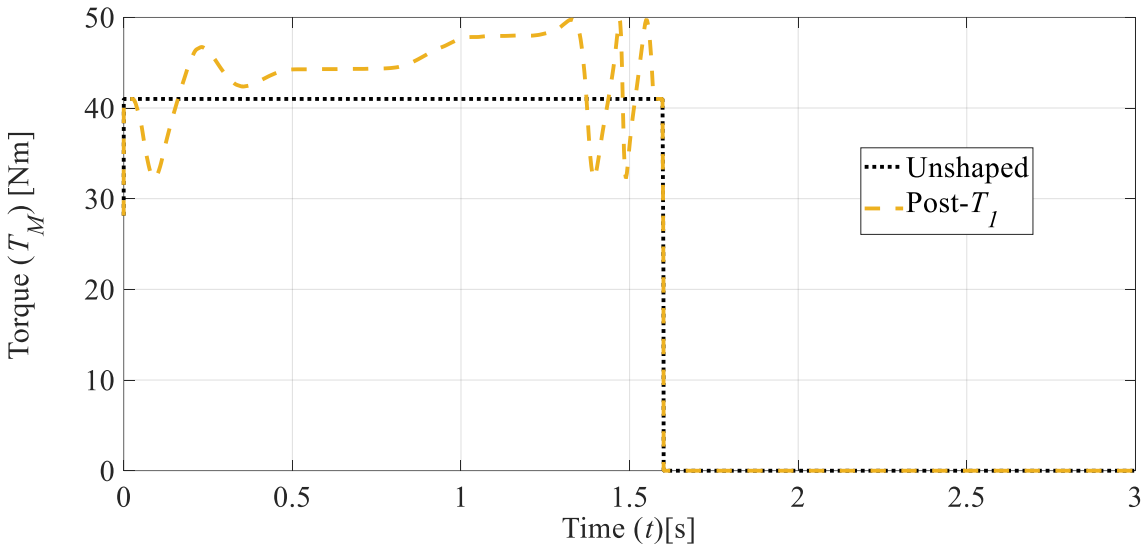

Figure 5-25 – Experimental unshaped and post-T_1 inputs for the ICE crankshaft based on the refined model of the ICE for duration of TSCS application.

The post-T_1 input mitigates the undesirable frequency content of the crankshaft response. In place of observing the crankshaft response of the ICE with a Fourier transform, a wavelet transform can be used to create a magnitude scalogram, a plot of a signal's wavelet transform, to observe the frequency content as a function of time, which allows one to observe the effectiveness of the post-T_1 input for mitigating the nonlinear response of the ICE crankshaft. Figure 5-26a and Figure 5-26b present the scalograms of the crankshaft response to unshaped and post-T_1 inputs with an analytical Morse wavelet acting as the mother wavelet, respectively. The vertical axis of these plots uses a logarithmic scale, whereas the horizontal axis is linear.

Observing the plots, the post-T_1 input significantly reduces the time-dependent frequency content signifying a reduction in the nonlinearities of the crankshaft response. There is a reduction across the frequency spectrum under 100 Hz, especially in the low

frequency content occurring in the first 0.5 s of the response, which is where the peak low frequency content occurs. The post-T_1 input decreases the peak frequency content by 33.9% throughout the ICE restart region. Additionally, the total energy in the crankshaft response is reduced by 29.5% in this region. Although there were deviations in the model used in the development of the T_1 term, the post-T_1 input can reduce the frequency content of the crankshaft response without application of the command shaping process.

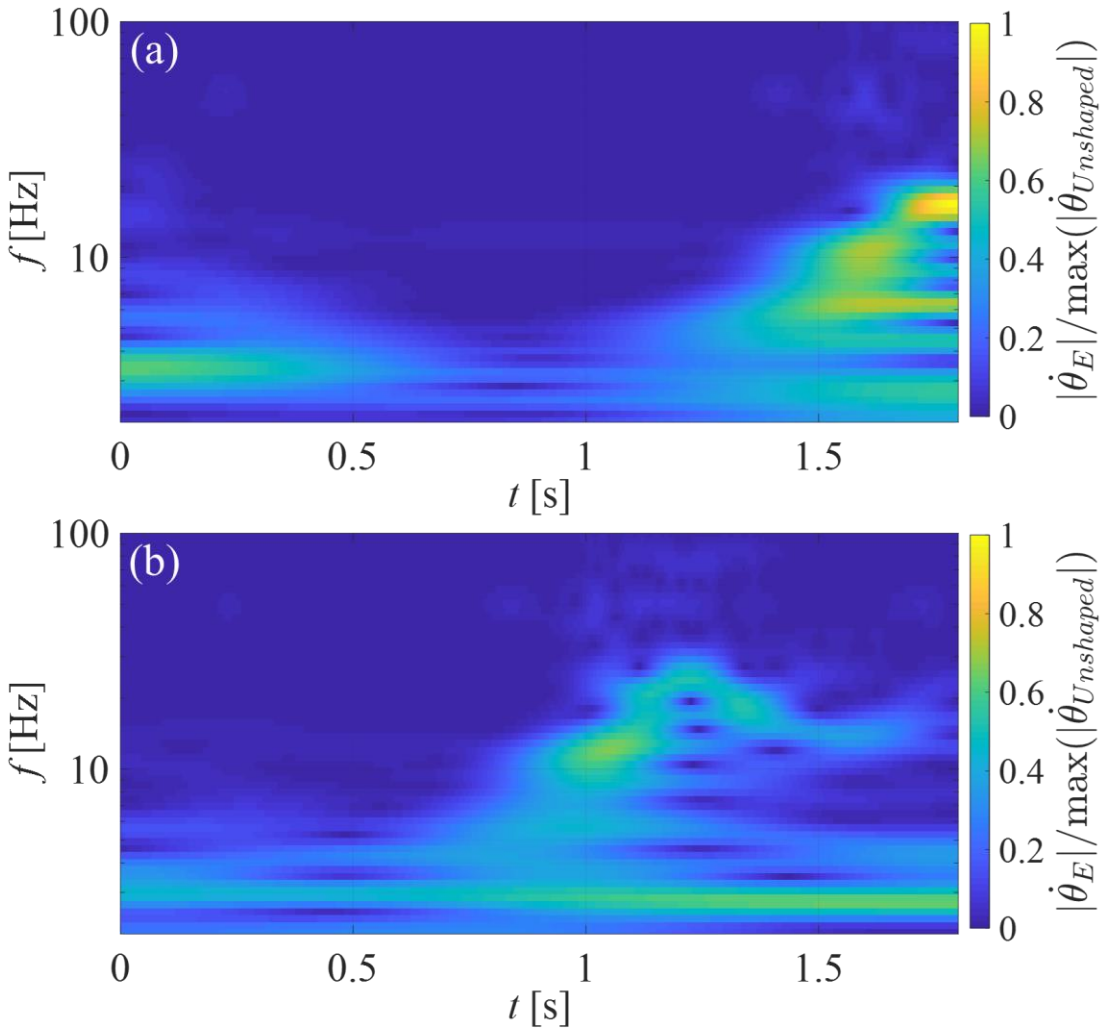

Figure 5-26 – Wavelet transform of the crankshaft response from (a) unshaped and (b) post-T_1 inputs.

T_1 is the first of two torque components required for the complete TSCS input given in Eq. (5.6), the other component, $T_{0_{Shaped}}$, is defined through a command shaping process. To determine which shaping process is the most effective, several shaping strategies were compared using a small step torque applied to the ICE. Figure 5-27 and Figure 5-28 show the resulting frequency content of the EM mounting plate. Figure 5-27 compares the ZV

shaping strategy to the two robust methods introduced, ZVD and EI, in the mitigation of the second vibration mode, denoted as M2 and located at 14 Hz.

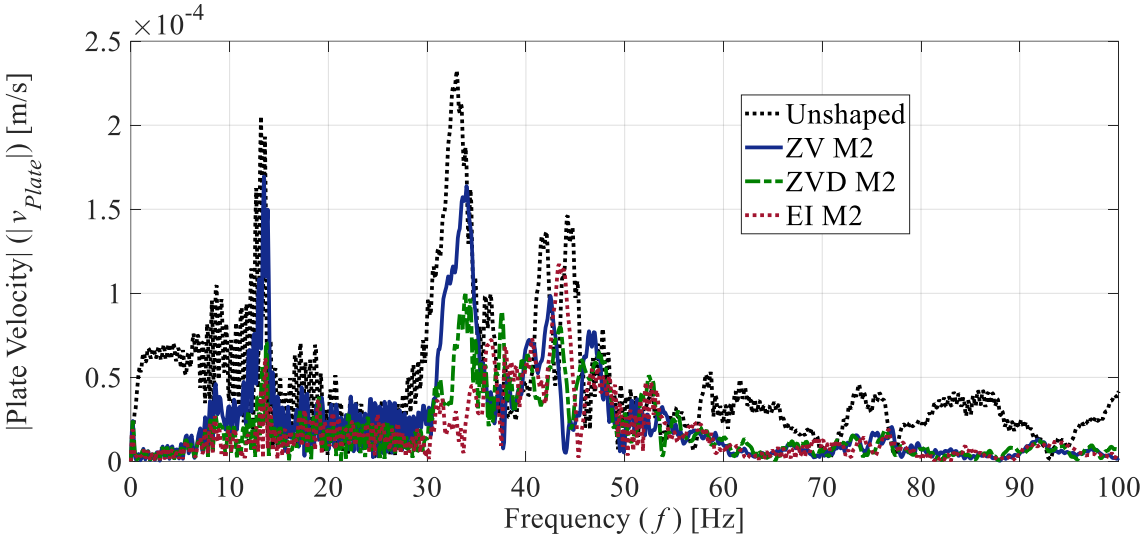

Figure 5-27 – Fourier transform of the EM mounting plate response to observe the impact of robust command shaping strategies on the mitigation of undesirable vibrations at the plate of the apparatus due to a step input.

Table 5-2 lists the reduction of the vibration amplitude of the first four dominant vibration modes, which are located at 6.3 Hz (Mode 1 [M1]), 14 Hz (Mode 2 [M2]), 35 Hz (Mode 3 [M3]), and 44 Hz (Mode 4 [M4]), for each strategy. The EI input shaping process reduces the effect of the dominant vibration modes the most with a peak reduction of 70.0% and 68.9% for modes 2 and 3, respectively. These reductions are significant since humans can perceive a peak magnitude change of 9.5% to 20.3% in a sinusoidal vibration, depending on the frequency of the vibrations [95, 96].

Table 5-2 – Vibration amplitude reduction with various command shaping methods applied to vibration mode 2 of the experimental apparatus.

Method	Design Mode	M1 Reduction [%]	M2 Reduction [%]	M3 Reduction [%]	M4 Reduction [%]
ZV	14 Hz	92.7	17.4	29.6	32.7
ZVD	14 Hz	93.6	65.5	57.2	45.1
EI	14 Hz	94.1	70.0	68.9	19.8

Figure 5-28 compares the performance of an EI input shaper designed for mode 2 to a convolved EI input shaper designed for vibration modes 2 and 3. Table 5-3 provides the reduction observed at the first four vibration modes due to each shaper. Designing an EI shaper for both mode 2 and 3 increases the reduction at these two dominant vibration modes by 12.1% and 16.3%, respectively. Both the EI shapers have significant impact in reducing the vibration amplitudes, but the EI input shaper designed for a single mode requires less than half the time to develop to its complete value when implemented with TSCS. Therefore, both EI shapers will be used in conjunction with the post-T_1 input to develop a complete TSCS input.

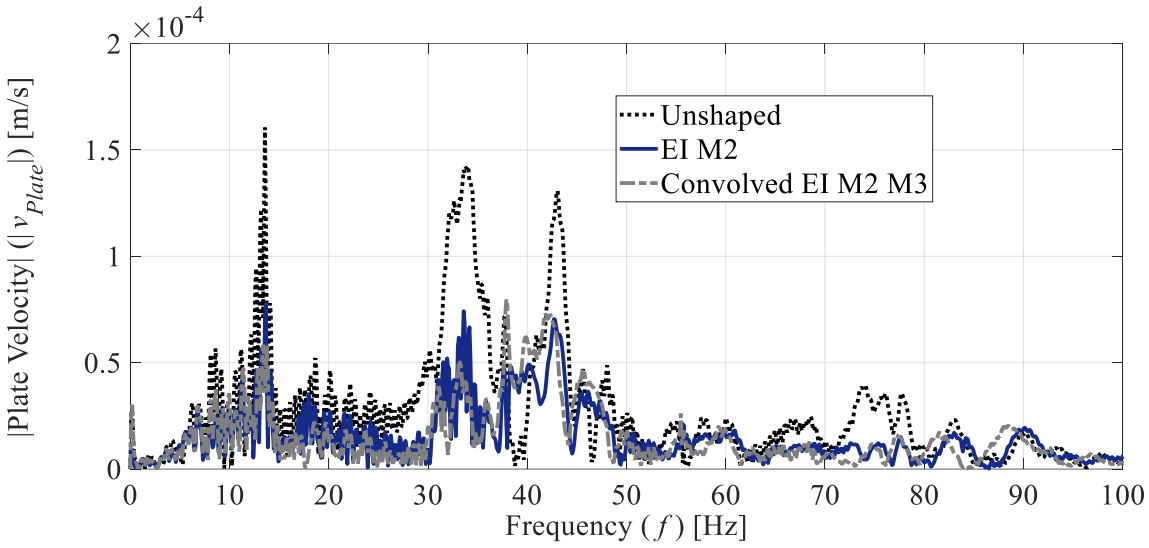

Figure 5-28 – Fourier transform of the EM mounting plate response to observe the impact of convolved input shaping on the mitigation of undesirable vibrations at the plate of the apparatus due to a step input.

Table 5-3 – Vibration amplitude reduction comparison between EI input shaping for vibration mode 2 and convolved EI input shaping for vibration modes 2 and 3 of the experimental apparatus.

Method	Design Mode	M1 Reduction [%]	M2 Reduction [%]	M3 Reduction [%]	M4 Reduction [%]
EI	14 Hz	37.0	51.5	47.6	46.1
Convolved EI	14 Hz / 35 Hz	35.0	63.6	63.9	44.2

The complete TSCS input can be formed by combining either an EI input shaper for vibration mode 1 or a convolved EI shaper for vibration modes 1 and 3 with the T_1 component defined with Eq. (5.7) and the Kohler ICE parameters found in Table B-4, since vibration mode 1 becomes more dominant than mode 2 with the EM torque required for a complete restart. The Parker EM of the apparatus can follow complete TSCS inputs with the maximum normalized mean square error between the torque demand and actual torque output averaging 2.2% for the complete TSCS inputs observed. Figure 5-29 contains the

frequency content of the EM mounting plate due to the application of complete TSCS inputs compared to unshaped and post-T_1 inputs.

As expected from simulation results, the post-T_1 input does not completely mitigate the undesirable frame vibrations. Adding the single-mode EI input shaper to the post-T_1 input reduces the vibration amplitude at the first two dominant vibration modes, mode 1 and 3, by 60.5% and 47.2%, respectively. These reductions are larger than those observed for the post-T_1 input, 39.0% and 35.0% for mode 1 and 3, respectively. The reduction of the vibration amplitude of mode 3 can be pushed further by using a convolved EI input shaper with the TSCS strategy to 83.3%. Table 5-4 gives the frame vibration amplitude reductions observed with the post-T_1 and TSCS inputs.

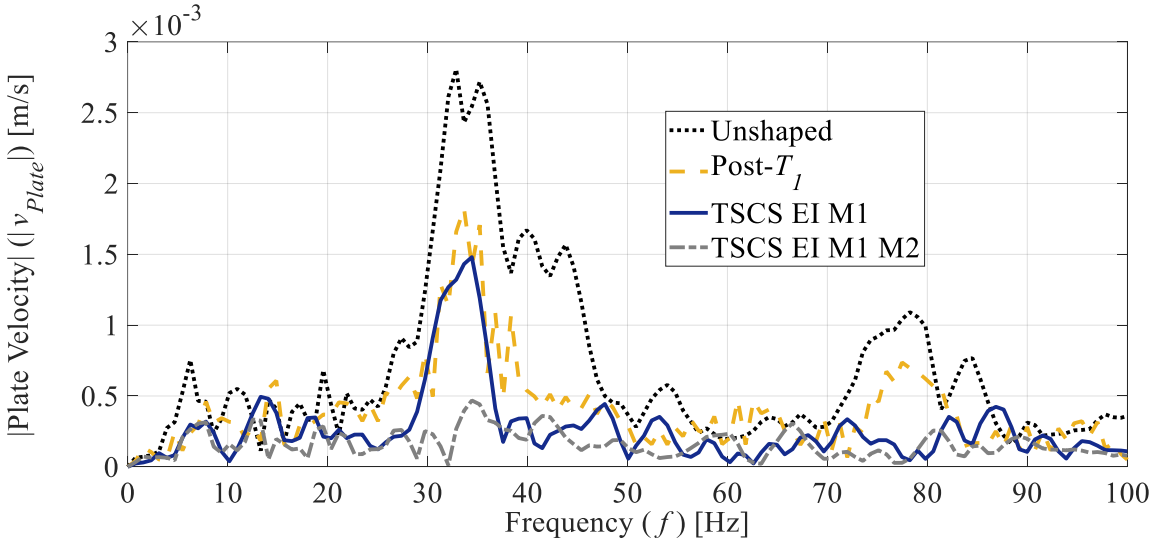

Figure 5-29 – Fourier transform of the EM mounting plate response to the unshaped, post-T_1, and TSCS inputs.

Table 5-4 – Frame vibration amplitude reduction for post-T_1 and TSCS inputs.

Method	Design Mode	M1 Reduction [%]	M2 Reduction [%]	M3 Reduction [%]	M4 Reduction [%]
Post-T_1	N/A	39.0	-10.6	35.0	67.4
TSCS - EI	6.3 Hz	60.5	10.2	47.2	71.7
TSCS - Convolved EI	6.3 Hz / 35 Hz	58.3	64.2	83.3	77.1

The TSCS input does not only mitigate the undesirable vibrations in the frame of the apparatus. As shown with the development of the post-T_1 input in Figure 5-26, the post-T_1 input significantly reduces the crankshaft frequency content around 10 Hz, which is most impactful for human comfort [92-94]. Figure 5-30 and Figure 5-31 provide the wavelet transform of the crankshaft response to unshaped, post-T_1, and TSCS inputs in the region where the frequency content is largest and focused around 10 Hz. Adding in the T_1 term alone reduces the peak frequency content by 37.1% while also making the system appear more linear due to the transient frequency content being significantly reduced, which can be observed by comparing Figure 5-30b and Figure 5-30a. In addition, the post-T_1 input reduces the total energy content in the crankshaft response by 24.6% in this region.

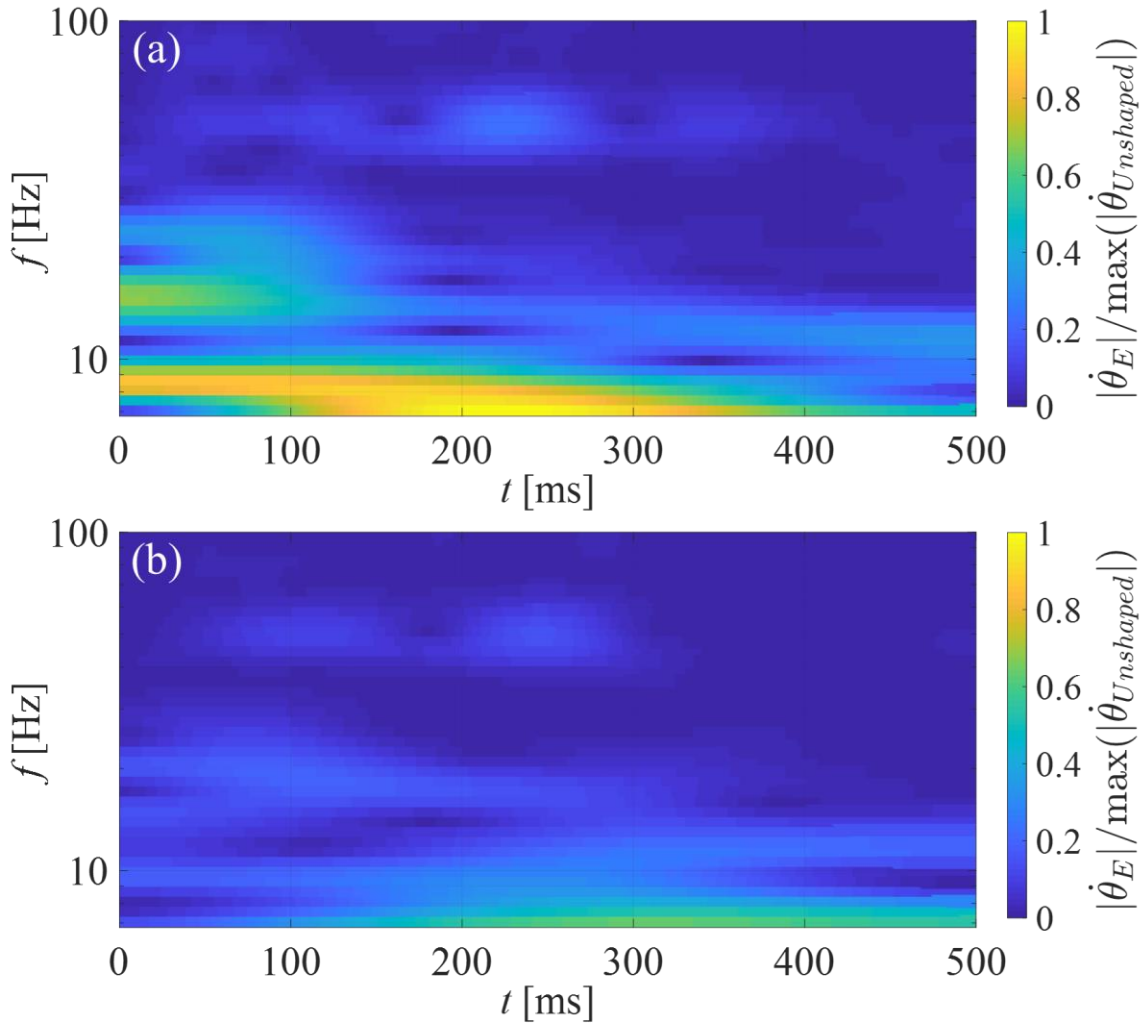

Figure 5-30 – Wavelet transform of the crankshaft response to (a) unshaped input and (b) post-T_1 input.

The frequency content is reduced even further to 46.4% and 60.0% of its original value by application of the complete TSCS input with single-mode and convolved EI input shapers, respectively. These reductions can be observed in Figure 5-31a and Figure 5-31b. Clearly the TSCS input effectively mitigates the undesirable oscillations in the crankshaft response as well as the response of the frame of the experimental apparatus despite deviations in the model used to develop the T_1 portion of the TSCS input.

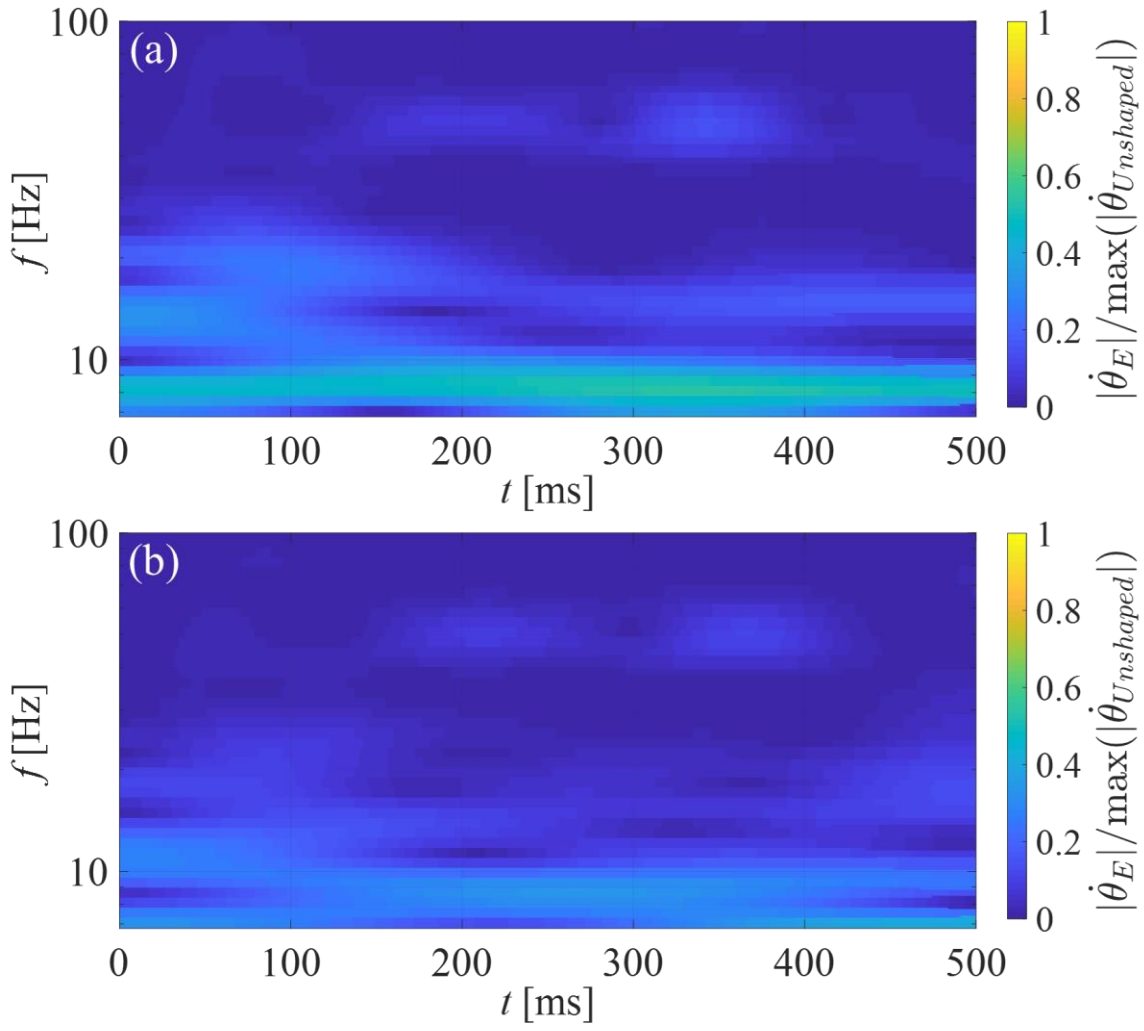

Figure 5-31 – Wavelet transform of the crankshaft response to (a) TSCS input with a single-mode EI shaper and (b) TSCS input with a convolved EI shaper.

These results also imply that the shaping portion of the TSCS strategy is not required for reduction of the undesirable vibrations in the crankshaft response, which was also observed in the simulations contained in Sections 3.3 and 5.1. However, the shaping portion of the TSCS further reduces undesirable vibrations and allows the designer to ensure that excitation of a specific frequency does not occur, as demonstrated in Figure 5-29.

5.5 Conclusions

The experimental apparatus outlined in this chapter allows for the ICE nonlinear dynamics to be observed during restart and shutdown and provides a platform to validate the TSCS strategy for ICE restart. A Parker PMAC EM is coupled through spur gears to a Kohler three-cylinder diesel engine. The motion of the powertrain is documented through an incremental encoder and the internal resolver of the EM. An LDV provides a measure of the vibrations of the frame of the apparatus. Isolation of the simple powertrain on a fixed frame provides a controlled environment in which to test TSCS, while maintaining a representation of a modern HEV powertrain. Using the equipped sensors, the apparatus can capture the undesirable oscillations in the powertrain during restart and shutdown. Applying TSCS to the Kohler ICE proves the strategy is effective in removing the undesirable vibrations in the powertrain and frame of the setup, even with deviations in the model used to develop the T_1 term. Robust command shaping strategies further extend the application and improve the efficacy of TSCS by reducing the impact of uncertainties in the vibration modes as well as increasing the frequency range mitigated through the command shaping process. In addition, the apparatus can also be used to conduct investigations on the applicability of TSCS to ICE shutdown as well as the possible improvements from higher fidelity ICE models and improved system identification.

CHAPTER 6. CONCLUDING REMARKS

6.1 Summary

An effective feedforward control methodology, TSCS, was introduced for nonlinear systems. TSCS was applied to several forms of the Duffing equation to directly compare it to existing feedforward control methodologies. In this comparison, it was shown that TSCS outperformed traditional feed forward control methodologies that require some form of linearization to apply them to a nonlinear system. The advantage of TSCS arises from the utilization of scale separation and application of the command shaping techniques to a linear system, which avoids the occurrence of large residual vibrations observed in the direction application of traditional techniques with large nonlinearities or input amplitudes present.

In addition, the Duffing oscillator was used to explore the impact of variations in system parameters and vibration modes. To alleviate issues arising from these variations, robust input shaping and extended Kalman filtering were introduced in conjunction with TSCS to mitigate residual vibrations arising from misidentification of vibration modes of the system along with mismatches between the assumed and actual system parameters. Additionally, TSCS was compared directly to feedback control methodologies, including feedback linearization, as applied to a Duffing oscillator with quadratic and cubic nonlinearities.

Once TSCS was proven to be an effective feedforward control methodology for nonlinear systems, it was applied to the problem of ICE restart. Simulation results presented for the TSCS strategy suggested a technique that effectively mitigated powertrain and chassis vibrations associated with reduced drivability, even in the existence of small to moderate uncertainty in system parameters. Compared to other methods to mitigate vibrations during ICE restart, TSCS benefits from being able to leverage existing hardware without a large cost, especially in HEVs where powerful EMs are already equipped in the powertrain.

Implementing TSCS on a physical vehicle will require robustness to inaccuracies in the vibration mode definitions of the vehicle as well as variations in engine parameters. To alleviate these possible issues, parameter estimation techniques, such as RLS and EKF, were introduced to estimate uncertain engine parameters, like the friction coefficients or the polar moment of inertia of the crankshaft and counterbalances. RLS provides a simple technique that can be used if the ICE geometry is accurately defined and the output torque from the engine is measured. If these requirements cannot be achieved, the EKF algorithm can be used when only the angular position and velocity are measured. In addition, robust command shaping was shown to mitigate the effect of inaccuracies in the specification of the vibration modes of the system. Parameter estimation techniques and robust command shaping broaden the applicability of TSCS.

In addition to ICE start/restart, TSCS can also be applied to mitigate the undesirable oscillations observed in the powertrain and chassis of a vehicle during ICE shutdown. Through the application of a rectangular torque profile during shutdown, TSCS can be

applied to mitigate undesirable oscillations during shutdown. The choice of the duration and amplitude of the initial torque profile affects the shutdown rate and efficacy of TSCS. Robust command shaping methods and parameter estimation techniques are still valid for mitigating the impact of uncertainties in system parameters as well as vibration modes of the system.

Finally, an experimental apparatus was developed to validate the TSCS strategy for ICE restart. The apparatus consists of a Kohler three-cylinder diesel engine coupled to a Parker PMAC EM on a stationary frame in a ventilated test cell. A Sevcon inverter is used to control the EM through the CANoe software environment, which allows for logging of CAN signals from the EM and onboard resolver. In addition to the CAN signals from the EM, an incremental encoder and LDV are also used to record the motion of the ICE and frame of the apparatus. Isolating this simple powertrain on a fixed frame supplies a controlled test environment to validate TSCS, while simulating a modern HEV powertrain. Through testing with the apparatus, TSCS was validated for a physical system.

6.2 Research contributions

The work presented in this dissertation delivers the following original contributions:

- TSCS has been introduced for feedforward control of nonlinear systems
    - The TSCS strategy outperforms direct input shaping methods in the cases considered
- Robust command shaping mitigates vibration mode variations in the application of TSCS

- Parameter estimation techniques, such as EKF, have been shown to decrease the impact of uncertainties in system parameters
- TSCS when combined with robust command shaping and parameter estimation techniques can provide a cost-effective method for mitigating vibration-related issues during ICE restart
- TSCS has also been proven theoretically to serve as an effective method to reduce undesirable vibrations during ICE shutdown for HEVs and modern conventional powertrains equipped with an engine stop-start feature
- An experimental apparatus was developed to capture the undesirable vibrations in the powertrain and frame, representing a vehicle chassis, during ICE restart and shutdown
- TSCS was validated for ICE restart using the developed experimental apparatus

6.3 Recommendations for future work

6.3.1 Experimental verification of two-scale command shaping applied to internal combustion engine shutdown

In addition to validating TSCS applied to ICE restart, the developed experimental apparatus can be leveraged to validate TSCS for mitigation of vibration-related issues during ICE shutdown. The EM of the experimental setup can be used to apply a shaped torque profile designed with TSCS to bring the ICE from its idle angular velocity to a stationary position. With TSCS, the torque profile must be shaped during its initiation and conclusion after shutdown is completed. As stated previously, the duration and amplitude

of the unshaped rectangular profile applied to the ICE for shutdown will impact the efficacy of TSCS as well as the rate of shutdown.

6.3.2 Development of real-time parameter estimation techniques with two-scale command shaping

The parameter estimation techniques presented in this work, EKF and RLS, were formulated to be completed offline. However, these methods can be used online in conjunction with TSCS. If formulated in an online manner, the parameter estimation techniques can be used to actively update any uncertain parameters associated with the application of TSCS. Uncertainties in parameters associated with application to consumer vehicles can arise for various reasons, such as aging of components, changes in oil properties, vehicle modifications, and environmental changes. These methods can also be written in a feedforward manner, which prevents the application of TSCS from requiring any feedback.

6.3.3 Application of two-scale command shaping to other automotive-related problems

Due to the straightforward nature of TSCS, the strategy may also prove useful for other HEV-related drivability issues. Vibration-related issues could occur in HEVs during mode transitions, clutch engagements, and torque coordination between the ICE and EM. These possible applications for TSCS will be explored to determine the possible benefit over traditional mitigation techniques. A prime candidate for application of TSCS is the

mitigation of starting judder in vehicles arising from clutch engagement during the starting process [97].

6.3.4 Application of two-scale command shaping to other dynamic systems

In addition to automotive applications, TSCS could be effective in other dynamic systems, such as various hybrid dynamical systems [98]. One such hybrid dynamical system that has physical applicability is the impact oscillator [99]. TSCS could be applied to an impact oscillator to provide a feedforward technique to move the system without impact and minimal residual oscillations. Examples of impact oscillators include gear trains, bearings, and nonlinear vibration absorbers [99].

TSCS could also prove valuable in the application of command shaping to micro- and nano-scale systems. Al Ba'ba'a *et al.* demonstrated that command shaping could be used to induce band gap-like behaviour in elastic monatomic lattices [100]. TSCS can be applied alongside such techniques to increase the efficacy of the induced band gap-like behaviour in microstructures.

APPENDIX A. ADDITIONAL EQUATIONS

The linearized state matrix of the augmented system for the estimation of the nonlinear coefficient and linear natural frequency of the undamped Duffing oscillator with cubic and quadratic nonlinearities is

$$\mathrm{A}_A(k) = \left.\frac{\partial f_A}{\partial x_a}\right|_{x_A=\hat{x}_A(k-1)}$$

$$= \begin{bmatrix} 0 & 0 & 1 & 0 \\ -\widehat{\omega}_n(k-1)^2 - \hat{\varepsilon}(k-1)\left(3\hat{x}(k-1)^2 + 2\hat{x}(k-1)\right) & 0 & -(\hat{x}(k-1)^3 + \hat{x}(k-1)^2) & -2\widehat{\omega}_n(k-1)\hat{x}(k-1) \\ 0 & 0 & 0 & 0 \\ 0 & 0 & 0 & 0 \end{bmatrix} \tag{A.1}$$

The linearized state matrix of the augmented system for the estimation of the friction parameters of an ICE is given by

$$\mathbf{A}_A(k) = \left.\frac{\partial \boldsymbol{f}}{\partial \boldsymbol{x}_a}\right|_{x_A=\hat{x}_A(k-1)}$$

$$= \begin{bmatrix} 0 & 0 & 1 & 0 & 0 & 0 & 0 & 0 \\ 0 & 0 & 0 & 1 & 0 & 0 & 0 & 0 \\ \dfrac{-k_{CL} - \frac{\partial T_{Friction}}{\partial \hat{\theta}_E}(k-1) + \frac{\partial T_{Indicated}}{\partial \hat{\theta}_E}(k-1)}{J_E + J_M} & \dfrac{k_{CL}}{J_E + J_M} & \dfrac{-c_{CL} - 4\hat{k}_{\omega_1}(k-1) - 8\hat{k}_{\omega_2}(k-1)\hat{\theta}_E(k-1)}{J_E + J_M} & \dfrac{c_{CL}}{J_E + J_M} & \dfrac{-1}{J_E + J_M} & \dfrac{-p\left(\hat{\theta}_E(k-1)\right)}{J_E + J_M} & \dfrac{-4\hat{\theta}_E(k-1)}{J_E + J_M} & \dfrac{-4\hat{\theta}_E(k-1)^2}{J_E + J_M} \\ \dfrac{k_{CL}}{J_{CL}} & \dfrac{-k_{CL}}{J_{CL}} & \dfrac{c_{CL}}{J_{CL}} & \dfrac{-c_{CL}}{J_{CL}} & 0 & 0 & 0 & 0 \\ 0 & 0 & 0 & 0 & 0 & 0 & 0 & 0 \\ 0 & 0 & 0 & 0 & 0 & 0 & 0 & 0 \\ 0 & 0 & 0 & 0 & 0 & 0 & 0 & 0 \\ 0 & 0 & 0 & 0 & 0 & 0 & 0 & 0 \end{bmatrix} \tag{A.2}$$

When estimating the inertia of the crankshaft and counterbalances, the linearized state matrix is defined as

$$\mathbf{A}_A(k) = \left.\frac{\partial \boldsymbol{f}}{\partial \boldsymbol{x}_a}\right|_{x_A=\hat{x}_A(k-1)} = \begin{bmatrix} 0 & 0 & 1 & 0 & 0 \\ 0 & 0 & 0 & 1 & 0 \\ \dfrac{-k_{CL} - \frac{\partial T_{Friction}}{\partial \hat{\theta}_E}(k-1) + \frac{\partial T_{Indicated}}{\partial \hat{\theta}_E}(k-1)}{\hat{J}_{EM}(k-1)} & \dfrac{k_{CL}}{\hat{J}_{EM}(k-1)} & \dfrac{-c_{CL} - 4k_{\omega_1} - 8k_{\omega_2}\hat{\theta}_E(k-1)}{\hat{J}_{EM}(k-1)} & \dfrac{c_{CL}}{\hat{J}_{EM}(k-1)} & \dfrac{\partial \boldsymbol{f}}{\partial \hat{J}_{EM}}(k-1) \\ \dfrac{k_{CL}}{J_{CL}} & \dfrac{-k_{CL}}{J_{CL}} & \dfrac{c_{CL}}{J_{CL}} & \dfrac{-c_{CL}}{J_{CL}} & 0 \\ 0 & 0 & 0 & 0 & 0 \end{bmatrix} \tag{A.3}$$

where $\frac{\partial \boldsymbol{f}}{\partial \hat{J}_{EM}}(k-1)$ is given by

$$\frac{\partial \boldsymbol{f}}{\partial \hat{J}_{EM}}(k-1) = \frac{-1}{\hat{J}_{EM}(k-1)^2}\Big(T_{Indicated}\left(\hat{\theta}_E(k-1)\right) - T_{Friction}\left(\hat{\theta}_E(k-1), \hat{\dot{\theta}}_E(k-1)\right) + T_M(t) + k_{CL}\left(\hat{\theta}_{CL}(k-1) - \hat{\theta}_E(k-1)\right) + c_{CL}\left(\hat{\dot{\theta}}_{CL}(k-1) - \hat{\dot{\theta}}_E(k-1)\right)\Big) \tag{A.4}$$

APPENDIX B. ADDITIONAL DATA

Table B-1 – 1.3 L JTD inline four-cylinder ICE model parameters.

Parameter	Value
Crank radius (r), m [71]	4.10E-02
Connecting rod length (l), m [71]	7.18E-02
Clearance volume (V_C), m^3 [71]	1.84E-05
Cylinder bore (B), m [71]	6.96E-02
Swept cylinder volume (V_S), m^3 [71]	3.12E-04
Compression ratio (C_R), Unitless [71]	1.80E+01
Angle between firing events (θ_{FE}), ° [69]	1.80E+02
Specific heat ratio (γ), Unitless	1.36E+00
Polytropic process constant (C), $Pam^{3\gamma}$	3.87E-02
Start of premixed combustion (θ_{SOCP}), ° [71]	-1.60E+00
Premixed combustion duration ($\Delta\theta_P$), ° [71]	5.24E+00
Premixed combustion shape factor (m_P), Unitless [71]	1.41E+00
Premixed combustion Wiebe correlation parameter (a_P), Unitless [71]	5.00E+00
Mass of fuel injected during premixed combustion (m_{iP}), kg [71]	8.00E-06
Fraction of fuel burned during premixed combustion (x_{fP}), Unitless [71]	3.30E-01
Start of main combustion (θ_{SOCM}), ° [71]	1.89E+00
Main combustion duration ($\Delta\theta_M$), ° [71]	5.24E+00
Main combustion shape factor (m_M), Unitless [71]	1.09E+00
Main combustion Wiebe correlation parameter (a_M), Unitless [71]	5.00E+00
Mass of fuel injected during main combustion (m_{iM}), kg [71]	8.00E-06
Fraction of fuel burned during main combustion (x_{fM}), Unitless [71]	1.40E-01
Start of diffusive combustion (θ_{SOCD}), ° [71]	3.39E+00
Diffusive combustion duration ($\Delta\theta_D$), ° [71]	4.42E+01
Diffusive combustion shape factor (m_D), Unitless [71]	2.10E-01
Diffusive combustion Wiebe correlation parameter (a_D), Unitless [71]	5.00E+00
Mass of fuel injected during diffusive combustion (m_{iD}), kg [71]	8.00E-06
Fraction of fuel burned during diffusive combustion (x_{fD}), Unitless [71]	5.70E-01
Lower heating value of the diesel fuel (LHV), J/kg [71]	42.5E+06
Ambient pressure ($p_{Ambient}$), Pa	1.01E+05
ICE reciprocating component mass ($M_{Inertial}$), kg [5, 69, 71]	2.29E-01
Constant friction torque coefficient ($T_{Friction_0}$), Nm [5, 71]	8.75E-02
Pressure friction torque coefficient (k_p), Nm/Pa [5, 71]	1.25E-06
First-order angular velocity friction torque coefficient (k_{ω_1}), Nms/rad [5, 71]	6.75E-02
Second-order angular velocity friction torque coefficient (k_{ω_2}), Nms^2/rad^2 [5, 71]	1.80E-03

Table B-2 – Torsional model parameters for the experimental apparatus powertrain.

Parameter	Value
Approximate moment of inertia of the ICE crankshaft (J_E), kgm^2 [101]	8.00E-02
Moment of inertia of the EM rotor (J_M), kgm^2 [102]	2.83E-02
Moment of inertia of the inertial element (J_{IE}), kgm^2	1.40E-02
Moment of inertia of ICE spur gear (J_{G1}), kgm^2	1.06E-02
Moment of inertia of EM spur gear (J_{G2}), kgm^2	1.06E-02
Number of teeth on Gear 1 (N_{G1}), Unitless	6.00E+01
Number of teeth on Gear 2 (N_{G2}), Unitless	6.00E+01
Stiffness element between ICE and ICE spur gear (k_E), Nm/rad	1.42E+05
Stiffness element between ICE spur gear and inertial element (k_{IE}), Nm/rad	6.15E+04
Stiffness element between EM and EM spur gear (k_M), Nm/rad	4.45E+05

Table B-3 – Torsional model parameters for the experimental apparatus frame.

Parameter	Value
Approximate Moment of Inertia of the ICE block (J_{EB}), kgm^2 [103]	3.51E+00
Approximate Moment of Inertia of the EM housing (J_{MB}), kgm^2 [102]	3.20E-01
Moment of inertia representing the frame (J_F), kgm^2	1.33E+00
Mass of the ICE block (m_{EB}), kg [103]	9.20E+01
Mass of the EM housing (m_{MB}), kg [102]	3.80E+01
Width of the ICE (l_E), m [103]	4.39E-01
Height of the ICE (h_E), m [103]	5.16E-01
Diameter of the EM (d_M), m [102]	2.59E-01
Stiffness element representing ICE mounts (k_{CE}), Nm/rad	7.89E+03
Stiffness element representing EM mounts (k_{CM}), Nm/rad	5.25E+02
Stiffness element representing rubber pads of frame (k_F), Nm/rad	2.78E+04

Table B-4 –1.03 L Kohler inline three-cylinder ICE model parameters.

Parameter	Value
Crank radius (r), m [103]	3.88E-02
Connecting rod length (l), m [103]	6.79E-02
Clearance volume (V_C), m^3 [103]	1.57E-05
Cylinder bore (B), m [103]	7.50E-02
Swept cylinder volume (V_S), m^3 [103]	3.42E-04
Compression ratio (C_R), Unitless [103]	2.28E+01
Angle between firing events (θ_{FE}), ° [69]	2.40E+02
Specific heat ratio (γ), Unitless	1.36E+00
Polytropic process constant (C), $Pam^{3\gamma}$	3.88E-02
Start of premixed combustion (θ_{SOCP}), ° [71]	-1.60E+00
Premixed combustion duration ($\Delta\theta_P$), ° [71]	5.24E+00
Premixed combustion shape factor (m_P), Unitless [71]	1.41E+00
Premixed combustion Wiebe correlation parameter (a_P), Unitless [71]	5.00E+00
Mass of fuel injected during premixed combustion (m_{iP}), kg [71]	8.00E-06
Fraction of fuel burned during premixed combustion (x_{fP}), Unitless [71]	3.30E-01
Start of main combustion (θ_{SOCM}), ° [71]	1.89E+00
Main combustion duration ($\Delta\theta_M$), ° [71]	5.24E+00
Main combustion shape factor (m_M), Unitless [71]	1.09E+00
Main combustion Wiebe correlation parameter (a_M), Unitless [71]	5.00E+00
Mass of fuel injected during main combustion (m_{iM}), kg [71]	8.00E-06
Fraction of fuel burned during main combustion (x_{fM}), Unitless [71]	1.40E-01
Start of diffusive combustion (θ_{SOCD}), ° [71]	3.39E+00
Diffusive combustion duration ($\Delta\theta_D$), ° [71]	4.42E+01
Diffusive combustion shape factor (m_D), Unitless [71]	2.10E-01
Diffusive combustion Wiebe correlation parameter (a_D), Unitless [71]	5.00E+00
Mass of fuel injected during diffusive combustion (m_{iD}), kg [71]	8.00E-06
Fraction of fuel burned during diffusive combustion (x_{fD}), Unitless [71]	5.70E-01
Lower heating value of the diesel fuel (LHV), J/kg [71]	42.5E+06
Ambient pressure ($p_{Ambient}$), Pa	1.01E+05
ICE reciprocating component mass ($M_{Inertial}$), kg [5, 69, 71]	2.29E-01
Constant friction torque coefficient ($T_{Friction_0}$), Nm [5, 71]	7.50E-04
Pressure friction torque coefficient (k_p), Nm/Pa [5, 71]	3.26E-07
First-order angular velocity friction torque coefficient (k_{ω_1}), Nms/rad [5, 71]	3.20E-05
Second-order angular velocity friction torque coefficient (k_{ω_2}), Nms^2/rad^2 [5, 71]	9.71E-04

Table B-5 – Experimentally obtained vibration modes of the apparatus frame.

Parameter	Value
Vibration mode 1, Hz	6.3E+00
Vibration mode 2, Hz	1.4E+01
Vibration mode 3, Hz	3.5E+01
Vibration mode 4, Hz	4.4E+01
Vibration mode 5, Hz	5.5E+01
Vibration mode 6, Hz	6.0E+01
Vibration mode 7, Hz	7.3E+01
Vibration mode 8, Hz	8.6E+01

REFERENCES

[1] Daqaq, M.F., and Masoud, Z.N., 2006, "Nonlinear input-shaping controller for quay-side container cranes," Nonlinear Dynamics, **45**(1-2), pp. 149-170.

[2] Singhose, W., 2009, "Command shaping for flexible systems: A review of the first 50 years," International Journal of Precision Engineering and Manufacturing, **10**(4), pp. 153-168.

[3] Daqaq, M., Reddy, C., and A. Nayfeh, 2008, "Input-shaping control of nonlinear MEMS," Nonlinear Dynamics, **54**(1-2), pp. 167-179.

[4] Daqaq, M.F., 2006, "Adaptation of nontraditional control techniques to nonlinear micro and macro mechanical systems," Ph.D. thesis, Virginia Polytechnic Institute and State University, Blacksburg, VA.

[5] Canova, M., Guezennec, Y., and Yurkovich, S., 2009, "On the control of engine start/stop dynamics in a hybrid electric vehicle," ASME Journal of Dynamic Systems, Measurement and Control, **131**(6), pp. 061005.

[6] Park, K., Lee, J., and Park, J., 2013, "Torque control of a vehicle with electronic throttle control using an input shaping method, **14**(2), pp. 189-194.

[7] Wilbanks, J.J., and Leamy, M.J., 2017, "Two-Scale Command Shaping for Reducing Powertrain Vibration during Engine Restart," ASME Journal of Dynamic Systems, Measurement, and Control, **139**(9), pp. 091004.

[8] Singer, N.C., and Seering, W.P., 1990, "Preshaping command inputs to reduce system vibration," ASME Journal of Dynamic Systems, Measurement, and Control, **112**(1), pp. 76-82.

[9] Vaughan, J., Yano, A., and Singhose, W., 2008, "Comparison of robust input shapers," Journal of Sound and Vibration, **315**(4), pp. 797-815.

[10] Singhose, W., Seering, W., and Singer, N., 1994, "Residual vibration reduction using vector diagrams to generate shaped inputs," ASME Journal of Mechanical Design, **116**(2), pp. 654-659.

[11] Vaughan, J., and Singhose., W., 2010, "Reducing Multiple Modes of Vibration by Digital Filtering and Input Shaping," ASME 2010 Dynamic Systems and Control Conference, Cambridge, MA, Sept. 12-15, pp. 591-597.

[12] Smith, O.J., 1957, "Posicast control of damped oscillatory systems," Proceedings of the IRE, **45**(9), pp. 1249-1255.

[13] Smith, O.J., 1958, *Feedback control systems,* McGraw-Hill, New York, NY.

[14] Singer, N.C., 1989, "Residual vibration reduction in computer controlled machines," Ph.D. thesis, Massachusetts Institute of Technology, Cambridge, MA.

[15] Singhose, W., Seering, W., and Singer, N.C., 1997, "Time-optimal negative input shapers ," ASME Journal of Dynamic Systems, Measurement, and Control, **119**(2), pp. 198-205.

[16] Pao, L.Y., and Singhose, W., 1995, "On the equivalence of minimum time input shaping with traditional time-optimal control,"Fourth IEEE Conference on Control Applications, Albany, NY, Sept. 28-29, pp. 1120-1125.

[17] Alsop, C., Forster, G., and Holmes, F., 1965, "Ore unloader automation—a feasibility study," IFAC Tokyo Symposium on Systems Engineering for Control Systems, Tokyo, JP, pp. 295-305.

[18] Singhose, W., Kim, D., and Kenison, M., 2008, "Input shaping control of double-pendulum bridge crane oscillations," ASME Journal of Dynamic Systems, Measurement, and Control, **130**(3), pp. 034504.

[19] Singhose, W., Porter, L., Kenison, M., and Kriikku, E., 2000, "Effects of hoisting on the input shaping control of gantry cranes," Control Engineering Practice, **8**(10), pp. 1159-1165.

[20] Vaughan, J., Kim, D., and Singhose, W., 2010, "Control of tower cranes with double-pendulum payload dynamics," IEEE Transactions on Control Systems Technology, **18**(6), pp. 1345-1358.

[21] Popa, D.O., Byoung, H.K., Wen, J.T., Stephanou, H.E., Skidmore, G., and Geisberger, A., 2003, "Dynamic modeling and input shaping of thermal bimorph MEMS actuators," in 2003 IEEE International Conference on Robotics and Automation, Taipai, Taiwan, Sept. 14-19, pp. 1470-1475.

[22] Togai, K., and Platten, M., 2012, "Input Torque Shaping for Driveline NVH Improvement and Torque Profile Approximation Problem with Combustion Pressure," FISITA 2012 World Automotive Congress, Beijing, China, Nov, 27-30, pp. 151-165.

[23] Singhose, W., Derezinski, S., and Singer, N., 1996, "Extra-insensitive input shapers for controlling flexible spacecraft," Journal of Guidance, Control, and Dynamics, **19**(2), pp. 385-391.

[24] Sorensen, K.L., 2008, "Operational performance enhancement of human operated flexible systems," Ph.D. thesis, Georgia Institute of Technology, Atlanta, GA.

[25] Bradley, T.H., Danielson, J., Lawrence, J., and Singhose, W., 2008, "Command shaping under nonsymmetrical acceleration and braking dynamics," Journal of Vibration and Acoustics, **130**(5), pp. 054503.

[26] Blackburn, D., Singhose, W., Kitchen, J. Patrangenaru, V., Lawrence, J., Kamoi, T., and Taura, A., 2010, "Command shaping for nonlinear crane dynamics," Journal of Vibration and Control, **16**(4), pp. 477-501.

[27] Smith, J.Y., Kozak, K., and Singhose, W., 2002, "Input shaping for a simple nonlinear system," 2002 American Control Conference,Anchorage, AK, May 8-10, pp. 821-826.

[28] Morrow, W. R., Gallagher, K. S., Collantes, G., and Lee, H., 2010, "Analysis of Policies to Reduce Oil Consumption and Greenhouse-Gas Emissions From the U.S. Transportation Sector," Energy Policy, **38**(3), pp. 1305–1320.

[29] Vimmerstedt, L., Brown, A., Heath, G., Mai, T., Ruth, M., Melaina, M., Simpkins, T., Steward, D., and Warner, E., 2012, "High Penetration of Renewable Energy in the Transportation Sector: Scenarios, Barriers, and Enablers," World Renewable Energy Forum, Denver, CO, NREL Report No. CP-6A20-54442.

[30] Intergovernmental Panel on Climate Change, 2015, *Climate Change 2014: Mitigation of Climate Change*, Cambridge University Press, New York, NY.

[31] Creutzig, F., Jochem, P., Edelenbosch, O.Y., Mattauch, L., van Vurren, D.P., McCollum, D., and Minx, J., 2015, "Transport: A roadblock to climate change mitigation?" Science, **350**(6263): p. 911-912.

[32] Brooke, L., 2014, "GM Unveils More Efficient 2016 Volt Powertrain," SAE Automotitive Engingeering Magazine, **1**(8), p. 12.

[33] Taub, E.A., 2016, "Start-Stop Technology Is Spreading (Like It or Not)," The New York Times, New York, NY, accessed Aug. 6, 2018, https://www.nytimes.com/2016/04/08/automobiles/wheels/start-stop-technology-is-coming-to-cars-like-it-or-not.html.

[34] Vettraino, J.P., 2016, "2017 Mercedes-Benz E-Class first drive: A luxury standby gets a tech megadose," Autoweek, Detroit, MI, accessed Aug. 6, 2018, https://autoweek.com/ article/car-reviews/2017-mercedes-benz-e300-first-drive.

[35] Hellwig, E., 2015, "2015 Porsche Macan S: Rough Start/Stop System," Edmunds, Santa Monica, CA, accessed Aug. 6, 2018, https://www.edmunds.com/porsche/macan/2015/long-term-road-test/2015-porsche-macan-rough-start-stop-system.html.

[36] Rechtin, M., 2013, "Why this BMW's stop-start is a non-starter," Automotive News, Detroit, MI, accessed Aug. 6, 2018, http://www.autonews.com/article/20130928/BLOG06/130929889/why-this-bmws-stop-start-is-a-non-starter.

[37] Kum, D., Peng, H., and Bucknor, N. K., 2011, "Supervisory Control of Parallel Hybrid Electric Vehicles for Fuel and Emission Reduction," ASME Journal of Dynamic Systems, Measurement, and Control, **133**(6), pp. 061010.

[38] Zuo, Y. H., Xiang, C. L., Yan, Q. D., and Wang, Y. Z., 2010, "Engine Start Control Strategy Research for Parallel–Series Hybrid Electrical Vehicles," Eighth World Congress on Intelligent Control and Automation (WCICA), Jinan, China, July 7–9, pp. 2097–2102.

[39] Wang, C. L., Yin, C. L., Luo, G., Guo, Z. Q., and Gai, F. X., 2011, "Start and Acceleration Optimization of a Parallel Hybrid Electric Vehicle," Journal of Automobile Engineering, **225(**5), pp. 591–607.

[40] Wilbanks, J.J., Leamy, M.J., 2016, "Analyzing the Robustness of Two-Scale Command Shaping for Reducing Powertrain Vibration During Engine Restart," ASME 2016 International Design Engineering Technical Conferences and Computers and Information in Engineering Conference, Charlotte, NC, Aug. 21-24, pp. V008T10A008.

[41] Singh, T., and Vadali, S., "Robust time-delay control," ASME Journal of Dynamic Systems, Measurement, and Control, **115**(2A), pp. 303-306.

[42] Rew, K.H., Ha, C.W., and Kim, K.S., 2013, "An impulse-time perturbation approach for enhancing the robustness of extra-insensitive input shapers," Automatica, **49**(11), pp. 3425-3431.

[43] Bodson, M., 1998, "An adaptive algorithm for the tuning of two input shaping methods," Automatica, **34**(6), pp. 771-776.

[44] Cutforth, C.F., and Pao, L.Y., 2004, "Adaptive input shaping for maneuvering flexible structures," Automatica, **40**(4), pp. 685-693.

[45] Pereira, E., Trapero, J.R., Díaz, I. M., and Feliu, V., 2009, "Adaptive input shaping for manoeuvring flexible structures using an algebraic identification technique," Automatica, **45**(4), pp. 1046-1051.

[46] Chowdhary, G., and Jategaonkar, R., 2010, "Aerodynamic parameter estimation from flight data applying extended and unscented Kalman filter," Aerospace Science and Technology, **14**(2), pp. 106-117.

[47] Leonard, A., 2016, "Vehicle tracking using ultra-wideband radar," M.S. thesis, Georgia Institute of Technology, Atlanta, GA.

[48] Ljung, L., 1999, *System identification: theory for the user*, Prentice Hall, Englewood Cliffs, NJ.

[49] Marquardt, D.W., 1963, "An algorithm for least-squares estimation of nonlinear parameters," Journal of the Society for Industrial and Applied Mathematics, **11**(2), pp. 431-441.

[50] Davis, M.H., and Vinter, R.B., 2013, *Stochastic modelling and control*, Chapman and Hall, London, England.

[51] Billings, S., and Voon, W., 1984, *Least squares parameter estimation algorithms for non-linear systems,* International Journal of Systems Science, **15**(6), pp. 601-615.

[52] Slotine, J.J.E., and Li, W., 1991, *Applied nonlinear control*, Prentice-Hall, Englewood Cliffs, NJ.

[53] Ryu, J., Rossetter, E. J., and Gerdes, J. C., 2002, "Vehicle Sideslip and Roll Parameter Estimation Using GPS," 6th International Symposium on Advanced Vehicle Control (AVEC), Hiroshima, Japan, Sept. 9–13, pp. 373–380.

[54] Bae, H.S., Ryu, J., and Gerdes, J.C., 2001, "Road grade and vehicle parameter estimation for longitudinal control using GPS," 2001 IEEE Conference on Intelligent Transportation Systems, Oakland, CA, Aug. 25-29, pp. 166-171.

[55] Unger, J., Hametner, C., Jakubek, S., and Quasthoff, M., 2014, :A novel methodology for non-linear system identification of battery cells used in non-road hybrid electric vehicles," Journal of Power Sources, **269**(2014), pp. 883-897.

[56] Sood, A.K., Fahs, A.A., and Henein, N.A., 1985, "Engine Fault Analysis: Part II---Parameter Estimation Approach," IEEE Transactions on Industrial Electronics, **32**(4), pp. 301-307.

[57] Duffing, G., 1918, *Erzwungene Schwingungen bei veränderlicher Eigenfrequenz und ihre technische Bedeutung*, R. Vieweg & Sohn, Braunschweig, Germany.

[58] Kovacic, I., and Brennan, M.A., 2011, *The Duffing equation: nonlinear oscillators and their behaviour*, John Wiley & Sons, West Sussex, United Kingdom.

[59] Nayfeh, A. H., and Mook, D. T., 2008, *Nonlinear Oscillations*, Wiley, New York, NY.

[60] K Kevorkian, J., and Cole, J. D., 1996, *Multiple Scale and Singular Perturbation Methods*, Springer, New York, NY.

[61] Nayfeh, A.H., 2011, *Introduction to Perturbation Techniques*, John Wiley & Sons, Hoboke, NJ.

[62] Singhose, W.E., Porter, L.J., and Singer, N.C., 1995, "Vibration reduction using multi-hump extra-insensitive input shapers," 1995 American Control Conference, Seattle, WA, Jun. 21-23, pp. 3830-3834.

[63] McGee, L.A. and Schmidt, S.F., 1985, "Discovery of the Kalman filter as a practical tool for aerospace and industry," NASA-TM-86847, NASA Ames Research Center, Moffett Field, CA.

[64] Gelb, A., 1974, *Applied optimal estimation*, MIT Press, Cambridge, MA.

[65] Montgomery, D.C., Runger, G.C., and Hubele, N.F., 2009, *Engineering statistics*, John Wiley & Sons, Hoboken, NJ.

[66] Jategaonkar, R. V. and Plaetschke, E., 1988, "Estimation of aircraft parameters using filter error methods and extended Kalman filter," DFVLR-FB, **88** (15).

[67] Grewal, M. S. and Andrews, A. P., 2001, *Kalman filtering: theory and practice using MATLAB*, John Wiley & Sons, New York, NY.

[68] Julier, S. J. and Uhlmann, J. K., 2004, "Unscented filtering and nonlinear estimation," Proceedings of the IEEE, **92**(3): p. 401-422.

[69] Ramos, J. I., 1989, *Internal Combustion Engine Modeling*, Hemisphere Publishing Corporation, New York.

[70] Taylor, C. F., 1985, *The Internal Combustion Engine in Theory and Practice (Thermodynamics, Fluid Flow, Performance)*, Vol. 1, MIT Press, Cambridge, MA

[71] Ponti, F., Serra, G., and Siviero, C., *"A Phenomenological Combustion Model for Common Rail Multi-Jet Diesel Engine,"* ASME 2004 Internal Combustion Engine Division Fall Technical Conference, Long Beach, CA, Oct. 24-27, pp. 437-446.

[72] Miyamoto, N., Chikahisa, T., Murayama, T., and Sawyer, R., 1985, "Description and Analysis of Diesel Engine Rate of Combustion and Performance Using Wiebe's Functions," SAE Technical Paper No. 850107

[73] Murayama, T., Miyamoto, N., Yamada, T., Kawashima, J. C., and Itow, K., 1982, "A Method to Improve the Solubility and Combustion Characteristics of Alcohol-Diesel Fuel Blends," SAE Technical Paper No. 821113.

[74] Chen, S. K., and Flynn, P. F., 1965, "Development of a Single Cylinder Compression Ignition Research Engine," SAE Technical Paper No. 650733.

[75] Canaparo, A., 2014, “Ferrari FF (F151) Powertrain Specification Data,” Ferrari S.p.A., Maranello, Italy.

[76] Iskra Avtoelektrika, D. D., 2008, “Integrated Starter Motor Generators Specifications,” Iskra Avtoelektrika D.D., Polje, Slovenia, accessed November 5, 2015, https://www.kwikwap.co.za/electrodiesel/docs/DC%20Integrated%20Flywheel %20Generator.pdf.

[77] Mantic Clutch, 2011, “Clutch Technical Specifications,” Mantic Engineering, Victoria, Australia, accessed Dec. 8, 2015, http://mantic.com.au/sub_technical/ multi_v_single.html.

[78] General Motors, 2015, “2016 Chevrolet Camaro Powertrain CAD Data (EcoCAR 3),” General Motors, Detroit, MI.

[79] Zero-Max, 2015, “Flexible Shaft Coupling Specifications,” Zero-Max, Plymouth, MN, accessed Dec. 7, 2015, http://www.zero-max.com/flexible-shaft-couplingsc-1-l-en.html.

[80] Ooi, L. E., and Ripin, Z. M., 2011, “Dynamic Stiffness and Loss Factor Measurement of Engine Rubber Mount by Impact Test,” Mater. Des., 32(4), pp. 1880–1887.

[81] Fiat Chrysler Automobiles, 2003, “The Diesel of the Future: 1.3 Multijet 16v,” Fiat Chrysler Automobiles, London, England, accessed Nov. 5, 2015, http://www.fiat press.com/ press/ detail/6523.

[82] Miller, J. M., 2004, *Propulsion Systems for Hybrid Vehicles*, Vol. 45, IET, Stevenage, UK.

[83] Heydinger, G. J., Bixel, R. A., Garrott, W. R., Pyne, M., Howe, J. G., and Guenther, D. A., 1999, “Measured Vehicle Inertial Parameters—NHTSA’s Data Through November 1998,” SAE Technical Paper No. 1999-01-1336.

[84] Alkhatib, F., 2013, “Techniques for Engine Mount Modeling and Optimization,” Ph.D. thesis, University of Wisconsin-Milwaukee, Milwaukee, WI.

[85] Moseler, O. and R. Isermann, 2000, "Application of model-based fault detection to a brushless DC motor," IEEE Transactions on Industrial Electronics, **47**(5), pp. 1015-1020.

[86] Rodriguez, F. and A. Emadi, 2007, "*A novel digital control technique for brushless DC motor drives,"* IEEE Transactions on Industrial Electronics, **54**(5), pp. 2365-2373.

[87] Larminie, J., and Lowry, J., 2004, Electric Vehicle Technology Explained,Wiley, New York, NY.

[88] Singhose, W., Porter, L. J., Tuttle, T. D., and Singer, N., 1997, "Vibration Reduction Using Multi-Hump Input Shapers," ASME Journal of Dynamic Systems, Measurement, and Control, **119**(2), pp. 320–326.

[89] Narendra, K.S., and Annaswamy, A.M., 1987, "Persistent excitation in adaptive systems," International Journal of Control, **45**(1), pp. 127-160.

[90] Wilbanks, J.J., and Leamy, M.J., "Uncertain Parameter Estimation Approaches for Increasing the Effectiveness of Command-Shaped Engine Restart Strategies," ASME 2017 International Design Engineering Technical Conferences and Computers and Information in Engineering Conference, Cleveland, OH, Aug. 6-9, pp. V008T12A011.

[91] Wilbanks, J.J., and Leamy, M.J., 2018, "Two-Scale Command Shaping for Feedforward Control of Nonlinear Systems," Nonlinear Dynamics, **92**(3), pp. 885-903.

[92] Frolov, K., 1981, *Protection against vibrations and shocks*, Vol. 6, Mashinostroyenie, Moscow, Russia.

[93] Karnovsky, I.A., and Lebed, E., 2016, *Theory of vibration protection*, Springer, Cham, Switzerland.

[94] Knothe, K., and Stichel, S., 2017, *Rail Vehicle Dynamics*, Springer, Cham, Switzerland, Chapter 7.

[95] Forta, N.G., Morioka, M., and Griffin, M.J., 2009, "Difference thresholds for the perception of whole-body vertical vibration: dependence on the frequency and magnitude of vibration," Ergonomics, **52**(10), pp. 1305-1310.

[96] Griffin, M.J., 2012, *Handbook of human vibration*, Academic Press Incorporated, San Diego, CA.

[97] Li, L., Lu, Z., Liu, X.L., Sun, T., Jing, X., and Shangguan, W.B., 2018, "Modeling and analysis of friction clutch at a driveline for suppressing car starting judder," Journal of Sound and Vibration, **424**, pp. 335-351.

[98] Goebel, R., Sanfelice, R.G., and Teel, A.R., "Hybrid dynamical systems," IEEE Control Systems, **29**(2), pp. 28-93.

[99] Bishop, S., 1994, "Impact oscillators," Philosophical Transaction of the Royal Society A: Mathematical, Physical, and Engineering Sciences, **347**(1683), pp. 347-351.

[100] Al Ba'ba'a, H., Callanan, J., Nouh, M., and Singh, T., 2018, "Band gap synthesis in elastic monatomic lattices via input shaping," Meccanica, **53**(11-12), pp. 1-18.

[101] Hudson, J.W., 1997, "*Development and calibration of a torsional engine model for a three-cylinder, two-stroke diesel engine*," M.S. thesis, Naval Postgraaduate School, Monterey, CA.

[102] Parker Hannafin Electromechanical Automation, 2015, "Global Vehicle Motors Technical Manual," Parker Hannafin, Offenberg, Germany, accessed Jan. 15, 2017, http://www.parker.com/Literature/Electromechanical%20Europe/User%20Guides /PVD3668_GB%20GVM.pdf.

[103] Kohler Company Engine Division, 2013, "*KDW 1003 Owner's Manual*," Kohler Company, Kohler, WI, http://www.kohlerengines.com/onlinecatalog/pdf/ ed00530 28440_ om_ kdw702_1003_1404.pdf.